

5-2018

## Mass Spectrometric Methods Development for the Characterization of Components in Complex Mixtures for Enhanced Oil Recovery Operations and for Drug Development

Ravikiran Yerabolu  
*Purdue University*

Follow this and additional works at: [https://docs.lib.purdue.edu/open\\_access\\_dissertations](https://docs.lib.purdue.edu/open_access_dissertations)

---

### Recommended Citation

Yerabolu, Ravikiran, "Mass Spectrometric Methods Development for the Characterization of Components in Complex Mixtures for Enhanced Oil Recovery Operations and for Drug Development" (2018). *Open Access Dissertations*. 1894.  
[https://docs.lib.purdue.edu/open\\_access\\_dissertations/1894](https://docs.lib.purdue.edu/open_access_dissertations/1894)

This document has been made available through Purdue e-Pubs, a service of the Purdue University Libraries.  
Please contact [epubs@purdue.edu](mailto:epubs@purdue.edu) for additional information.

**MASS SPECTROMETRIC METHODS DEVELOPMENT FOR THE  
CHARACTERIZATION OF COMPONENTS IN COMPLEX MIXTURES  
FOR ENHANCED OIL RECOVERY OPERATIONS AND FOR DRUG  
DEVELOPMENT**

by

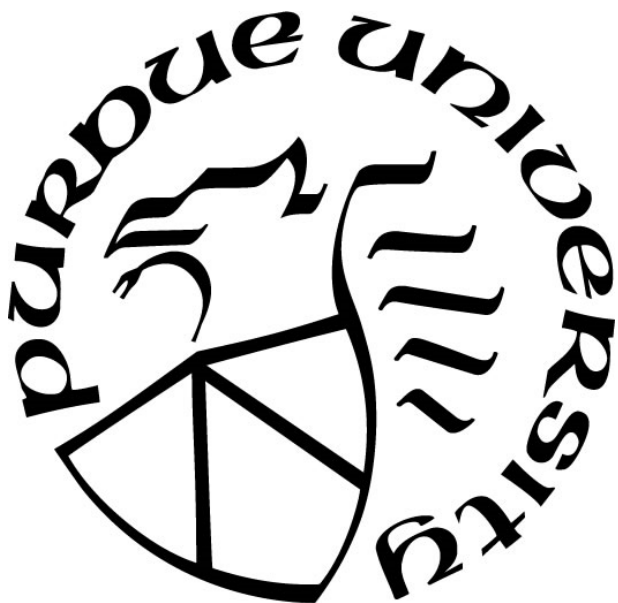
**Ravikiran Yerabolu**

**A Dissertation**

*Submitted to the Faculty of Purdue University*

*In Partial Fulfillment of the Requirements for the degree of*

**Doctor of Philosophy**



Department of Chemistry

West Lafayette, Indiana

May 2018

**THE PURDUE UNIVERSITY GRADUATE SCHOOL**  
**STATEMENT OF COMMITTEE APPROVAL**

Dr. Hilikka I. Kenttämäa, Chair  
Department of Chemistry

Dr. Chengde Mao  
Department of Chemistry

Dr. Peter T. Kissinger  
Department of Chemistry

Dr. Christopher Uyeda  
Department of Chemistry

**Approved by:**

Dr. Christine A. Hrycyna  
Head of the Graduate Program

*To my beloved brother,*

*Vijay Kethireddy*

*Without your support and unconditional love, I would not have become who I am  
today.*

## ACKNOWLEDGMENTS

Firstly, I would like to express my sincere gratitude to my advisor, Professor Hilkka I. Kenttämäa. Her scientific acumen, supervision and her willingness to dedicate her valuable time towards training graduate students were instrumental in my success. In addition to learning advanced analytical skills, I have gained experience working in collaborations, critical thinking and writing, and being able to communicate my research results efficiently while working in her lab. I would like to heartfully thank her for creating such a great platform.

Also, there are many past and present members of the Kenttämäa group, who have been instrumental in my success. I would like to thank Dr. Huaming Sheng, Dr. James Riedeman, Dr. Weijuan Tang, Dr. Christopher Marcum, Dr. Mohammed Sabir and Dr. Tiffany Jarrell for their help, advice and mentorship during the beginning of my career in graduate school. Dr. Raghavendhar Kotha, Dr. Mckay Easton, Dr. Priya Murria, Dr. Hanyu Zhu, Dr. Chunfen Jin, John Kong, Mark Romanczyk, Edouard Niyonsaba, Jeremy Manheim, Leah Felice Easterling and Rashmi Kumar have been contemporaries, who I much enjoyed working with, in finding answers to challenging research problems. As a part of my graduate research, I have also had an excellent opportunity to work on collaborative projects with Pioneer Oil Company and AstraZeneca. I would like to thank my collaborators, especially, Dr. Cliff T. Johnston, Dr. Minli Zhang and Dr. Chungang Gu for their valuable insights and support.

I would like to express my heartfelt gratitude for my mom, dad, and sister who have always stood by me and been very supportive throughout my life. I would like to acknowledge my wife for bearing with me and believing in me. You have been a real motivation, and I am fortunate to have you by my side. I also want to acknowledge my friends, Manali, Yamini Tej, Rajani, Sravya, Bharath and Pavan for their encouragement. Finally, but most importantly, I would like to thank

my brother, Vijay and his wife, Trupthi, who has always been supportive of my goals and encouraged me to continue my studies in graduate school and pursue a Ph.D.

## TABLE OF CONTENTS

LIST OF TABLES.....	x
LIST OF FIGURES .....	xii
ABSTRACT.....	xx
CHAPTER 1. INTRODUCTION AND OVERVIEW .....	1
1.1 Introduction.....	1
1.2 Thesis Overview .....	2
1.3 References.....	5
CHAPTER 2. INSTRUMENTATION AND EXPERIMENTAL ASPECTS OF LINEAR QUADRUPOLE ION TRAP MASS SPECTROMETERS, HIGH RESOLUTION ORBITRAP MASS SPECTROMETERS AND TIME-OF-FLIGHT MASS SPECTROMETERS.....	6
2.1 Introduction.....	6
2.2 Linear Quadrupole Ion Trap (LQIT) Mass Spectrometer.....	7
2.2.1 Atmospheric Pressure Ionization (API) Region .....	10
2.2.2 The Ion Optics Region.....	10
2.2.3 Ion Trap (Mass Analyzer) Region.....	12
2.2.4 Ion Detection Region.....	13
2.3 Ion Trap Scan Functions .....	15
2.3.1 Ion Trapping .....	15
2.3.1.1 Trapping Ions in the Radial (xy) Direction .....	15
2.3.1.2 Trapping Ions in the Axial (z) Direction .....	18
2.3.1.3 Stabilizing Ions in the Trap by Using Helium.....	19
2.3.2 Ion Ejection for Detection .....	20
2.3.3 Ion Isolation.....	21
2.3.4 Collision-activated Dissociation.....	24
2.4 Ion/Molecule Reactions .....	27
2.5 Ionization Methods .....	30
2.5.1 Electrospray Ionization (ESI) .....	30
2.5.2 Atmospheric Pressure Chemical Ionization (APCI).....	34
2.5.3 Atmospheric Pressure Photo Ionization (APPI) .....	35
2.5.4 Electron Ionization (EI) in GCxGC/TOF MS .....	37
2.6 Orbitrap Mass Spectrometry.....	38

2.6.1	Equations of Motion for Ions in the Orbitrap .....	41
2.6.2	Ion Injection.....	42
2.6.3	Ion Detection .....	43
2.7	Medium Energy Collision-activated Dissociation (MCAD) .....	44
2.8	Chromatography/Mass Spectrometry .....	46
2.8.1	High-performance Liquid Chromatography/Mass Spectrometry (HPLC/MS) .....	46
2.8.2	Two-Dimensional Gas Chromatography/Mass Spectrometry (GCxGC/MS) .....	46
2.8.2.1	Two-Dimensional Gas Chromatography (GCxGC) .....	47
2.8.2.2	GCxGC Method Development .....	50
2.8.2.2.1	Modulation Period.....	50
2.8.2.2.2	Temperature Ramp and Temperature Off-set .....	52
2.8.2.3	Folded Flight Path Time-of-Flight Mass Analyzer (FFP TOF) .....	53
2.9	References.....	55
<b>CHAPTER 3. IDENTIFICATION OF SULFONE AND AROMATIC CARBOXYLIC ACID FUNCTIONALITIES IN PROTONATED ORGANIC MOLECULES BY USING ION-MOLECULE REACTIONS FOLLOWED BY COLLISION-ACTIVATED DISSOCIATION IN A LINEAR QUADRUPOLE ION TRAP MASS SPECTROMETER .....</b>		
3.1	Introduction.....	60
3.2	Experimental.....	61
3.2.1	Chemicals .....	61
3.2.2	Sample Preparation.....	61
3.2.3	Instrumentation.....	62
3.2.4	Computational Studies.....	63
3.3	Results and Discussion .....	63
3.3.1	Reactions of TMMS with Protonated Monofunctional Sulfones .....	67
3.3.2	Reactions of TMMS with Protonated Polyfunctional Sulfones .....	72
3.3.3	Reactions of TMMS with Protonated Aromatic Carboxylic Acids.....	75
3.3.4	Reactions of TMMS With Protonated Hydroxybenzoic Acid Isomers .....	90
3.3.5	Reactions of TMMS with Protonated Compounds Containing Sulfonamide and Aliphatic Carboxylic Acid Functionalities .....	94
3.4	Conclusions.....	98
3.5	References.....	101



CHAPTER 4. MOLECULAR PROFILING OF CRUDE OIL BY USING DISTILLATION PRECIPITATION FRACTIONATION MASS SPECTROMETRY (DPF-MS).....	104
4.1 Introduction.....	104
4.2 Experimental Section.....	106
4.2.1 Sample.....	106
4.2.2 Chemicals and Materials.....	106
4.2.3 Separation of Crude Oil into Fractions.....	107
4.3 Mass Spectrometry.....	108
4.3.1 GCxGC/TOF Mass Spectrometry.....	108
4.3.2 LQIT Orbitrap XL Mass Spectrometry.....	111
4.3.3 Ionization Methods.....	113
4.3.4 Data Processing of High Resolution Mass Spectral Data.....	114
4.4 FTIR Analysis.....	116
4.5 Results and Discussion.....	116
4.5.1 Separation of Crude Oil.....	119
4.5.2 Characterization of Individual Fractions by FTIR Spectroscopy.....	125
4.5.3 Identification of an Ionization Method for Each Individual Fraction.....	128
4.5.4 Characterization of Crude Oil Fractions by Using High-resolution Mass Spectrometry.....	135
4.5.4.1 Average Molecular Weight (Avg MW) of the Crude Oil.....	138
4.5.4.2 Molecular Profiling of Crude Oil.....	142
4.5.4.2.1 RDB Equivalence Plots.....	142
4.5.4.2.2 Compound Class Distributions.....	145
4.6 Conclusions.....	152
4.7 References.....	154
CHAPTER 5. METHOD DEVELOPMENT FOR THE IDENTIFICATION AND QUANTITATION OF TRACERS IN OIL RESERVOIR BRINE BY USING SOLID-PHASE EXTRACTION FOLLOWED BY HIGH PERFORMANCE LIQUID CHROMATOGRAPHY/TANDEM MASS SPECTROMETRY.....	157
5.1 Introduction.....	157
5.2 Experimental.....	158
5.2.1 Sample Collection and Storage.....	158
5.2.2 Chemicals, Reagents, and Solvents.....	159
5.2.3 Instrumentation.....	159

5.2.4	Materials .....	160
5.3	Procedures.....	160
5.3.1	Sample Preparation.....	160
5.3.2	HPLC and MS <sup>n</sup> Analysis Conditions.....	161
5.4	Results and Discussion .....	162
5.4.1	LC/MS Method Development .....	163
5.4.1.1	Extraction Using Solid Phase Extraction.....	164
5.4.1.2	Mass Spectrometer Optimization .....	165
5.4.1.3	MS/MS Analysis.....	166
5.4.1.3.1	Optimization of MRM Conditions .....	169
5.4.2	Method Assessment.....	170
5.4.3	Results for Oil Reservoir Brine Samples.....	173
5.5	Conclusions.....	176
5.6	References.....	177
	VITA.....	179
	PUBLICATIONS.....	180

## LIST OF TABLES

Table 3.1 Reaction products of TMMS (PA = 202 kcal/mol) (MS <sup>2</sup> experiments), fragment ions formed upon cad of the product ions (MS <sup>3</sup> experiments), and the different reaction pathways' branching ratios for protonated compounds containing n-oxide, nitro, hydroxycarboxamido, sulfoxide, amino, hydroxylamino, aniline, imino and hydroxyl functionalities. ....	64
Table 3.2 Ionic products formed for several protonated sulfones upon reactions with TMMS (PA = 202 kcal/mol) (MS <sup>2</sup> experiments), CAD product ions of [TMMS Adduct + H-MeOH] <sup>+</sup> product ions (MS <sup>3</sup> experiments), and the different reaction pathways' branching ratios. ....	69
Table 3.3 Ionic reaction products of TMMS (PA = 202 kcal/mol) (MS <sup>2</sup> experiments), fragment ions formed upon cad of [TMMS Adduct + H-MeOH] <sup>+</sup> product ions (MS <sup>3</sup> experiments, CAD energy 10) and of [TMMS Adduct + H - 2 MeOH] <sup>+</sup> fragment ions (MS <sup>4</sup> experiments, CAD energy 20), and the different reaction pathways' branching ratios for protonated sulfonamide model compounds.....	70
Table 3.4 Ionic products formed for protonated aromatic and aliphatic carboxylic acids, some with additional functionalities, upon reactions with TMMS (PA = 202 kcal/mol) (MS <sup>2</sup> experiments), CAD product ions of [TMMS Adduct + H - MeOH] <sup>+</sup> product ions (MS <sup>3</sup> experiments), CAD product ions of [TMMS Adduct + H - 2 MeOH] <sup>+</sup> (MS <sup>4</sup> experiments), and the different reaction pathways' branching ratios.....	77
Table 3.5 Calculated acidities/proton affinities of different possible protonation/deprotonation sites (B3LYP/6-311++G(d,p) level of theory) for molecules earlier reported in the literature to be deprotonated/protonated at different sites upon ESI.....	89
Table 4.1 List of chemicals, their purities, and their suppliers. ....	106
Table 4.2 Parameters optimized for the chromatographic fractionation and detection of maltenes by using a Combi-flash Rf 200 liquid chromatograph with photodiode array (PDA) detector and external evaporative light scattering (ELSD) detector. ....	108
Table 4.3 Optimal conditions used for the analysis of the distillate fraction (I) of crude oil by GC/GC/(EI)TOF. ....	109
Table 4.4 Optimal conditions and columns used for analysis of hexane eluted compounds before and after solid phase extraction. ....	110
Table 4.5 Ionization methods and optimal ion source parameters for direct injection high-resolution mass spectral analysis of crude oil fractions.....	112
Table 4.6 Gravimetric weight percent distribution of crude oil fractions obtained using DPF separation method. ....	124
Table 4.7. FTIR absorption bands and their functional group assignments. ....	126

Table 4.8 Experimental errors in Avg MW obtained using optimized ionization methods for five different model compound mixtures. ....	139
Table 4.9 Avg MW of crude oil determined from the Avg MW of individual fractions (determined using Equations 4.2 – 4.6) and their percent gravimetric weights. ....	140
Table 4.10 Compound class percentage distributions derived from high-resolution mass spectral data for the six fractions and their gravimetric weight percentages as well as the compound class distributions (highlighted in yellow) for the crude oil. ....	147
Table 5.1 Gradient conditions for the HPLC separation (lower flow rate of 0.4 mL/min was used initially to prevent backpressure spike). ....	161
Table 5.3 Multiple reaction monitoring conditions .....	169
Table 5.3 Results on levels of 2-fluorobenzoic acids in ppb (ng/mL) in the analyzed samples.....	175

## LIST OF FIGURES

Figure 2.1 Components of the linear quadrupole ion trap (LQIT) mass spectrometer, including the atmospheric pressure ionization source, API stack, ion optics, mass analyzer, and detector. Operational pressures for each region of the instrument are also indicated. ....	9
Figure 2.2 Quadrupoles that have the same RF voltage applied to opposite poles but 180 out-of-phase voltages between neighboring poles. ....	11
Figure 2.3 Typical DC offset potentials applied to the different sections of the LQIT to facilitate z-directional transmission of ions from the ion source into the ion trap. ....	12
Figure 2.4 The partitions and the slits of the LQIT. The length of front, center and back sections of the trap are indicated. ....	13
Figure 2.5 The ion detection system is composed of a conversion dynode and an electron multiplier. Ions ejected through the slits in the X-electrodes of LQIT collide with the surface of the conversion dynode to generate secondary particles. These secondary particles enter the electron multiplier, generating a cascade of electrons upon collisions with the surface, which in turn produce more electrons upon collisions with the surface, eventually generating a measurable ion current in the anode cup. ....	14
Figure 2.6 Mathieu stability diagram describing the ion motion inside the trap. The circles of different colors and sizes represent ions of different m/z ratios, larger circles being the ions of larger m/z and vice versa. The ions will have stable trajectories in the overlapping regions. The unstable regions of the ions are also indicated. ....	17
Figure 2.7 A DC potential well is created to regulate axial (z-axis) motion of ions by applying three DC trapping potentials, one for each section of the LQIT rods. Larger DC potential is applied to the front (DC 1) and back sections (DC 2) of the ion trap than to the center section (DC 3). The circles of different colors indicate different ions trapped in the potential well. ....	19
Figure 2.8 Mathieu stability diagram. The depiction of trapped ion ejection in the LQIT. Ions can be ejected at the stability limit (0.908) by using the mass-selective instability scan/q-scan or by x-rod bipolar resonance ejection. The application of resonance ejection increases resolution because ions of a specific m/z leave the trap in a more condensed manner. ....	21
Figure 2.9 a) Mathieu stability diagram showing ions in the stability region. B) The main RF voltage is ramped until the ion of interest attains a q-value of 0.830, resulting in the ejection of ions of lower m/z values than the ion of interest from the trap. C) Tailored isolation waveform is applied, ejecting ions of greater m/z values than the ion of interest from the trap. ....	23

Figure 2.10 a) The q-value of the isolated ion is reduced from 0.880 to 0.250 by lowering the main RF amplitude. B) A supplementary RF voltage (tickle voltage) is applied at a q value of 0.250 to excite the ions resonantly, thereby causing energetic collisions with helium. Fragment ions are produced upon collisions with helium. C) The fragment ions are separated based on their m/z-values by using the q-scan or mass selective instability scan with resonant ejection at a q value of 0.880. ....	26
Figure 2.11 The Brauman double-well potential energy surface for a simple ion-molecule reaction in the gas phase. ....	28
Figure 2.12 External reagent inlet manifold for introduction of helium/reagent gas mixtures. The valves shown above are open to the manifold, allowing the diluted reagent/helium mixture into the ion trap via a control valve. ....	29
Figure 2.13 ESI ionization process. The region between the ESI needle and the mass spectrometer inlet shows the process of solvent evaporation and ion desolvation leading to the production of ions. ....	33
Figure 2.14 Schematics of an ESI tip demonstrating the use of sheath and auxiliary gases to nebulize and collimate the spray.....	33
Figure 2.15 APCI ionization generation process in positive ion mode. ....	34
Figure 2.16 Illustration of the APPI ionization process mediated by a protic solvent in positive ion mode.....	36
Figure 2.17 Diagram of the EI source.....	38
Figure 2.18 Thermo Scientific LTQ Orbitrap XL. The red line indicates the injection of ion packets from C-trap into orbitrap through the orbitrap injection optics. ....	40
Figure 2.19 Figure is showing the injection of ion packets into the orbitrap by the C-trap. The red line indicates the ion trajectory. The image current produced by the axial oscillation (z-axis) of the ions is measured. Voltage ramp is applied to the inner electrode.....	43
Figure 2.20 Typical DC offset potentials applied to the ion trap, C-trap, and MCAD collision cell. A) Potentials applied to induce MCAD fragmentation for an ion of interest. B) Typical voltages applied to send the MCAD fragment ions into the C-trap, which enables their detection by Orbitrap. ....	45
Figure 2.21 Components of the GCxGC/TOF mass spectrometer used in this research. The folded flight path mass analyzer is abbreviated as FFP mass analyser in the figure. ....	47
Figure 2.22 A) The two-dimensional GCxGC system with four-jet N <sub>2</sub> cryo modulators (two cold and two hot jets). B) The depiction of a relatively broad portion of the separated elutes from the first column being cryo-focused, modulated and separated in the second column into three narrow peaks.....	49

- Figure 2.23 A) The two-stage modulation in four jet cryo-modulator. B) All the events included in the modulation period and the time distributions between different modulation stages and hot and cold pulses are shown. The ChromaTOF software allows the user to define the duration of the hot pulse and the modulation period. The cold pulse duration is automatically calculated by the software. .... 51
- Figure 2.24 Typical temperature program for the primary oven, secondary oven, modulator, front inlet and transfer line for GCxGC. The black arrows indicate the modulator temperature off-set. .... 52
- Figure 2.25 Folded flight path mass analyzer constitutes the electrostatic focusing gridless mirrors and periodic ion lenses. The blue line indicates the flight path of the ions. .... 54
- Figure 3.1 (A) The MS<sup>2</sup> spectrum of protonated dimethyl sulfone (m/z 95) measured after 300 ms reaction with TMMS. The most abundant product ion (m/z 199) corresponds to [TMMS adduct + H - MeOH]<sup>+</sup>. The other product ion is the protonated TMMS reagent (m/z 137). (B) MS<sup>3</sup> spectrum measured after collision-activated dissociation (CAD) of [TMMS adduct + H - MeOH]<sup>+</sup>. The fragment ions of m/z 75, 105 and 123 are diagnostic to sulfone functionality. .... 68
- Figure 3.2 Proposed reaction pathways and potential energy surfaces calculated (M06-2X/6-311++G(d,p) level of theory) for (A) exergonic proton transfer and formation of [TMMS adduct + H - MeOH]<sup>+</sup> upon reaction of protonated dimethyl sulfone with TMMS, and (B) endergonic formation of a diagnostic fragment ion (m/z 105) upon CAD of [TMMS adduct + H - MeOH]<sup>+</sup> product ion. The pathway for the formation of this fragment ion (m/z 105) is assumed to be barrierless. Energy values in parentheses indicate transition state free energies. .... 73
- Figure 3.3 The proton affinities calculated for different protonation sites in methionine sulfone and alendazole sulfone (B3LYP/6-31G++(d,p) level of theory). (A) The site with the highest proton affinity in methionine sulfone is the amino nitrogen, with a proton affinity 23 kcal mol<sup>-1</sup> greater than that of the sulfone functionality. (B) The site with the greatest proton affinity in alendazole sulfone is the nitrogen in the imidazole ring, with a proton affinity 9 kcal mol<sup>-1</sup> greater than that of the sulfone functionality. The higher proton affinity of the imine nitrogen can be attributed to intramolecular hydrogen bonding between the imine nitrogen and the nearby carboxyl oxygen (not shown). .... 74
- Figure 3.4 (A) MS<sup>2</sup> spectrum measured after 300 ms reaction of the protonated benzoic acid with TMMS. The most abundant product ion (m/z 227) corresponds to [TMMS adduct + H - MeOH]<sup>+</sup>. The other product ion (m/z 137) arises from proton transfer to TMMS. (B) MS<sup>3</sup> spectrum measured after CAD of isolated [TMMS adduct + H - MeOH]<sup>+</sup> (m/z 227). The major fragment ion (m/z 195) corresponds to elimination of methanol. (C) MS<sup>4</sup> spectrum measured after CAD of [TMMS adduct + H - 2 MeOH]<sup>+</sup> (m/z 195). The most abundant fragment ion (m/z 151) corresponds to CO<sub>2</sub> loss (44 Da). The other fragment ion corresponds to a loss of C<sub>2</sub>H<sub>6</sub>O<sub>2</sub>Si with MW of 90 Da. .... 81

- Figure 3.5 Proposed reaction pathways and potential energy surfaces calculated at M06-2X/6-311++G(d,p) level of theory for (A) spontaneous proton transfer and formation of [TMMS adduct + H - MeOH]<sup>+</sup> upon reaction of protonated benzoic acid with TMMS, (B) elimination of methanol after isolation and upon CAD of [TMMS adduct + H - MeOH]<sup>+</sup>, and (C) characteristic loss of molecules with MW of 44 Da (CO<sub>2</sub>) (indicated by solid line) and 90 Da (C<sub>2</sub>H<sub>6</sub>O<sub>2</sub>Si) (indicated by dashed line) observed upon CAD of [TMMS adduct + H - 2 MeOH]<sup>+</sup>. Energy values in parentheses indicate transition state energy barriers..... 82
- Figure 3.6 (A) MS<sup>2</sup> spectrum measured after 300 ms reaction of the protonated benzoic acid with <sup>13</sup>C label on the carboxylic acid moiety with TMMS. The most abundant product ion (m/z 228) corresponds to [TMMS Adduct + H - MeOH]<sup>+</sup>. The other product ion (m/z 137) corresponds to protonated TMMS. (B) MS<sup>3</sup> spectrum measured after CAD of [TMMS Adduct + H - MeOH]<sup>+</sup> (m/z 228) shows elimination of methanol (m/z 196). (C) MS<sup>4</sup> spectrum measured after CAD for the methanol elimination product (m/z 196) shows <sup>13</sup>CO<sub>2</sub> loss (45 Da). the other fragment ion corresponds to a loss of C<sub>2</sub>H<sub>6</sub>O<sub>2</sub>Si (mw 90 Da)..... 85
- Figure 3.7 (a) MS<sup>2</sup> spectrum measured after 300 ms reaction of protonated 2,6-dimethylbenzoic acid with TMMS shows a major product ion (m/z 255) corresponding to [TMMS Adduct + H - MeOH]<sup>+</sup>. The other product ion (m/z 133) corresponds to [M+H-H<sub>2</sub>O]<sup>+</sup>. (b) MS<sup>3</sup> spectrum measured after CAD of [TMMS Adduct + H - MeOH]<sup>+</sup> (m/z 255) shows a major fragment ion (m/z 223) corresponding to elimination of methanol. (c) MS<sup>4</sup> spectrum measured after CAD of the methanol elimination product (m/z 223) shows a major fragment ion (m/z 133) corresponding to a loss of C<sub>2</sub>H<sub>6</sub>O<sub>2</sub>Si (MW 90 Da). The other fragment ion corresponds to a loss of CO<sub>2</sub> (44 Da)..... 86
- Figure 3.8 The proton affinities calculated for different protonation sites in (A) sulindac, (B) 4-acetamidobenzoic acid, (C) 4-methoxy-3-nitrobenzoic acid and (D) 3-aminobenzoic acid (B3LYP/6-31G++(d,p) level of theory). The most basic site in each molecule is colored blue. .... 88
- Figure 3.9 The mass spectrum measured after 300 ms reaction of the protonated 2-hydroxybenzoic acid with TMMS. (A) Spontaneous formation of [TMMS adduct + H]<sup>+</sup> (m/z 275), [TMMS adduct + H - MeOH]<sup>+</sup> (m/z 243) and [TMMS adduct + H - 2 MeOH]<sup>+</sup> (m/z 211) was observed. (B) MS<sup>3</sup> spectrum measured after CAD of [TMMS adduct + H - MeOH]<sup>+</sup> (m/z 243). The major fragment ion (m/z 211) corresponds to elimination of methanol. (C) MS<sup>4</sup> spectrum measured after CAD of [TMMS adduct + H - 2 MeOH]<sup>+</sup> (m/z 211). The most abundant fragment ion corresponds to the loss of formaldehyde (MW 30 Da). The other fragment ion corresponds to a loss of CO<sub>2</sub> (MW 44 Da). .... 90



- Figure 3.10 Proposed reaction pathways and calculated potential energy surfaces (M06-2X/6-311++G(d,p) level of theory) for (A) spontaneous proton transfer and formation of [TMMS adduct + H - MeOH]<sup>+</sup> upon reaction of protonated 2-hydroxybenzoic acid with TMMS (MS<sub>2</sub> experiment), (B) elimination of methanol upon CAD of [TMMS adduct + H - MeOH]<sup>+</sup> (MS<sub>3</sub> experiment), and (C) diagnostic loss of molecules with MW of 44 Da (CO<sub>2</sub>) (pathway indicated by solid line) and 30 Da (CH<sub>2</sub>O) (pathway indicated by dashed line) observed upon CAD of [TMMS adduct + H - 2 MeOH]<sup>+</sup> (MS<sub>4</sub> experiment). ..... 93
- Figure 3.11 (A) The MS<sup>2</sup> spectrum measured after 400 ms reaction of protonated benzene sulfonamide with TMMS shows the product ion [TMMS Adduct + H - MeOH]<sup>+</sup> (m/z 262) diagnostic also for aromatic carboxylic acids and sulfones. (B) MS<sup>3</sup> spectrum measured after CAD of isolated [TMMS adduct + H - MeOH]<sup>+</sup> (m/z 262) showed the fragment ion of m/z 230 corresponding to the elimination of methanol, as observed for other carboxylic acid model compounds. (C) MS<sup>4</sup> spectrum measured after CAD of [TMMS adduct + H - 2 MeOH]<sup>+</sup> (m/z 230) showed no fragment ions corresponding to CO<sub>2</sub> loss (44 Da) or loss of C<sub>2</sub>H<sub>6</sub>O<sub>2</sub>Si with a MW of 90 Da (characteristic of carboxylic acids), but it showed a fragment ion of m/z 91 that may be diagnostic for sulfonamides and aliphatic carboxylic acids..... 95
- Figure 3.12 (A) The MS<sup>2</sup> spectrum measured after 500 ms reaction of the protonated hexanoic acid with TMMS shows the diagnostic product ion [TMMS Adduct + H - MeOH]<sup>+</sup> (m/z 211) observed for aromatic carboxylic acids and sulfones. (B) The MS<sub>3</sub> spectrum measured after CAD of isolated [TMMS adduct+H-MeOH]<sup>+</sup> (m/z 211) shows a fragment ion (m/z 189) corresponding to the elimination of methanol as observed for aromatic carboxylic acid model compounds. (C) The MS<sup>4</sup> spectrum measured after CAD of [TMMS adduct + H - 2 MeOH]<sup>+</sup> (m/z 189) showed fragment ions corresponding to loss of CO<sub>2</sub> (44 Da) or loss of C<sub>2</sub>H<sub>6</sub>O<sub>2</sub>Si (90 Da), enabling the differentiation of the aromatic carboxylic acid functionality from aliphatic carboxylic acid functionality. The fragment ion of m/z 91 was only observed for aliphatic carboxylic acids and sulfonamides. .... 96
- Figure 3.13 Calculated potential energy surface (at the M06-2X/6-311++G(d,p) level of theory) for (A) proton transfer and formation of [TMMS adduct + H - MeOH]<sup>+</sup> resulting from reaction of protonated methanesulfonamide with TMMS (MS<sub>2</sub> experiment), (B) elimination of methanol upon CAD of [TMMS adduct + H - MeOH]<sup>+</sup> (MS<sub>3</sub> experiment), and (C) formation of ion of m/z 91 (CH<sub>3</sub>O(CH<sub>3</sub>)Si<sup>+</sup>OH) upon CAD of [TMMS adduct + H - 2 MeOH]<sup>+</sup> (MS<sub>4</sub> experiment). An analogous mechanism applies to aliphatic carboxylic acids..... 97
- Figure 3.14 A general scheme for identification of aromatic carboxylic acid functionality (A), sulfone functionality (B), and sulfonamide and aliphatic carboxylic acid functionalities together (they cannot be differentiated) (C) by MS<sup>n</sup> experiments employing ion-molecule reactions of protonated analytes with TMMS reagent..... 99

- Figure 4.1 APCI/N<sub>2</sub>/CS<sub>2</sub> mass spectrum of an equimolar mixture (1 mM) of seven nonpolar model compounds measured using an injection flow rate of 5 μL/min. Linear alkane and alkene yielded several fragment ions, including those of m/z 57, 70, 71 and 85. Cycloalkanes generated molecular ions (M<sup>+</sup>•) as well as [M-H]<sup>+</sup> ions. Alkylaromatic compounds and the alkyne generated predominantly stable molecular ions. .... 117
- Figure 4.2 APPI/N<sub>2</sub>/CS<sub>2</sub> mass spectrum of an equimolar mixture comprising of seven model compounds obtained at an injection flow rate of 5 μL/min and a tube lens voltage of 50 V. .... 118
- Figure 4.3 DPF scheme for separation of crude oil into six fractions I - VI. .... 120
- Figure 4.4 Auto column-ELSD/UV chromatogram of maltenes, indicating the separation of maltenes into three fractions. The presence of both ELSD and UV signals in the later eluting part of the n-hexane-eluted fraction indicates co-elution of aromatic compounds along with aliphatic compounds (no UV absorption). .... 121
- Figure 4.5 Total ion chromatogram measured using GCxGC/(+EI)TOF for A) n-C<sub>6</sub>H<sub>14</sub>-eluted compounds (fractions III and IV), and B) heavy saturated compounds (fraction III) separated from n-C<sub>6</sub>H<sub>14</sub>-eluted compounds by using solid phase extraction. Linear and branched saturated, aromatic and cyclic saturated compounds are color coded. A small percentage (8%) of carryover of aromatic compounds into the heavy saturated compounds was observed even after solid phase extraction. .... 123
- Figure 4.6 A) (+) ESI mass spectrum of methanol eluted fraction of maltenes indicating the presence of polymers in a contaminated crude oil sample. The red dotted line indicates polypropoxylates (repeating unit 58 Da) and the blue dotted line indicates polyethoxylates (repeating unit 44 Da). B) (+) ESI mass spectrum of methanol eluted fraction of a pristine non-contaminated crude oil. This mass spectrum indicates that no compounds other than contaminants eluted with methanol elution. .... 125
- Figure 4.7 FTIR spectra from 3600-2600 cm<sup>-1</sup> and 2000-600 cm<sup>-1</sup> measured for the crude oil fractions. .... 126
- Figure 4.8 APCI/N<sub>2</sub>/CS<sub>2</sub>, APCI/N<sub>2</sub>/toluene and APCI/N<sub>2</sub>/methanol mass spectra of an equimolar mixture (1 mM) containing aromatic and heteroaromatic model compounds. While APCI/N<sub>2</sub>/CS<sub>2</sub> successfully ionized all the four model compounds in the model mixture at roughly equal efficiencies, the other two methods could not replicate the same. .... 129
- Figure 4.9 APCI/N<sub>2</sub>/CS<sub>2</sub> mass spectrum of an equimolar mixture of three aromatic compounds containing long alkyl chains. .... 130
- Figure 4.10 (A) APCI/O<sub>2</sub>/n-hexane mass spectrum measured at an injection flow rate of 5 μL min<sup>-1</sup> and tube lens voltage of 20 V and (B) APCI/N<sub>2</sub>/CS<sub>2</sub> mass spectrum measured at an injection flow rate of 5 μL min<sup>-1</sup> and tube lens voltage of 30 V for an equimolar mixture (1 mM) comprised of saturated hydrocarbon model compounds (no ions were observed below m/z 200). .... 131

- Figure 4.11 APCI/N<sub>2</sub>/CS<sub>2</sub> mass spectrum of an equimolar mixture (1 mM) of nonaromatic heteroatom containing model compounds obtained at an injection flow rate of 5 μL/min and a tube lens voltage of 50 V. While amines produced only protonated analyte ion, other analytes produced more than one ion type per analyte (\*denotes chemical noise peaks). ..... 132
- Figure 4.12 APCI/N<sub>2</sub>/n-hexane, methanol mass spectrum of an equimolar mixture (1 mM) of nonaromatic polar compounds measured at an injection flow rate of 1 μL min<sup>-1</sup> and tube lens voltage of 50 V (\* denotes solvent peaks). ..... 133
- Figure 4.13 APCI/N<sub>2</sub>/hexane, methanol mass spectrum of an equimolar mixture (0.1 mM) of nonaromatic heteroatom containing model compounds obtained at a flow rate of 10 μL/min and a tube lens voltage of 50 V. Adduct formation was observed at higher flow rates (>5 μL/min). ..... 134
- Figure 4.14 Instruments and ionization methods used for high-resolution mass spectral analysis of the six fractions of crude oil. .... 135
- Figure 4.15 A) GCxGC/(+EI)TOF total ion chromatogram for the distillate (fraction I) of the crude oil. The aromatic hydrocarbons are color coded in red and saturated hydrocarbons in black. B) Positive ion mode APCI mass spectra obtained for the five nonvolatile crude oil fractions (fractions II–VI). Avg MW denotes the weighted average molecular weight (discussed below). ..... 137
- Figure 4.16 APCI/N<sub>2</sub>/CS<sub>2</sub> mass spectrum of unfractionated crude oil obtained at an injection flow rate of 5 μL/min and a tube lens voltage of 50 V. Avg MW denotes the weighted average molecular weight (All the ions observed in the mass spectrum were considered to determine the molecular weight). ..... 141
- Figure 4.17 Color-mapped bubble plots of the ring and double bond (RDB) equivalence versus carbon number for ionized compounds derived from the six crude oil fractions that were separated and characterized by using the DPF MS method. Bubble size indicates the relative abundance of the ions. .... 143
- Figure 4.18 Compound class distributions and their percentage relative abundances for crude oil fractions separated and analyzed by using the DPF MS method. The y-axis indicates the assigned elemental compositions by using abbreviations such as NS<sub>2</sub>, which implies compounds containing one nitrogen and two sulfur atoms, in addition to hydrogen and carbon atoms. .... 146
- Figure 4.19 Weight percentages of compound classes in crude oil, consolidated from the data obtained for individual fractions. .... 149
- Figure 4.20 CAD mass spectra obtained by using the same “normalized” CAD energy (25 arbitrary units) for the radical cation of m/z 400 derived from three different fractions of the crude oil. The different fragmentation patterns are highlighted using a red dotted line. .... 150
- Figure 4.21 CAD mass spectra of different ions derived from the heteroaromatic compounds and asphaltenes fractions, highlighting the similarity in fragmentation patterns. .... 151

Figure 4.22 CAD mass spectra of ions of m/z 397 and 411 (protonated molecules) derived from polar compounds (fraction VI), indicating characteristic losses of polar molecules, such as water and formaldehyde.....	151
Figure 5.1 Sample preparation and analysis workflow.....	161
Figure 5.2 The chromatogram corresponding to the selective ion monitoring analysis (of ions of m/z 139,143 and 155) of reservoir brine blank sample spiked with 2-fluorobenzoic acid (m/z 139), 2-fluorobenzoic-d4 acid (m/z 143) and 2-chlorobenzoic acid (m/z 155) each at 0.25 µg/mL concentration. The selected ion monitoring generated simple chromatograms of selected masses .....	166
Figure 5.3 A) The chromatogram corresponding to the selective ion monitoring analysis of reservoir brine spiked with 2-fluorobenzoic acid (m/z 139) at 0.33 µg/mL concentration. The chromatogram generated is complicated and the peak eluting at 5.02 minutes corresponds to 2-fluorobenzoic acid and is partially obscured by isobaric ions derived from the matrix B) The chromatogram corresponding to the multiple reaction monitoring analysis of the same sample discussed in part A. Monitoring the specific fragment ion (m/z 95) produced from ionized parent ion (m/z 139) after CAD, clearly shows the peak corresponding to 2-fluorobenzoic acid, by eliminating the interference from co-eluting isobaric ions.....	168
Figure 5.4 The overlay 3D MS/MS chromatograms for a reservoir sample spiked with 2-fluorobenzoic-d4 acid, 2-fluorobenzoic acid and 2-chlorobenzoic acid at about 5 µg/mL concentrations. Monitoring both the precursor ion and the fragment ion associated with the precursor ion makes the method more sensitive and selective compared to selected ion monitoring.....	170
Figure 5.5 Calibration curve for 2-fluorobenzoic acid and 2-fluorobenzoic-d4 acid. The calibration curve equations for seven different concentrations of standards are provided in the figure.....	172
Figure 5.6 Chromatogram of oil reservoir brine sample (no 12) spiked with two internal standards. A) The chromatogram showing the MRM transitions of 2-fluorobenzoic acid, 2-fluorobenzoic-d4 acid, and 2-chlorobenzoic acid B) The UV absorption spectrum of the sample at 214 nm wavelength. The peaks corresponding to the tracer and the internal standards is obscured in the matrix of other UV absorbing compounds present in the matrix, not allowing for identification or quantitation.....	174

## ABSTRACT

Author: Yerabolu, Ravikiran. PhD

Institution: Purdue University

Degree Received: May 2018

Title: Mass Spectrometric Methods Development for the Characterization of Components in Complex Mixtures for Enhanced Oil Recovery Operations and for Drug Development.

Committee Chair: Hilkka I. Kenttämäa.

High-resolution tandem mass spectrometry ( $MS^n$ ) coupled with separation techniques, such as high-performance liquid chromatography (HPLC) and gas chromatography (GC), has proven to be a valuable tool for the molecular level characterization of complex mixtures. The utilization of different methods, such as collision-activated dissociation (CAD) and gas-phase ion/molecule reactions, facilitates structural elucidation of the components in complex mixtures. This thesis primarily focuses on the development of tandem mass spectrometric methods for solving analytical challenges associated with the characterization of complex mixtures produced during enhanced oil recovery (EOR) operations and in drug discovery.

Chapter 2 describes the instrumentation used for the research discussed in this thesis. In Chapter 3, the gas-phase reactivity of protonated polyfunctional model compounds toward trimethoxymethylsilane (TMMS) reagent and the utility of this reagent in the mass spectrometric identification of sulfone and aromatic functionalities in drug metabolites is discussed. Chapter 4 discusses an analytical methodology, namely Distillation Precipitation Fractionation Mass Spectrometry (DPF-MS), developed to perform molecular level profiling of crude oil. This analytical methodology involves the optimization of different mass spectrometric and ionization methods for the semi-quantitative molecular level characterization of crude oil and its fractions. Chapter 5 discusses a sensitive analytical method developed for the identification and quantitation of a tracer (2-fluorobenzoic acid) in oil reservoir brine produced during enhanced oil recovery.

This method is based on solid-phase extraction followed by multiple reaction monitoring (MRM)-based HPLC-MS<sup>n</sup>.

## CHAPTER 1. INTRODUCTION AND OVERVIEW

### 1.1 Introduction

Mass spectrometry (MS) has emerged over the years as a powerful analytical technique capable of solving complex problems across a wide variety of different research areas.<sup>1-4</sup> Commercial mass spectrometers, which have evolved tremendously over the years from J.J. Thompson prototype,<sup>5</sup> are known for their versatility, sensitivity, specificity, and speed.<sup>6</sup>

The success of MS experiments depends on four events: evaporation, ionization, ion separation and detection.<sup>7</sup> The analytes present in the mixture are initially brought into the gas phase by evaporation (step 1) followed or accompanied by ionization (step 2). The analyte ions generated by ionization are separated based on their mass-to-charge ( $m/z$ ) ratios (step 3). Finally, once the analyte ions are appropriately separated, they are detected to measure the  $m/z$ -value and abundance of the ions (step 4). A typical mass spectrum ( $MS^1$ ) displays the results of the analysis with the mass-to-charge ( $m/z$ ) ratios of the ions on the x-axis and their abundance (usually relative) on the y-axis. These results depending on the ionization method provides the analyst with molecular weight information and some structural information. For example, isotope peaks can be used to confirm the presence of certain elements in the ionized molecule, such as bromine, boron, etc. The “Nitrogen rule” can be applied to determine the possible number of nitrogen atoms present in the ionized molecule. Further, using mass spectrometers that allow extremely accurate mass measurements, elemental compositions of the ions can also be determined.

To obtain further structural information for ionized analytes by mass spectrometry, tandem mass spectrometry experiments ( $MS^n$ ) are usually employed. The most commonly used  $MS^n$  approaches involve subjecting an isolated ion to collision-activated dissociation (CAD) or ion/molecule reactions. In CAD experiments, isolated ions are subjected to energetic gas-phase

collisions with neutral atoms or molecules (often nitrogen, helium or argon) to produce structurally informative fragment ions. In ion/molecule reaction experiments, isolated ions are allowed to react with a reagent gas (often a volatile organic compound) to generate structurally diagnostic reaction products. By examining the fragment ions/product ions, structural information about the parent ion can be obtained.<sup>8</sup>

## 1.2 Thesis Overview

The research discussed in this thesis mainly focused on developing analytical methodologies based on mass spectrometry to characterize complex mixtures produced during enhanced oil recovery (EOR) operations and upon drug metabolism. Chapter 2 introduces the background of mass spectrometry and provides detailed information on the instrumentation and experimental aspects relevant to this thesis.

Chapter 3 discusses a tandem mass spectrometric approach developed based on gas-phase ion-molecule reactions for drug metabolite identification. The project discussed in this chapter was conducted in collaboration with AstraZeneca. The gas-phase reactivity of protonated model compounds containing one or more of 22 different functional groups toward trimethoxymethylsilane (TMMS) was studied to explore the utility of this reagent in the mass spectrometric identification of specific functionalities in protonated drug metabolites. Only protonated analytes with a carboxylic acid, a sulfone or a sulfonamide functionality were found to produce diagnostic adducts that had lost a methanol molecule upon reactions with TMMS. CAD of these adduct ions ( $MS^3$  experiments) produced characteristic fragment ions of  $m/z$  75, 105 and 123 for sulfones while an adduct that has lost a second methanol molecule was observed for carboxylic acids and sulfonamides. Further CAD of the methanol elimination fragment ion ( $MS^4$  experiments) resulted in the diagnostic elimination of neutral molecules  $CO_2$  (MW = 44 Da) and



$C_2H_6O_2Si$  (MW = 90 Da) for aromatic carboxylic acids. In contrast, both aliphatic carboxylic acids and sulfonamides (up on CAD of methanol elimination product) yielded a fragment ion of  $m/z$  91 ( $C_2H_7O_2Si^+$ ), among other products, in the  $MS^4$  experiments. Potential energy surfaces were calculated (at the M06-2X/6-311++G(d,p) level of theory) to explore the mechanisms of above reactions.

The research discussed in the following chapters, 4 and 5, was conducted in collaboration with Pioneer Oil company. In Chapter 4, a new approach (distillation precipitation fractionation mass spectrometry (DPF-MS) method) is introduced for the molecular level characterization of crude oil. This method involves the separation of crude oil into six fractions followed by a high-resolution mass spectral analysis optimized for each individual fraction. The separation methods used for fractionation of crude oil include distillation, precipitation, fractionation in an auto column and solid phase extraction. The fractions were initially examined by using Fourier transform infrared spectroscopy to determine the bulk chemical nature of each individual fraction, such as the extent of aromaticity, polarity, etc. Based on this bulk information, model compounds representative of the compounds in each fraction were selected and employed to develop the optimal high-resolution mass spectrometric analysis method for each fraction. The most important aspect of this work is the optimization of the ionization method separately for each fraction so that all compounds in the fraction are ionized at approximately the same efficiency to generate only one type of stable ions containing the intact molecule. This allows the DPF-MS method to produce reasonably accurate relative abundances for different compounds present in each fraction, thereby making the method semi-quantitative. The compositional data thus obtained for the individual fractions were utilized to provide meaningful molecular level information for the crude oil. This method excels over previous methods since the inclusion of a mass balance for each fraction allows

for data consolidation, which provides an accurate overall analysis, including average molecular weight and distribution of aromatic compounds over the different fractions. Furthermore, fractionation of the crude oil enables detection of compound classes that cannot be detected in the unfractionated oil. Chapter 5 discusses a method developed for the detection of tracers, especially 2-fluorobenzoic acid, in oil reservoir brine via solid-phase extraction and multiple reaction monitoring (MRM)-based HPLC-MS<sup>n</sup> quantitation. The method developed and discussed in this chapter was used for the identification and quantitation of 2-fluorobenzoic acid in oil reservoir brine samples obtained from four different production wells of Pioneer oil company.

### 1.3 References

- (1) Geoghegan, K. F.; Kelly, M. A. Biochemical Applications of Mass Spectrometry in Pharmaceutical Drug Discovery. *Mass Spectrom. Rev.* **2005**, *24* (3), 347–366.
- (2) Herrero, M.; Simó, C.; García-Cañas, V.; Ibáñez, E.; Cifuentes, A. Foodomics: MS-Based Strategies in Modern Food Science and Nutrition. *Mass Spectrom. Rev.* **2012**, *31* (1), 49–69.
- (3) Marshall, A. G.; Rodgers, R. P. Petroleomics: Chemistry of the Underworld. *Proc. Natl. Acad. Sci. U. S. A.* **2008**, *105* (47), 18090–18095.
- (4) Richardson, S. D. Environmental Mass Spectrometry: Emerging Contaminants and Current Issues. *Anal. Chem.* **2008**, *80* (12), 4373–4402.
- (5) Thomson, J. J. Rays of Positive Electricity and Their Application to Chemical Analyses; Longmans, Green and Co.: London, New York, 1913.
- (6) McLuckey, S. A.; Wells, J. M. Mass Analysis at the Advent of the 21st Century. *Chem. Rev.* **2001**, *101* (2), 571–606.
- (7) Schalley, C. A. Mass Spectrometry—Principles and Applications: Edmond de Hoffmann and Vincent Stoobant (Eds.), Wiley, Chichester, 2001, 2nd Edition, 407 Pp, ISBN 0-471-48565-9. *Int. J. Mass Spectrom.* **2002**, *214* (1), 173.
- (8) Busch, K. L.; Glish, G. L.; McLuckey, S. A. Mass Spectrometry/Mass Spectrometry: Techniques and Applications of Tandem Mass Spectrometry; VCH Publishers: New York, N.Y., 1988.

## CHAPTER 2. INSTRUMENTATION AND EXPERIMENTAL ASPECTS OF LINEAR QUADRUPOLE ION TRAP MASS SPECTROMETERS, HIGH RESOLUTION ORBITRAP MASS SPECTROMETERS AND TIME-OF-FLIGHT MASS SPECTROMETERS

### 2.1 Introduction

Tandem mass spectrometry ( $MS^n$ ) is a powerful analytical technique that has been widely used to address a variety of challenging and complex problems in pharmaceutical, petrochemical, environmental, and clinical fields.<sup>1-7</sup> The rapid growth of mass spectrometry applications over the years has been driven by the continuous development of novel instrumentation and advanced methodologies.

The analysis of any chemical species by using mass spectrometry requires at least three steps: a) desorption and ionization of the chemical species, b) separation of the gas-phase ions based on their  $m/z$  ratio, and c) detection of the separated ions. However, most current mass spectrometers can perform additional experiments called tandem mass spectrometry experiments ( $MS^n$ ) in order to provide more information regarding the structures of unknown ions. Tandem mass spectrometry ( $MS^n$ ) involves at least two stages of mass analysis ( $MS^2$ ), but often more ( $MS^n$ ), with fragmentation or a chemical reaction occurring in between the stages. The most commonly used  $MS^n$  approach involves the isolation of the ion of interest and then subjecting that ion to energetic gas-phase collisions with neutral atoms or molecules (often nitrogen, helium or argon) to induce fragmentation. The structural information is elucidated based on the fragment ions produced. This technique is termed as collision-induced dissociation (CID) or collision-activated dissociation (CAD). Another  $MS^n$  approach involves the isolation of the ion of interest which then is allowed to react with a reagent (often volatile organic molecules) to produce diagnostic ionic reaction products via gas-phase ion-molecule reactions. Often, the fragment ions or product ions

generated upon  $MS^n$  experiments are further isolated and subjected to another stage of reactions to obtain more structural information.

$MS^n$  experiments are performed differently in scanning mass spectrometers compared to trapping mass spectrometers. Scanning mass spectrometers perform tandem-in-space experiments; *i.e.*, most of the events, such as ion isolation, dissociation/ion-molecule reactions, and detection occur in different areas of the mass spectrometer. Trapping mass spectrometers are said to perform tandem-in-time experiments, which means that most of the above-discussed events occur in the same region of the mass spectrometer but at different times. All the experiments discussed in this dissertation were performed using trapping mass spectrometers, specifically, linear quadrupole ion trap (LQIT) mass spectrometers. The fundamental aspects of this instrument and the different  $MS^n$  techniques employed for this dissertation are discussed further in this chapter.

## 2.2 Linear Quadrupole Ion Trap (LQIT) Mass Spectrometer

Linear quadrupole ion traps (LQITs) were first introduced in 2002.<sup>8-10</sup> The relative simplicity of these ion traps for mass-selective operation has led to the rapid discovery of different applications suitable for them.<sup>11</sup> The LQIT instruments are similar in performance to traditional 3-D quadrupole ion traps<sup>12</sup> (QIT), but with significant performance enhancements regarding sensitivity and versatility.<sup>8</sup> Thermo Scientific LTQ mass spectrometers equipped with Surveyor Plus HPLC systems were used in this dissertation. Xcaliber and LTQ Tune software were used for data processing and instrument control.

A schematic of the Thermo LTQ instrument used in this research is shown in Figure 2.1. This LQIT mass spectrometer can be divided into four regions. These regions include a) atmospheric pressure ionization (API) region, b) ion optics region, c) ion trap (mass analyzer) region, and d) detector region. These regions are operated at different pressures. The API region

includes an ionization source operating at ambient pressure (760 Torr), and an API stalk maintained at  $\sim 1$  Torr by using two Edwards E2M30 rotary-vane mechanical pumps (650 L/min). The ion optics, ion trap, and detector regions are differentially pumped by a triple ported Leybold TW 220/150/15S turbo molecular pump. The ion optics region just past the API stalk is pumped (at a rate of 25 L/s) to reach a pressure of 0.5 Torr – 100 mTorr. The remaining part of the ion optics, which is separated from the previous region by a lens (lens 0), is pumped (at a rate of 300 L/s) down to a pressure of  $\sim 10^{-3}$  Torr. The ion trap region is separated from the ion optics region by a lens (lens 1), which is maintained (by pumping at a rate of 400 L/s) at a low pressure of  $1 \times 10^{-5}$  Torr. The pressure is monitored using a hot cathode ionization gauge.

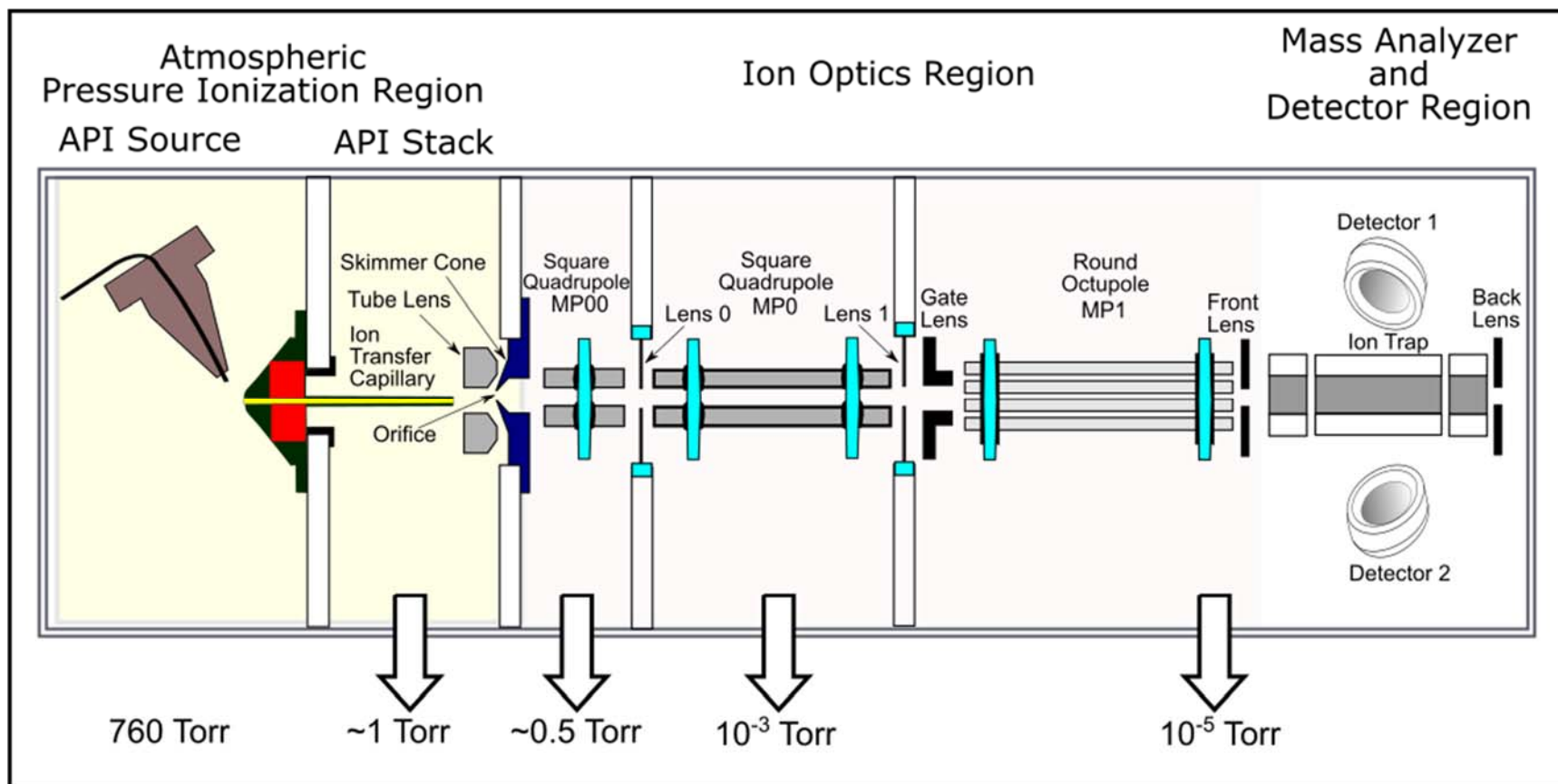


Figure 2.1 Components of the linear quadrupole ion trap (LQIT) mass spectrometer, including the atmospheric pressure ionization source, API stack, ion optics, mass analyzer, and detector. Operational pressures for each region of the instrument are also indicated.

### 2.2.1 Atmospheric Pressure Ionization (API) Region

The API region contains an API ionization source and an API stack. The ionization source allows the evaporation of the molecules, for ionization by using methods such as electrospray ionization (ESI), atmospheric pressure photoionization (APPI) and atmospheric pressure chemical ionization (APCI). These ionization techniques are further discussed in detail in Section 2.4. The API stack consists of an ion transfer capillary, a tube lens, and a skimmer cone, which facilitate transfer and desolvation of ions on their way into the ion optics region. The ions generated in the ionization source are first drawn into the ion transfer capillary via a negative pressure gradient. The heated capillary facilitates desolvation of the ions and a DC voltage (positive voltage applied in positive mode ionization and vice versa) applied to it facilitates ion transfer. The tube lens voltage redirects these ions into the ion optics region via an off-center orifice of the skimmer cone. The skimmer cone orifice is set off-center to prevent neutral molecules from entering the ion optics region.

### 2.2.2 The Ion Optics Region

The ion optics region moves the ions from the API region into the ion trap (mass analyzer) without contacting any of the solid internal parts of the mass spectrometer. This is achieved by a series of ion guides that use a combination of DC and RF voltages and a vacuum gradient. The ions that are transmitted through the skimmer cone are guided through a series of ion guides, namely, a two square quadrupole ion guides (Q00 and Q0) and a round-rod octupole ion guide (Q1).<sup>8</sup> These RF frequency applied to opposite poles of the ion guides restrict the motion of the ions in the x- and y-direction. In the multipole, opposite poles are connected such that the same amplitude and frequency is applied to both. The adjacent rods are also supplied with the same amplitude and frequency but 180° out of phase. As a result, an oscillating RF field is generated



between the rods such that when one set is positive, the other set is negative and vice versa (shown in Figure 2.2). This causes the ions to travel through the multipoles in a circular oscillatory fashion, focusing the ions to a tighter beam.

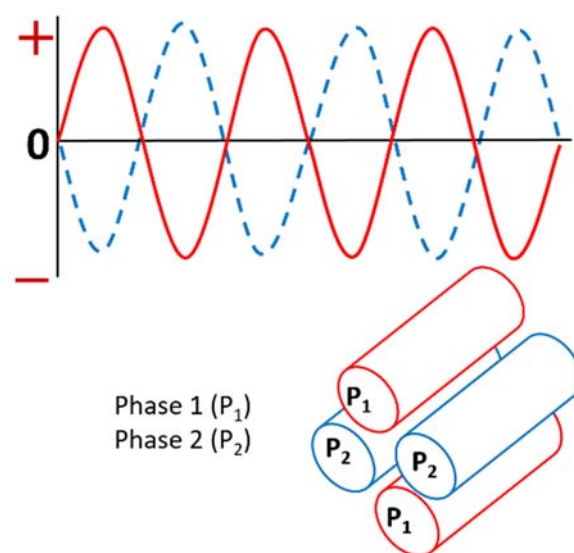


Figure 2.2 Quadrupoles that have the same RF voltage applied to opposite poles but 180 out-of-phase voltages between neighboring poles.

In between ion guides, there are lenses across which a DC voltage is applied. These lenses facilitate ion transfer from one ion guide to another. However, as the ions exit the multipole Q00, which is in the high-pressure region, the ions have zero kinetic energy in the z-direction. To accelerate the ions and make them continue towards ion trap region, a DC potential gradient is applied (in addition to the RF voltages) to all the ion guides. A typical DC potential gradient can be seen in Figure 2.3.

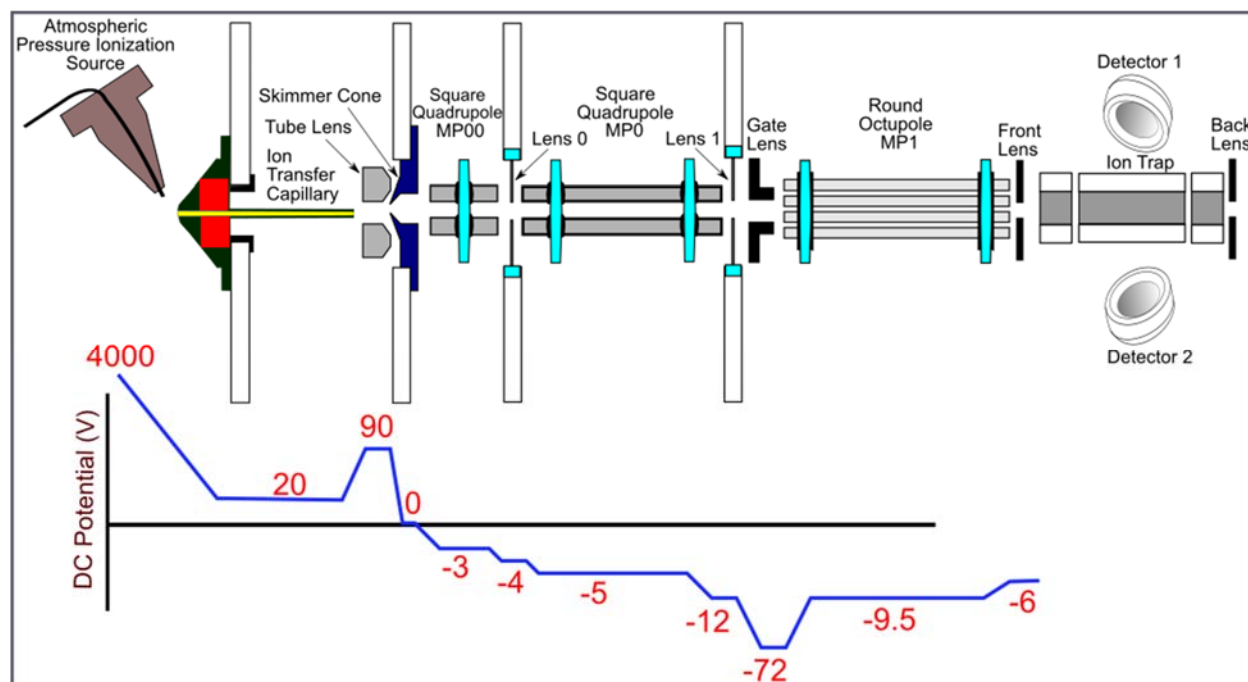


Figure 2.3 Typical DC offset potentials applied to the different sections of the LQIT to facilitate z-directional transmission of ions from the ion source into the ion trap.

### 2.2.3 Ion Trap (Mass Analyzer) Region

The ion trap region includes a front lens, the linear quadrupole ion trap mass analyzer and a back lens. The ion trap is composed of four hyperbolic electrodes that are partitioned into three sections (front, center, and back). The two-center x- electrodes contain slits, through which ions are ejected for detection (Figure 2.4). The ions enter the ion trap region via the front lens. The ions are trapped in the x-y direction (radial motion) by applying RF voltages in the same manner as for the ion optics multipoles discussed above (same frequency and amplitude for opposite electrodes and  $180^\circ$  out of phase for adjacent electrodes). In addition to these RF voltages, a supplemental RF potential with a variable frequency and amplitude was applied to the x-electrodes to enable ion excitation, isolation and ejection. The ion motion in the z-direction (axial motion) is controlled by

DC voltages applied to the different sections of the ion trap. Further details about ion motion, ion injection and ejection are detailed under Section 2.3.

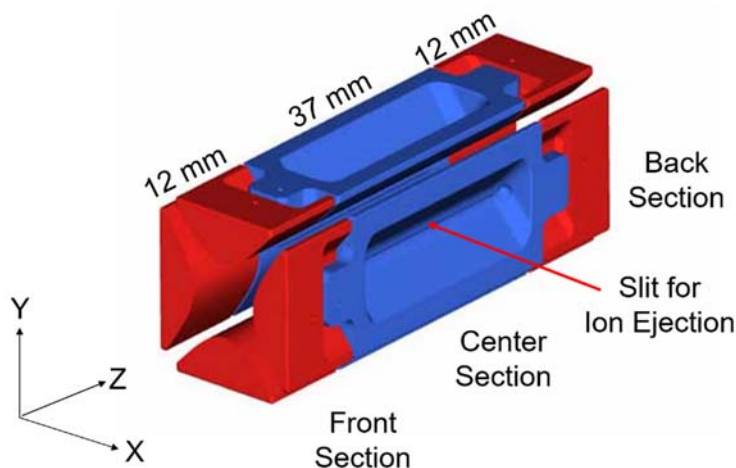


Figure 2.4 The partitions and the slits of the LQIT. The length of front, center and back sections of the trap are indicated.

#### 2.2.4 Ion Detection Region

A detector is located on either side of the ion trap, and both the detectors consist of a conversion dynode and an electron multiplier, as seen in Figure 2.1. The ions are directed towards the curved surface of the conversion dynodes by applying a large attractive potential gradient ( $\pm 15$  kV). Once ions hit the dynode, secondary particles, such as electrons or positive or negative ions are generated. Typically, when negative analyte ions hit the surface of a dynode, positive ions are generated, whereas when positive analyte ions hit the surface, both negative ions and electrons are generated as secondary particles.<sup>13,14</sup> These secondary particles are driven towards the electron multiplier by a potential gradient between the conversion dynode and the multiplier. Each secondary particle strikes the surface of the electron multiplier, causing the ejection of one or more

electrons according to set amplification factor (gain). Due to the funnel shape of the cathode, this process occurs multiple times creating a cascade of electrons, eventually creating a large measurable current which is proportional to the number of ions originally ejected from the ion trap. The measured current is cross-referenced with the time event of the RF amplitude ion ejection scan, and the measured current reported as ion abundance, is assigned an  $m/z$  value and thus generating a mass spectrum. The schematics of the ion detection system are provided in Figure 2.5.

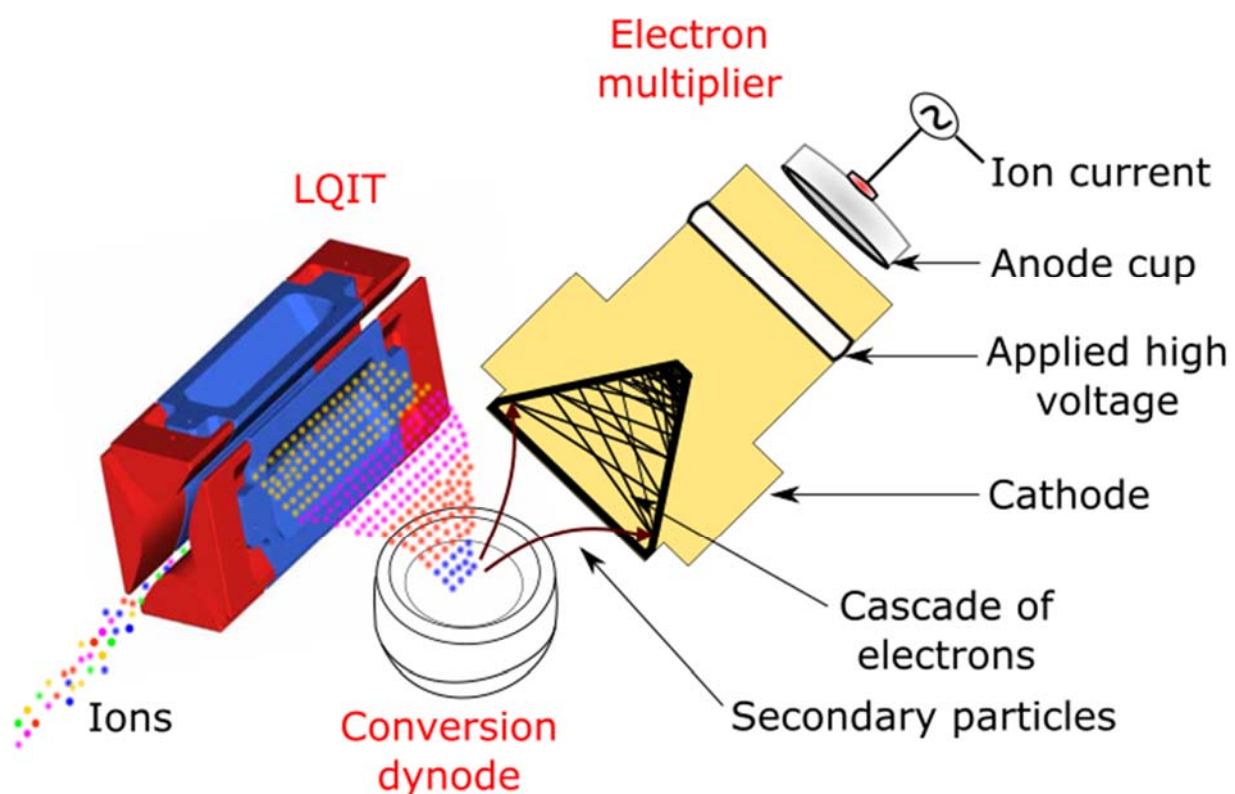


Figure 2.5 The ion detection system is composed of a conversion dynode and an electron multiplier. Ions ejected through the slits in the X-electrodes of LQIT collide with the surface of the conversion dynode to generate secondary particles. These secondary particles enter the electron multiplier, generating a cascade of electrons upon collisions with the surface, which in turn produce more electrons upon collisions with the surface, eventually generating a measurable ion current in the anode cup.

## 2.3 Ion Trap Scan Functions

The ion traps can perform four main functions that include ion trapping, isolation, excitation, and ejection. Details of these functions are discussed further.

### 2.3.1 Ion Trapping

Ions are trapped in the ion trap by using a combination of DC and RF potentials applied to the electrodes, and the helium buffer gas in the ion trap. While DC and RF potentials regulate the radial and axial motion of ions, helium is used to collisionally stabilize the ions into the center of the trap.

#### 2.3.1.1 Trapping Ions in the Radial (x and y) Direction

In LQIT, the RF and DC voltages are applied to all the four electrodes to create a two-dimensional quadrupolar RF-field.<sup>15</sup> The potential ( $\Phi_0$ ) thus generated is governed by the following equation:

$$\pm\Phi_0 = \pm(U - V \cos \Omega t) \quad (2.1)$$

Where  $U$  is the applied DC voltage and  $V$  is the amplitude of the RF voltage with an angular frequency  $\Omega$

Therefore, the ions within this quadrupolar RF field experience a potential in the x-y plane ( $\Phi_{x,y}$ )

which can be written in the form of an equation as follows (reference):

$$\Phi_{x,y} = \frac{\Phi_0(x^2 - y^2)}{r_0^2} = \frac{(U - V \cos \Omega t)(x^2 - y^2)}{r_0^2} \quad (2.2)$$

where  $r_0$  is the radius of the circle inscribed by the quadrupole rods.

Therefore, the ions are subjected to the following forces (F) in the x- and y-directions:

$$F_x = m \frac{d^2 x}{dt^2} = -ze \frac{d\Phi}{dx} \quad (2.3)$$

$$F_y = m \frac{d^2 y}{dt^2} = -ze \frac{d\Phi}{dy} \quad (2.4)$$

where  $m$  is the mass of the ion,  $z$  is the number of charges in the ion, and  $e$  is the charge of an electron ( $1.602 \times 10^{-19}$  Coulombs)

The equations governing the ion motion in the x-y plane are derived from above equations 2.2-2.4 and are given below<sup>10,16</sup>:

$$\frac{d^2 x}{dt^2} + \frac{2ze}{mr_0^2} (U - V \cos \Omega t) x = 0 \quad (2.5)$$

$$\frac{d^2 y}{dt^2} + \frac{2ze}{mr_0^2} (U - V \cos \Omega t) y = 0 \quad (2.6)$$

Above equations indicate that the ions with  $x$  and  $y$  values smaller than  $r_0$  will have stable trajectories in the ion trap. These equations have very close similarity to the Mathieu equation<sup>10,12</sup> given below.

$$\frac{d^2 u}{d\xi^2} + (a_u + 2q_u \cos 2\xi) u = 0 \quad (2.7)$$

By substituting the parameter  $\xi = \frac{\Omega t}{2}$ , equations 1.5 and 1.6 can be expressed as Mathieu equations<sup>10,12</sup> as shown below:

$$q_u = q_x = (-)q_y = \frac{4zeV}{mr_0^2 \Omega^2} \quad (2.8)$$

$$a_u = a_x = (-)a_y = \frac{8zeU}{mr_0^2 \Omega^2} \quad (2.9)$$

where  $a_u$  and  $q_u$  are known as the Mathieu stability parameters. These stability parameters have different values for the different regions in the Mathieu stability diagram, as shown in Figure 2.6.

The stability diagram describes the stability of ion trajectories in the trap in terms of parameters  $a$  and  $q$ . In simple terms, if the ions' stability parameters  $a$  and  $q$  are within the stability region of the Mathieu stability diagram, the ions will be trapped, and if one or both is outside the region, they will either collide with the walls of the ion trap or get ejected through the x-rod slits. Ions of different  $m/z$  values have different  $q_u$  values at a given main RF amplitude as shown in Figure 2.6.

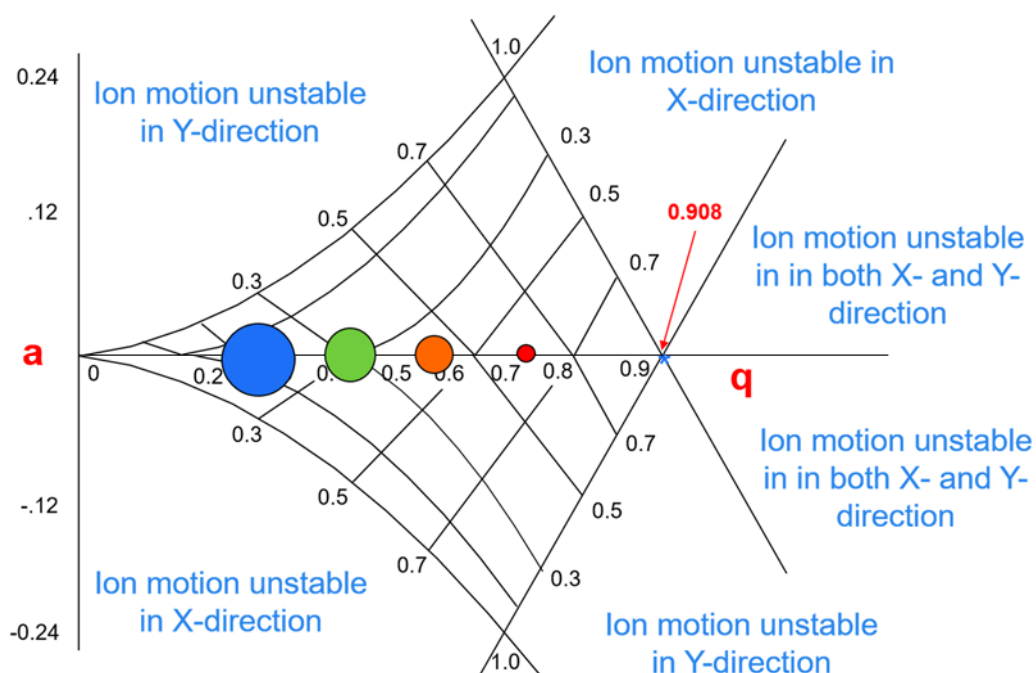


Figure 2.6 Mathieu stability diagram describing the ion motion inside the trap. The circles of different colors and sizes represent ions of different  $m/z$  ratios, larger circles corresponding to ions of larger  $m/z$  and vice versa. The ions will have stable trajectories in the overlapping regions. The unstable regions of the ions are also indicated.

The ions can be manipulated in the overlapping stability region by varying the main RF amplitude. Increasing the RF amplitude results in the increase of  $q_u$  value for any given ion. By ramping the RF amplitude, ions can be ejected out of the trap in the order of their  $m/z$  values (low  $m/z$  to high  $m/z$ ). When the ions reach a  $q_u$  value of 0.908, they become unstable in the x-direction

and are ejected from the trap. While some of the ions collide with the walls of the ion trap, others come out of the slits of the x-electrodes and can be detected by the electron multipliers. This method of scanning the ions is popularly known as “mass selective instability scan” or “q-scanning.” Each ion oscillates at a particular frequency ( $\omega_u$ ) in the LQIT, and this frequency is given by the following equation:

$$\omega_u = \frac{\beta_u \Omega}{2} \quad (2.10)$$

where  $\Omega$  is the angular frequency of the RF field applied to the rods of the ion trap,  $\beta_u$  is the Dehmelt approximation<sup>17</sup> for  $q_u$  values less than 0.4. The value of this approximation can be expressed as follows:

$$\beta_u = \sqrt{a_u + \frac{1}{2}q_u^2} \quad (2.11)$$

Based on Equation 2.11, the maximum value for  $\beta_u$  is 1. Therefore, the maximum secular frequency for an ion motion ( $\omega_u$ ) is  $\frac{1}{2}$  the RF angular frequency ( $\Omega$ ) applied to the electrodes. It is worth to note that the secular frequency of ion motion is directly proportional to its  $q_u$  value and inversely proportional to its  $m/z$  value. Therefore, ions of smaller  $m/z$  values have larger  $q_u$  values and will oscillate at higher secular frequencies compared to ions with larger  $m/z$  values.

### 2.3.1.2 Trapping Ions in the Axial (z) Direction

In order to regulate the axial (z-axis) motion of ions, the LQIT uses three axial DC potentials, one for each section of the LQIT electrodes as shown in Figure 2.7. Initially, the ions are driven into the ion trap by applying a lower DC potential for front section (DC 1) and even lower potential for center section (DC 2). The ions entering the trap are then confined to the trap by increasing the DC potential for both the front (DC 1) and back sections (DC 2), thereby creating



a potential well. The potential well traps the ions in the axial direction, maintaining them in the center section as shown in Figure 2.7.

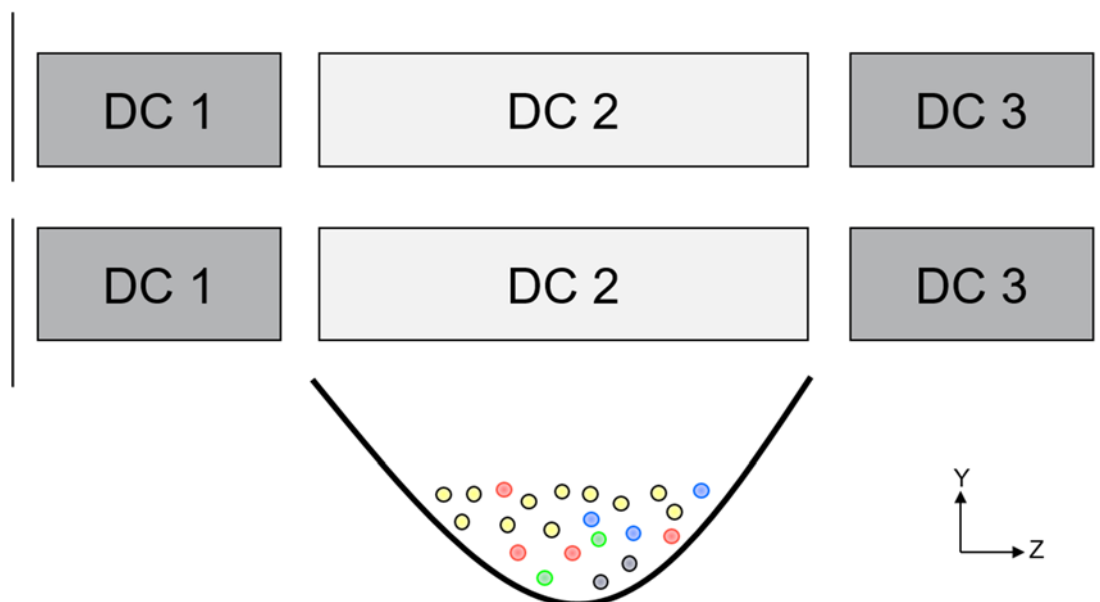


Figure 2.7 A DC potential well is created to regulate axial ( $z$ -axis) motion of ions by applying three DC trapping potentials, one for each section of the LQIT rods. Larger DC potential is applied to the front (DC 1) and back sections (DC 2) of the ion trap than to the center section (DC 3). The circles of different colors indicate different ions trapped in the potential well.

### 2.3.1.3 Stabilizing Ions in the Trap by Using Helium

Although the DC potential applied to the trap confines the ions axially, more efficient trapping can be achieved using helium as a collisional cooling gas within the ion trap. The presence of helium in the ion trap helps in keeping the ions in the center of the center section, thereby facilitating ion ejection to the detector and increasing sensitivity and mass spectral resolution.

### 2.3.2 Ion Ejection for Detection

As mentioned above, ions can be ejected from the trap by increasing the RF amplitude (q-scanning). Increase in the RF amplitude results in the increase of the ions' q value, and when this value reaches 0.908, the ions become unstable in the x-direction and are ejected from the trap. (Figure 2.8).<sup>18</sup> However, this method of ion ejection is not ideal for detection as the ions exit the trap in an uncontrolled manner, where only a few ions reach the electron multiplier for detection.<sup>18</sup>

To improve ion ejection for detection, the LQIT utilizes a technique called “x-electrode bipolar resonance ejection”.<sup>17</sup> In this technique, ions are ejected at a lower q-value of 0.88 (see Figure 2.8 ).<sup>17,19</sup> To achieve the ejection of ions at this q-value, a supplemental RF voltage is applied to the x-electrodes of the LQIT allowing them to be ejected at a lower q-value (0.88). By increasing the RF amplitude, the secular frequencies of oscillation of all trapped ions also increase. When ions' q-value reaches 0.88, their oscillatory frequency comes in resonance with the supplementary RF voltage. This resonance causes the ions to gain additional kinetic energy, which leads to a fast increase in the ions' oscillation amplitude and eventual ejection of the ions from the trap. Since the supplementary frequency is applied selectively to x-electrodes, the ions will only be ejected in the x-direction out of the slits in the x-electrodes.<sup>8</sup> By using the bipolar excitation approach, the ions are ejected as a tight ion packet in a more condensed manner, compared to q-scanning ejection method and therefore increased resolution and better sensitivity.<sup>19,20</sup> The ejected ions are then directed towards the detectors for detection.

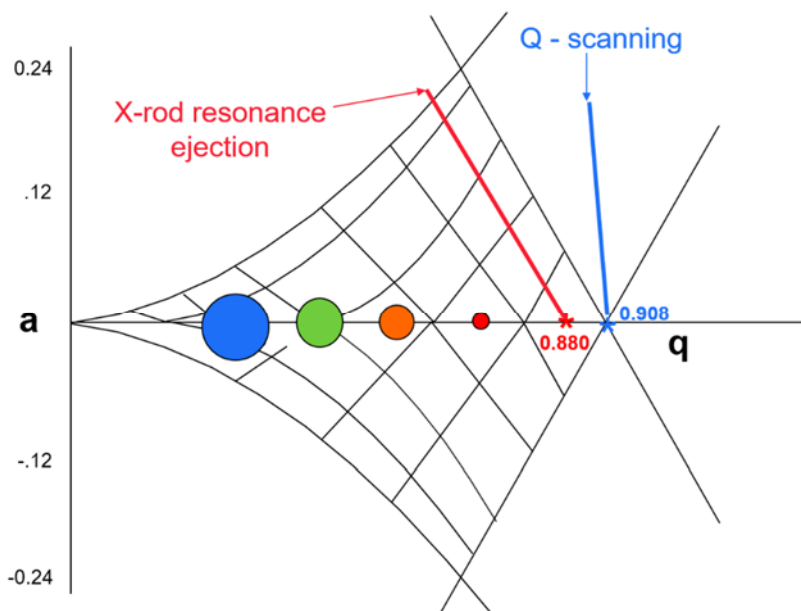


Figure 2.8 Mathieu stability diagram. The depiction of trapped ion ejection in the LQIT. Ions can be ejected at the stability limit (0.908) by using the mass-selective instability scan/q-scan or by x-rod bipolar resonance ejection. The application of resonance ejection increases resolution because ions of a specific  $m/z$  leave the trap in a more condensed manner.

### 2.3.3 Ion Isolation

Multi-stage tandem mass spectrometry ( $MS^n$ ) involves at least two stages of mass analysis ( $MS^2$ ), but often more ( $MS^n$ ), with fragmentation or an ion-molecule reaction occurring between the stages. To perform any stage of a tandem mass spectrometry experiment, an ion of interest must be first isolated. Ion isolation is performed in LQIT by taking advantage of the fact that ions at different  $q$  values oscillate at different frequencies and each frequency corresponds to a unique, specific  $m/z$  value. When isolating an ion, the RF voltage is ramped until the desired ion's  $q$  value reaches 0.803. This results in the ejection of all the ions having lower mass than the ion of interest. After this ramp, a broadband excitation waveform is applied to the x-electrodes at all the frequencies ( $q$  values) of the ions (5-500 kHz), except for a notch at  $q = 0.803$  which corresponds to the ion of interest. As a result, all the unwanted ions are ejected out of the ion trap (Figure 2.9).

The width of the notch is determined by the width of the isolation window, which is defined by the user.

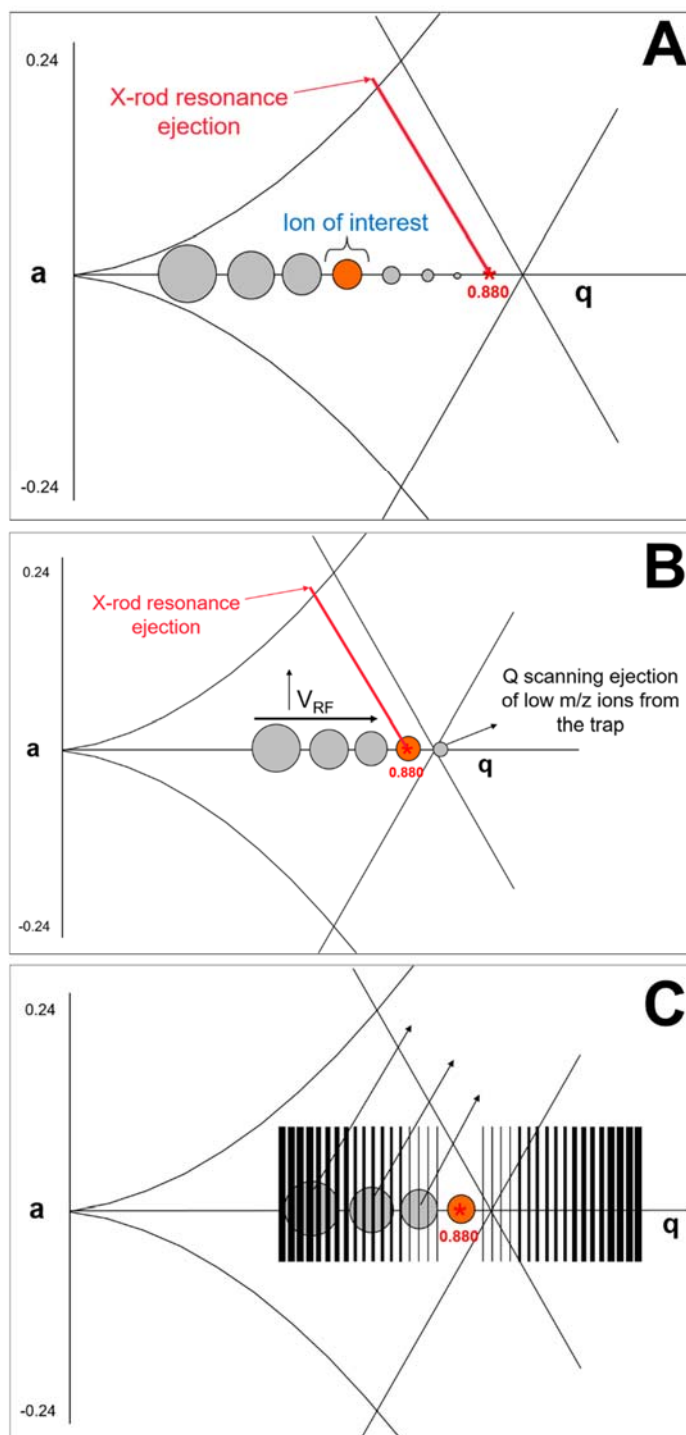


Figure 2.9 a) Mathieu stability diagram showing ions in the stability region. B) The main RF voltage is ramped until the ion of interest attains a  $q$ -value of 0.830, resulting in the ejection of ions of lower  $m/z$  values than the ion of interest from the trap. C) Tailored isolation waveform is applied, ejecting ions of greater  $m/z$  values than the ion of interest from the trap.

#### 2.3.4 Collision-activated Dissociation

Ions isolated in the ion trap can be studied by using either ion-molecule reactions or dissociation reactions. Collision-activated dissociation (CAD) is a type of dissociation reaction that is used for the experiments discussed in this thesis and therefore is discussed in detail below.

CAD in LQIT is a method wherein the isolated ion of interest is accelerated and subjected to fragmentation by allowing the ion to undergo multiple low-energy collisions with helium.<sup>21,22</sup> The process of CAD in LQIT ion traps starts with lowering the RF amplitude for the ion of interest until it reaches a low  $q$ -value, typically 0.25. The ion is then accelerated by using dipolar resonance excitation. To achieve this, a supplementary RF voltage (tickle voltage) of small amplitude and with a frequency equal to the ion's resonance frequency is applied to the  $x$ -electrode typically for 30 ms.<sup>8</sup> This RF voltage is not strong enough to eject the ions from the trap but can enhance the ion motion in radial direction, resulting in the increase of its kinetic energy. Upon collisions of this accelerated ion with helium gas in the ion trap, its kinetic energy is converted into its internal energy, causing it to dissociate. The fragment ions are mass analyzed as discussed in Section 2.3.2. A detailed illustration of the steps of ion isolation, CAD and mass analysis of the fragment ions is given in Figure 2.10.

As discussed above, the activation  $q$  value can be varied. The  $q$  value at which the ions are activated is crucial for CAD experiments. The choice of  $q$  value determines the low  $m/z$  cut-off for the fragment ions that can be trapped after fragmentation as well as the amount of kinetic energy that the ion of interest gains.<sup>8</sup> For example, if the ion is activated at a higher  $q$ -value, the ion oscillates at a higher frequency (higher kinetic energy), thereby experiencing more energetic collisions with helium, resulting in more extensive fragmentation. However, as the  $q$  value is increased, the observable mass range for the fragment ions is narrowed as the activated ion has a

q-value closer to the instability limit, resulting in lower mass cut-off. Therefore, the q value must be wisely chosen for CAD experiments. Typically, q value of 0.25 is used for CAD to achieve a balance between the extent of fragmentation and low mass cut-off.

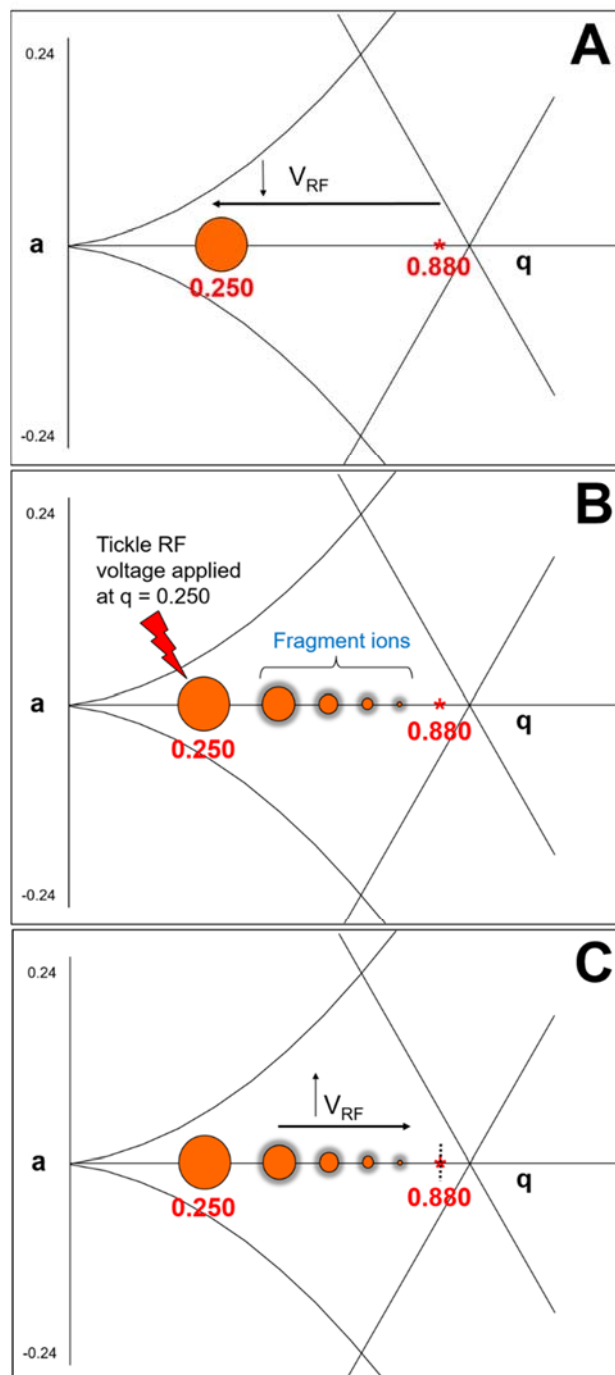


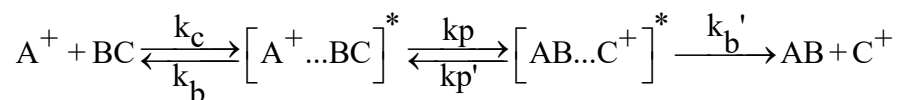
Figure 2.10 a) The  $q$ -value of the isolated ion is reduced from 0.880 to 0.250 by lowering the main RF amplitude. B) A supplementary RF voltage (tickle voltage) is applied at a  $q$  value of 0.250 to excite the ion resonantly, thereby causing energetic collisions with helium. Fragment ions are produced upon collisions with helium. C) The fragment ions are separated based on their  $m/z$ -values by using the  $q$ -scan or mass selective instability scan with resonant ejection at a  $q$  value of 0.880.



## 2.4 Ion-Molecule Reactions

In addition to CAD experiments, gas phase ion-molecule reactions have proven to be a powerful tool for the structural elucidation of isolated ions.<sup>23-28</sup> The isolated ion of interest is allowed to react for a variable time with a gaseous neutral reagent introduced into the ion trap via an external mixing manifold. After the reaction, the product ions are detected as described in Section 2.3.2.

The double-well potential energy surface model proposed by Brauman has provided a rational understanding of the outcomes of gas phase ion-molecule reactions (Figure 2.11).<sup>29,30</sup> According to this model, ion-molecule reactions are proposed to occur via the formation of a reactant complex and a product complex separated by an entropically restricted energy barrier. Figure 2.11 illustrates the model in the case of positively charged molecules, and the process is schematically represented below.



where,  $k_c$  is the rate of collision,  $k_b$  is the rate of dissociation to separated reactants,  $k_p$  and  $k_p'$  are the rates of chemical transformations, and  $k_b'$  is the rate of dissociation to separated products

Gas phase ion-molecule reactions proceed by the initial formation of a reactant collision complex of an ion and a neutral molecule due to long-range ion-dipole and/or ion-induced dipole forces. These forces lower the potential energy of the reactant complex by providing solvation energy that is now available for the collision complex to overcome reaction barriers (such as transition states). The height of the energy barrier dictates whether the reaction will proceed towards producing reaction products or reverse back to reactants. The energy difference between the separated reactants and the transition state ( $\Delta E$ ; Figure 2.11) correlates with the rate at which the gas phase reactions occur.<sup>30</sup> Unlike reactions that occur in solution (where energy can be

obtained from heated solvent molecules), the reactions in the gas phase occur only when the overall reaction is exothermic as the total energy of the system is conserved in high vacuum.

Many gas phase ion-molecule reactions do not occur at the collision rate ( $k_c$ ) due to the entropically favored dissociation ( $k_b$ ) of the reactant complex back to separated reactants.<sup>30</sup> The transition state that leads to the formation of products is usually tighter than the transition state leading to separated reactants and therefore lower in entropy. This means that the dissociation to generate separated reactants is often faster than product formation, even when the net reaction is exothermic, and the barrier is low in energy.

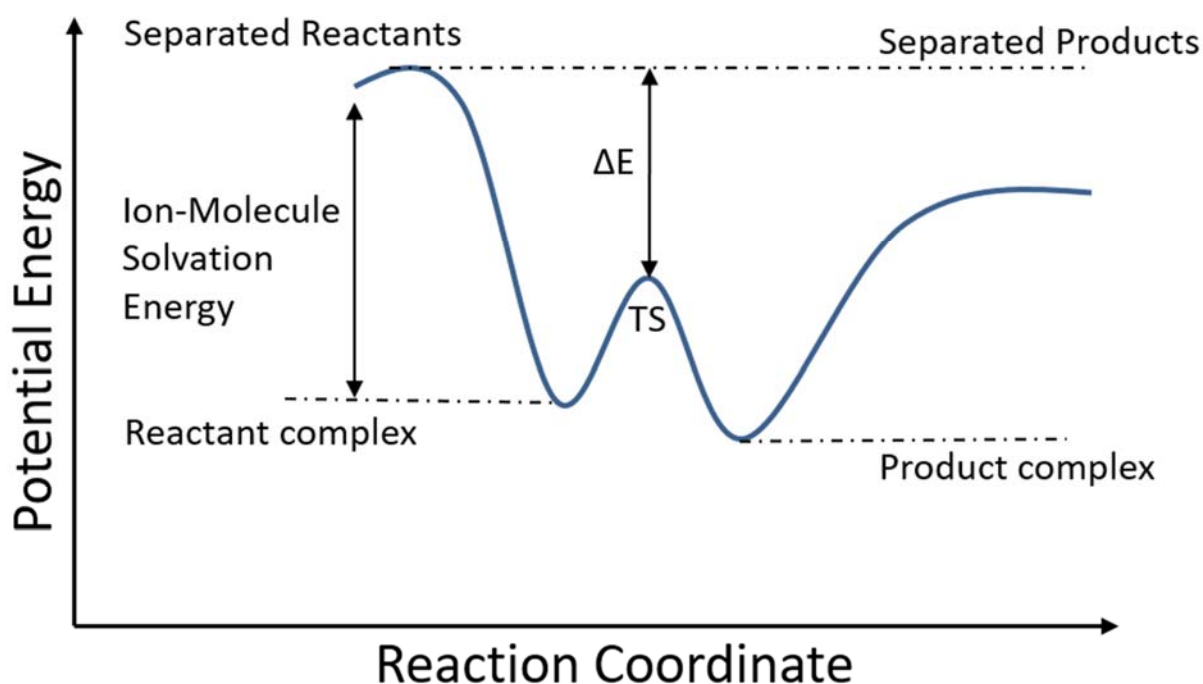


Figure 2.11 The Brauman double-well potential energy surface for a simple ion-molecule reaction in the gas phase.

To allow the introduction of reagents into the ion trap, an external reagent manifold was used. The external reagent inlet manifold was initially designed and developed by Gronert and co-workers.<sup>31,32</sup> The schematics of the external reagent manifold setup used in the experiments discussed in this thesis are provided in Figure 2.12. In this setup, the reagent is continuously introduced into the helium line of the manifold via a syringe pump. This introduced reagent is rapidly evaporated by heating the syringe port and surrounding area of the manifold to an appropriate temperature. The amount of He/reagent mixture entering the ion trap of the mass spectrometer is controlled by using a control valve (Granville-Phillips leak valve) and by diverting part of the mixture to waste. After experiments were completed each day, the manifold was isolated from the mass spectrometer and connected to a vacuum pump to minimize contamination.

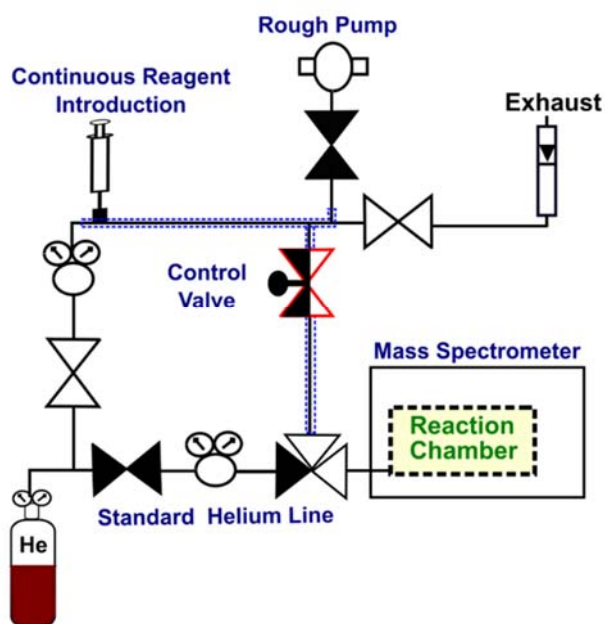


Figure 2.12 External reagent inlet manifold for introduction of helium/reagent gas mixtures. The valves shown above are open to the manifold, allowing the diluted reagent/helium mixture into the ion trap via a control valve.

## 2.5 Ionization Methods

Many different ionization methods have been developed over the years for the ionization of analytes of interest. The first developed ionization methods, such as electron impact ionization,<sup>33</sup> and chemical ionization,<sup>34,35</sup> required the analytes to be volatile so that they can be evaporated prior to ionization. However, with the advancement of mass spectrometry technologies, mass spectrometry is now capable of analyzing non-volatile analytes. This was achieved by the introduction of a variety of new ionization methods that coupled the desorption and ionization of analyte molecules. These methods include electrospray ionization (ESI),<sup>36-38</sup> desorption electrospray ionization (DESI),<sup>39</sup> atmospheric pressure chemical ionization (APCI),<sup>40</sup> atmospheric pressure photoionization (APPI),<sup>41</sup> matrix-assisted laser desorption/ionization (MALDI),<sup>42</sup> field desorption/field ionization (FD/FI),<sup>43,44</sup> and fast-atom bombardment (FAB).<sup>45</sup> Several ionization methods utilized in this research are discussed below.

### 2.5.1 Electrospray Ionization (ESI)

Since the introduction of ESI technique by Masamichi Yamashita and John Fenn in 1989,<sup>36</sup> it has gained popularity for its ability to bring ionized large polar analytes into the gas phase. Many large compounds, such as polymers and biopolymers, and compounds that previously could not be analyzed by using MS are now easily analyzed using this evaporation/ionization technique.<sup>37</sup> ESI is a soft ionization method by which species present in solution are transferred into gas-phase as ions, with minimal or no fragmentation.

During a typical ESI experiment, the solution containing the analytes undergoes three main processes, a) generation of charged droplets from a high voltage capillary tip, upon injection of solution containing analytes; b) repeated solvent evaporation and droplet disintegration from the charged droplets to produce smaller charged droplets; c) finally ejection of gas phase ions from

these charged droplets. The ionization process is depicted in Figure 2.13. While the first two processes are well understood, the last process, that is, the exact process for this formation of ions from the charged droplets is widely debated, and several hypotheses based on the theory and experimental evidence were discussed in the literature.<sup>46-48</sup> Herein two important models proposed for the ion formation are discussed.

When a solution containing the analytes is injected through the capillary that has a high-voltage applied to the tip (3-5 kV), an electrochemical reaction of the solvent occurs causing the electron flow to or from the metal capillary based on its polarity. As a result, Taylor cone<sup>49-51</sup> is formed at the end of the capillary, which further ejects a plume of electrically charged droplets. ESI is analogous to the current controlled electrolytic cell, and therefore the number of electrically charged droplets produced in ESI is dependent on the current applied.<sup>52</sup> The charged droplets thus produced are held together because the surface tension of the droplet is larger than the Coulombic repulsions due to electric charge density at the surface. However, as the solvent evaporates, the electric charge density increases until it reaches an instability limit, known as the Rayleigh instability limit.<sup>53</sup> At this critical point, the droplets undergo Coulombic fissions producing smaller droplets. This process continues to repeat to produce very small droplets. The lifetime of these droplets is around 1 to few milliseconds and is mostly depends on parameters such as nature of solvents, ion spray voltage, sheath and auxiliary gas flow rates, the distance between the spraying nozzle of ESI and heated capillary of the mass spectrometer and so forth. From these very small charged droplets, analyte ions are ejected into the gas phase and enter the mass spectrometer via an ion transfer capillary.

The two important models that describe the formation of gas-phase ions from the small highly charged droplets includes charge residue model (CRM),<sup>54,55</sup> and the ion evaporation model

(IEM).<sup>56</sup> According to ion evaporation model, as the small charged droplets reach their Rayleigh instability limit, their surface charge becomes sufficiently large to allow for field desorption of the desolvated ions. In contrast, according to the charge residue model, the gas phase ions are generated from these charged droplets via the evaporation of the residual solvent molecules, giving the analyte most of the charges that the droplet carried. It is believed that the charge residue model applies better to large globular species such as proteins, whereas the low molecular weight analytes follow the ion evaporation model.<sup>57</sup> Although both the models proposed different pathways for the formation of gas-phase ions from small charged droplets, the models suggested that the ions are transferred directly from solution, indicating that the analyte ions are performed in the solution.

Nebulization gases such as nitrogen are supplied to the electrospray ionization source to assist in solvent evaporation and ion desolvation.<sup>58</sup> Nitrogen sheath gas is supplied near the tip of the capillary to help nebulize the solution into a fine mist or spray (see Figure 2.14) . An auxiliary nitrogen gas flow is utilized in the ionization source as shown in Figure 2.14 to assist in solvent evaporation as well as to collimate the spray.

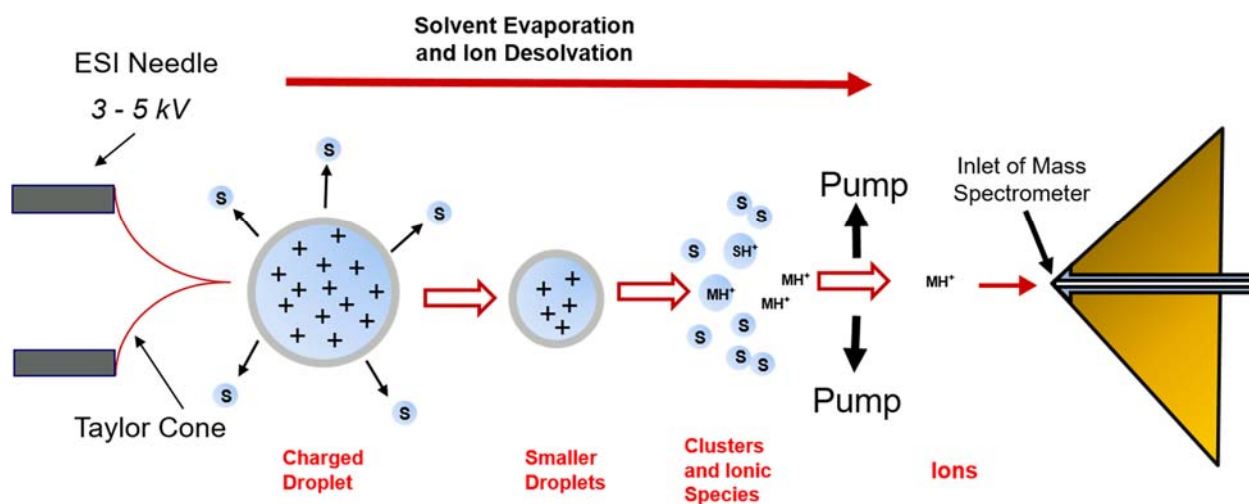


Figure 2.13 ESI ionization process. The region between the ESI needle and the mass spectrometer inlet shows the process of solvent evaporation and ion desolvation leading to the production of ions.

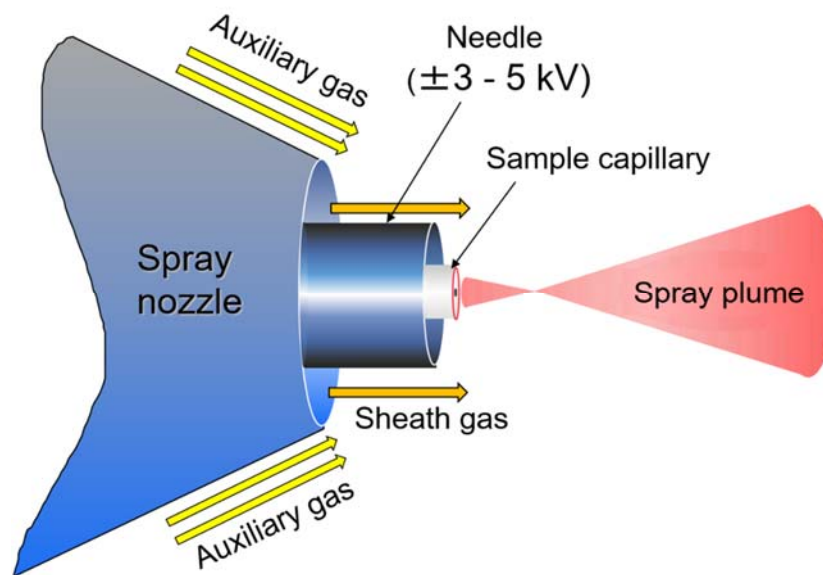


Figure 2.14 Schematics of an ESI tip demonstrating the use of sheath and auxiliary gases to nebulize and collimate the spray.

### 2.5.2 Atmospheric Pressure Chemical Ionization (APCI)

APCI is another soft ionization technique commonly used to evaporate and ionize analytes with medium to low polarity.<sup>40</sup> Although APCI source is similar in design to ESI source, the process of ionization is different. Unlike in ESI, ions are generated in the gas phase by using a high voltage corona discharge needle. In APCI, the analyte solution is injected into the ion source through a heated transfer capillary (300-500 °C) in the presence of nitrogen sheath gas, which produces a mist of fine droplets and eventually vapors of solvent and analyte molecules, which are now exposed to corona discharge needle (Figure 2.15). The corona discharge needle initially ionizes the nebulization gas ( $N_2$ ) to produce primary ions. These primary ions react with solvent molecules through a complex series of reactions forming solvent ions. These solvent ions undergo ion-molecule reactions with analyte molecules to form analyte ions. This process is analogous to chemical ionization (CI). The cascade of reactions initiated by corona discharge to generate analyte ions from an analyte in an aqueous solution is shown in Scheme 2.1.

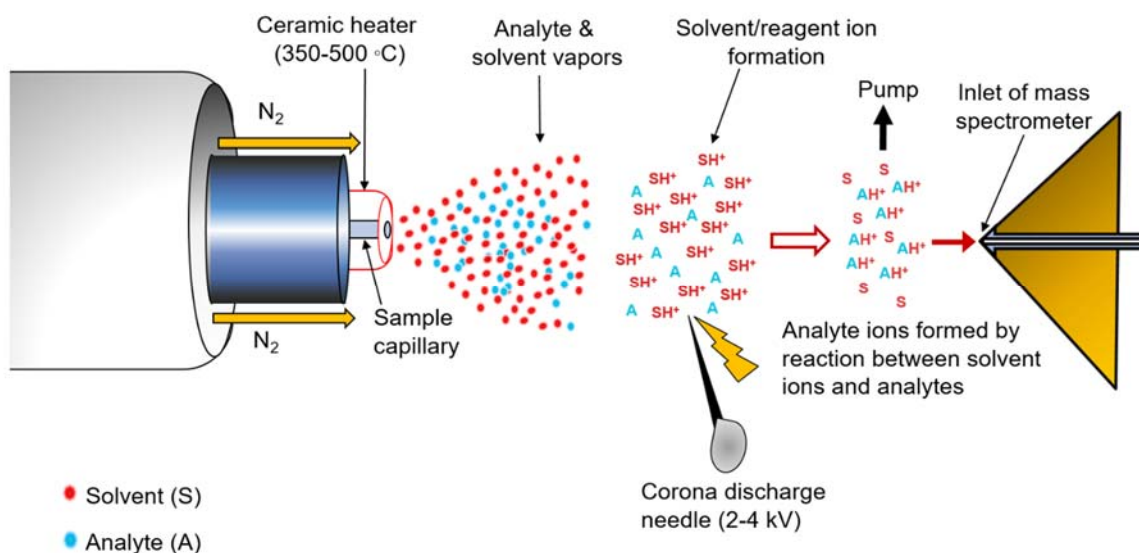
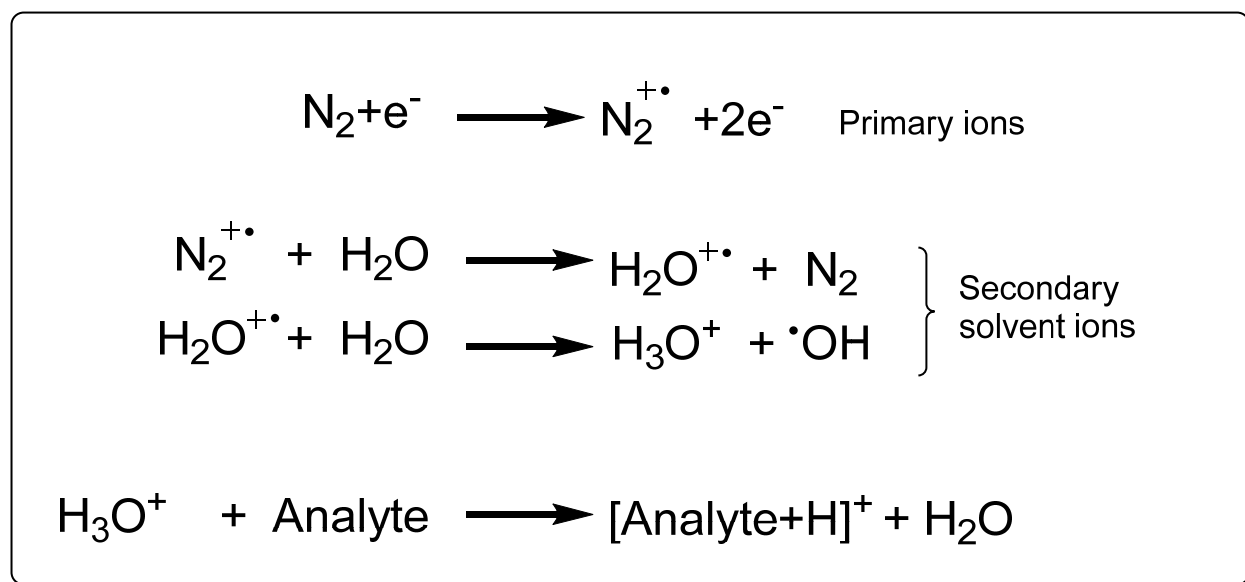


Figure 2.15 APCI ionization process in positive ion mode.





Scheme 2.1 APCI ionization mechanism for the generation of protonated analytes in positive ion mode when using water as a solvent.

### 2.5.3 Atmospheric Pressure Photo Ionization (APPI)

APPI is another ionization technique that is not as commonly used as APCI and ESI. This is because APPI ionization technique efficiently ionizes only moderately polar aromatic compounds. APPI generates analyte ions in a two-step process. First, the analyte dissolved in the solvent is thermally desolvated and evaporated by using an APCI probe to produce vapors of the analyte and solvent. The gaseous analyte and solvent molecules are ionized via a UV light source (Figure 2.16). Aromatic analyte molecules may absorb a photon (krypton lamp emits 10.0 to 10.6 eV photons) and get electronically excited. These excited analyte molecules may release an energetic electron and become radical cations. This requires the ionization energy (IE) of the analyte molecules to be lower than the energy of the photons (Scheme 2.2A). However, if the IE of the analyte molecules is higher than the energy of the photons, the energetically excited analyte

molecules may undergo photodissociation or photon emission. In such situations, selection of an appropriate light-absorbing solvent or dopant may assist the ionization of analyte molecules. The solvent-mediated cascade of reactions generating analyte ions is shown in Scheme 2.2B.

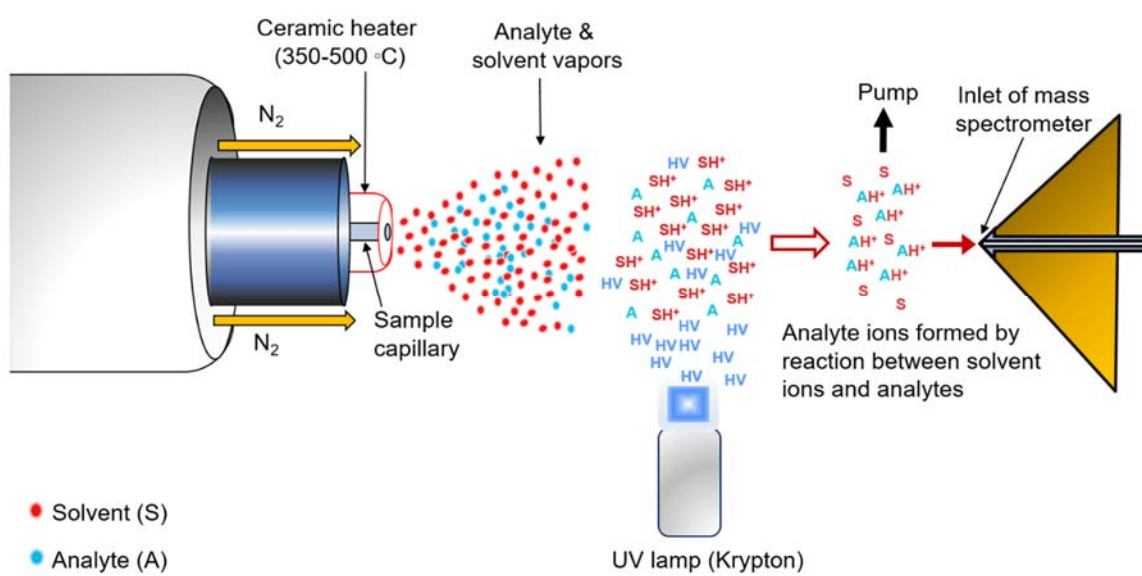
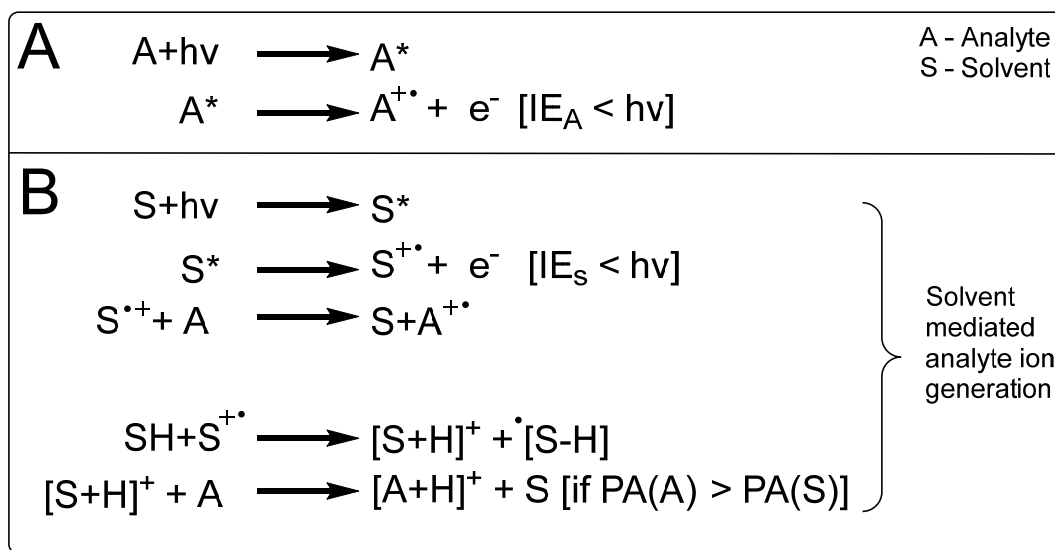


Figure 2.16 Illustration of the APPI ionization process mediated by a protic solvent in positive ion mode.



Scheme 2.2 Possible mechanisms for the generation of analyte ions upon positive mode APPI ionization. A) Direct ionization of an analyte. B) Solvent mediated ionization of an analyte.

#### 2.5.4 Electron Ionization (EI) in GCxGC/TOF MS

Electron ionization or electron impact ionization is the oldest ionization technique used in mass spectrometers.<sup>33</sup> In EI, the analyte molecules that are desorbed into the gas phase either thermally or by using some other evaporation method enter the ionization source, where they are bombarded with a beam of highly energetic electrons (typical kinetic energy  $\sim 70$  eV).<sup>59-61</sup> This is considered as a hard ionization method, as it uses highly energetic electrons which typically causes fragmentation. A schematic of an EI source is provided in Figure 2.17. Collisions of the energetic electrons with the gaseous analyte molecules result in the ejection of an electron from an analyte molecule, thus producing a molecular ion. If the excess energy deposited into the analyte ions exceeds their fragmentation threshold, the ions will undergo fragmentation. The EI ionization source was used for the characterization of volatile analytes extracted from crude oil by using GCxGC/TOF mass spectrometer.

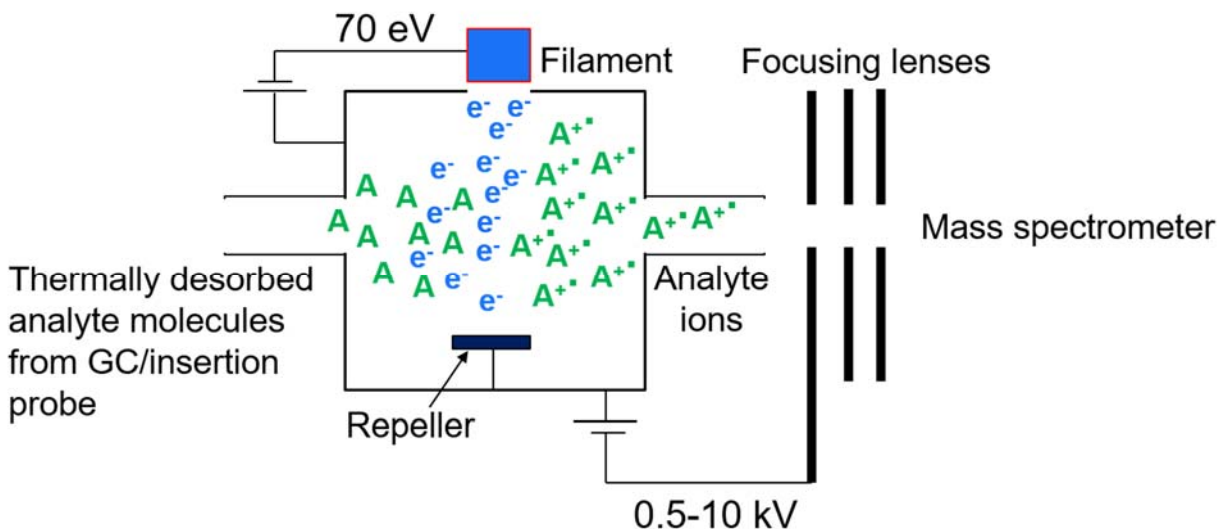


Figure 2.17 Diagram of the EI source.

## 2.6 Orbitrap Mass Spectrometry

The orbitrap mass spectrometer was first introduced by Alexander Makarov in 2000.<sup>62</sup> It is based on the concept of orbital trapping of ions around a center wire stretched along the axis of a cylindrical electrode initially proposed by Kingdon in the early 1920s.<sup>63</sup> While Kingdon configurations did not produce mass spectra, Makarov configurations were successful in trapping ions and producing mass spectra.

Orbitrap consists of an outer barrel like electrode and an inner co-axial spindle like electrode and each of these electrodes are connected independently to external voltages.<sup>64</sup> The space between the electrodes makes up the ion trapping volume, which is connected to a vacuum pump. The C-trap injects the ions of individual  $m/z$  values as tight packets, at a position offset from the center of the orbitrap. These ion packets are accelerated with enough tangential velocity, such that they will cycle parallelly around the spindle electrode (without colliding) with a set axial frequency that is related to their  $m/z$  value.<sup>63</sup> This axial frequency is utilized for ion detection. The image

current produced by the axial oscillation is measured, and the fourier transform operation is employed to convert frequency data into  $m/z$  values. For the experiments performed in this thesis, a Thermo Scientific LTQ Orbitrap XL mass spectrometer was utilized. A schematic for this instrument is shown in Figure 2.18.

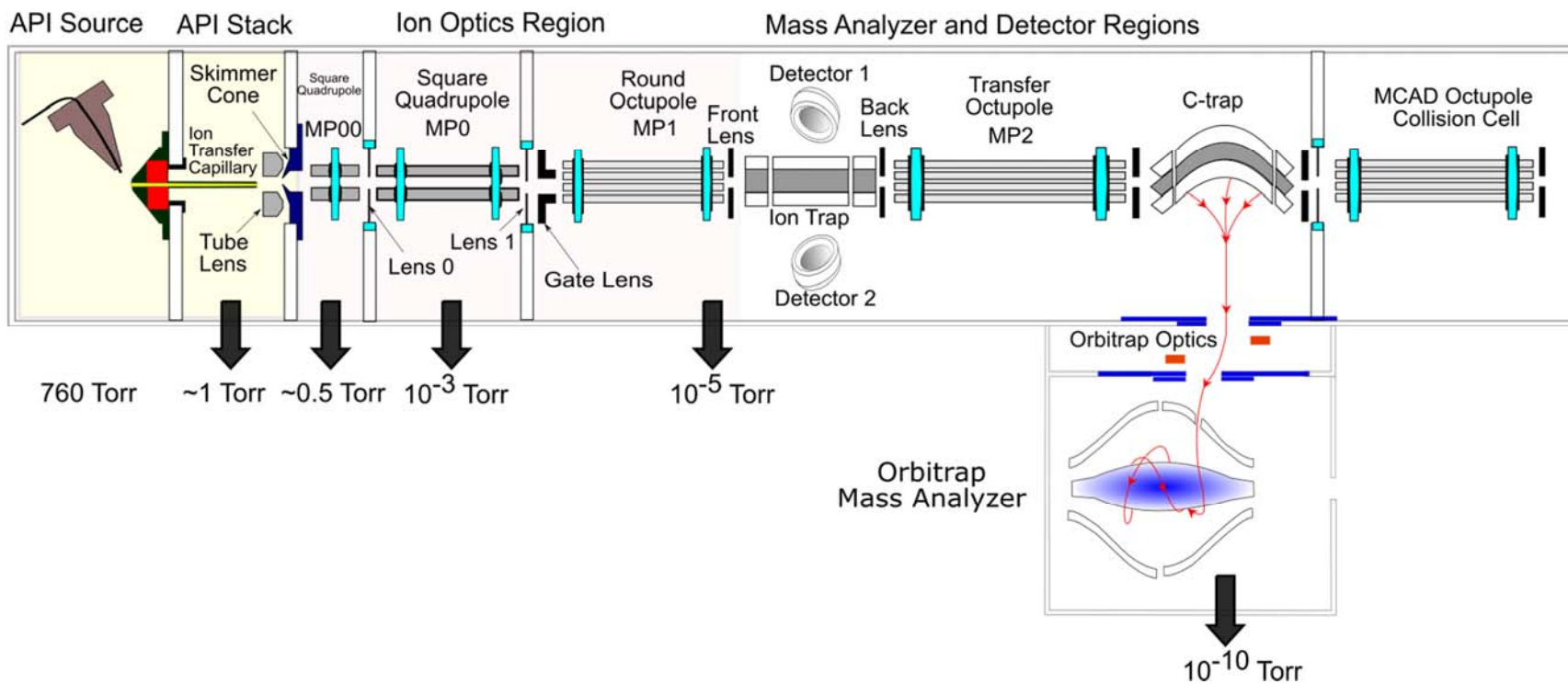


Figure 2.18 Thermo Scientific LTQ Orbitrap XL. The red line indicates the injection of ion packets from C-trap into orbitrap through the orbitrap injection optics.

### 2.6.1 Equations of Motion for Ions in the Orbitrap

The outer and inner electrodes of the orbitrap are precision machined to create the quadrupole logarithmic field with potential distribution,  $U$ , mathematically described below.<sup>62,65</sup>

$$U(r,z) = \frac{k}{2} \left( z^2 - \frac{r^2}{2} \right) + \frac{k}{2} (R_m)^2 \ln \left[ \frac{r}{R_m} \right] + C \quad (2.12)$$

where  $r$  and  $z$  are cylindrical coordinates ( $z = 0$  being the plane of symmetry),  $k$  is field curvature,  $R_m$  is the characteristic radius of an ion of mass  $m$  and  $C$  is a constant.

The ions entering this field acquire three characteristic frequencies of ion motion; rotation around the central electrode ( $\omega_\phi$ ), radial oscillations ( $\omega_r$ ), and axial oscillations along the  $z$ -axis ( $\omega_z$ ). The equations of motion in polar coordinates ( $\phi, r, z$ ) for ions of mass to charge ratio ( $m/q$ ) are given below

$$\frac{\partial^2 r}{\partial t^2} - r \left( \frac{\partial \phi}{\partial t} \right)^2 = -\frac{q}{m} \frac{k}{2} \left[ \frac{R_m^2}{r} - r \right] \quad (2.13)$$

$$\frac{d}{dt} \left[ r^2 \frac{\partial \phi}{\partial t} \right] = 0 \quad (2.14)$$

$$\frac{\partial^2 z}{\partial t^2} = -\frac{q}{m} kz \quad (2.15)$$

Out of the three characteristic frequencies ( $\omega_\phi$ ,  $\omega_r$  and  $\omega_z$ ), only the axial frequency along the  $z$ -axis is independent of the position and energy of the ions, and therefore only this frequency of ion motion can be used for the determination of the ion  $m/q$  value. The axial frequency of oscillation is given below

$$\omega_z = \sqrt{\left( \frac{q}{m} \right) k} \quad (2.16)$$

where,  $k$  is constant and derived from equation 1.13. The value of  $k$  is proportional to the voltage applied between the inner and outer electrodes.

### 2.6.2 Ion Injection

High resolution can be obtained with the orbitrap by measuring the image current of ions accurately. This requires the injection of ions of the same  $m/z$  value as a tight packet into the orbitrap which is achieved by using curved linear quadrupole ion trap called C-trap.

In the LQIT orbitrap, a transfer octupole delivers ions into a curved C-trap filled with nitrogen buffer gas. The buffer gas reduces the kinetic energy of the ions introduced into the C-trap by collisional cooling. Nitrogen gas is chosen over helium as a buffer gas due to better collisional damping and lower gas carryover toward the orbitrap.<sup>66</sup> To minimize nitrogen gas carry over from the C-trap into orbitrap, the ion packet is usually deflected by a set of transfer lenses (see Figure 2.19).<sup>66</sup> Once the ions are cooled, a large potential gradient is applied to accelerate and pulse the ion packets into the orbitrap.<sup>66</sup>

The C-trap has been designed to inject the ions of individual  $m/z$  values as tight packets, at a position offset from the center of the orbitrap. This allows for coherent axial oscillations of ion packets almost immediately after injection without the need for any external excitation.<sup>67,68</sup> Upon their entry, these ion packets are squeezed to move the ions towards the equator and the central electrode by ramping up the voltage of the central electrode. Since the rotational frequencies depend on the angles, initial positions, and ion energies, the ion packets are spread over the angular coordinate, forming a thin rotating ring around the central electrode allowing the possibility to accommodate more ions in the trap. After injection and before ion detection, the voltages on the central electrode are stabilized to avoid mass drifts.



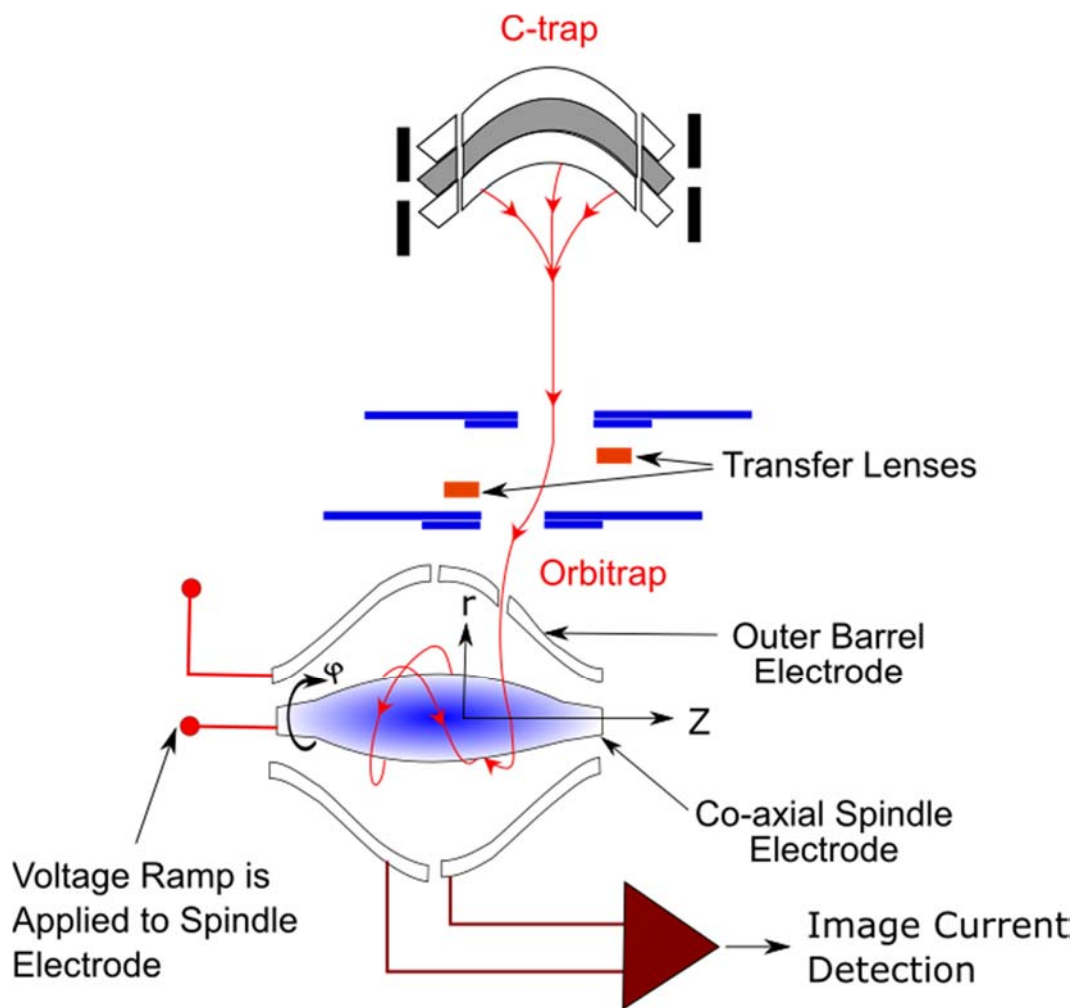


Figure 2.19 Figure is showing the injection of ion packets into the orbitrap by the C-trap. The red line indicates the ion trajectory. The image current produced by the axial oscillation (z-axis) of the ions is measured. Voltage ramp is applied to the inner electrode.

### 2.6.3 Ion Detection

The frequency of the axial motion of the ions is utilized for ion detection. The image current produced by the axial oscillation of the ions is measured, and a Fourier transform operation is employed to convert the recorded time-domain data into  $m/z$  values and related abundances and therefore producing the mass spectrum.<sup>65,69,70</sup> Since the detection of the ions is based on the

measurement of frequency, the orbitrap is non-destructive, and high mass resolution is obtainable.<sup>62,69,70</sup>

## 2.7 Medium Energy Collision-activated Dissociation (MCAD)

The LTQ Orbitrap XL mass spectrometer used in this thesis research is equipped with an octupole collision cell (referred here to as the MCAD (or medium-energy CAD) octupole) that enables triple quadrupole like CAD experiments (beam type CAD) (Figure 2.18). This collision cell is supplied with an RF voltage (2.6 MHz, 500 V p-p) and a variable DC voltage  $\pm 250$  V, and it is filled with a gas of choice (usually nitrogen) for CAD.<sup>71</sup>

In MCAD, the ions of interest are isolated in the ion trap and transferred into the C-trap that is held at ground potential. The ions are accelerated from the C-trap into the MCAD octupole at kinetic energy determined by the potential difference between the C-trap and the octupole. The fragment ions thus produced are transferred from the octupole back into the C-trap by raising the potential of the octupole. Typical DC offset potentials applied to different sections of the instrument during the MCAD process are shown in Figure 2.20. Unlike in CAD, MCAD supports multiple cleavage events not only because the ion kinetic energy of the ions is much higher and the target collision gas is much more massive, but also that the fragment ions produced in the octupole are also accelerated on their way back to C-trap, which may result in extensive fragmentation. One advantageous feature of MCAD is that the low mass region in the MS/MS spectra can be obtained using this approach, unlike in CAD.

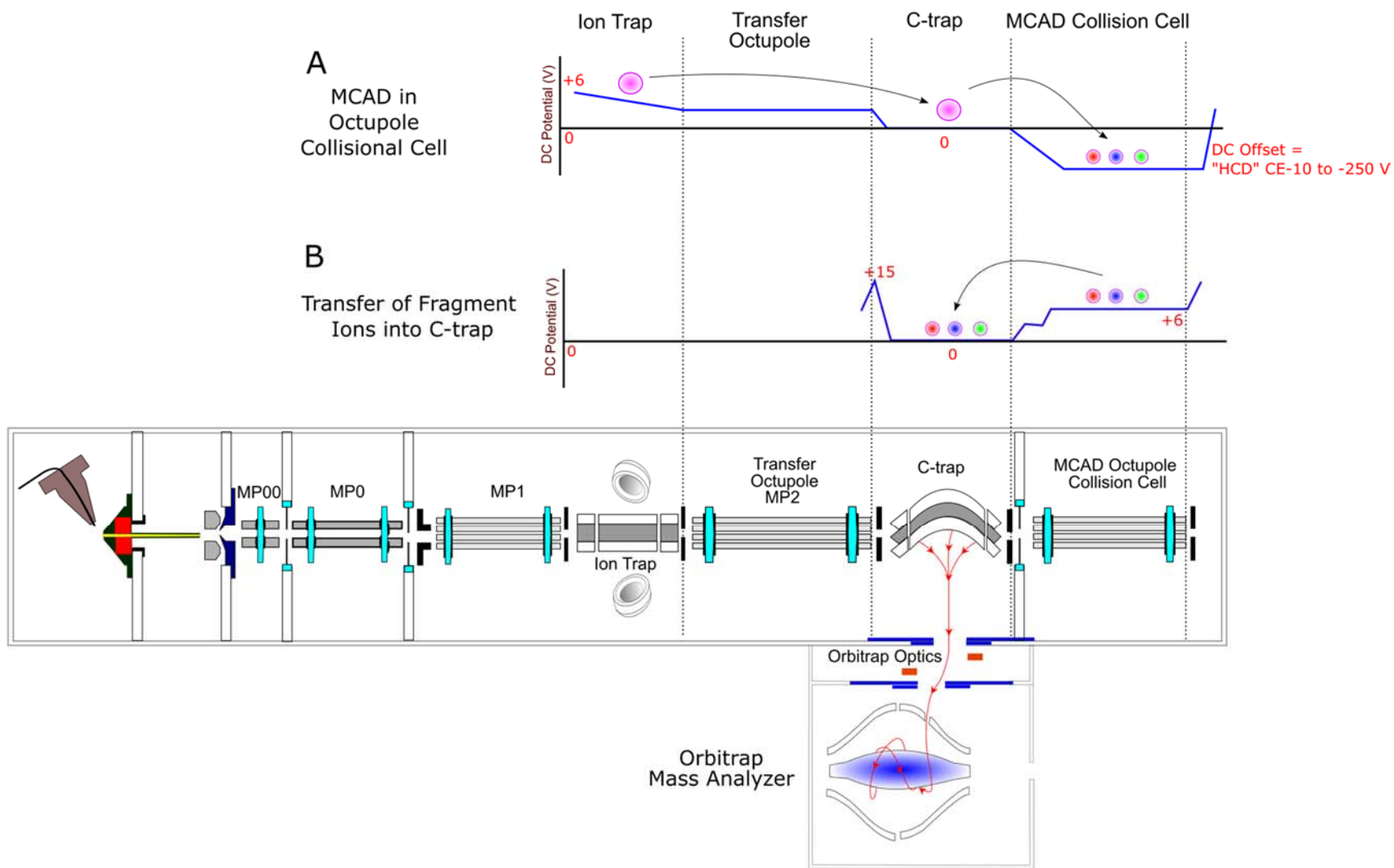


Figure 2.20 Typical DC offset potentials applied to the ion trap, C-trap, and MCAD collision cell. A) Potentials applied to induce MCAD fragmentation for an ion of interest. B) Typical voltages applied to send the MCAD fragment ions into the C-trap, which enables their detection by Orbitrap.

## 2.8 Chromatography/Mass Spectrometry

While tandem mass spectrometry is a powerful technique for complex mixture characterization, in many situations, chromatographic separation techniques such as gas chromatography and liquid chromatography are still needed, primarily to characterize complex mixtures that may contain isobaric and isomeric compounds. In this thesis research, high-performance liquid chromatography (HPLC) and 2-dimensional gas chromatography (GCxGC) coupled with mass spectrometers were used. The details are provided below.

### 2.8.1 High-performance Liquid Chromatography/Mass Spectrometry (HPLC/MS)

For HPLC separation experiments discussed in this thesis, a Thermo Scientific Surveyor Plus HPLC coupled with a PDA detector and a mass spectrometer was used. The basic components of this HPLC system include an autosampler, solvent reservoir, solvent degassers, quaternary high-pressure pumps, solvent mixer, sample injector valve, detectors and temperature regulated column compartment.

### 2.8.2 Two-Dimensional Gas Chromatography/Mass Spectrometry (GCxGC/MS)

For GCxGC/MS experiments performed in this thesis research, a LECO Pegasus 4D GCxGC/TOF instrument equipped with an Agilent 7890B gas chromatograph (Agilent Technologies, Santa Clara, CA) and a high-resolution time-of-flight (TOF) mass spectrometer (up to 50,000 resolution) was used. The schematics of the instrument are shown in Figure 2.21.

The GCxGC/TOF instrument consists of a two-dimensional GC system coupled with a folded flight path (FFP) TOF-mass analyzer. After separation of the compounds by using the two-dimensional GC, positive ion mode electron ionization (EI) (70 eV) was used to ionize the compounds upon entrance into the mass spectrometer. The ionized compounds were analyzed by

using the FFP TOF. The EI mass spectra measured for unknown compounds were compared to extensive EI mass spectral libraries for identification (NIST libraries). This analysis yields a list of identified compounds, their gas chromatographic peak areas and two retention times, their chemical formulas and chemical classes, and the accurate  $m/z$  values for the ionized analytes.

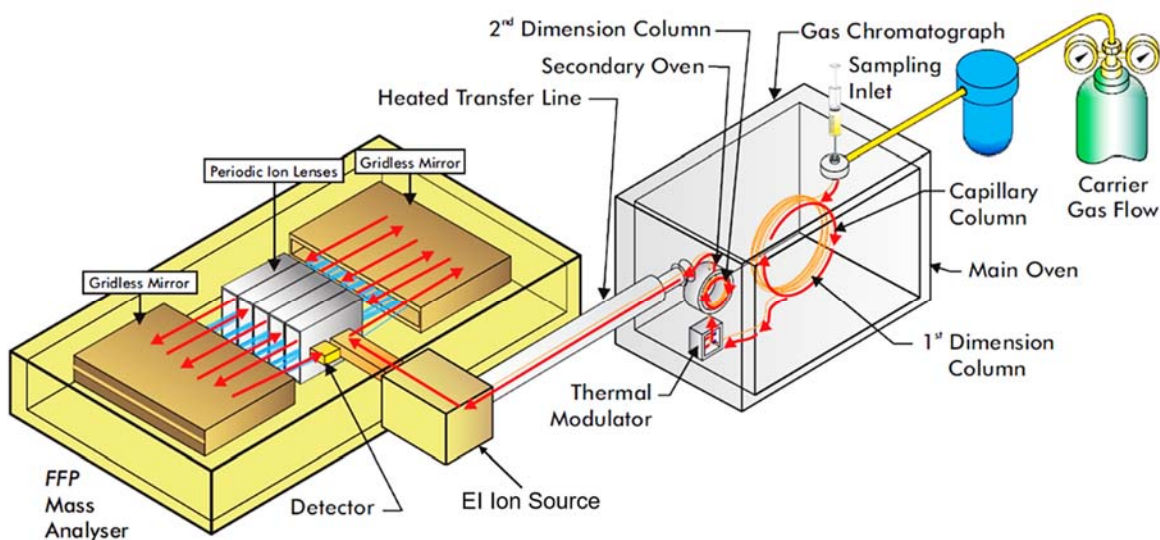


Figure 2.21 Components of the GCxGC/TOF mass spectrometer used in this research. The folded flight path mass analyser is abbreviated as FFP mass analyser in the figure.

### 2.8.2.1 Two-Dimensional Gas Chromatography (GCxGC)

GCxGC separates mixture components typically by using two columns with different polarities connected in series. The analytes separated on the first column are typically injected onto the second column by using a modulator. This concept was theoretically suggested by Giddings<sup>72</sup> in 1984 and was practically demonstrated by Liu and Philips in 1991 by using an on-column thermal modulator interface.<sup>73</sup>

The GCxGC system used in this research consists of an injector, primary column, modulator and secondary column. The primary and secondary columns are in two separate ovens to achieve independent temperature controls (Figure 2.22A). The modulator located between the two columns acts as an interface. The success of two-dimensional gas chromatography is highly dependent on the modulator's ability to accumulate, refocus and rapidly release eluates arriving from the primary column onto the secondary column.<sup>74</sup> Different types of modulators, such as thermal desorption modulators,<sup>73</sup> cryo-modulators,<sup>75</sup> and jet-based modulators<sup>76</sup> have been developed over the years. The modulation in the GC system used in this thesis research constituted an advanced version of a jet-based modulation system. The modulation in this device is achieved by using a dual-stage, quad-jet thermal modulator using liquid nitrogen as a coolant. The eluates leaving the primary column are cryo-focused by the coolant and are introduced into the secondary column by means of time synchronized system of hot and cold pulses between stage one and stage two of the modulator. The cryo-focusing during the modulation process enhances the signal-to-noise ratio for eluates and thereby increases sensitivity. GCxGC achieves a greater peak capacity (number of separated and detected peaks) than traditional one-dimensional GC by combining the benefits of increased sensitivity and enhanced chromatographic resolution.<sup>77</sup>

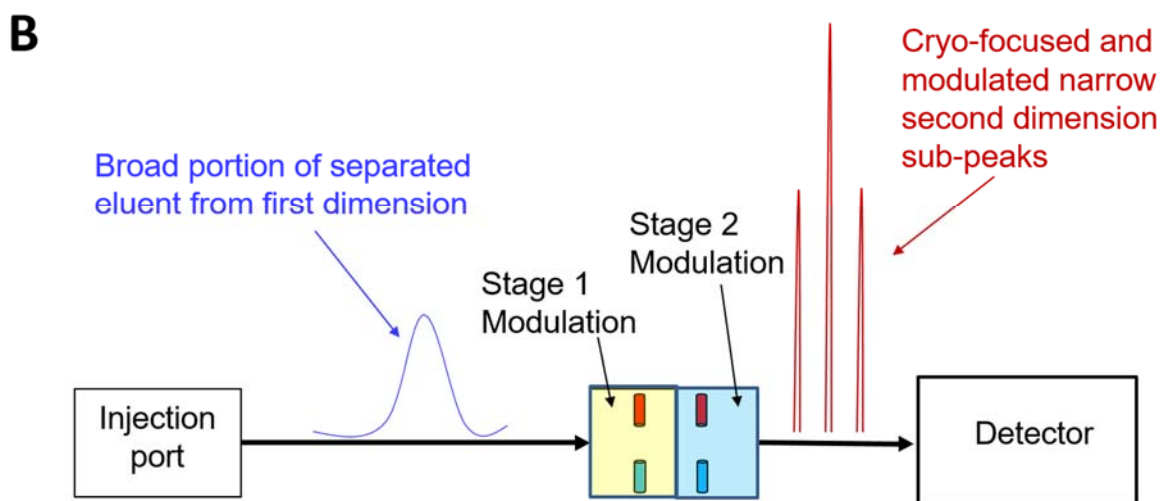
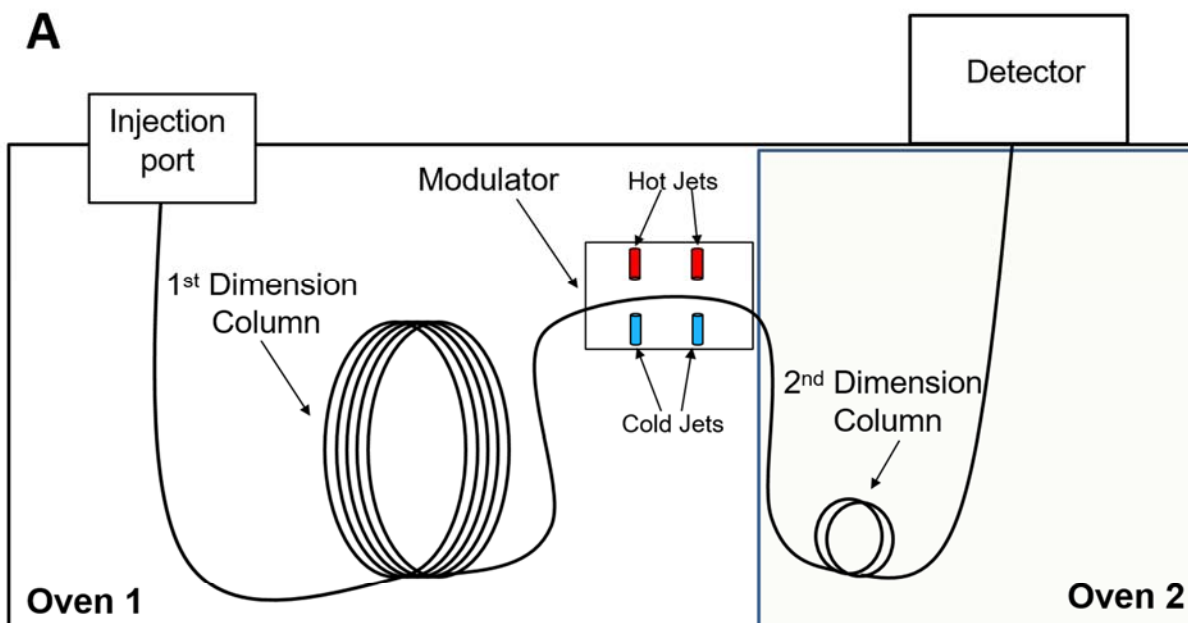


Figure 2.22 A) The two-dimensional GCxGC system with four-jet N<sub>2</sub> cryo modulators (two cold and two hot jets). B) The depiction of a relatively broad portion of the separated elutes from the first column being cryo-focused, modulated and separated in the second column into three narrow peaks.

### 2.8.2.2 GCxGC Method Development

Chromatographic resolution on GCxGC is impacted by the modulation period, secondary oven temperature offset, temperature ramp, modulator temperature offset, and hot and cold pulse timing. Therefore, optimization of all these parameters is required to obtain optimal results.<sup>72,78</sup>

#### 2.8.2.2.1 Modulation Period

All the events involved in both the stage one and stage two modulations are referred to as a modulation period (Figure 2.23). The modulation period must be optimized such that it is sufficiently long to allow enough time for all the compounds within a given modulation period to move through the second column and into the mass spectrometer but not too long to lower resolution. A too long modulation period traps the compounds in the modulator for so long that the second column gets overloaded, resulting in fewer resolved sub-peaks in the second dimension. The resolution in the first dimension is also lowered because the first-dimension chromatogram is reconstructed from the second-dimension chromatograms. On the other hand, when too short modulation periods are used, the next portion of cryo-focused eluate is released onto the second column even before the eluates from the previous modulation period reach the detector. This may cause the peaks corresponding to the analytes with longer retention times to show up among peaks corresponding to compounds released in a later modulation than in which they were injected. This phenomenon is called wrap-around. This can be avoided by selecting a modulation time that is longer than the elution time of the most detained analyte in the second column.



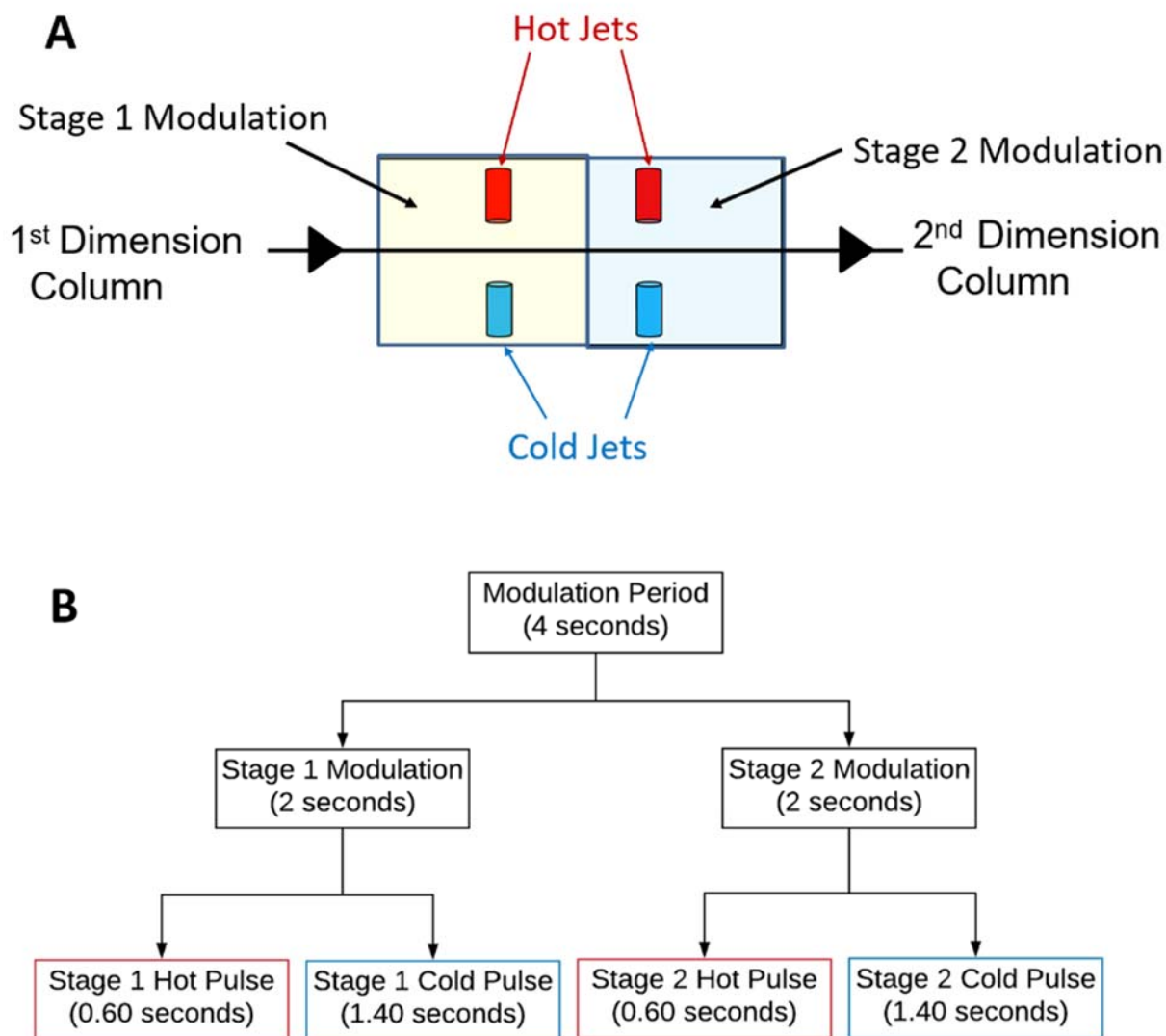


Figure 2.23 A) The two-stage modulation in four jet cryo-modulator. B) All the events included in the modulation period and the time distributions between different modulation stages and hot and cold pulses are shown. The ChromaTOF software allows the user to define the duration of the hot pulse and the modulation period. The cold pulse duration is automatically calculated by the software.

### 2.8.2.2.2 Temperature Ramp and Temperature Off-set

The temperature ramp is defined as the rate of change of temperature (in °C/min) for the primary oven, secondary oven, and the modulator. Typically, primary and secondary ovens and modulators are programmed to have identical temperature ramps (Figure 2.24). As the slope of the temperature ramp is increased, compounds will move through the columns faster and therefore have reduced retention times, and vice versa. The goal of method development is to achieve the sharpest peaks with acceptable levels of peak separation. As the temperature of the hot pulse is governed by the modulator temperature, the temperature of the modulator must be set at a higher value than the secondary oven temperature (temperature off-set) during temperature programming, to rapidly desorb the cryo-focused compounds that are trapped by the cold pulse.

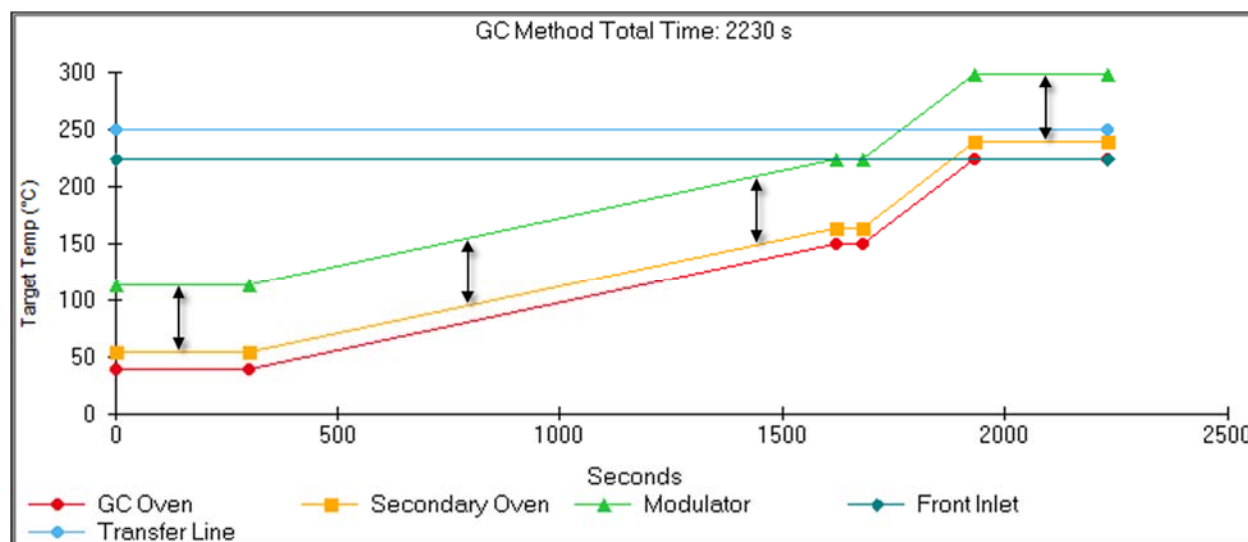


Figure 2.24 Typical temperature program for the primary oven, secondary oven, modulator, front inlet and transfer line for GCxGC. The black arrows indicate the modulator temperature off-set.

### 2.8.2.3 Folded Flight Path Time-of-Flight Mass Analyzer (FFP TOF)

High resolution mass analyzers, such as FT-ICRs and sector instruments, are beneficial for quantitative and qualitative analysis of complex mixtures. Although these mass analyzers provide high quality data, their use is limited by their low acquisition speeds. Mass spectrometers with TOF analyzers provide fast acquisition rates that can meet the requirements for a detector for GCxGC. However, for these instruments to achieve the resolving power of sector or FTMS instruments, a very long flight tube is necessary, which is not practical. To achieve high resolution, the LECO Pegasus 4D GCxGC/TOF instrument used in this thesis research was equipped with advanced folded flight path technology, which permits extended flight paths for ions, thus leading to increased resolving power.<sup>79,80</sup> This technology involves passing ions through several parallel sets of electrostatic focusing mirrors (Figure 2.25). In theory, the resolution of the instrument depends on the number of bounces the ion achieves between the mirrors before reaching the detector. The length of a single folded flight path was less than 20 m. This provided a resolution of  $\geq 25,000$ . To achieve a resolution of  $\geq 50,000$ , the flight path length was doubled ( the ions are allowed to travel through the entire folded flight path twice). This instrument can provide high resolution data at an acquisition rate of up to 200 spectra/second.

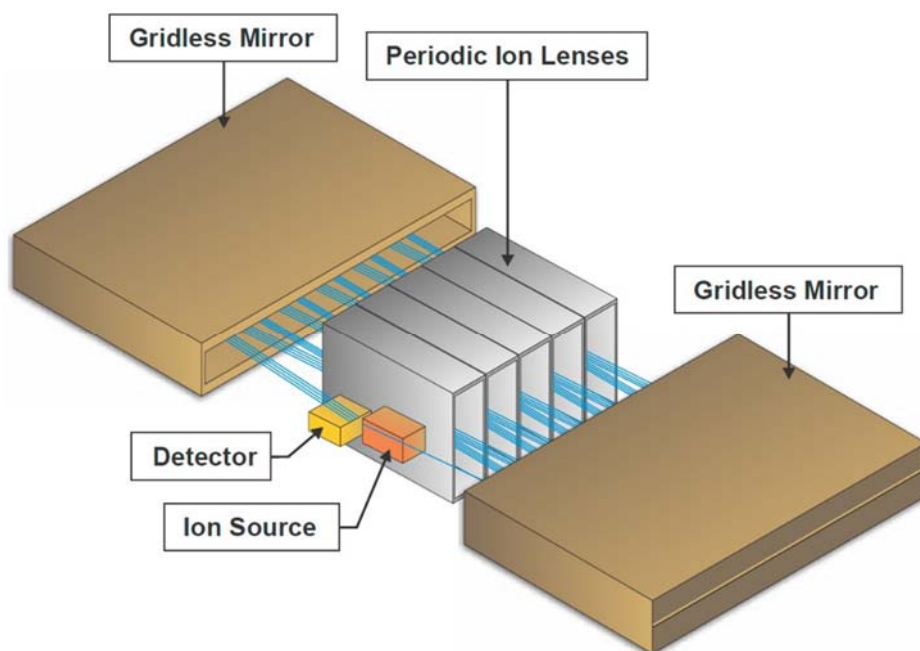


Figure 2.25 Folded flight path mass analyzer constitutes the electrostatic focusing gridless mirrors and periodic ion lenses. The blue line indicates the flight path of the ions.

## 2.9 References

- (1) Correa, D. N.; Santos, J. M.; Eberlin, L. S.; Eberlin, M. N.; Teunissen, S. F. Forensic Chemistry and Ambient Mass Spectrometry: A Perfect Couple Destined for a Happy Marriage? *Anal. Chem.* **2016**, *88* (5), 2515–2526.
- (2) Geoghegan, K. F.; Kelly, M. A. Biochemical Applications of Mass Spectrometry in Pharmaceutical Drug Discovery. *Mass Spectrom. Rev.* **2005**, *24* (3), 347–366.
- (3) Herrero, M.; Simó, C.; García-Cañas, V.; Ibáñez, E.; Cifuentes, A. Foodomics: MS-Based Strategies in Modern Food Science and Nutrition. *Mass Spectrom. Rev.* **2012**, *31* (1), 49–69.
- (4) Marshall, A. G.; Rodgers, R. P. Petroleomics: Chemistry of the Underworld. *Proc. Natl. Acad. Sci. U. S. A.* **2008**, *105* (47), 18090–18095.
- (5) Richardson, S. D. Environmental Mass Spectrometry: Emerging Contaminants and Current Issues. *Anal. Chem.* **2008**, *80* (12), 4373–4402.
- (6) Strathmann, F. G.; Hoofnagle, A. N. Current and Future Applications of Mass Spectrometry to the Clinical Laboratory. *Am. J. Clin. Pathol.* **2011**, *136* (4), 609–616.
- (7) Aczel, T. Applications of Mass Spectrometry in the Petrochemical Industry. In *Practical Mass Spectrometry*; Springer, Boston, MA, 1979; pp 289–325.
- (8) Schwartz, J. C.; Senko, M. W.; Syka, J. E. P. A Two-Dimensional Quadrupole Ion Trap Mass Spectrometer. *J. Am. Soc. Mass Spectrom.* **2002**, *13* (6), 659–669.
- (9) Hager, J. W. A New Linear Ion Trap Mass Spectrometer. *Rapid Commun. Mass Spectrom.* **2002**, *16* (6), 512–526.
- (10) Douglas, D. J.; Frank, A. J.; Mao, D. Linear Ion Traps in Mass Spectrometry. *Mass Spectrom. Rev.* **2005**, *24* (1), 1–29.
- (11) March, R. E. An Introduction to Quadrupole Ion Trap Mass Spectrometry. *J. Mass Spectrom.* **1997**, *32* (4), 351–369.
- (12) March, R. E.; Todd, J. F. J. Quadrupole Ion Trap Mass Spectrometry, 2nd ed.; Wiley-Interscience: Hoboken, N.J., 2005.
- (13) Mellon, F. A. Mass Spectrometry | Principles and Instrumentation. In *Encyclopedia of Food Sciences and Nutrition (Second Edition)*; Caballero, B., Ed.; Academic Press: Oxford, 2003; pp 3739–3749.
- (14) Stanton, H. E.; Chupka, W. A.; Inghram, M. G. Electron Multipliers in Mass Spectrometry; Effect of Molecular Structure. *Rev. Sci. Instrum.* **1956**, *27* (2), 109–109.
- (15) March, R. E. An Introduction to Quadrupole Ion Trap Mass Spectrometry. *J. Mass Spectrom.* **1997**, *32* (4), 351–369.
- (16) Douglas, D. j. Linear Quadrupoles in Mass Spectrometry. *Mass Spectrom. Rev.* **2009**, *28* (6), 937–960.
- (17) Kaiser, R. E.; Graham Cooks, R.; Stafford, G. C.; Syka, J. E. P.; Hemberger, P. H. Operation of a Quadrupole Ion Trap Mass Spectrometer to Achieve High Mass/Charge Ratios. *Int. J. Mass Spectrom. Ion Process.* **1991**, *106* (Supplement C), 79–115.

- (18) Stafford, J.; Kelley, P. E.; Syka, J. E. P.; Reynolds, W. E.; Todd, J. F. J. Recent Improvements in and Analytical Applications of Advanced Ion Trap Technology. *Int. J. Mass Spectrom. Ion Process.* **1984**, *60* (1), 85–98.
- (19) Schwartz, J. C.; Syka, J. E. P.; Jardine, I. High Resolution on a Quadrupole Ion Trap Mass Spectrometer. *J. Am. Soc. Mass Spectrom.* **1991**, *2* (3), 198–204.
- (20) de Hoffmann, E. Tandem Mass Spectrometry: A Primer. *J. Mass Spectrom.* **1996**, *31* (2), 129–137.
- (21) Shukla, A. K.; Futrell, J. H. Tandem Mass Spectrometry: Dissociation of Ions by Collisional Activation. *J. Mass Spectrom.* **2000**, *35* (9), 1069–1090.
- (22) Sleno, L.; Volmer, D. A. Ion Activation Methods for Tandem Mass Spectrometry. *J. Mass Spectrom.* **2004**, *39* (10), 1091–1112.
- (23) Brodbelt, J. S. Analytical Applications of Ion-Molecule Reactions. *Mass Spectrom. Rev.* **1997**, *16* (2), 91–110.
- (24) Eberlin, M. N. Structurally Diagnostic Ion/Molecule Reactions: Class and Functional-Group Identification by Mass Spectrometry. *J. Mass Spectrom.* **2006**, *41* (2), 141–156.
- (25) Friedman, L. Ion-Molecule Reactions. *Annu. Rev. Phys. Chem.* **1968**, *19* (1), 273–300.
- (26) Green, M. K.; Lebrilla, C. B. Ion-Molecule Reactions as Probes of Gas-Phase Structures of Peptides and Proteins. *Mass Spectrom. Rev.* **1997**, *16* (2), 53–71.
- (27) Gronert, S. Mass Spectrometric Studies of Organic Ion/Molecule Reactions. *Chem. Rev.* **2001**, *101* (2), 329–360.
- (28) Osburn, S.; Ryzhov, V. Ion–Molecule Reactions: Analytical and Structural Tool. *Anal. Chem.* **2013**, *85* (2), 769–778.
- (29) Brauman, J. I. Some Historical Background on the Double-Well Potential Model. *J. Mass Spectrom.* **1995**, *30* (12), 1649–1651.
- (30) Olmstead, W. N.; Brauman, J. I. Gas-Phase Nucleophilic Displacement Reactions. *J. Am. Chem. Soc.* **1977**, *99* (13), 4219–4228.
- (31) Gronert, S. Estimation of Effective Ion Temperatures in a Quadrupole Ion Trap. *J. Am. Soc. Mass Spectrom.* **1998**, *9* (8), 845–848.
- (32) Gronert, S. Mass Spectrometric Studies of Organic Ion/Molecule Reactions. *Chem. Rev.* **2001**, *101* (2), 329–360.
- (33) Dempster, A. J. A New Method of Positive Ray Analysis. *Phys. Rev.* **1918**, *11* (4), 316–325.
- (34) Munson, M. S. B.; Field, F. H. Chemical Ionization Mass Spectrometry. I. General Introduction. *J. Am. Chem. Soc.* **1966**, *88* (12), 2621–2630.
- (35) Fales, H. M.; Milne, G. W.; Pisano, J. J.; Brewer, H. B.; Blum, M. S.; MacConnell, J. G.; Brand, J.; Law, N. Biological Applications of Electron Ionization and Chemical Ionization Mass Spectrometry. *Recent Prog. Horm. Res.* **1972**, *28*, 591–626.
- (36) Fenn, J. Electrospray Ionization Mass Spectrometry: How It All Began. *J. Biomol. Tech.* **2002**, *13* (3), 101–118.

- (37) Fenn, J. B.; Mann, M.; Meng, C. K.; Wong, S. F.; Whitehouse, C. M. Electrospray Ionization for Mass Spectrometry of Large Biomolecules. *Science* **1989**, *246* (4926), 64–71.
- (38) Yamashita, M.; Fenn, J. B. Electrospray Ion Source. Another Variation on the Free-Jet Theme. *J. Phys. Chem.* **1984**, *88* (20), 4451–4459.
- (39) Takáts, Z.; Wiseman, J. M.; Gologan, B.; Cooks, R. G. Mass Spectrometry Sampling Under Ambient Conditions with Desorption Electrospray Ionization. *Science* **2004**, *306* (5695), 471–473.
- (40) Carroll, D. I.; Dzidic, I.; Stillwell, R. N.; Haegele, K. D.; Horning, E. C. Atmospheric Pressure Ionization Mass Spectrometry. Corona Discharge Ion Source for Use in a Liquid Chromatograph-Mass Spectrometer-Computer Analytical System. *Anal. Chem.* **1975**, *47* (14), 2369–2373.
- (41) Robb, D. B.; Covey, T.; Bruins, A. Atmospheric Pressure Photoionization: An Ionization Method for Liquid Chromatography-Mass Spectrometry. *Anal. Chem.* **2000**, *72* (15), 3653–3659.
- (42) Karas, M.; Bachmann, D.; Hillenkamp, F. Influence of the Wavelength in High-Irradiance Ultraviolet Laser Desorption Mass Spectrometry of Organic Molecules. *Anal. Chem.* **1985**, *57* (14), 2935–2939.
- (43) Beckey, H. D. Field Desorption Mass Spectrometry: A Technique for the Study of Thermally Unstable Substances of Low Volatility. *Int. J. Mass Spectrom. Ion Phys.* **1969**, *2* (6), 500–502.
- (44) Gomer, R.; Inghram, M. G. Applications of Field Ionization to Mass Spectrometry. *J. Am. Chem. Soc.* **1955**, *77* (2), 500–500.
- (45) Barber, M.; Bordoli, R. S.; Sedgwick, R. D.; Tyler, A. N. Fast Atom Bombardment of Solids as an Ion Source in Mass Spectrometry. *Nature* **1981**, *293* (5830), 270.
- (46) Kebarle, P.; Peschke, M. On the Mechanisms by Which the Charged Droplets Produced by Electrospray Lead to Gas Phase Ions. *Anal. Chim. Acta* **2000**, *406* (1), 11–35.
- (47) Kebarle, P.; Tang, L. From Ions in Solution to Ions in the Gas Phase - the Mechanism of Electrospray Mass Spectrometry. *Anal. Chem.* **1993**, *65* (22), 972A–986A.
- (48) Cole, R. B. Some Tenets Pertaining to Electrospray Ionization Mass Spectrometry. *J. Mass Spectrom.* **2000**, *35* (7), 763–772.
- (49) Taylor, S. G. Disintegration of Water Drops in an Electric Field. *Proc R Soc Lond A* **1964**, *280* (1382), 383–397.
- (50) Taylor, S. G. The Force Exerted by an Electric Field on a Long Cylindrical Conductor. *Proc R Soc Lond A* **1966**, *291* (1425), 145–158.
- (51) Taylor, S. G. Electrically Driven Jets. *Proc R Soc Lond A* **1969**, *313* (1515), 453–475.
- (52) Van Berkel, G. J.; Zhou, F. Electrospray as a Controlled-Current Electrolytic Cell: Electrochemical Ionization of Neutral Analytes for Detection by Electrospray Mass Spectrometry. *Anal. Chem.* **1995**, *67* (21), 3958–3964.
- (53) Gomez, A.; Tang, K. Charge and Fission of Droplets in Electrostatic Sprays. *Phys. Fluids* **1994**, *6* (1), 404–414.

- (54) Nguyen, S.; Fenn, J. B. Gas-Phase Ions of Solute Species from Charged Droplets of Solutions. *Proc. Natl. Acad. Sci.* **2007**, *104* (4), 1111–1117.
- (55) Schmelzeisen-Redeker, G.; Büttfering, L.; Röllgen, F. W. Desolvation of Ions and Molecules in Thermospray Mass Spectrometry. *Int. J. Mass Spectrom. Ion Process.* **1989**, *90* (2), 139–150.
- (56) Iribarne, J. V.; Thomson, B. A. On the Evaporation of Small Ions from Charged Droplets. *J. Chem. Phys.* **1976**, *64* (6), 2287–2294.
- (57) Konermann, L.; Ahadi, E.; Rodriguez, A. D.; Vahidi, S. Unraveling the Mechanism of Electrospray Ionization. *Anal. Chem.* **2013**, *85* (1), 2–9.
- (58) Bruins, A. P.; Covey, T. R.; Henion, J. D. Ion Spray Interface for Combined Liquid Chromatography/Atmospheric Pressure Ionization Mass Spectrometry. *Anal. Chem.* **1987**, *59* (22), 2642–2646.
- (59) Märk, T. D. Fundamental Aspects of Electron Impact Ionization. *Int. J. Mass Spectrom. Ion Phys.* **1982**, *45*, 125–145.
- (60) Märk, T. D. Electron Impact Ionization of Plasma Edge Atoms. In *Atomic and Molecular Processes in Fusion Edge Plasmas*; Springer, Boston, MA, 1995; pp 59–89.
- (61) Gross, J. H. Electron Ionization. In *Mass Spectrometry*; Springer, Berlin, Heidelberg, 2004; pp 193–222.
- (62) Makarov, A. Electrostatic Axially Harmonic Orbital Trapping: A High-Performance Technique of Mass Analysis. *Anal. Chem.* **2000**, *72* (6), 1156–1162.
- (63) Kingdon, K. H. A Method for the Neutralization of Electron Space Charge by Positive Ionization at Very Low Gas Pressures. *Phys. Rev.* **1923**, *21* (4), 408–418.
- (64) Makarov, A.; Hardman, M. E.; Schwartz, J. C.; Senko, M. W. Mass Spectrometry Method and Apparatus. US6995364 B2, February 7, 2006.
- (65) Hardman, M.; Makarov, A. A. Interfacing the Orbitrap Mass Analyzer to an Electrospray Ion Source. *Anal. Chem.* **2003**, *75* (7), 1699–1705.
- (66) Makarov, A.; Denisov, E.; Kholomeev, A.; Balschun, W.; Lange, O.; Strupat, K.; Horning, S. Performance Evaluation of a Hybrid Linear Ion Trap/Orbitrap Mass Spectrometer. *Anal. Chem.* **2006**, *78* (7), 2113–2120.
- (67) Senko, M. Linear Quadrupole Mass Spectrometer. US6403955 B1, June 11, 2002.
- (68) Badman, E. R.; Patterson, G. E.; Wells, J. M.; Santini, R. E.; Cooks, R. G. Differential Non-Destructive Image Current Detection in a Fourier Transform Quadrupole Ion Trap. *J. Mass Spectrom.* **1999**, *34* (8), 889–894.
- (69) Zubarev, R. A.; Makarov, A. Orbitrap Mass Spectrometry. *Anal. Chem.* **2013**, *85* (11), 5288–5296.
- (70) Hu, Q.; Noll, R. J.; Li, H.; Makarov, A.; Hardman, M.; Graham Cooks, R. The Orbitrap: A New Mass Spectrometer. *J. Mass Spectrom. JMS* **2005**, *40* (4), 430–443.
- (71) Olsen, J. V.; Macek, B.; Lange, O.; Makarov, A.; Horning, S.; Mann, M. Higher-Energy C-Trap Dissociation for Peptide Modification Analysis. *Nat. Methods* **2007**, *4* (9), 709–712.



- (72) Giddings, J. C. Theory of Minimum Time Operation in Gas Chromatography. *Anal. Chem.* **1962**, *34* (3), 314–319.
- (73) Liu, Z.; Phillips, J. B. Comprehensive Two-Dimensional Gas Chromatography Using an On-Column Thermal Modulator Interface. *J. Chromatogr. Sci.* **1991**, *29* (6), 227–231.
- (74) Dallüge, J.; Beens, J.; Brinkman, U. A. T. Comprehensive Two-Dimensional Gas Chromatography: A Powerful and Versatile Analytical Tool. *J. Chromatogr. A* **2003**, *1000* (1–2), 69–108.
- (75) Kinghorn, R. M.; Marriott, P. J. High Speed Cryogenic Modulation – A Technology Enabling Comprehensive Multidimensional Gas Chromatography. *J. High Resolut. Chromatogr.* **1999**, *22* (4), 235–238.
- (76) Kristenson, E. M.; Korytár, P.; Danielsson, C.; Kallio, M.; Brandt, M.; Mäkelä, J.; Vreuls, R. J. .; Beens, J.; Brinkman, U. A. T. Evaluation of Modulators and Electron-Capture Detectors for Comprehensive Two-Dimensional GC of Halogenated Organic Compounds. *J. Chromatogr. A* **2003**, *1019* (1–2), 65–77.
- (77) Ong, R. C. Y.; Marriott, P. J. A Review of Basic Concepts in Comprehensive Two-Dimensional Gas Chromatography. *J. Chromatogr. Sci.* **2002**, *40* (5), 276–291.
- (78) Mostafa, A.; Edwards, M.; Górecki, T. Optimization Aspects of Comprehensive Two-Dimensional Gas Chromatography. *J. Chromatogr. A* **2012**, *1255*, 38–55.
- (79) Verentchikov, A. N. Multi-Reflecting Time-of-Flight Mass Spectrometer with Orthogonal Acceleration. US7772547 B2, August 10, 2010.
- (80) Toyoda, M.; Okumura, D.; Ishihara, M.; Katakuse, I. Multi-Turn Time-of-Flight Mass Spectrometers with Electrostatic Sectors. *J. Mass Spectrom.* **2003**, *38* (11), 1125–1142.

## **CHAPTER 3. IDENTIFICATION OF SULFONE AND AROMATIC CARBOXYLIC ACID FUNCTIONALITIES IN PROTONATED ORGANIC MOLECULES BY USING ION-MOLECULE REACTIONS FOLLOWED BY COLLISION-ACTIVATED DISSOCIATION IN A LINEAR QUADRUPOLE ION TRAP MASS SPECTROMETER**

### 3.1 Introduction

Drug metabolite identification is an essential task in drug discovery and development for a number of reasons,<sup>1-5</sup> e.g., for studying metabolic clearance mechanisms of parent drug and relevant enzymology, for assessing whether a metabolite is pharmacologically active, and for adequate safety testing in preclinical animal species to sufficiently cover the systemic exposure of drug metabolites in humans. LC-MS/MS is the workhorse to identify drug metabolites at low concentrations in complex sample matrices.<sup>1,2</sup> However, structural elucidation of metabolites by LC-MS/MS or MS<sup>n</sup> based on collision-activated dissociation (CAD) is not always possible due to inability to differentiate isomeric metabolites. On the other hand, other commonly used analytical methods, such as NMR and X-ray crystallography, would require a relatively large amount of a purified sample for structural characterization, and may not work for a metabolite with poor stability. In such situations, gas-phase ion-molecule reactions may be utilized to probe the structural differences in the isomeric analyte ions.<sup>6,7</sup> For example, we have previously reported the structural determination for an N-oxide metabolite among three possible isomers formed upon different heteroatom oxidations on a 2-aminothiazole moiety by using gas-phase ion-molecule reactions.<sup>8,9</sup> Tandem mass spectrometric methods based on ion/molecule reactions hold great promise in the identification of functional groups in polyfunctional organic molecules, such as epoxide,<sup>10</sup> sulfone,<sup>11,12</sup> amido,<sup>13</sup> carbonyl,<sup>14</sup> polyol,<sup>15</sup> hydroxylamino,<sup>16</sup> N-oxide and sulfoxide<sup>17</sup> functionalities.

Silane reagents are volatile and commonly used as reagents in organic synthesis due to their ability to exhibit hypervalency.<sup>18</sup> The research presented here focuses on the use of a silane reagent (trimethoxymethylsilane or TMMS) in the gas phase to derivatize protonated sulfones, sulfonamides and carboxylic acids via addition followed by elimination of methanol. One or two collision-activated dissociation (CAD) experiments of the derivatized analytes allows the differentiation and identification of the sulfone and aromatic carboxylic acid functionalities in protonated polyfunctional model compounds. Sulfonamides and aliphatic carboxylic acids could not be differentiated from each other. Quantum chemical calculations were performed to explore the reaction mechanisms.

## 3.2 Experimental

### 3.2.1 Chemicals

Most chemicals were purchased from Sigma-Aldrich, and they had purities  $\geq 98\%$ . Omeprazole sulfone, sulindac, and albendazole sulfone were purchased from Santa Cruz Biotechnology (Dallas, Texas, USA). All chemicals were used without further purification.

### 3.2.2 Sample Preparation

Stock solutions of all the analytes were prepared at a concentration of 0.1 mM in acetonitrile and were diluted as needed using a mixture of 50% methanol and 50% water.

### 3.2.3 Instrumentation

Experiments were conducted in a Thermo Scientific LTQ linear quadrupole ion trap (LQIT) mass spectrometer equipped with electrospray ionization (ESI) source. All analytes were ionized via (+) ESI. The analyte solutions were directly injected into the ESI source at a flow rate of 15  $\mu\text{L min}^{-1}$  by using a 500  $\mu\text{L}$  Hamilton syringe. ESI source conditions were as follows: 3 kV spray voltage, 20-30 (arbitrary units) of sheath gas ( $\text{N}_2$ ), 10 (arbitrary units) of auxiliary gas ( $\text{N}_2$ ), and 275  $^\circ\text{C}$  capillary temperature. The variables for the ion optics were optimized for each analyte by using the auto-tune feature of the LTQ Tune plus software interface.

In collision-activated dissociation (CAD) experiments, the advanced scan feature of the LTQ tune software interface was used to isolate ions and perform CAD. The isolation parameters were: an isolation width of 2 units, an activation q value of 0.25 and an activation time of 30 ms. The ions were then subjected to CAD (collision energy 15 arbitrary units) by using helium buffer gas as the collision gas.

An external manifold for introducing reagent gas mixtures into quadrupole ion traps via the helium line was first proposed by Gronert.<sup>19,20</sup> A schematic of the external manifold used in this research was published earlier<sup>21</sup>, and the schematics of the manifold used in this study is discussed in Chapter 2. The reagent TMMS was introduced into the trap via the manifold by using syringe pumps operating at a flow rate of 3  $\mu\text{L/h}$ . The manifold surrounding the syringe port was maintained at a temperature of 125  $^\circ\text{C}$  to ensure evaporation of the neutral reagent (TMMS). Reaction time was 300 ms for all experiments except those where no products were detected after this time. In those cases, a reaction time of 2000 ms was also used to verify the absence of products. At the end of the experiment, the manifold was isolated from the instrument and placed under vacuum at a high temperature (300  $^\circ\text{C}$ ) to bake out the remaining reagent from the manifold.

### 3.2.4 Computational Studies

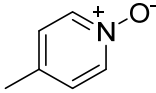
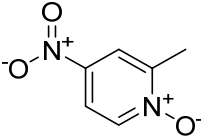
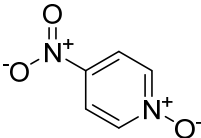
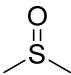
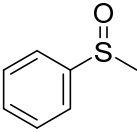
Lowest energy conformers for neutral and protonated molecules were identified using Maestro 7.0 Macro Model. Geometry optimizations and single point energy calculations were completed with Gaussian 09.<sup>22</sup> Calculations of proton affinities were performed at the B3LYP/6-31G++(d,p) level of theory. The optimized molecular structures and energies for the potential energy surfaces were calculated at the M06-2X/6-311++G(d,p) level of theory. Stationary points were characterized by frequency calculations to confirm a correct number of imaginary frequencies. All transition state structures were determined to contain exactly one negative frequency.

### 3.3 Results and Discussion

Gas-phase reactivity of protonated model compounds with different functional groups toward TMMS (proton affinity (PA) = 202 kcal/mol calculated at the B3LYP/6-31++G(d,p) level of theory) was studied in a linear quadrupole ion trap (LQIT) mass spectrometer to explore the utility of this reagent in identification of specific functionalities. Analytes containing one or more of 22 different functional groups were explored.

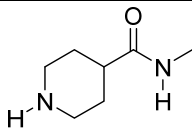
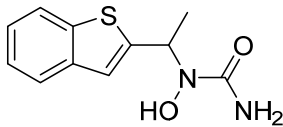
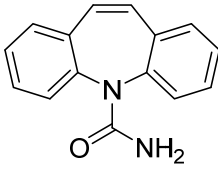
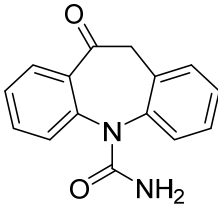
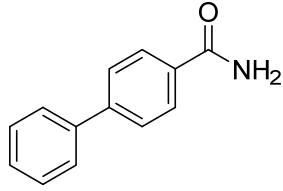
All protonated compounds, with the exception of those containing a sulfone, sulfonamide or aliphatic or aromatic carboxylic acid, were found to react with TMMS to only produce a stable TMMS adduct ( $[\text{TMMS adduct} + \text{H}]^+$ ; Table 3.1). Furthermore, CAD of the  $[\text{TMMS adduct} + \text{H}]^+$  gave back the protonated analytes in MS<sup>3</sup> experiments. Thus, the gas-phase reactions with TMMS provide no structural information about these functionalities.

Table 3.1 Reaction products of TMMS (PA = 202 kcal/mol) (MS<sup>2</sup> experiments), fragment ions formed upon cad of the product ions (MS<sup>3</sup> experiments), and the different reaction pathways' branching ratios for protonated compounds containing n-oxide, nitro, hydroxycarboxamido, sulfoxide, amino, hydroxylamino, aniline, imino and hydroxyl functionalities.

			Fragment ions (m/z)
	[TMMS adduct + H] <sup>+</sup> (246)	100%	(110) [M+H] <sup>+</sup>
4-Picoline <i>N</i> -oxide (110)			
	206 <sup>a</sup>	[TMMS adduct + H] <sup>+</sup> (291) 100%	(155) [M+H] <sup>+</sup>
4-Nitro-2-picoline <i>N</i> -oxide (155)			
	-	[TMMS adduct + H] <sup>+</sup> (277) 68% [TMMS + H] <sup>+</sup> (137) 32%	(141) [M+H] <sup>+</sup>
4-Nitropyridine <i>N</i> -oxide (141)			
	211 <sup>a</sup>	[TMMS adduct + H] <sup>+</sup> (215) 100%	(79) [M+H] <sup>+</sup>
Dimethyl sulfoxide (79)			
	215 <sup>a</sup>	[TMMS adduct + H] <sup>+</sup> (277) 100%	141 [M+H] <sup>+</sup>
Methyl phenyl sulfoxide (141)			

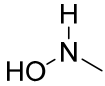
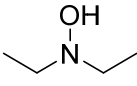
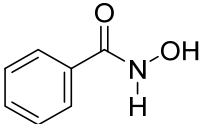
<sup>a</sup> Calculated at the B3LYP/6-31++G(d,p) level of theory (kcal/mol).

Table 3.1, continued

Analyte (M) (m/z of protonated analyte)	PA (kcal/ mol)	Observed reaction products (m/z) and their branching ratios (MS <sup>2</sup> )	Fragment ions (m/z) formed upon CAD of [TMMS Adduct + H] <sup>+</sup> (MS <sup>3</sup> )
 N-Methylpiperidine-4-carboxamide (143)	238 <sup>a</sup>	No Products	Not Applicable
 Zileuton (237)	-	[TMMS adduct + H] <sup>+</sup> (373) 100%	(237) [M+H] <sup>+</sup>
 Carbamazepine (237)	226 <sup>a</sup>	[TMMS adduct + H] <sup>+</sup> (373) 100%	237 [M+H] <sup>+</sup>
 Oxcarbazepine (253)	219 <sup>a</sup>	[TMMS adduct + H] <sup>+</sup> (389) 77% [TMMS adduct + H - 17] <sup>+</sup> (372) 3%	253 [M+H] <sup>+</sup>
 Biphenyl-4-carboxamide (198)	217 <sup>a</sup>	[TMMS adduct + H] <sup>+</sup> (334) 100%	198 [M+H] <sup>+</sup>

<sup>a</sup> Calculated at the B3LYP/6-31++G(d,p) level of theory (kcal/mol).

Table 3.1, continued

Analyte (M) (m/z of protonated analyte)	PA (kcal/ mol)	Observed reaction products (m/z) and their branching ratios (MS <sup>2</sup> )	Fragment ions (m/z) formed upon CAD of [TMMS Adduct + H] <sup>+</sup> (MS <sup>3</sup> )
 <i>N</i> -Methylhydroxylamine (48)	-	[TMMS adduct + H] <sup>+</sup> (184) 100%	48 [M+H] <sup>+</sup>
 <i>N,N</i> -Diethylhydroxylamine (90)	-	[TMMS adduct + H] <sup>+</sup> (226) 100%	90 [M+H] <sup>+</sup>
 Benzhydroxamic acid (138)	212 <sup>a</sup>	[TMMS adduct + H] <sup>+</sup> (274) 100%	138 [M+H] <sup>+</sup>

<sup>a</sup> Calculated at the B3LYP/6-31++G(d,p) level of theory.

On the contrary, when protonated sulfones (Table 3.2), sulfonamides (Table 3.3) and aliphatic and aromatic carboxylic acids (Table 3.4) were allowed to react with TMMS, a characteristic addition/methanol elimination product, [TMMS adduct + H - MeOH]<sup>+</sup>, was formed, in addition to the TMMS adduct (Table 3.1). This observation allows the differentiation of these four functionalities from the other functionalities studied. Based on one or two CAD experiments on the [TMMS adduct + H - MeOH]<sup>+</sup> products, the aromatic carboxylic acids, and sulfones can be differentiated from each other and also from aliphatic carboxylic acids and sulfonamides (Table



3.1, Table 3.2, Table 3.3 and Table 3.4). Aliphatic carboxylic acids and sulfonamides could not be differentiated from each other. These observations are discussed in detail below.

### 3.3.1 Reactions of TMMS with Protonated Monofunctional Sulfones

The MS<sup>2</sup> spectra measured after reactions between TMMS and protonated sulfone-containing compounds showed a dominant addition/methanol elimination product, [TMMS adduct + H - MeOH]<sup>+</sup> and protonated TMMS (Table 3.2). Isolation and CAD of the [TMMS adduct + H - MeOH]<sup>+</sup> product ion yielded diagnostic fragment ions of m/z 75, 105 (most abundant fragment ion) and 123 in MS<sup>3</sup> experiments (Table 3.2). Observation of these fragment ions indicates the likely presence of a sulfone functionality in the analyte (Table 3.2). The reaction of dimethyl sulfone with TMMS is taken as an example for further discussion. The MS<sup>2</sup> spectrum of protonated dimethyl sulfone (m/z 95) measured after reaction with TMMS and the MS<sup>3</sup> spectrum measured after CAD of [TMMS adduct + H - MeOH]<sup>+</sup> product (m/z 199) are shown in Figure 3.1.

The observed spontaneous proton transfer from protonated dimethyl sulfone to the TMMS reagent and the formation of [TMMS adduct + H - MeOH]<sup>+</sup> product ion (MS<sup>2</sup> spectrum; Figure 3.1) upon reaction of protonated dimethyl sulfone with TMMS reagent suggests that both reactions are exergonic. Quantum chemical calculations (at the M06-2X/6-311++G(d,p) level of theory) corroborate this (Figure 3.2A). Calculations suggest that the formation of the [TMMS adduct + H - MeOH]<sup>+</sup> product is initiated by the spontaneous transfer of a proton (exergonic by 4.5 kcal/mol) from the protonated analyte to the methoxy group in the reagent (TMMS). The proton transfer is followed by spontaneous formation of the [TMMS adduct + H - MeOH]<sup>+</sup> product ion (exergonic by 12.6 kcal/mol) via nucleophilic attack by one of the oxygen atoms in dimethyl sulfone at the silicon atom in protonated TMMS reagent, resulting in the loss of a methanol molecule. The barrier for this reaction is small (Gibbs free energy barrier = 0.7 kcal/mol).

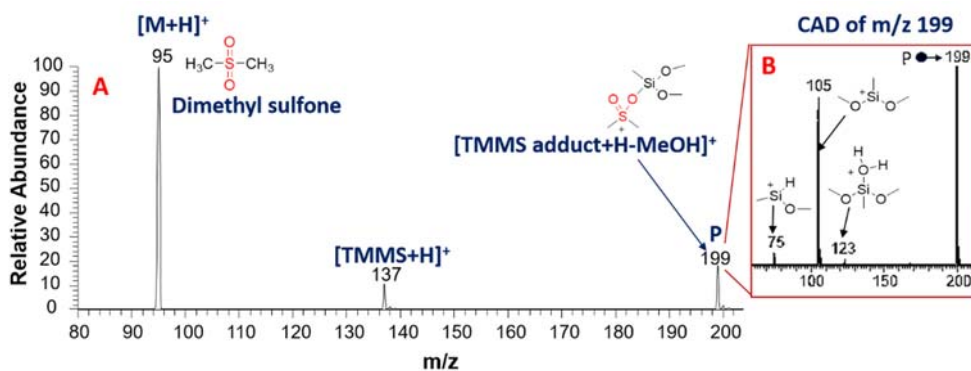
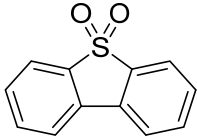
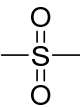
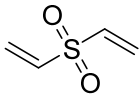
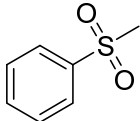
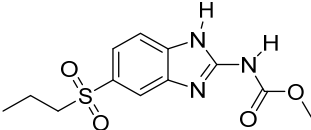
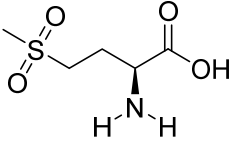
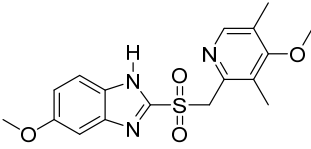


Figure 3.1 (A) The MS<sup>2</sup> spectrum of protonated dimethylsulfone ( $m/z$  95) measured after 300 ms reaction with TMMS. The most abundant product ion ( $m/z$  199) corresponds to [TMMS adduct + H - MeOH]<sup>+</sup>. The other product ion is the protonated TMMS reagent ( $m/z$  137). (B) MS<sup>3</sup> spectrum measured after collision-activated dissociation (CAD) of [TMMS adduct + H - MeOH]<sup>+</sup>. The fragment ions of  $m/z$  75, 105 and 123 are diagnostic to sulfone functionality.

CAD of the [TMMS adduct + H - MeOH]<sup>+</sup> product ( $m/z$  199) produced an abundant fragment ion of  $m/z$  105 (dimethoxymethylsilyl cation,  $(\text{CH}_3\text{O})_2\text{SiCH}_3^+$ ; Figure 3.1B) via a heterolytic cleavage of a Si-O bond in an MS<sup>3</sup> experiment. Since no transition state was found for this Si-O bond cleavage, it is assumed to be barrierless. The Gibbs free energy required for this bond cleavage is calculated to be 57.3 kcal/mol (at the M06-2X/6-311++G(d,p) level of theory; Figure 3.2B).

Table 3.2 Ionic products formed for several protonated sulfones upon reactions with TMMS (PA = 202 kcal/mol) (MS<sup>2</sup> experiments), CAD product ions of [TMMS Adduct + H-MeOH]<sup>+</sup> product ions (MS<sup>3</sup> experiments), and the different reaction pathways' branching ratios.

Analyte (m/z of protonated analyte)	PA	Observed ionic reaction products (m/z) and their branching ratios	Fragment ions' m/z values (MW of neutral fragments) and branching ratios for CAD of [TMMS Adduct + H - MeOH] <sup>+</sup>	
 Dibenzothiophene sulfone (217)	206 <sup>a</sup>	[TMMS adduct + H - MeOH] <sup>+</sup> (321) 99% [TMMS adduct + H] <sup>+</sup> (353) 1%	105 (216) 123 (198) 75 <sup>b</sup> (246)	95% 5%
 Dimethyl sulfone (95)	193 <sup>a</sup>	[TMMS adduct + H - MeOH] <sup>+</sup> (199) 78% [TMMS + H] <sup>+</sup> (137) 22%	105 (94) 75 (124) 123 (76)	91% 6% 3%
 Vinyl sulfone (119)	206 <sup>a</sup>	[TMMS adduct + H - MeOH] <sup>+</sup> (223) 88% [TMMS + H] <sup>+</sup> (137) 11% [TMMS adduct + H] <sup>+</sup> (255) 1%	105 (118) 75 (148) 123 (100)	85% 11% 4%
 Methyl phenyl sulfone (157)	201 <sup>a</sup>	[TMMS adduct + H - MeOH] <sup>+</sup> (261) 98% [TMMS + H] <sup>+</sup> (137) 2%	105 (156) 123 (138) 75 (186)	94% 3% 3%
 Albendazole sulfone (298)	222 <sup>a</sup>	[TMMS adduct + H] <sup>+</sup> (434) 100%	Not Applicable	
 Methionine sulfone (182)	223 <sup>a</sup>	[TMMS adduct + H] <sup>+</sup> (318) 100%	Not Applicable	
 Omeprazole sulfone (362)	238 <sup>a</sup>	No Products were observed	Not Applicable	

<sup>a</sup> Calculated in kcal/mol at the B3LYP/6-31++G(d,p) level of theory

<sup>b</sup> Could not be observed in the mass spectrum due to low-mass cutoff

Table 3.3 Ionic reaction products of TMMS (PA = 202 kcal/mol<sup>a</sup>) (MS<sup>2</sup> experiments), fragment ions formed upon cad of [TMMS Adduct + H-MeOH]<sup>+</sup> product ions (MS<sup>3</sup> experiments, CAD energy 10) and of [TMMS Adduct + H - 2 MeOH]<sup>+</sup> fragment ions (MS<sup>4</sup> experiments, CAD energy 20), and the different reaction pathways' branching ratios for protonated sulfonamide model compounds.

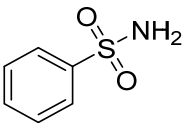
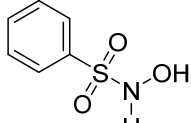
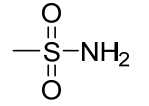
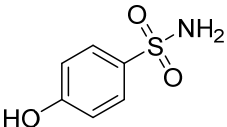
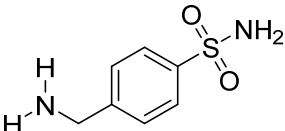
 Benzenesulfonamide (158)	203 <sup>a</sup>	[TMMS adduct + H - MeOH] <sup>+</sup> (262) 7% Protonated TMMS (137) 3%	[TMMS Adduct + H - 2 MeOH] <sup>+</sup> (230)	91 (139) 30% 151 (79) 22% 200 (30) 21% 184 (46) 14% 167 (63) 8% 137 (93) 5%	
 N-Hydroxybenzenesulfonamide (174)	211 <sup>a</sup>	[TMMS adduct + H - MeOH] <sup>+</sup> (278) 94% Protonated TMMS (137) 6%	[TMMS Adduct + H - 2 MeOH] <sup>+</sup> (246)	151 (95) 63% 215 (31) 35% 91 (155) 2%	
 Methanesulfonamide (96)	-	[TMMS adduct + H - MeOH] <sup>+</sup> (200) 52% Protonated TMMS (137) 48%	[TMMS Adduct + H - 2 MeOH] <sup>+</sup> (168)	138 (30) 57% 91 (77) 43%	
<sup>a</sup> Calculated at the B3LYP/6-31++G(d,p) level of theory (kcal/mol).					

Table 3.3, continued

Analyte (m/z of protonated analyte)	PA (kcal/mol)	Observed reaction products (m/z) and their branching ratios (MS <sup>2</sup> )	Fragment ions (m/z) formed upon CAD of [TMMS Adduct + H – MeOH] <sup>+</sup> (MS <sup>3</sup> )	Fragment ions' m/z (MW of neutral fragment) formed upon CAD of [TMMS adduct + H – 2 MeOH] <sup>+</sup> (MS <sup>4</sup> )
 4-Hydroxybenzenesulfonamide  (174)	206 <sup>a</sup>	[TMMS adduct + H - MeOH] <sup>+</sup> (278) 100%	[TMMS Adduct + H - 2 MeOH] <sup>+</sup> (246)	167 (79) 44% 216 (30) 33% <u>91</u> (155) 23%
 4-(Aminomethyl)benzenesulfonamide  (187)	215 <sup>a</sup>	[TMMS adduct + H] <sup>+</sup> (323) 100%	Not Applicable	Not Applicable

<sup>a</sup> Calculated at the B3LYP/6-31++G(d,p) level of theory (kcal/mol).

### 3.3.2 Reactions of TMMS with Protonated Polyfunctional Sulfones

The characteristic reactivity of protonated sulfone model compounds toward the TMMS reagent was not observed for three of the polyfunctional model compounds, *i.e.*, omeprazole sulfone, methionine sulfone and albendazole sulfone (see Table 3.2). Protonated omeprazole sulfone does not react with TMMS. The substantially greater proton affinity of the analyte (calculated PA = 238 kcal/mol) than that of the TMMS reagent (calculated PA = 202 kcal/mol) ( $\Delta$ PA = 36 kcal/mol) prevents the initial proton transfer from the protonated analyte to the reagent, and hence the entire reaction, under the conditions employed in this study. This phenomenon has been reported previously for similar ion-molecule reactions.<sup>23</sup>

In contrast to omeprazole sulfone, protonated albendazole sulfone and methionine sulfone do react with TMMS to form [TMMS adduct + H]<sup>+</sup>, but they do not form the expected product, an adduct that has lost methanol, as observed for other sulfones. These compounds are probably protonated at a nitrogen-functionality rather than the sulfone functionality. Since protonated nitrogen-compounds do not form [TMMS adduct + H - CH<sub>3</sub>OH]<sup>+</sup> but instead [TMMS adduct + H]<sup>+</sup> (Table 3.1), methanol loss is not expected to occur for sulfones protonated on a nitrogen-functionality.

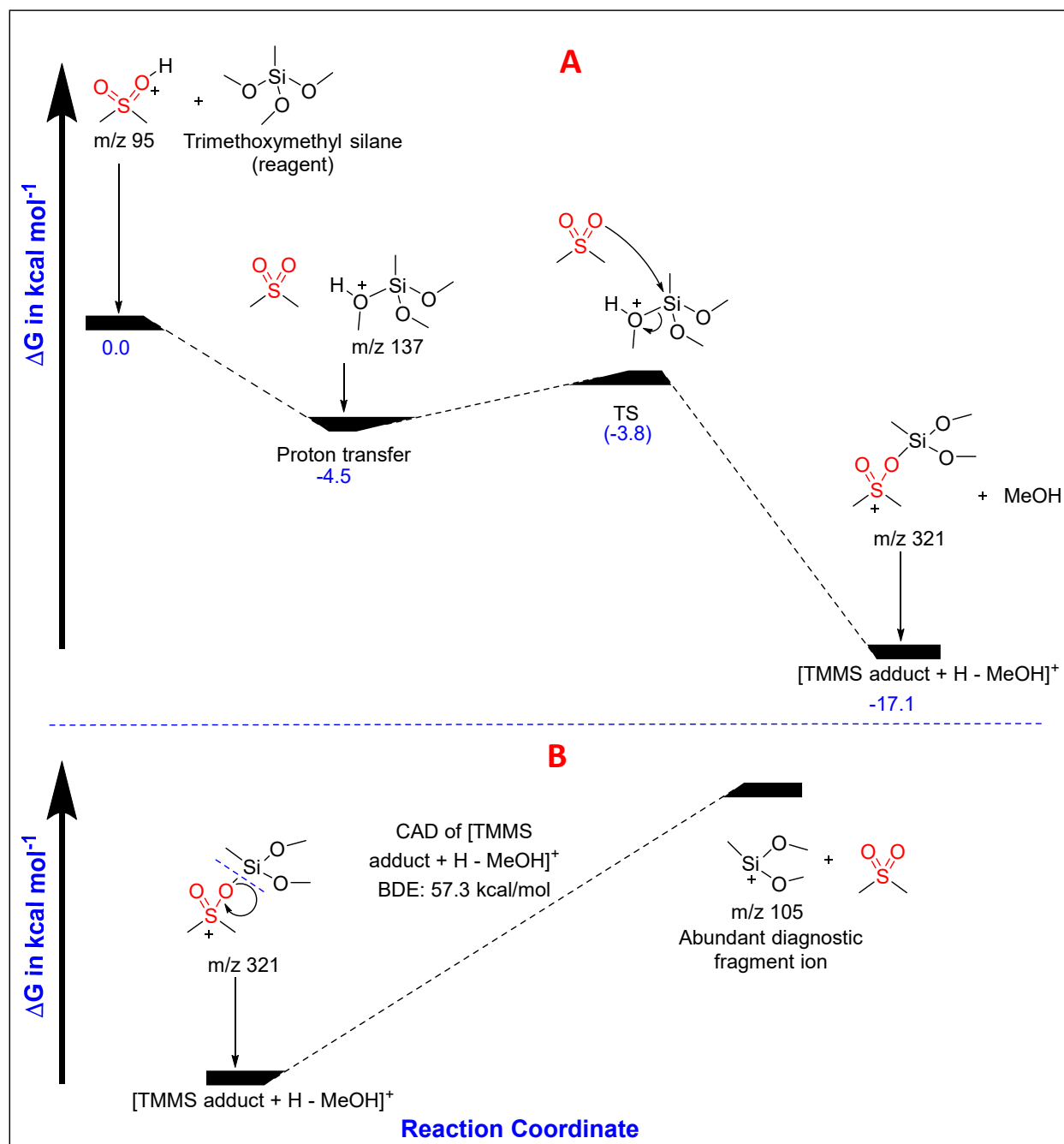


Figure 3.2 Proposed reaction pathways and potential energy surfaces calculated (M06-2X/6-311++G(d,p) level of theory) for (A) exergonic proton transfer and formation of [TMMS adduct + H - MeOH]<sup>+</sup> upon reaction of protonated dimethyl sulfone with TMMS, and (B) endergonic formation of a diagnostic fragment ion (m/z 105) upon CAD of [TMMS adduct + H - MeOH]<sup>+</sup> product ion. The pathway for the formation of this fragment ion (m/z 105) is assumed to be barrierless. Energy values in parentheses indicate transition state free energies.

DFT calculations on omeprazole sulfone and albendazole sulfone and their protonated forms provide some support for above hypothesis. For methionine sulfone, the preferable protonation site is the amino-nitrogen (calculated PA = 223 kcal/mol) that is substantially more basic than the sulfone (calculated PA = 200 kcal/mol), with a proton affinity difference of 23 kcal/mol (see Figure 3.3A for the proton affinities of the different protonation sites in methionine sulfone). For albendazole sulfone, protonation is expected to preferentially occur at the more basic nitrogen atom in the imidazole ring (calculated PA = 222 kcal/mol) rather than the sulfone site (calculated PA = 213 kcal/mol). However, the difference in proton affinities between the imidazole ring nitrogen and sulfone is much lower for this compound than for omeprazole sulfone (only 9 kcal/mol; see Figure 3.3B for proton affinities at different sites in albendazole sulfone). This issue is addressed later in this chapter.

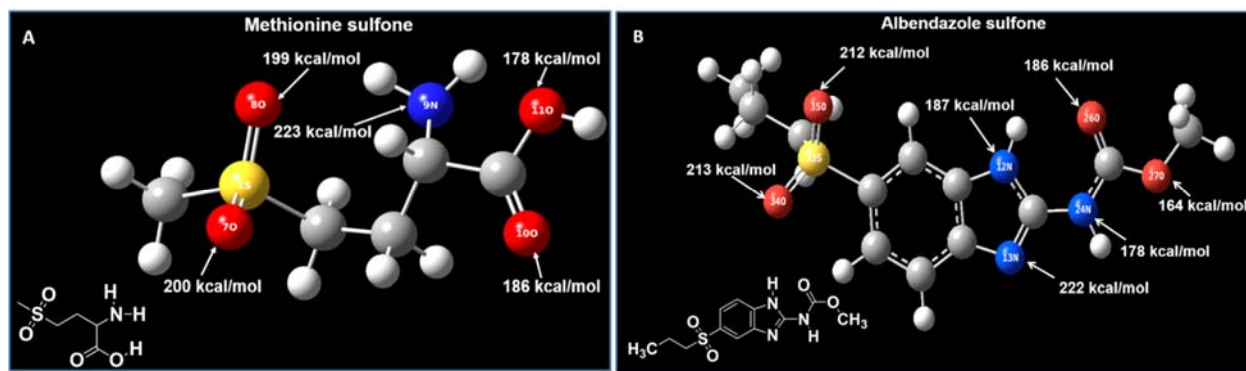


Figure 3.3 The proton affinities calculated for different protonation sites in methionine sulfone and albendazole sulfone (B3LYP/6-31G++(d,p) level of theory). (A) The site with the highest proton affinity in methionine sulfone is the amino nitrogen, with a proton affinity 23 kcal mol<sup>-1</sup> greater than that of the sulfone functionality. (B) The site with the greatest proton affinity in albendazole sulfone is the nitrogen in the imidazole ring, with a proton affinity 9 kcal mol<sup>-1</sup> greater than that of the sulfone functionality. The higher proton affinity of the imine nitrogen can be attributed to intramolecular hydrogen bonding between the imine nitrogen and the nearby carboxyl oxygen (not shown).



### 3.3.3 Reactions of TMMS with Protonated Aromatic Carboxylic Acids

The MS<sup>2</sup> spectra measured after reactions between TMMS and protonated aromatic carboxylic acids (M) show formation of [TMMS adduct + H]<sup>+</sup>, [TMMS adduct + H - MeOH]<sup>+</sup>, [TMMS adduct + H - 2 MeOH]<sup>+</sup> and/or [M + H]<sup>+</sup> - H<sub>2</sub>O (Table 2). CAD of [TMMS adduct + H]<sup>+</sup> gives back the protonated analyte (MS<sup>3</sup> experiments), which provides no further structural information. However, CAD of [TMMS adduct + H - MeOH]<sup>+</sup> yields [TMMS adduct + H - 2 MeOH]<sup>+</sup> ions (MS<sup>3</sup> experiments). Upon CAD of these [TMMS adduct + H - 2 MeOH]<sup>+</sup> fragment ions (MS<sup>4</sup> experiments) or upon CAD of [TMMS adduct + H - 2 MeOH]<sup>+</sup> ions formed in MS<sup>2</sup> experiments (MS<sup>3</sup> experiments), characteristic losses of molecules of MW 44 Da and MW 90 Da were observed. These losses can be used to identify the presence of an aromatic carboxylic acid functionality not only in monofunctional aromatic carboxylic acids but also in polyfunctional aromatic carboxylic acids containing different functional groups, such as acetamido, amino, nitro, hydroxyl and methoxy groups (Table 3.4). Benzoic acid is used below as an example for further discussion.

Formation of both protonated TMMS and [TMMS adduct + H - MeOH]<sup>+</sup> was observed upon reactions of protonated benzoic acid with TMMS (Figure 3.4; Table 3.4). Quantum chemical calculations (M06-2X/6-311++G(d,p) level of theory) suggest that the formation of the [TMMS adduct + H - MeOH]<sup>+</sup> product (m/z 227) is initiated by spontaneous proton transfer (exergonic by 5.3 kcal/mol) from protonated benzoic acid to a methoxy group in TMMS (Figure 3.5), just like for sulfones. The proton transfer is followed by highly favorable reactant complex formation (exergonic by 25.1 kcal/mol). This complex is stabilized by two hydrogen bonds (Figure 3.5). Subsequently, nucleophilic attack of the carbonyl group at the silicon atom in protonated TMMS results in the formation of [TMMS adduct + H - MeOH]<sup>+</sup> product via loss of methanol (exergonic

by 19.6 kcal/mol relative to the separated reactants; Gibbs free energy of activation is -8.5 kcal/mol relative to the separated reactants).

Table 3.4 Ionic products formed for protonated aromatic and aliphatic carboxylic acids, some with additional functionalities, upon reactions with TMMS (PA = 202 kcal/mol<sup>a</sup>) (MS<sup>2</sup> experiments), CAD product ions of [TMMS Adduct + H - MeOH]<sup>+</sup> product ions (MS<sup>3</sup> experiments), CAD product ions of [TMMS Adduct + H - 2 MeOH] (MS<sup>4</sup> experiments), and the different reaction pathways' branching ratios.

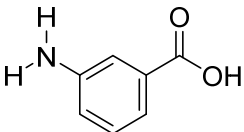
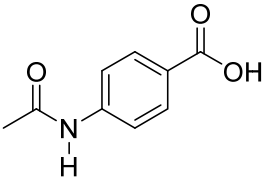
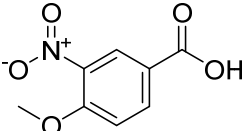
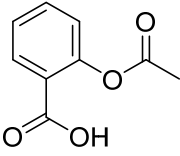
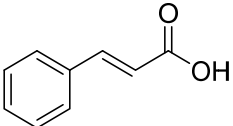
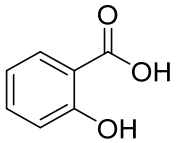
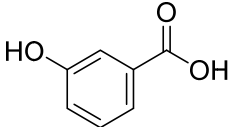
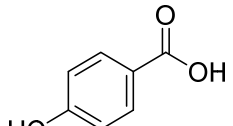
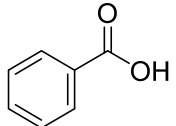
Analyte (m/z of protonated analyte)	PA	Observed ionic reaction products (m/z) and their branching ratios (MS <sup>2</sup> )	m/z values of [TMMS Adduct + H - 2MeOH] <sup>+</sup> formed upon CAD of [TMMS Adduct + H - MeOH] <sup>+</sup> (MS <sup>3</sup> )	m/z values (MW of neutral fragments) and branching ratios of fragment ions from CAD of [TMMS Adduct + H - 2MeOH] <sup>+</sup> (MS <sup>4</sup> )
 3-Aminobenzoic acid (138)	205 <sup>a</sup>	[TMMS adduct + H] <sup>+</sup> (274) 84% [TMMS adduct + H - MeOH] <sup>+</sup> (242) 16%	(210)	166 (44) 63% 120 (90) 37%
 4-Acetamidobenzoic acid (180)	208 <sup>a</sup>	[TMMS adduct + H] <sup>+</sup> (316) 94% [TMMS adduct + H - MeOH] <sup>+</sup> (284) 6%	(252)	162 (90) 72% 208 (44) 28%
 4-Methoxy-3-nitrobenzoic acid (198)	202 <sup>a</sup>	[TMMS adduct + H - MeOH] <sup>+</sup> (302) 100%	(270)	226 (44) 87% 180 (90) 13%
 Acetyl salicylic acid (181)	-	[TMMS adduct + H] <sup>+</sup> (317) 92% [TMMS adduct + H - MeOH] <sup>+</sup> (285) 8%	(253)	195 (58) 36% 163 (90) 29% 209 (44) 25% 222 (31) 10%

Table 3.4, continued

		m/z values of [TMMS				
	203 <sup>a</sup>	[TMMS adduct + H - MeOH] <sup>+</sup> (253) [M + H] <sup>+</sup> - H <sub>2</sub> O (131) [TMMS adduct + H] <sup>+</sup> (285)	64% 20% 16%	(221)	177 (44) 131 (90)	87% 13%
<i>trans</i> -Cinnamic acid (149)						
	201 <sup>a</sup>	[TMMS adduct + H - 2 MeOH] <sup>+</sup> (211) [TMMS + H] <sup>+</sup> (137) [TMMS adduct + H - MeOH] <sup>+</sup> (243) [M + H] <sup>+</sup> - H <sub>2</sub> O (121)	48% 21% 18% 13%	(211)	181 (30) 167 (44)	65% 35%
2-Hydroxybenzoic acid (139)						
	-	[TMMS adduct + H - MeOH] <sup>+</sup> (243) [TMMS + H] <sup>+</sup> (137) [TMMS adduct + H - 2 MeOH] <sup>+</sup> (211)	78% 15% 7%	(211)	167 (44) 121 (90) 183 (28)	66% 18% 16%
3-Hydroxybenzoic acid (139)						
	199 <sup>a</sup>	[TMMS adduct + H - MeOH] <sup>+</sup> (243) [TMMS + H] <sup>+</sup> (137)	89% 11%	(211)	167 (44) 121 (90)	84% 16%
4-Hydroxybenzoic acid (139)						
	194 <sup>a</sup>	[TMMS adduct + H - MeOH] <sup>+</sup> (227) [TMMS + H] <sup>+</sup> (137)	75% 25%	(195)	151 (44) 105 (90)	65% 35%
Benzoic acid (123)						

<sup>a</sup> Calculated at the B3LYP/6-31++G(d,p) level of theory (kcal/mol).

Table 3.4, continued

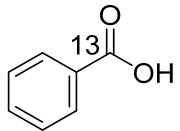
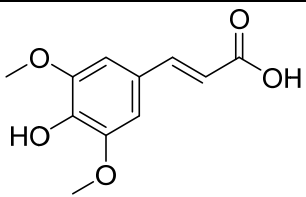
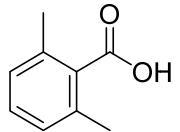
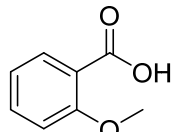
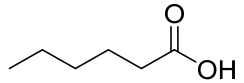
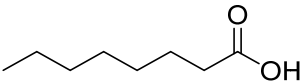
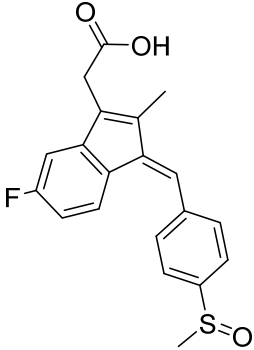
		m/z values of [TMMS				
	194 <sup>a</sup>	[TMMS adduct + H - MeOH] <sup>+</sup> (228) [TMMS + H] <sup>+</sup> (137)	79% 21%	(196)	151 (45) 106 (90)	68% 32%
Benzoic acid <sup>13</sup> C (124)						
	-	[TMMS adduct + H] <sup>+</sup> (361) [M + H] <sup>+</sup> - H <sub>2</sub> O (207) [TMMS adduct + H - MeOH] <sup>+</sup> (329)	77% 22% 1%	(297)	253 (44) 207 (90)	68% 32%
Sinapic acid (225)						
	-	[TMMS adduct + H - MeOH] <sup>+</sup> (255) [TMMS adduct + H] <sup>+</sup> (287) [M + H] <sup>+</sup> - H <sub>2</sub> O (133)	73% 17% 10%	(223)	133 (90) 179 (44)	87% 13%
2,6-Dimethylbenzoic acid (151)						
	-	[TMMS adduct + H] <sup>+</sup> (289) [TMMS adduct + H - MeOH] <sup>+</sup> (257) [TMMS adduct + H - 2MeOH] <sup>+</sup> (225) [M + H] <sup>+</sup> - H <sub>2</sub> O (135)	90% 5% 3% 2%	(225)	181 (44) 135 (90)	63% 37%
2-Methoxybenzoic acid (153)						
	-	[TMMS adduct + H - MeOH] <sup>+</sup> (221) [TMMS + H] <sup>+</sup> (137)	77% 23%	(189)	147 (42) 91 (98) 81 (108)	39% 32% 29%
Hexanoic acid (117)						

Table 3.4, continued

Analyte (m/z of protonated analyte)	PA	Observed ionic reaction products (m/z) and their branching ratios (MS <sup>2</sup> )	m/z values of [TMMS Adduct + H – 2MeOH] <sup>+</sup> formed upon CAD of [TMMS Adduct + H - MeOH] <sup>+</sup> (MS <sup>3</sup> )	m/z values (MW of neutral fragments) and branching ratios of fragment ions from CAD of [TMMS Adduct + H - 2MeOH] <sup>+</sup> (MS <sup>4</sup> )
 Octanoic acid (145)	-	[TMMS adduct + H - MeOH] <sup>+</sup> (249) 85% [TMMS + H] <sup>+</sup> (137) 15%	(217)	147 (70) 52% 109 (108) 21% 91 (126) 17% 129 (88) 10%
 Sulindac (357)	-	[TMMS adduct + H] <sup>+</sup> (493) 100%	Not applicable	Not applicable

<sup>a</sup> Calculated at the B3LYP/6-31++G(d,p) level of theory (kcal/mol).

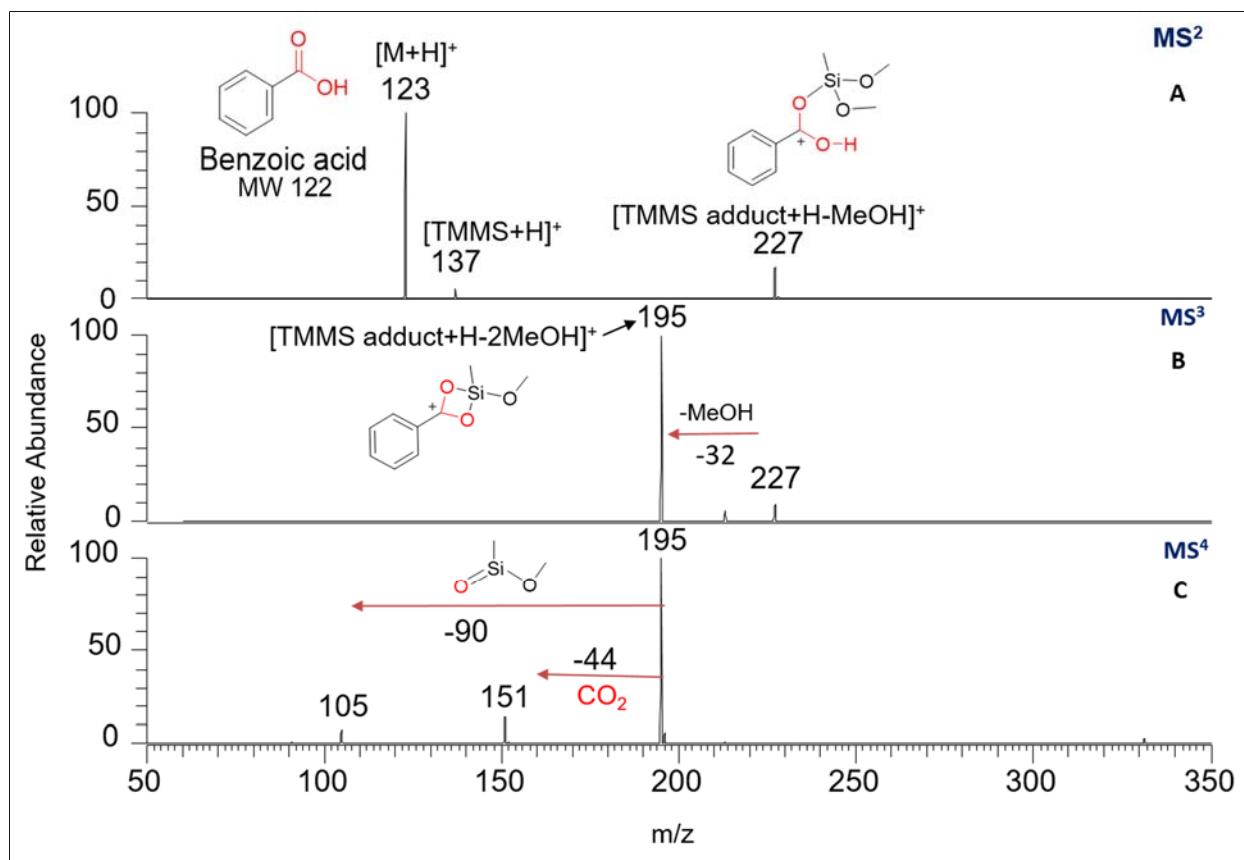


Figure 3.4 (A) MS<sup>2</sup> spectrum measured after 300 ms reaction of the protonated benzoic acid with TMMS. The most abundant product ion (m/z 227) corresponds to [TMMS adduct + H - MeOH]<sup>+</sup>. The other product ion (m/z 137) arises from proton transfer to TMMS. (B) MS<sup>3</sup> spectrum measured after CAD of isolated [TMMS adduct + H - MeOH]<sup>+</sup> (m/z 227). The major fragment ion (m/z 195) corresponds to elimination of methanol. (C) MS<sup>4</sup> spectrum measured after CAD of [TMMS adduct + H - 2 MeOH]<sup>+</sup> (m/z 195). The most abundant fragment ion (m/z 151) corresponds to CO<sub>2</sub> loss (44 Da). The other fragment ion corresponds to a loss of C<sub>2</sub>H<sub>6</sub>O<sub>2</sub>Si with MW of 90 Da.

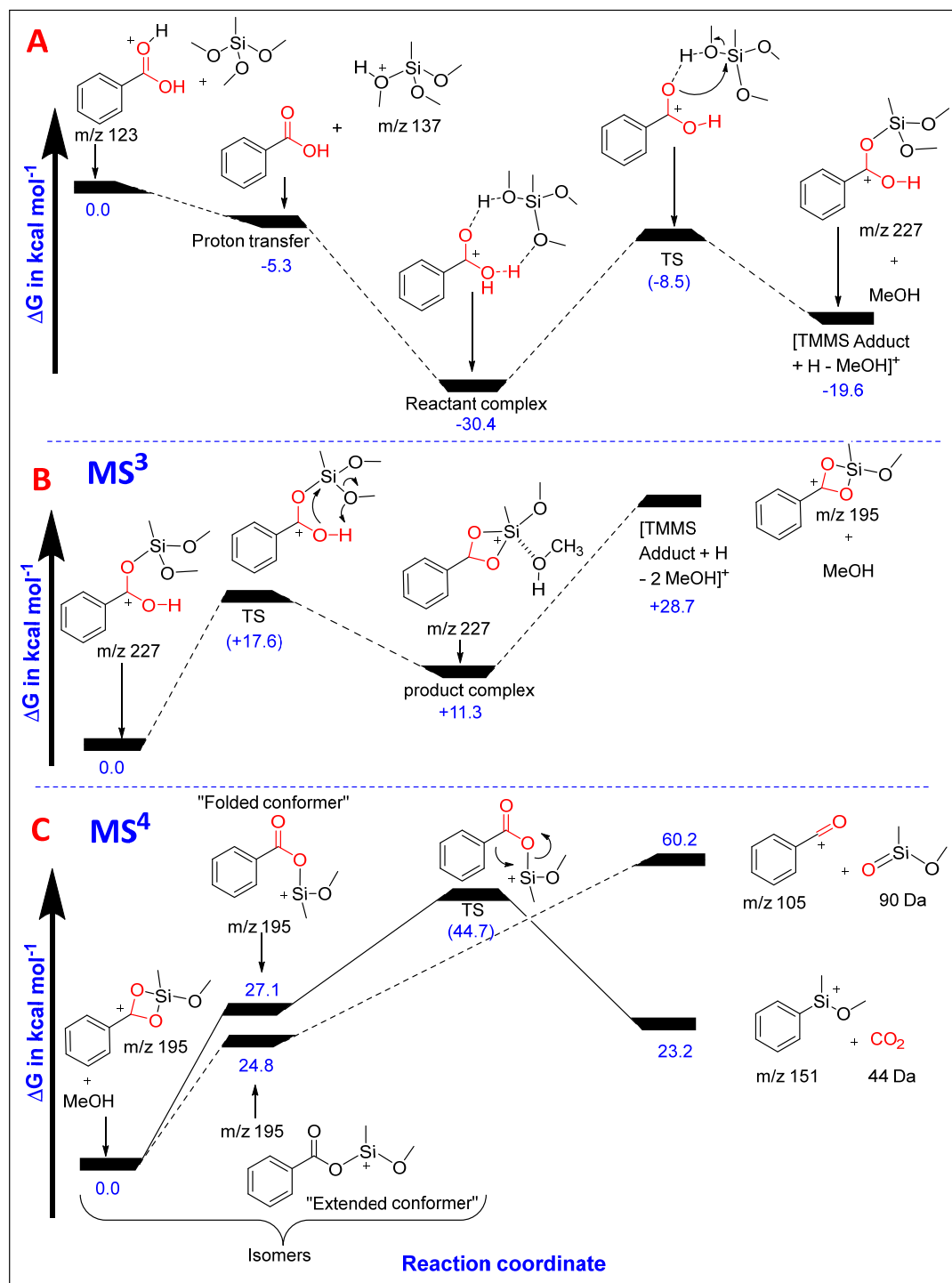


Figure 3.5 Proposed reaction pathways and potential energy surfaces calculated at M06-2X/6-311++G(d,p) level of theory for (A) spontaneous proton transfer and formation of [TMMS adduct + H - MeOH]<sup>+</sup> upon reaction of protonated benzoic acid with TMMS, (B) elimination of methanol after isolation and upon CAD of [TMMS adduct + H - MeOH]<sup>+</sup>, and (C) characteristic loss of molecules with MW of 44 Da (CO<sub>2</sub>) (indicated by solid line) and 90 Da (C<sub>2</sub>H<sub>6</sub>O<sub>2</sub>Si) (indicated by dashed line) observed upon CAD of [TMMS adduct + H - 2 MeOH]<sup>+</sup>. Energy values in parentheses indicate transition state energy barriers.



CAD of the [TMMS adduct + H - MeOH]<sup>+</sup> product ion (m/z 227) discussed above yielded [TMMS adduct + H - 2 MeOH]<sup>+</sup> fragment ion (m/z 195) via loss of a methanol molecule (MS<sup>3</sup> experiment; Figure 3.4B). Based on calculations, this loss is initiated by proton transfer from the hydroxyl group of the carboxylic acid moiety to a methoxy group of TMMS and has a Gibbs free energy of activation of 17.6 kcal/mol. It leads to a product complex of methanol loosely bound to an ion of m/z 195 (Figure 3.4B and Figure 3.5B), which dissociates to give the final products (the total reaction is endergonic by 28.7 kcal/mol).

CAD of the [TMMS adduct + H - 2 MeOH]<sup>+</sup> fragment ion (m/z 195) discussed above resulted in the diagnostic losses of neutral molecules of MW 44 Da (CO<sub>2</sub>) and MW 90 Da (CH<sub>3</sub>OSi(O)CH<sub>3</sub>; MS<sup>4</sup> experiment; Figure 3.4C). Figure 3.5C shows the calculated potential energy surface for these reactions. Based on calculations, [TMMS adduct + H - 2 MeOH]<sup>+</sup> initially isomerizes into two distinct conformations by breaking one of the Si-O bonds in the four-membered ring in the fragmenting ion. The two conformers are called here a “folded” conformer and an “extended” conformer. The “extended” conformer has a Gibbs free energy of 24.8 kcal/mol relative to the most stable form of the [TMMS adduct + H - 2 MeOH]<sup>+</sup> fragment ion. This conformer is characterized by protraction of the silicon atom and methoxy group away from the benzene ring. This conformer fragments into an ion with m/z 105 upon loss of CH<sub>3</sub>OSi(O)CH<sub>3</sub> (MW 90 Da) by cleavage of the carbonyl-oxygen bond. Breaking this bond is endergonic by 35.4 kcal/mol.

The “folded conformer” has a Gibbs free energy of 27.1 kcal/mol relative to the most stable form of the [TMMS adduct + H - 2 MeOH]<sup>+</sup> fragment ion. This isomer is characterized by the silicon and methoxy groups folding towards the benzene ring where the positively charged silicon atom can interact with the π-electron system of the benzene ring. Upon CAD, an *ipso*-substitution

occurs, involving breaking the phenyl-CO and Si-O bonds to release CO<sub>2</sub> (MW 44 Da). This process has a Gibbs free energy barrier of 17.6 kcal/mol relative to the “folded” conformer. The formation of the fragment ion of m/z 151 requires less energy than the ion of m/z 105 (formed via loss of CH<sub>3</sub>OSi(O)CH<sub>3</sub> with MW 90 Da), thus explaining the higher relative abundance of the ion of m/z 151 in the MS<sup>4</sup> spectrum measured after CAD of [TMMS adduct + H – 2 MeOH]<sup>+</sup> fragment ion (Figure 3.4C).

The identity of the carbon atom eliminated as CO<sub>2</sub> was confirmed by examining fragmentation of benzoic acid with a <sup>13</sup>C-label on the carboxylic acid functionality. Instead of eliminating CO<sub>2</sub>, this molecule eliminated <sup>13</sup>CO<sub>2</sub> (MW 45 Da) in the MS<sup>4</sup> experiment (Table 3.4, Figure 3.6C). Support for the proposed *ipso*-substitution mechanism was obtained by examining the reactivity of 2,6-dimethylbenzoic acid toward TMMS reagent (Figure 3.7). The methyl groups in dimethylbenzoic acid occupy the *ortho*-positions, which sterically hinders *ipso*-substitution. Indeed, the fragment ion formed via loss of CO<sub>2</sub> upon CAD of the [TMMS adduct + H – 2 MeOH]<sup>+</sup> fragment ion derived from dimethylbenzoic acid had a significantly lower abundance than the fragment ion formed via loss of CH<sub>3</sub>OSi(O)CH<sub>3</sub> with MW 90 Da (MS<sup>4</sup> mass spectrum, Figure 3.7C) while for benzoic acid, the fragment ion formed via CO<sub>2</sub> loss dominates (Figure 3.4C).

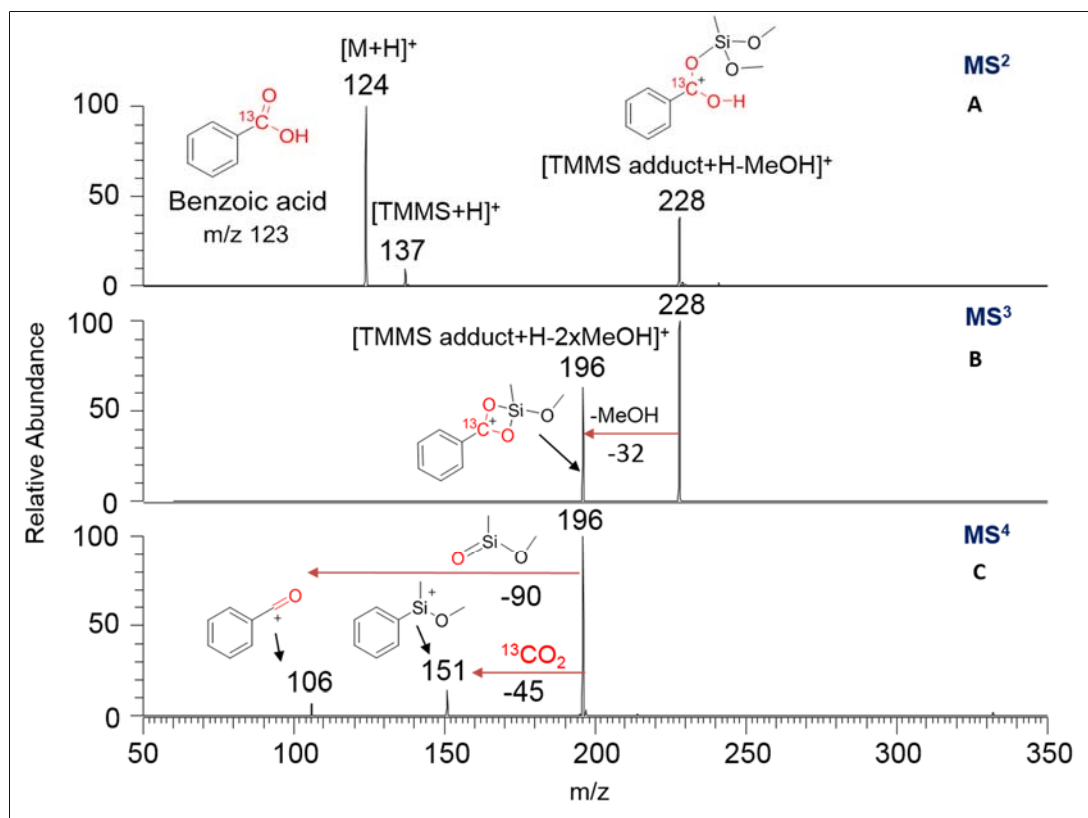


Figure 3.6 (A) MS<sup>2</sup> spectrum measured after 300 ms reaction of the protonated benzoic acid with  $^{13}C$  label on the carboxylic acid moiety with TMMS. The most abundant product ion (m/z 228) corresponds to  $[TMMS\ Adduct + H - MeOH]^+$ . The other product ion (m/z 137) corresponds to protonated TMMS. (B) MS<sup>3</sup> spectrum measured after CAD of  $[TMMS\ Adduct + H - MeOH]^+$  (m/z 228) shows elimination of methanol (m/z 196). (C) MS<sup>4</sup> spectrum measured after CAD for the methanol elimination product (m/z 196) shows  $^{13}CO_2$  loss (45 Da). the other fragment ion corresponds to a loss of  $C_2H_6O_2Si$  (MW 90 Da).

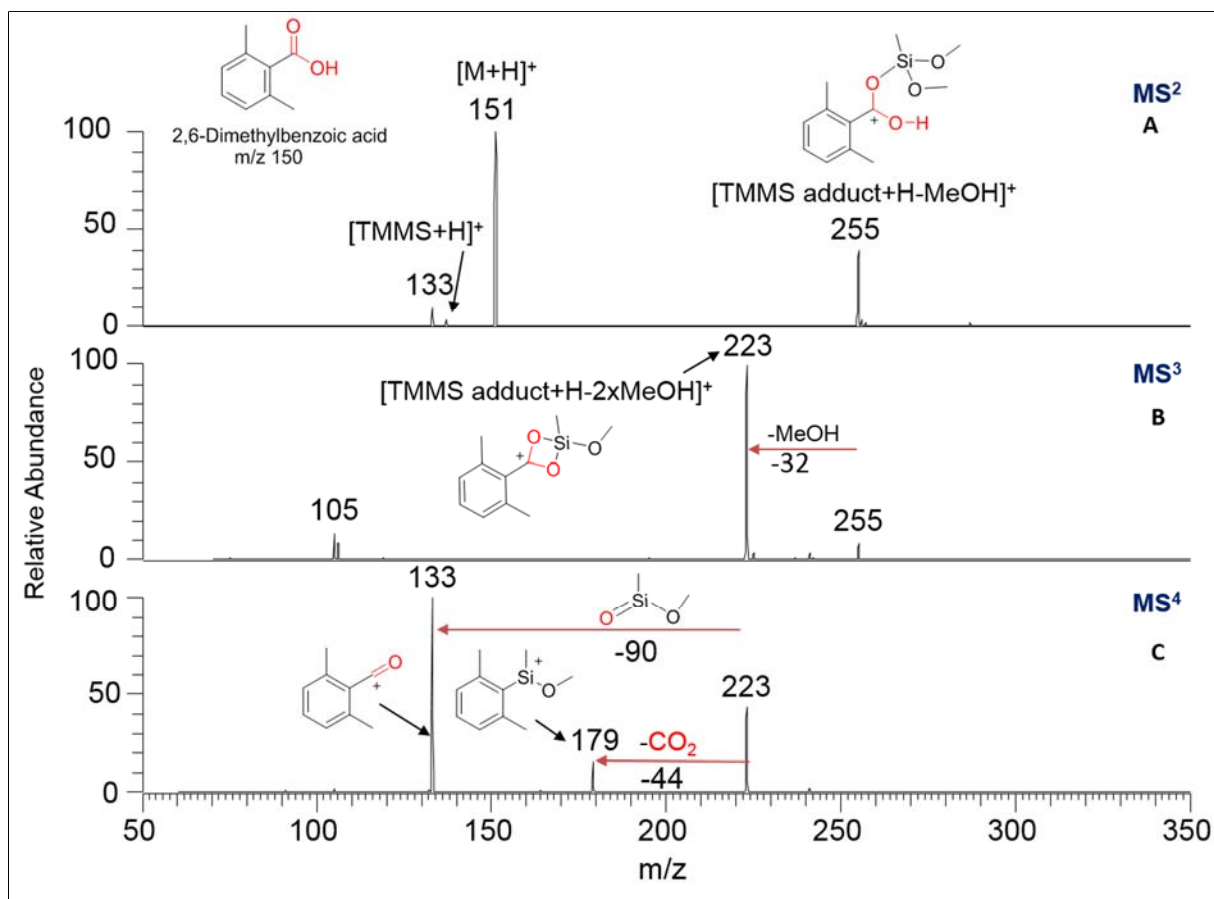


Figure 3.7 (a) MS<sup>2</sup> spectrum measured after 300 ms reaction of protonated 2,6-dimethylbenzoic acid with TMMS shows a major product ion (m/z 255) corresponding to [TMMS Adduct + H - MeOH]. The other product ion (m/z 133) corresponds to [M+H-H<sub>2</sub>O]<sup>+</sup>. (b) MS<sup>3</sup> spectrum measured after CAD of [TMMS Adduct + H - MeOH]<sup>+</sup> (m/z 255) shows a major fragment ion (m/z 223) corresponding to elimination of methanol. (c) MS<sup>4</sup> spectrum measured after CAD of the methanol elimination product (m/z 223) shows a major fragment ion (m/z 133) corresponding to loss of C<sub>2</sub>H<sub>6</sub>O<sub>2</sub>Si (MW 90 Da). The other fragment ion corresponds to a loss of CO<sub>2</sub> (44 Da).

The diagnostic reactivity described above for protonated aromatic carboxylic acids was not observed for sulindac (Table 3.4). Protonated sulindac forms the [TMMS adduct + H]<sup>+</sup> product upon reactions with TMMS but not the methanol elimination product that was observed for other aromatic carboxylic acids (Table 3.4). This finding is rationalized by the presence of substantially more basic functionality, a sulfoxide group (proton affinity (PA) = 224 kcal/mol; see Figure 3.8 for comparison of the PAs for the various protonation sites in sulindac). The sulfoxide functionality

has a PA 23 kcal/mol greater than the carboxylic acid site (201 kcal/mol). Hence, protonation is likely to occur preferentially at the sulfoxide group. This explains the lack of formation of the product ions diagnostic of aromatic carboxylic acid functionalities, as protonated sulfoxides do not yield these product ions (Figure 3.1).

In contrast to sulindac, the expected [TMMS adduct + H - MeOH]<sup>+</sup> product ion was observed for three other polyfunctional analytes containing functionality that is more basic than the carboxylic acid site, namely 3-aminobenzoic acid, 4-acetamidobenzoic acid and 4-methoxy-3-nitrobenzoic acid. The observed reactivity suggests that these compounds get protonated at both the carboxylic acid group and the more basic site upon ESI. Indeed, the formation of two protomers for 3-aminobenzoic acid upon ESI has been previously reported.<sup>24-27</sup> Further, the calculated PA differences between the two functionalities in these three compounds are only 8 kcal/mol or less (Figure 3.8) and hence substantially smaller than for sulindac (23 kcal/mol). Based on literature, protonation at two different sites in a polyfunctional molecule upon ESI can occur when the PA difference of these sites is 10 kcal/mol or less.<sup>9</sup> We calculated the PA or acidity differences for basic and acidic sites in several molecules reported in the literature<sup>24,25,28-30</sup> to get protonated or deprotonated, respectively, at two sites upon ESI, and found these differences to be 8 kcal/mol or less (Table 3.5). This evidence supports our hypothesis that sulindac, with a huge PA difference of 23 kcal/mol, can only get protonated at the most basic site. However, the other compounds discussed above, with a proton affinity difference of 8 kcal/mol or less, can get protonated at several sites and hence display reactivity diagnostic of the carboxylic acid functionality.

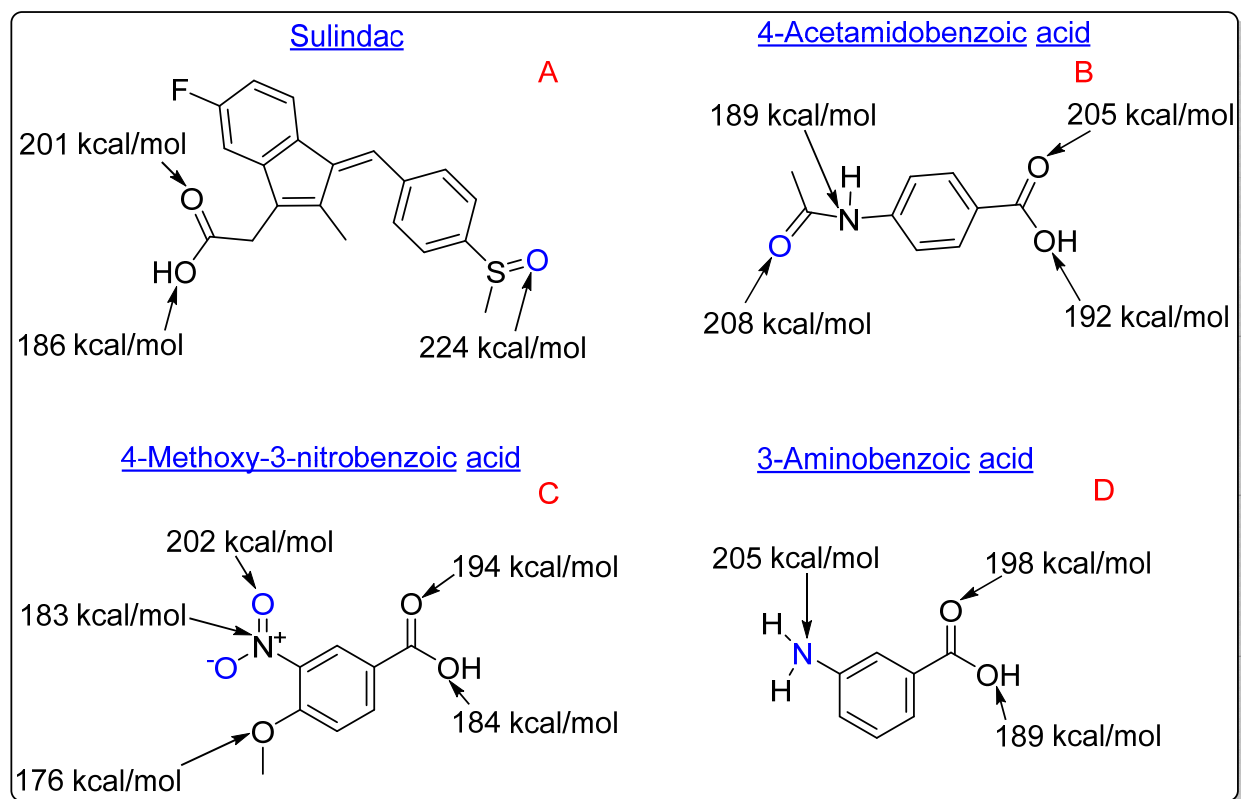
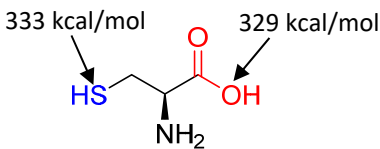
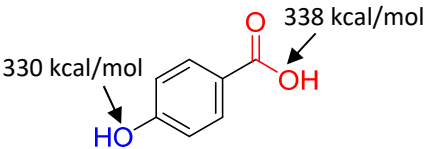
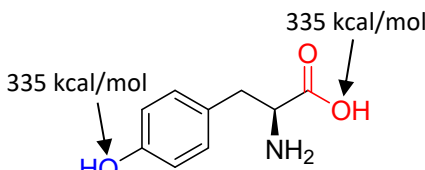
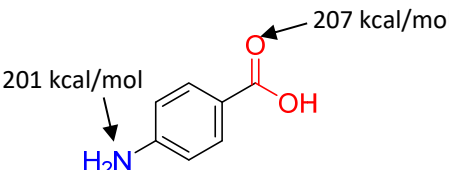
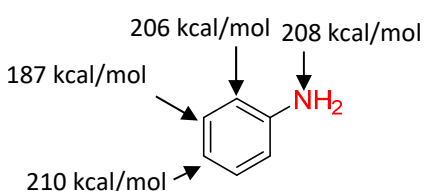


Figure 3.8 The proton affinities calculated for different protonation sites in (A) sulindac, (B) 4-acetamidobenzoic acid, (C) 4-methoxy-3-nitrobenzoic acid and (D) 3-aminobenzoic acid (B3LYP/6-31G++(d,p) level of theory). The most basic site in each molecule is colored blue.

Table 3.5 Calculated acidities/proton affinities of different possible protonation/deprotonation sites (B3LYP/6-311++G(d,p) level of theory) for molecules earlier reported in the literature to be deprotonated/protonated at different sites upon ESI.

Analyte Gas-phase acidities/PAs (kcal/mol)	Ion formation reported in the literature	Difference in gas-phase acidity/PA (in kcal/mol) for the functionalities
 <p>Cysteine</p>	Thiolate and carboxylate anions are generated. <sup>21,24</sup>	4 kcal/mol
 <p>p-Hydroxybenzoic acid</p>	Phenoxyate and carboxylate anions are generated. <sup>20</sup>	8 kcal/mol
 <p>Tyrosine</p>	Phenoxyate and carboxylate anions are generated. <sup>20</sup>	0 kcal/mol
 <p>p-Aminobenzoic acid</p>	Protonated carboxylic acid and amino groups are generated. <sup>25</sup>	6 kcal/mol
 <p>Aniline</p>	Protonated amino group and the benzene ring are generated. <sup>26</sup>	2 kcal/mol

### 3.3.4 Reactions of TMMS With Protonated Hydroxybenzoic Acid Isomers

Although protonated 3-hydroxybenzoic and 4-hydroxybenzoic acid isomers react as expected, their 2-hydroxy isomer does not. Upon CAD, [TMMS adduct + H - 2 MeOH]<sup>+</sup> fragment ions (obtained in MS<sup>3</sup> experiments) derived from 2-hydroxybenzoic acid fragment via loss of CO<sub>2</sub> (MW 44 Da) and CH<sub>2</sub>O (MW 30 Da) (MS<sup>4</sup> experiments, see Figure 3.9C) instead of loss of CO<sub>2</sub> (MW 44 Da) and C<sub>2</sub>H<sub>6</sub>O<sub>2</sub>Si (MW 90 Da), as observed for other carboxylic acids. In order to understand the reasons for this difference, the mechanisms for the reactions of protonated 2-hydroxybenzoic acid were explored computationally.

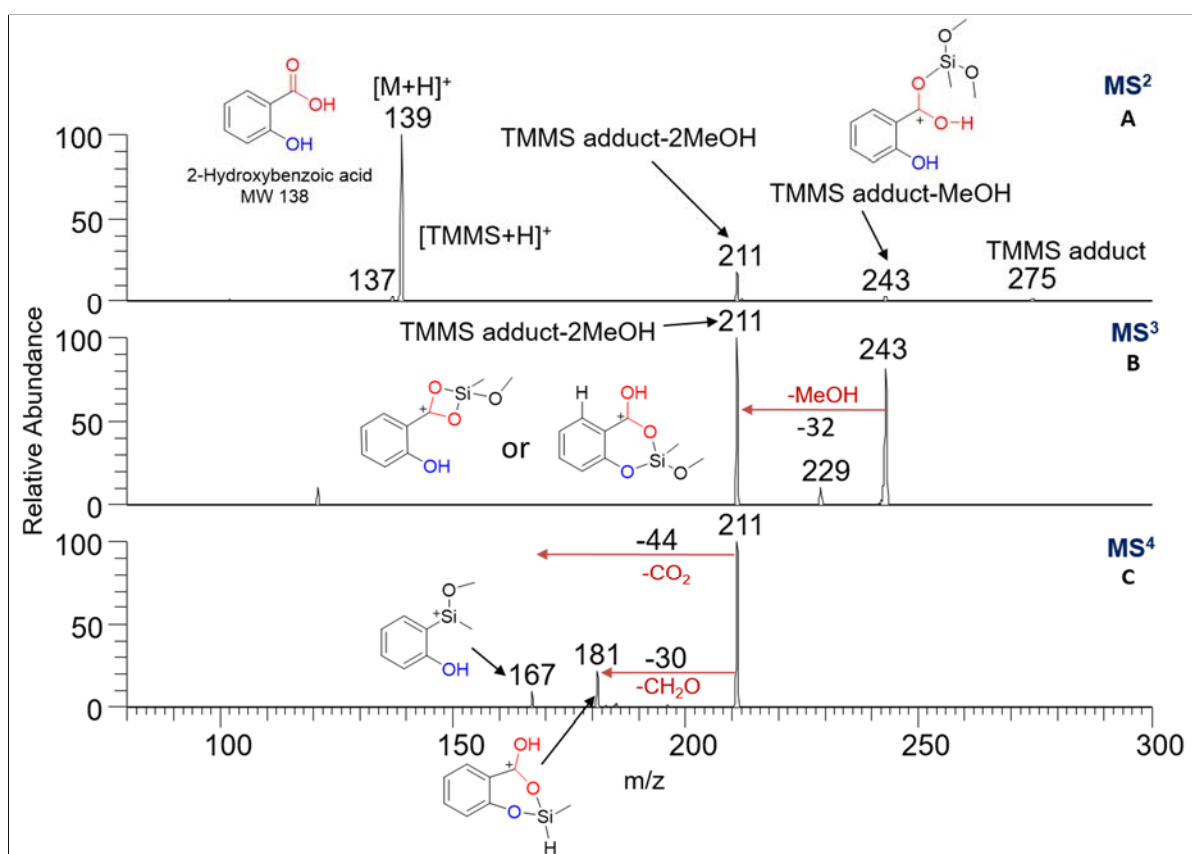


Figure 3.9 The mass spectrum measured after 300 ms reaction of protonated 2-hydroxybenzoic acid with TMMS. (A) Spontaneous formation of [TMMS adduct + H]<sup>+</sup> (m/z 275), [TMMS adduct + H - MeOH]<sup>+</sup> (m/z 243) and [TMMS adduct + H - 2 MeOH]<sup>+</sup> (m/z 211) was observed. (B) MS<sup>3</sup> spectrum measured after CAD of [TMMS adduct + H - MeOH]<sup>+</sup> (m/z 243). The major fragment ion (m/z 211) corresponds to elimination of methanol. (C) MS<sup>4</sup> spectrum measured after CAD of [TMMS adduct + H - 2 MeOH]<sup>+</sup> (m/z 211). The most abundant fragment ion corresponds to the loss of formaldehyde (MW 30 Da). The other fragment ion corresponds to loss of CO<sub>2</sub> (MW 44 Da).



Figure 8A shows the calculated PES for the exothermic proton transfer followed by the formation of the  $[\text{TMMS adduct} + \text{H} - \text{MeOH}]^+$  product upon reaction of TMMS with protonated 2-hydroxybenzoic acid ( $\text{MS}^2$  experiment). Figure 3.10B shows the PES for the formation of  $[\text{TMMS adduct} + \text{H} - 2 \text{MeOH}]^+$  fragment ions ( $m/z$  211) upon CAD of  $[\text{TMMS adduct} + \text{H} - \text{MeOH}]^+$  ( $m/z$  243) ( $\text{MS}^3$  experiment). Two different conformations of the  $[\text{TMMS adduct} + \text{H} - \text{MeOH}]^+$  product ion ( $m/z$  243) proceed through different pathways to yield two isomeric  $[\text{TMMS adduct} + \text{H} - 2 \text{MeOH}]^+$  fragment ions, one with a four-membered and the other with a six-membered ring containing the silicon atom ( $\text{MS}^4$  experiment), as shown in Figure 3.10B. Figure 3.10C shows the PES for the elimination of  $\text{CH}_2\text{O}$  and  $\text{CO}_2$  from the  $[\text{TMMS adduct} + \text{H} - 2 \text{MeOH}]^+$  fragment ions upon CAD.  $\text{CH}_2\text{O}$  loss occurs from the more stable isomer containing the six-membered ring and has a Gibbs free energy barrier of +72.1 kcal/mol.  $\text{CO}_2$  loss occurs from the isomer containing the four-membered ring in exactly the similar fashion as described above for benzoic acid and has a Gibbs free energy barrier of +61.1 kcal/mol relative to the lowest energy  $[\text{TMMS adduct} + \text{H} - 2 \text{MeOH}]^+$  isomer. Although the barrier for  $\text{CO}_2$  loss is lower than the barrier for  $\text{CH}_2\text{O}$  loss, the relative abundance of the product ion corresponding to  $\text{CH}_2\text{O}$  loss is greater in the  $\text{MS}^4$  spectrum (Figure 3.9C). This is due to the relative stabilities of the isomeric  $[\text{TMMS adduct} + \text{H} - 2 \text{MeOH}]^+$  ions containing four- and six-membered rings. As seen in Figure 3.10B, the isomer containing the six-membered ring is substantially more stable and has a lower TS energy. Hence, this isomer is likely formed in greater abundance, leading to a greater abundance of the fragment ion formed via  $\text{CH}_2\text{O}$  loss. Due to its greater energy requirements (Figure 3.6C),  $\text{CH}_3\text{OSi}(\text{O})\text{CH}_3$  (MW 90) loss cannot compete with above processes.

While the  $[\text{TMMS adduct} + \text{H} - 2 \text{MeOH}]^+$  fragment ions derived from 2-hydroxybenzoic acid preferentially undergo  $\text{CH}_2\text{O}$  elimination over  $\text{CO}_2$  elimination, the  $\text{CH}_2\text{O}$  elimination

pathway is not available for the 3- and 4-hydroxybenzoic acids as their hydroxy-substituents are too far away from the carboxylic acid moiety to form the six-membered isomer of [TMMS adduct + H - 2 MeOH]<sup>+</sup> fragment ions needed for CH<sub>2</sub>O loss. This difference allows the distinction of the *ortho*-isomer from the *meta*- and *para*-isomers.

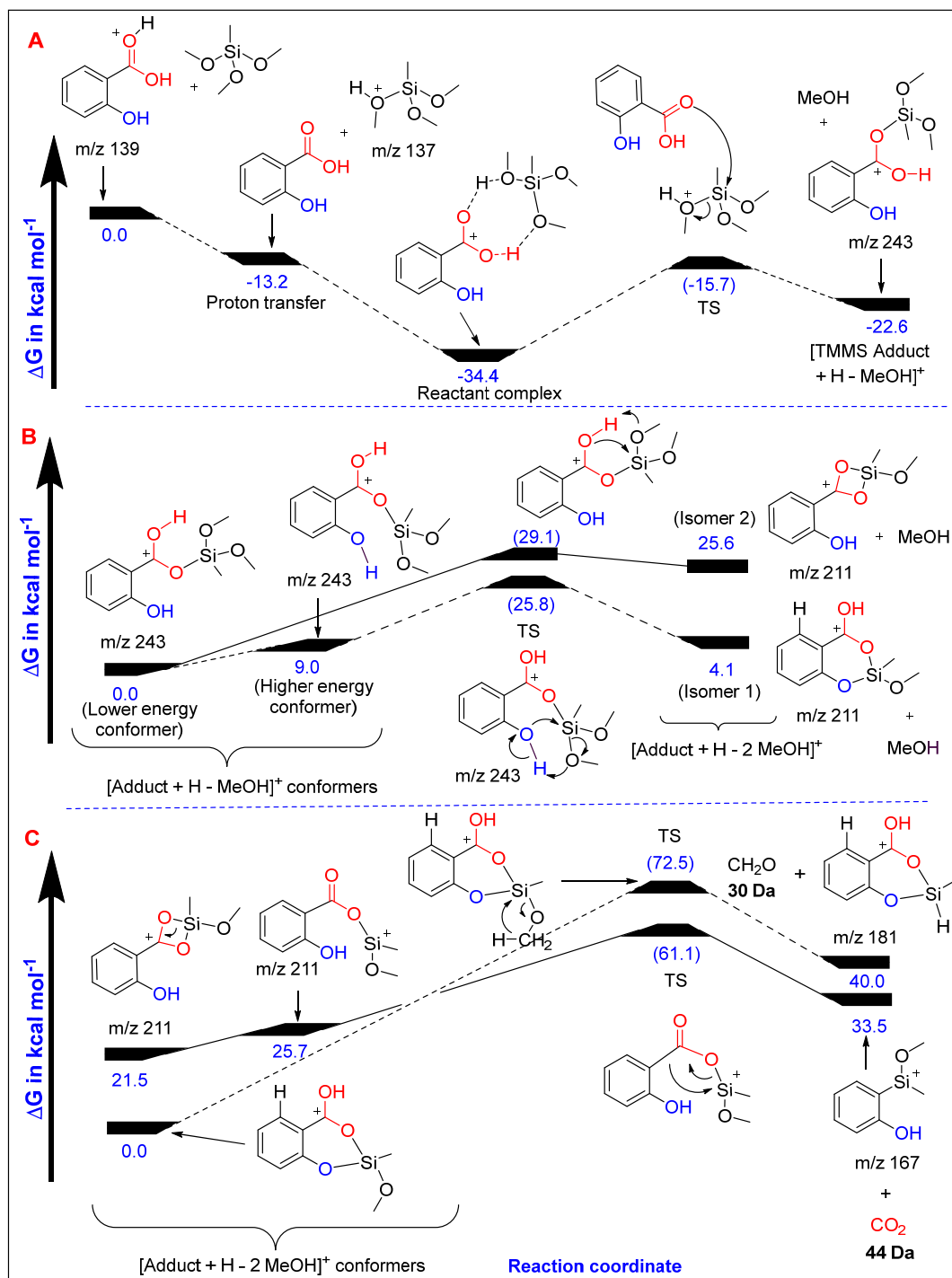


Figure 3.10 Proposed reaction pathways and calculated potential energy surfaces (M06-2X/6-311++G(d,p) level of theory) for (A) spontaneous proton transfer and formation of [TMMS adduct + H - MeOH]<sup>+</sup> upon reaction of protonated 2-hydroxybenzoic acid with TMMS (MS<sup>2</sup> experiment), (B) elimination of methanol upon CAD of [TMMS adduct + H - MeOH]<sup>+</sup> (MS<sup>3</sup> experiment), and (C) diagnostic loss of molecules with MW of 44 Da (CO<sub>2</sub>) (pathway indicated by solid line) and 30 Da (CH<sub>2</sub>O) (pathway indicated by dashed line) observed upon CAD of [TMMS adduct + H - 2 MeOH]<sup>+</sup> (MS<sup>4</sup> experiment).

### 3.3.5 Reactions of TMMS with Protonated Compounds Containing Sulfonamide and Aliphatic Carboxylic Acid Functionalities

Protonated compounds containing sulfonamide or aliphatic carboxylic acid functionality yielded the  $[\text{TMMS adduct} + \text{H} - \text{MeOH}]^+$  product upon reaction with TMMS, similarly to sulfones and aromatic carboxylic acids. Unlike sulfones but similar to aromatic carboxylic acids, CAD of the  $[\text{TMMS adduct} + \text{H} - \text{MeOH}]^+$  product yielded  $[\text{TMMS adduct} + \text{H} - 2 \text{MeOH}]^+$  fragment ions. Further CAD on these fragment ions yielded several fragment ions (Table 3.4 and Table 3.3). The  $\text{MS}^n$  spectra measured for protonated benzene sulfonamide (Figure 3.11) and hexanoic acid (Figure 3.12) are presented in supporting information as examples. Interestingly, both sulfonamides and aliphatic carboxylic acids show the fragment ion of  $m/z$  91 in their mass spectra although none of the other compounds do. A feasible mechanism for this reaction is shown in Figure 3.13.

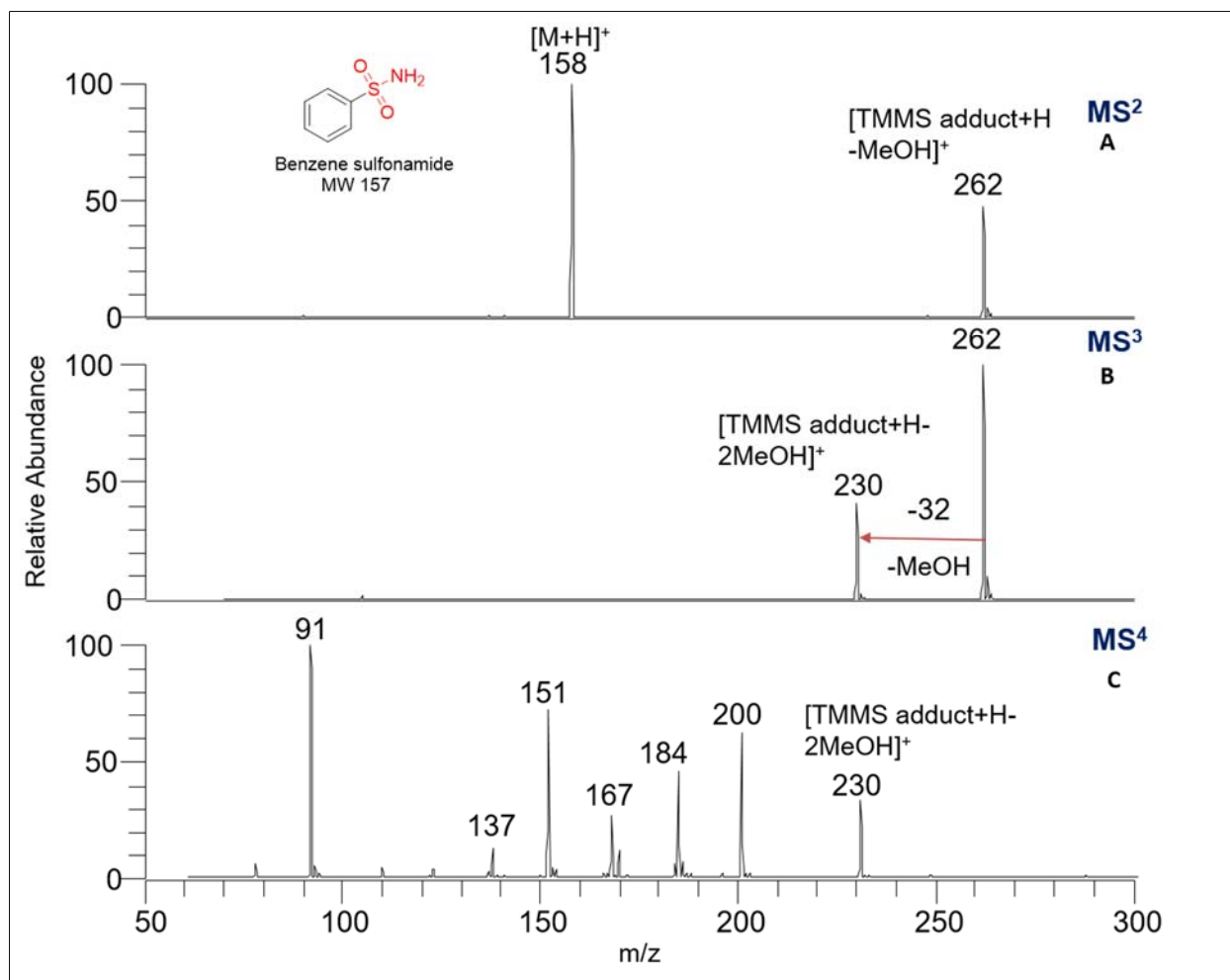


Figure 3.11 (A) The MS<sup>2</sup> spectrum measured after 400 ms reaction of protonated benzene sulfonamide with TMMS shows the product ion [TMMS Adduct + H - MeOH]<sup>+</sup> (m/z 262) diagnostic also for aromatic carboxylic acids and sulfones. (B) MS<sup>3</sup> spectrum measured after CAD of isolated [TMMS adduct + H - MeOH]<sup>+</sup> (m/z 262) showed the fragment ion of m/z 230 corresponding to the elimination of methanol, as observed for other carboxylic acid model compounds. (C) MS<sup>4</sup> spectrum measured after CAD of [TMMS adduct + H - 2 MeOH]<sup>+</sup> (m/z 230) showed no fragment ions corresponding to CO<sub>2</sub> loss (44 Da) or loss of C<sub>2</sub>H<sub>6</sub>O<sub>2</sub>Si with a MW of 90 Da (characteristic of carboxylic acids), but it showed a fragment ion of m/z 91 that may be diagnostic for sulfonamides and aliphatic carboxylic acids.

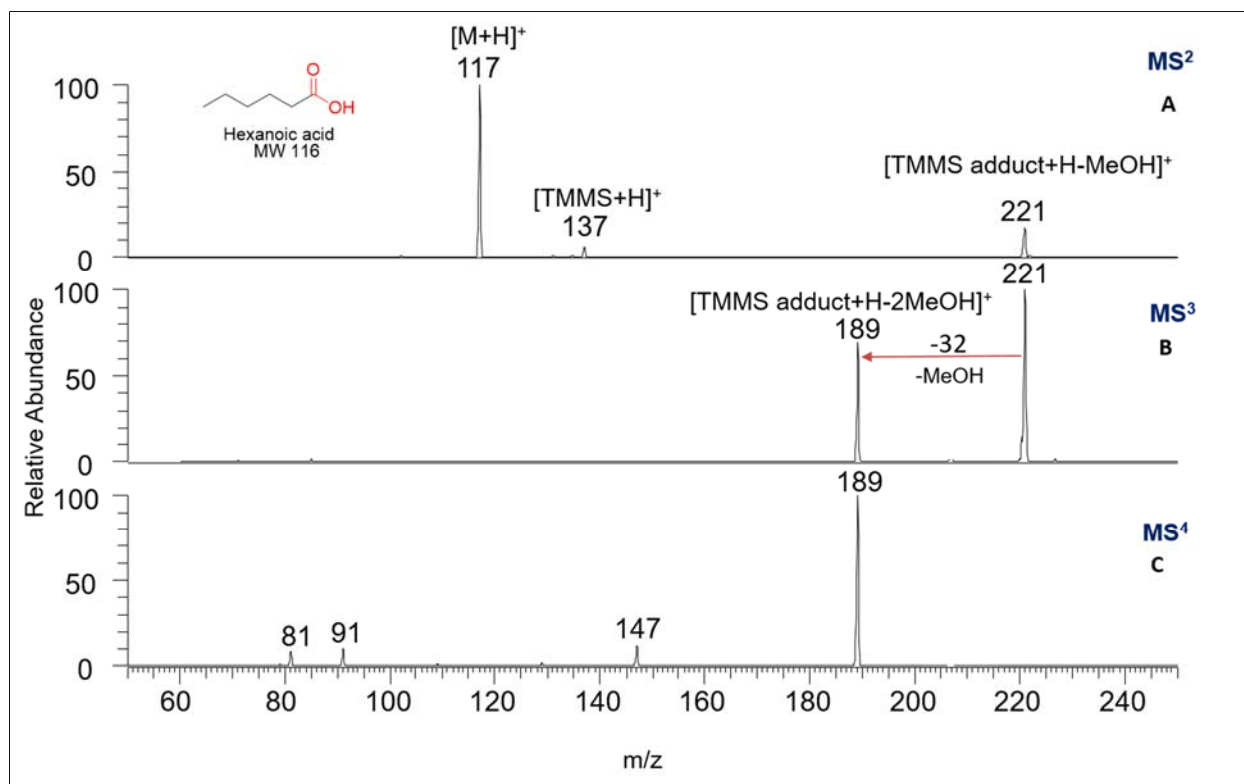


Figure 3.12 (A) The MS<sup>2</sup> spectrum measured after 500 ms reaction of the protonated hexanoic acid with TMMS shows the diagnostic product ion [TMMS Adduct + H - MeOH]<sup>+</sup> (m/z 211) observed for aromatic carboxylic acids and sulfones. (B) The MS<sup>3</sup> spectrum measured after CAD of isolated [TMMS adduct+H-MeOH]<sup>+</sup> (m/z 211) shows a fragment ion (m/z 189) corresponding to the elimination of methanol as observed for aromatic carboxylic acid model compounds. (C) The MS<sup>4</sup> spectrum measured after CAD of [TMMS adduct + H - 2 MeOH]<sup>+</sup> (m/z 189) showed fragment ions corresponding to loss of CO<sub>2</sub> (44 Da) or loss of C<sub>2</sub>H<sub>6</sub>O<sub>2</sub>Si (90 Da), enabling the differentiation of the aromatic carboxylic acid functionality from aliphatic carboxylic acid functionality. The fragment ion of m/z 91 was only observed for aliphatic carboxylic acids and sulfonamides.

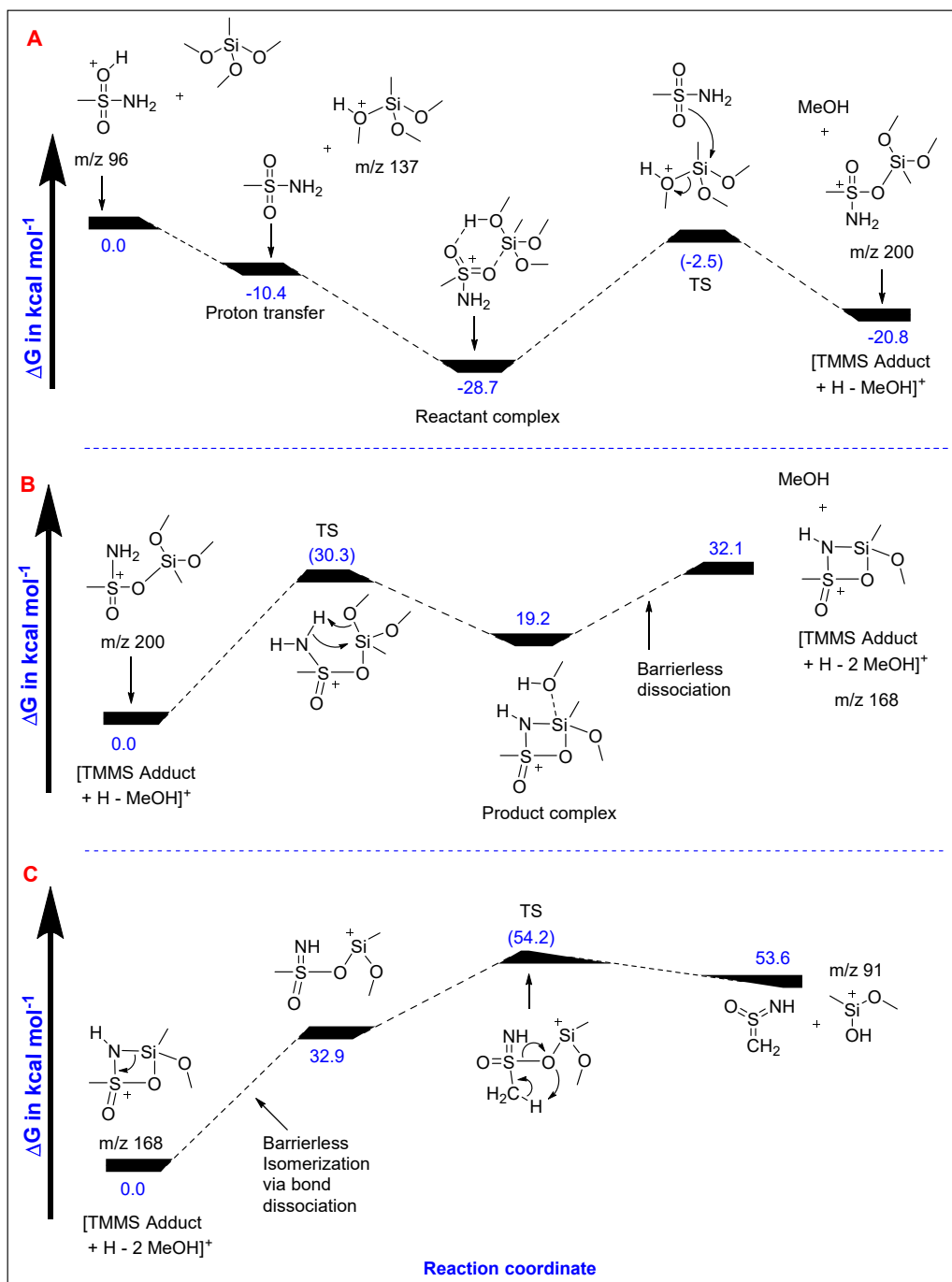


Figure 3.13 Calculated potential energy surface (at the M06-2X/6-311++G(d,p) level of theory) for (A) proton transfer and formation of [TMMS adduct + H - MeOH]<sup>+</sup> resulting from reaction of protonated methanesulfonamide with TMMS (MS<sup>2</sup> experiment), (B) elimination of methanol upon CAD of [TMMS adduct + H - MeOH]<sup>+</sup> (MS<sup>3</sup> experiment), and (C) formation of ion of m/z 91 (CH<sub>3</sub>O(CH<sub>3</sub>)Si<sup>+</sup>OH) upon CAD of [TMMS adduct + H - 2 MeOH]<sup>+</sup> (MS<sup>4</sup> experiment). An analogous mechanism applies to aliphatic carboxylic acids.

### 3.4 Conclusions

In this study, gas-phase ion molecule reactions of trimethoxymethylsilane (TMMS) reagent along with MS<sup>n</sup> experiments based on CAD were demonstrated to allow the differentiation of sulfone, carboxylic acid and sulfonamide functionalities in protonated polyfunctional model compounds from many other functionalities in a modified linear quadrupole ion trap mass spectrometer (Figure 3.14). When compounds containing above functional groups were allowed to react with TMMS, characteristic [TMMS adduct + H - MeOH]<sup>+</sup> product ions were formed (MS<sup>2</sup> experiments). Isolation and CAD of these product ions yielded fragment ions of m/z 75, 105 and 123 diagnostic for sulfones (MS<sup>3</sup> experiments). In contrast, CAD of the product ions derived from aromatic and aliphatic carboxylic acids and sulfonamides resulted in the elimination of a second methanol molecule upon CAD (MS<sup>3</sup> experiments). Subsequently, CAD of these fragment ions derived from aromatic carboxylic acids resulted in the elimination of molecules of MW 44 Da and 90 Da (MS<sup>4</sup> experiments). On the other hand, CAD of the fragment ions (produced in MS<sup>3</sup> experiments) derived from sulfonamides and aliphatic carboxylic acids yielded many different fragment ions, including one common fragment ion of m/z 91 that was not observed for any of the other functionalities. This fragment ion may be diagnostic for aliphatic carboxylic acids and sulfonamides. Above observations enable the differentiation of sulfones and aromatic carboxylic acids from each other and from sulfonamides and aliphatic carboxylic acids, as well as from all the other functionalities studied. Differentiation of aliphatic carboxylic acids and sulfonamides was not possible although they can be differentiated from all other functionalities.



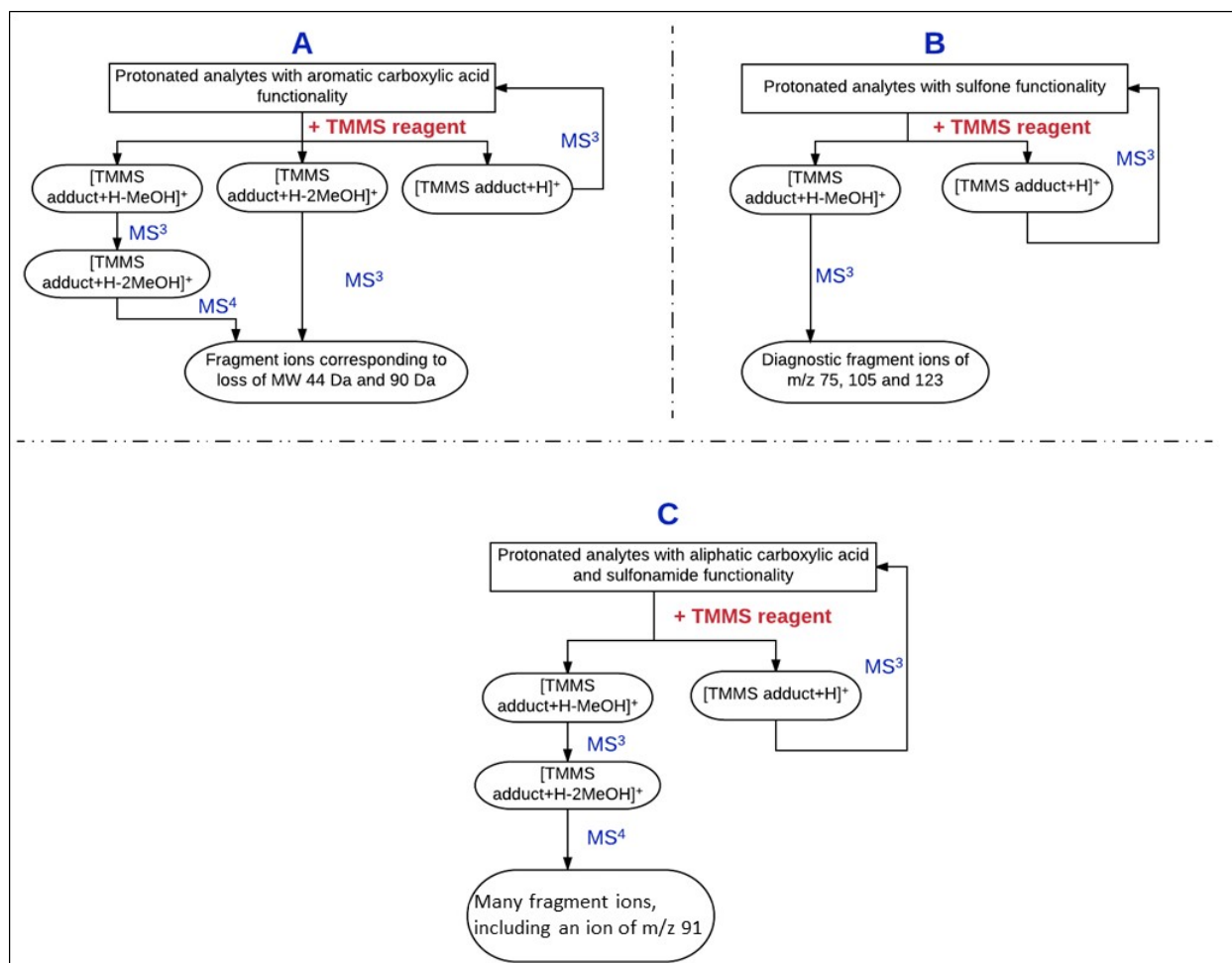


Figure 3.14 A general scheme for identification of aromatic carboxylic acid functionality (A), sulfone functionality (B), and sulfonamide and aliphatic carboxylic acid functionalities together (they cannot be differentiated) (C) by  $MS^n$  experiments employing ion-molecule reactions of protonated analytes with TMMS reagent.

Finally, the above methodology was successfully applied in the identification of aromatic carboxylic acid and sulfone functionalities in polyfunctional compounds. However, four such protonated polyfunctional compounds, *i.e.*, alendazole sulfone, methionine sulfone, omeprazole sulfone and sulindac, failed to yield the expected diagnostic products. For methionine sulfone, omeprazole sulfone and sulindac, this behavior is rationalized by the presence of functionality that is substantially more basic (for sulindac and methionine sulfone, by 23 kcal/mol, and for

omeprazole sulfone, by 36 kcal/mol) than the sulfone or carboxylic acid functionality. However, this PA difference is only 9 kcal/mol for albendazole sulfone. Based on the literature,<sup>20,23,24,27,28,29</sup> molecules with two basic or acidic sites differing in PA or acidity by 8 kcal/mol or less can be protonated/deprotonated at both sites upon ESI. In only one case, the PA difference was reported to be 10 kcal/mol.<sup>20</sup> Hence, PA differences greater than 8 kcal/mol appear to prevent ionization of more than one site generally.

### 3.5 References

- (1) Wen, B.; Zhu, M. Applications of Mass Spectrometry in Drug Metabolism: 50 Years of Progress. *Drug Metab. Rev.* **2015**, *47* (1), 71–87.
- (2) Ma, S.; Chowdhury, S. K. Data Acquisition and Data Mining Techniques for Metabolite Identification Using LC Coupled to High-Resolution MS. *Bioanalysis* **2013**, *5* (10), 1285–1297.
- (3) Grillo, M. P. Detecting Reactive Drug Metabolites for Reducing the Potential for Drug Toxicity. *Expert Opin. Drug Metab. Toxicol.* **2015**, *11* (8), 1281–1302.
- (4) Gao, H.; Jacobs, A.; White, R. E.; Booth, B. P.; Obach, R. S. Meeting Report: Metabolites in Safety Testing (MIST) Symposium-Safety Assessment of Human Metabolites: What's REALLY Necessary to Ascertain Exposure Coverage in Safety Tests? *AAPS J.* **2013**, *15* (4), 970–973.
- (5) Stepan, A. F.; Mascitti, V.; Beaumont, K.; Kalgutkar, A. S. Metabolism-Guided Drug Design. *Med. Chem. Commun.* **2013**, *4* (4), 631–652.
- (6) Bjarnason, A.; Taylor, J. W.; Kinsinger, J. A.; Cody, R. B.; Weil, D. A. Isomer Discrimination of Disubstituted Benzene Derivatives through Gas-Phase Iron(I) Ion Reactions in a Fourier-Transform Mass Spectrometer. *Anal. Chem.* **1989**, *61* (17), 1889–1894.
- (7) Fu, M.; Duan, P.; Li, S.; Habicht, S. C.; Pinkston, D. S.; Vinueza, N. R.; Kenttämä, H. I. Regioselective Ion-Molecule Reactions for the Mass Spectrometric Differentiation of Protonated Isomeric Aromatic Diamines. *The Analyst* **2008**, *133* (4), 452–454.
- (8) Zhang, M.; Eismin, R.; Kenttämä, H.; Xiong, H.; Wu, Y.; Burdette, D.; Urbanek, R. Identification of 2-Aminothiazolobenzazepine Metabolites in Human, Rat, Dog, and Monkey Microsomes by Ion-Molecule Reactions in Linear Quadrupole Ion Trap Mass Spectrometry. *Drug Metab. Dispos. Biol. Fate Chem.* **2015**, *43* (3), 358–366.
- (9) Sheng, H.; Tang, W.; Yerabolu, R.; Max, J.; Kotha, R. R.; Riedeman, J. S.; Nash, J. J.; Zhang, M.; Kenttämä, H. I. Identification of N-Oxide and Sulfoxide Functionalities in Protonated Drug Metabolites by Using Ion-Molecule Reactions Followed by Collisionally Activated Dissociation in a Linear Quadrupole Ion Trap Mass Spectrometer. *J. Org. Chem.* **2016**, *81* (2), 575–586.
- (10) Eismin, R.; Fu, M.; Yem, S.; Widjaja, F.; Kenttämä, H. Identification of Epoxide Functionalities in Protonated Monofunctional Analytes by Using Ion/Molecule Reactions and Collision-Activated Dissociation in Different Ion Trap Tandem Mass Spectrometers. *J. Am. Soc. Mass Spectrom.* **2012**, *23* (1), 12–22.
- (11) Tang, W.; Sheng, H.; Kong, J. Y.; Yerabolu, R.; Zhu, H.; Max, J.; Zhang, M.; Kenttämä, H. I. Gas-Phase Ion-molecule Reactions for the Identification of the Sulfone Functionality in Protonated Analytes in a Linear Quadrupole Ion Trap Mass Spectrometer. *Rapid Commun. Mass Spectrom.* **2016**, *30* (12), 1435–1441.
- (12) Sheng, H.; Williams, P. E.; Tang, W.; Riedeman, J. S.; Zhang, M.; Kenttämä, H. I. Identification of the Sulfone Functionality in Protonated Analytes via Ion/Molecule Reactions in a Linear Quadrupole Ion Trap Mass Spectrometer. *J. Org. Chem.* **2014**, *79* (7), 2883–2889.

- (13) Campbell, K. M.; Watkins, M. A.; Li, S.; Fiddler, M. N.; Winger, B.; Kenttämää, H. I. Functional Group Selective Ion/Molecule Reactions: Mass Spectrometric Identification of the Amido Functionality in Protonated Monofunctional Compounds. *J. Org. Chem.* **2007**, *72* (9), 3159–3165.
- (14) Somuramasami, J.; Winger, B. E.; Gillespie, T. A.; Kenttämää, H. I. Identification and Counting of Carbonyl and Hydroxyl Functionalities in Protonated Bifunctional Analytes by Using Solution Derivatization Prior to Mass Spectrometric Analysis via Ion-Molecule Reactions. *J. Am. Soc. Mass Spectrom.* **2009**, *21* (5), 773–784.
- (15) Watkins, M. A.; Winger, B. E.; Shea, R. C.; Kenttämää, H. I. Ion–Molecule Reactions for the Characterization of Polyols and Polyol Mixtures by ESI/FT-ICR Mass Spectrometry. *Anal. Chem.* **2005**, *77* (5), 1385–1392.
- (16) Dupre, Andrea S. The Roles of Silanes as Coupling Reagents and in Deoxygenative Alkylations.
- (17) Sheng, H.; Tang, W.; Yerabolu, R.; Max, J.; Kotha, R. R.; Riedeman, J. S.; Nash, J. J.; Zhang, M.; Kenttämää, H. I. Identification of N-Oxide and Sulfoxide Functionalities in Protonated Drug Metabolites by Using Ion-Molecule Reactions Followed by Collisionally Activated Dissociation in a Linear Quadrupole Ion Trap Mass Spectrometer. *J. Org. Chem.* **2015**.
- (18) Dupre, Andrea S. The Roles of Silanes as Coupling Reagents and in Deoxygenative Alkylations. Dissertation, Louisiana State University: Baton Rouge, 2003.
- (19) Gronert, S. Quadrupole Ion Trap Studies of Fundamental Organic Reactions. *Mass Spectrom. Rev.* **2005**, *24* (1), 100–120.
- (20) Gronert, S. Estimation of Effective Ion Temperatures in a Quadrupole Ion Trap. *J. Am. Soc. Mass Spectrom.* **1998**, *9* (8), 845–848.
- (21) Habicht, S. C.; Vinueza, N. R.; Amundson, L. M.; Kenttämää, H. I. Comparison of Functional Group Selective Ion–Molecule Reactions of Trimethyl Borate in Different Ion Trap Mass Spectrometers. *J. Am. Soc. Mass Spectrom.* **2011**, *22* (3), 520–530.
- (22) Gaussian 09, Revision E.01, Frisch, M. J.; Trucks, G. W.; Schlegel, H. B.; Scuseria, G. E.; Robb, M. A.; Cheeseman, J. R.; Scalmani, G.; Barone, V.; Mennucci, B.; Petersson, G. A.; Nakatsuji, H.; Caricato, M.; Li, X.; Hratchian, H. P.; Izmaylov, A. F.; Bloino, J.; Zheng, G.; Sonnenberg, J. L.; Hada, M.; Ehara, M.; Toyota, K.; Fukuda, R.; Hasegawa, J.; Ishida, M.; Nakajima, T.; Honda, Y.; Kitao, O.; Nakai, H.; Vreven, T.; Montgomery, J. A., Jr.; Peralta, J. E.; Ogliaro, F.; Bearpark, M.; Heyd, J. J.; Brothers, E.; Kudin, K. N.; Staroverov, V. N.; Kobayashi, R.; Normand, J.; Raghavachari, K.; Rendell, A.; Burant, J. C.; Iyengar, S. S.; Tomasi, J.; Cossi, M.; Rega, N.; Millam, J. M.; Klene, M.; Knox, J. E.; Cross, J. B.; Bakken, V.; Adamo, C.; Jaramillo, J.; Gomperts, R.; Stratmann, R. E.; Yazyev, O.; Austin, A. J.; Cammi, R.; Pomelli, C.; Ochterski, J. W.; Martin, R. L.; Morokuma, K.; Zakrzewski, V. G.; Voth, G. A.; Salvador, P.; Dannenberg, J. J.; Dapprich, S.; Daniels, A. D.; Farkas, Ö.; Foresman, J. B.; Ortiz, J. V.; Cioslowski, J.; Fox, D. J. Gaussian, Inc., Wallingford CT, 2009. .
- (23) Watkins, M. A.; Price, J. M.; Winger, B. E.; Kenttämää, H. I. Ion-Molecule Reactions for Mass Spectrometric Identification of Functional Groups in Protonated Oxygen-Containing Monofunctional Compounds. *Anal. Chem.* **2004**, *76* (4), 964–976.

- (24) Tian, Z.; Kass, S. R. Does Electrospray Ionization Produce Gas-Phase or Liquid-Phase Structures? *J. Am. Chem. Soc.* **2008**, *130* (33), 10842–10843.
- (25) Tian, Z.; Pawlow, A.; Poutsma, J. C.; Kass, S. R. Are Carboxyl Groups the Most Acidic Sites in Amino Acids? Gas-Phase Acidity, H/D Exchange Experiments, and Computations on Cysteine and Its Conjugate Base. *J. Am. Chem. Soc.* **2007**, *129* (17), 5403–5407.
- (26) Campbell, J. L.; Le Blanc, J. C. Y.; Schneider, B. B. Probing Electrospray Ionization Dynamics Using Differential Mobility Spectrometry: The Curious Case of 4-Aminobenzoic Acid. *Anal. Chem.* **2012**, *84* (18), 7857–7864.
- (27) Chang, T. M.; Prell, J. S.; Warrick, E. R.; Williams, E. R. Where's the Charge? Protonation Sites in Gaseous Ions Change with Hydration. *J. Am. Chem. Soc.* **2012**, *134* (38), 15805–15813.
- (28) Woo, H.-K.; Lau, K.-C.; Wang, X.-B.; Wang, L.-S. Observation of Cysteine Thiolate and  $-S \cdots H-O$  Intermolecular Hydrogen Bond. *J. Phys. Chem. A* **2006**, *110* (46), 12603–12606.
- (29) Tian, Z.; Kass, S. R. Gas-Phase versus Liquid-Phase Structures by Electrospray Ionization Mass Spectrometry. *Angew. Chem. Int. Ed.* **2009**, *48* (7), 1321–1323.
- (30) Lalli, P. M.; Iglesias, B. A.; Toma, H. E.; Sa, G. F.; Daroda, R. J.; Silva Filho, J. C.; Szulejko, J. E.; Araki, K.; Eberlin, M. N. Protomers: Formation, Separation and Characterization via Travelling Wave Ion Mobility Mass Spectrometry: Protomers: Separation by TWIM and Characterization by Post-TWIM CID. *J. Mass Spectrom.* **2012**, *47* (6), 712–719.

## CHAPTER 4. MOLECULAR PROFILING OF CRUDE OIL BY USING DISTILLATION PRECIPITATION FRACTIONATION MASS SPECTROMETRY (DPF-MS)

### 4.1 Introduction

The light oil deposits of the world are depleting, which has generated a need to better understand the chemical composition of crude oil of different origins. For example, this information would enable producers to more accurately predict the possible interactions between oil, surfactants, and reservoir rock, and thereby predict the efficiency and economic feasibility of oil recovery.<sup>1-3</sup> Further, the ability to obtain an accurate estimate of the average molecular weight of crude oil would facilitate the optimization of refinery processes.<sup>4</sup> This is especially important for conversion of crude oil via reactions such as alkylation, dimerization, cracking, and hydrotreating, since access to an accurate average molecular weight would enable a better estimation of the amount of reagent required for the conversion.<sup>4</sup>

The challenge of analyzing crude oil is that it is a complex mixture, predicted to contain as many or more compounds than the number of genes in the human genome.<sup>5</sup> To study such complex mixtures, powerful high-resolution mass spectrometers, such as Fourier transform ion cyclotron resonance or orbitrap mass spectrometers, are desirable.<sup>6,7</sup> These high-resolution instruments can be used to determine the elemental compositions of ionized crude oil components, which facilitates sorting them into different compound classes, such as heteroatom classes (containing oxygen, nitrogen and/or sulfur) or compound types (*e.g.*, with varying degrees of unsaturation or aromaticity). While the information provided by these techniques is invaluable, problems associated with the ionization methods employed include inefficient ionization, competition for ionization, and matrix effects, all of which may reduce sensitivity toward or even entirely prevent

the detection of some components of crude oil. Indeed, most of these studies have employed atmospheric pressure chemical ionization (APCI) for nonpolar analytes,<sup>8</sup> atmospheric pressure photoionization (APPI) for aromatic analytes<sup>7,9</sup> and electrospray ionization (ESI) for polar analytes<sup>10,11</sup>. Unfortunately, all these methods selectively ionize only some of the crude oil components.

Above problems of competition for ionization and matrix effects are reduced when the mass analysis is preceded by a chromatographic separation.<sup>12-14</sup> Chromatography reduces the complexity of the mixture by separating it into fractions, but it does not necessarily eliminate issues with differing ionization efficiencies of the mixture components.

In this paper, a new separation and characterization method for crude oil is introduced, titled Distillation Precipitation Fractionation Mass Spectrometry (DPF MS). DPF MS involves separation of the crude oil into several fractions that contain compounds with similar chemical characteristics, followed by molecular level characterization of each fraction by using an optimized mass spectrometric method. The novelty of this method lies in the optimization of the ionization and mass spectrometry method separately for each fraction by using representative model compounds so that all compounds in each fraction are ionized at approximately the same efficiency to yield stable ionized molecules, which makes the DPF-MS method semi-quantitative. Following the weighing and analysis of each fraction, consideration of mass balance facilitated the molecular profiling of the fractionated crude oil.

## 4.2 Experimental Section

### 4.2.1 Sample

Freshly collected crude oil from an Illinois oil basin was provided by the Pioneer Oil Company (Illinois). The crude oil was collected and stored in amber colored glass bottles to prevent oxidation, and the container was tightly sealed with a screw cap to prevent loss of volatile compounds. The viscosity and density of the crude oil (at 20 °C) were measured to be 12.28 cP and 0.87 gm/cc, respectively.

### 4.2.2 Chemicals and Materials

HPLC grade n-hexane (C<sub>6</sub>H<sub>14</sub>), dichloromethane (CH<sub>2</sub>Cl<sub>2</sub>) and isopropanol (i-C<sub>3</sub>H<sub>7</sub>OH) were used as eluents in flash chromatography. Normal-Phase silica (40 g) auto column was purchased from Teledyne Isco, Inc. A total of 23 model compounds were used in this study. Table 4.1 in the gives details of the model compounds used and their purities.

Table 4.1 List of chemicals, their purities, and their suppliers.

Chemicals	Supplier	Purity
1-Methylfluorene	Sigma-Aldrich	98.0%
3-Butylpyridine	Sigma-Aldrich	98.0%
5-Nonanone	Sigma-Aldrich	98.0%
n-Butylamine	Sigma-Aldrich	99.5%
Carbazole	Sigma-Aldrich	95.0%
Cycloheptane	Aldrich	98.00%
1-Decene	Sigma-Aldrich	> 95.0%
n-Decylbenzene	Sigma-Aldrich	> 97.0% (GC)
Dibenzofuran	Aldrich	98.0%
Dibenzothiophene	Sigma-Aldrich	98.0%
n-Dodecylbenzene	Sigma-Aldrich	> 97.0% (GC)
n-Heptadecyl-benzene	Sigma-Aldrich	> 97.0% (GC)
n-Hexylamine	Sigma-Aldrich	99.0%



Table 4.1, continued

Chemicals	Supplier	Purity
n-Hexylbenzene	Aldrich	97.0%
1-Hexyne	Aldrich	97.0%
Isopropyl sulfide	Sigma-Aldrich	99.0%
Methylcyclopentane	Aldrich	97.0%
1-Pentadecane	Aldrich	> 98.0%
1-Phenyldodecane	Aldrich	97.0%
3-Ethylcarbazole	Aldrich	97.0%
5- $\alpha$ -Cholestane	Sigma	$\geq$ 97.0%
Squalane	Aldrich	99.0%
Pentatriacontane	Sigma-Aldrich	$\geq$ 98.0% (GC)

#### 4.2.3 Separation of Crude Oil into Fractions

Crude oil was separated into six fractions by using different techniques. As a first step, the most volatile compounds in the crude oil were separated by vacuum distillation at room temperature to yield fraction I (distillate) to avoid their loss during fractionation. The remaining residue was separated into asphaltenes (fraction II) and maltenes (all remaining fractions) through precipitation of the asphaltenes by using hexane as reported in the literature.<sup>15</sup> Maltenes were further chromatographically separated into three fractions ( $C_6H_{14}$ -eluted fractions III and IV combined,  $CH_2Cl_2$ -eluted fraction V, and  $i-C_3H_7OH$ -eluted fraction VI) on an auto column (Combi-flash Rf 200 from Teledyne Isco, Inc.) by using hexane ( $C_6H_{14}$ ), dichloromethane ( $CH_2Cl_2$ ) and isopropanol ( $i-C_3H_7OH$ ) as eluents. The  $C_6H_{14}$ -eluted fractions were further separated into fractions III and IV by using a solid phase extraction technique reported in the literature.<sup>16,17</sup> Further details of each separation step are provided in Table 4.2. All the fractions were weighted gravimetrically to obtain mass balance and recovery.

Table 4.2 Parameters optimized for the chromatographic fractionation and detection of maltenes by using a Combi-flash Rf 200 liquid chromatograph with photodiode array (PDA) detector and external evaporative light scattering (ELSD) detector.

<b>Parameters</b>	
<b>Redisep Column</b>	Silica 40 g
<b>Run Length</b>	15.0 min
<b>Loading Type</b>	Solid
<b>Detection 1</b>	$\lambda$ 1 (254 nm)
<b>Slope-Based Peak Width</b>	1 min
<b>Detection 1</b>	$\lambda$ 1 (280 nm)
<b>Slope-Based Peak Width</b>	1 min
<b>External Detector</b>	ELSD 340 CF
<b>Slope-Based Peak Width</b>	1 min
<b>Threshold</b>	0.05
<b>Spray Chamber (SC)</b>	45 °C
<b>Drift Tube (DT)</b>	55 °C
<b>Gain (Gx)</b>	PREP (5V)
<b>Flow Rate</b>	50 mL/min
<b>Equilibrium Volume</b>	Five column volumes
<b>Rack A</b>	18 mm x 150 mm tubes
<b>Collection Method</b>	Peaks only
<b>Peak Tube Volume</b>	Maximum
<b>Solvent A1</b>	n-Hexane
<b>Solvent B1</b>	Dichloromethane
<b>Solvent A2</b>	Isopropanol

### 4.3 Mass Spectrometry

#### 4.3.1 GCxGC/TOF Mass Spectrometry

A LECO Pegasus 4D GCxGC/TOF instrument equipped with an Agilent 7890B gas chromatograph (Agilent Technologies, Santa Clara, CA) and a high-resolution time-of-flight (TOF) mass spectrometer (up to 50,000 resolution) was used for the analysis of the volatile compounds (fraction I) in crude oil. Two columns (Rxi-17sil ms (intermediate polarity), 60 m and Rxi-1 ms (nonpolar), 4 m) were connected in series by using a modulator that enhances the peak capacity

available for the chromatographic system. After separation of the compounds, positive ion mode electron ionization (EI) (70 eV) was used to ionize the compounds upon entrance into the mass spectrometer. The EI mass spectra measured for unknown compounds were compared to extensive EI mass spectral libraries for identification (NIST libraries). This analysis yielded a list of identified compounds, their gas chromatographic peak areas and two retention times, their chemical formulas and chemical classes, and the accurate m/z values for the ionized analytes. Experimental conditions are detailed in Table 4.3.

Table 4.3 Optimal conditions used for the analysis of the distillate fraction (I) of crude oil by GC/GC/(EI)TOF.

<b>Detector</b>	LECO Pegasus 4D Time-of-Flight Mass Spectrometer operated in EI mode (70 eV)
<b>Acquisition rate</b>	100 spectra/s
<b>Acquisition Delay</b>	3 min
<b>Transfer Line Temperature</b>	300
<b>Source Temp</b>	220
<b>Column 1</b>	Rxi-17sil ms, 60 m x 0.25 mm ID, 0.25 $\mu$ m film thickness
<b>Column 2</b>	Rxi-1ms, 4 m x 0.25 mm ID, 0.25 $\mu$ m film thickness
<b>Column 1 Oven</b>	40 °C for 0.2 min, to 100 °C at 6 °C/min
<b>Column 2 Oven</b>	10 °C for 0.2 min, to 110 °C at 6 °C/min
<b>Modulation period</b>	8 s
<b>Modulator Temp Offset</b>	90°C (relative to the secondary Oven)
<b>Inlet</b>	Split (300:1) at 220 °C
<b>Injection</b>	0.1 $\mu$ L
<b>Carrier gas</b>	Helium, 1 mL/min
<b>Data processing</b>	
<b>S/N</b>	200
<b>Mass for Area calculation</b>	dt
<b>Spectral Match</b>	Peaks with a similarity index of 70% or more were assigned identities based on the mass spectral libraries

Additionally, GCxGC/(EI)TOF was used to optimize the solid phase extraction parameters for optimal separation of the C<sub>6</sub>H<sub>14</sub>-eluted fraction III from IV. The efficiency of solid phase extraction was evaluated by monitoring the percentage of coelution or carryover of different chemical classes of compounds into the separated fractions. Experimental conditions are detailed in Table 4.4.

Table 4.4 Optimal conditions and columns used for analysis of hexane eluted compounds before and after solid phase extraction.

<b>Detector</b>	LECO Pegasus 4D Time-of-Flight Mass Spectrometer operated in EI mode (70 eV)
<b>Acquisition rate</b>	100 spectra/s
<b>Acquisition Delay</b>	3 min
<b>Transfer Line Temperature</b>	300
<b>Source Temp</b>	260
<b>Column 1</b>	Rxi-5sil ms, 30 m x 0.25 mm ID, 0.25 µm film thickness
<b>Column 2</b>	Rxi-17sil ms, 1 m x 0.25 mm ID, 0.25 µm film thickness
<b>Column 1 Oven</b>	30 °C for 0.4 min, to 140 °C at 4 °C/min
<b>Column 2 Oven</b>	50 °C for 0.2 min, to 160 °C at 6 °C/min
<b>Modulation period</b>	6 s
<b>Modulator Temp Offset</b>	15°C (relative to the secondary Oven)
<b>Inlet</b>	Split (300:1) at 220 °C
<b>Injection</b>	0.1 µL
<b>Detector Voltage</b>	1800 Volts
<b>Carrier gas</b>	Helium, 1 mL/min

#### 4.3.2 LQIT Orbitrap XL Mass Spectrometry

All fractions (excluding the distillates fraction) were characterized using direct infusion positive ion mode atmospheric pressure chemical ionization (APCI) combined with high-resolution mass spectrometry. A linear quadrupole ion trap (LQIT) coupled with an orbitrap, LTQ Orbitrap XL mass spectrometer (Thermo Fischer Scientific, San Jose, CA), with a maximum resolution of 100,000 (at  $m/z$  400) was used for the analysis. The optimized ionization methods, including solvents and ionization reagents, tube lens voltages, types of the sheath and auxiliary gases, and temperatures, chosen for the analysis of the different fractions are shown in Table 4.5.

Table 4.5 Ionization methods and optimal ion source parameters for direct injection high-resolution mass spectral analysis of crude oil fractions.

	<b>Fraction II (asphaltenes)</b>	<b>Fraction III (saturated hydrocarbons)</b>	<b>Fraction IV (aromatic hydrocarbons)</b>	<b>Fraction V (heteroaromatic compounds)</b>	<b>Fraction VI (polar compounds)</b>
<b>Ionization Method and Mode</b>	(+)APCI	(+)APCI	(+)APCI	(+)APCI	(+)APCI
<b>Solvents</b>	Carbon disulfide	n-Hexane	Carbon disulfide	Carbon disulfide	n-Hexane, methanol (25:75)
<b>Type of Ions Produced Upon Ionization</b>	M <sup>+•</sup>	[M-H] <sup>+</sup>	+•	+•	[M+H] <sup>+</sup>
<b>Sample Concentration (mg mL<sup>-1</sup>)</b>	1	1	0.5	0.5	1
<b>Flow Rate (μL min<sup>-1</sup>)</b>	5	10 M	3	3	1
<b>Sheath and Auxillary Nebulization Gas</b>	N <sub>2</sub>	2	2 M	2	2
<b>Vaporizer Temperature (°C)</b>	400	150	300	300	300
<b>Sheath Gas Flow Rate (AU)<sup>a</sup></b>	40	60	20	20	40
<b>Auxillary Gas Flow Rate (AU)<sup>a</sup></b>	20	30	10	10	20
<b>Capillary Temperature (°C)</b>	350	50 N	275 <sub>N</sub>	275 <sub>N</sub>	275
<b>Discharge Current (mA)</b>	4.7 O	4.5	4.5	4.5	4.5
<b>Capillary Voltage (V)</b>	35	10	25	25	30
<b>Tube Lens Voltage (V)</b>	50	20	50	50	50

<sup>a</sup> AU = Arbitrary units

### 4.3.3 Ionization Methods

Positive ion mode atmospheric pressure ionization methods using different nebulizing gases and solvents, such as APCI/N<sub>2</sub>/CS<sub>2</sub>, APPI/N<sub>2</sub>/CS<sub>2</sub>, APCI/O<sub>2</sub>/n-hexane, APCI/N<sub>2</sub>/n-hexane, APCI/N<sub>2</sub>/n-hexane and methanol, APCI/N<sub>2</sub>/toluene, APCI/N<sub>2</sub>/methanol, and ESI/N<sub>2</sub>/methanol, were tested for specific fractions (II, III, IV, V and VI). Three different APCI techniques were identified to be most effective for these five fractions. APCI/N<sub>2</sub>/CS<sub>2</sub> was selected for the analysis of fractions II, IV, and V, APCI/O<sub>2</sub>/n-hexane for fraction III, and APCI/N<sub>2</sub>/n-hexane and methanol for fraction VI. The optimized parameters used for the ionization of compounds in these fractions are summarized in Table 4.5.

Xcaliber version 2.2 (Thermo Fischer Scientific, Inc, San Jose, CA) was used for data acquisition and analysis. The normalized peak height threshold for peak picking was 5%. After peak picking, elemental formulas were assigned based on accurately measured m/z values that were within 3 ppm from the theoretical value (accepted mass accuracy with external calibration). Elements used for formula assignments were carbon, hydrogen, nitrogen, oxygen and sulfur. While no limits were placed on the number of carbons and hydrogens used for the elemental composition assignment, limits of 4 nitrogen, 5 oxygen, and 5 sulfur atoms were used. The degree of unsaturation, also known as ring and double bond (RDB) equivalence, represents the number of rings plus the number of double bonds in a molecule. This value was calculated based on the assigned elemental composition by using Equation 4.1. Data sorting for plotting the graphs and heteroatom classification was performed using Excel. RDB equivalence versus carbon number plots and heteroatom distribution plots were prepared by using OriginPro (version 93E).

#### 4.3.4 Data Processing of High-Resolution Mass Spectral Data

Xcaliber version 2.2 (Thermo Fischer Scientific, Inc, San Jose, CA) was used for data acquisition and analysis. The normalized peak height threshold for peak picking was 5%. After peak picking, elemental formulas were assigned based on accurately measured m/z values that were within 3 ppm from the theoretical value (accepted mass accuracy with external calibration). Elements used for formula assignments were carbon, hydrogen, nitrogen, oxygen and sulfur. While no limits were placed on the number of carbons and hydrogens used for the elemental composition assignment, limits of 4 nitrogen, 5 oxygen, and 5 sulfur atoms were used. Data sorting for plotting the graphs and heteroatom classification was performed using Excel. RDB equivalence versus carbon number plots and heteroatom distribution plots were prepared by using OriginPro (version 93E). Different equations used during for data processing and analysis such as average molecular weight determination, RDB equivalence are provided below.

The degree of unsaturation, also known as a ring and double bond (RDB) equivalence, represents the number of rings plus the number of double bonds in a molecule. Ring and double bond (RDB) equivalence were calculated for ions with elemental formulas  $C_cH_hN_nO_oS_s$  as shown below in Equation (4.1) below.

$$\text{RDB equivalence} = c - \frac{h}{2} + \frac{n}{2} + 1 \quad (4.1)$$

The experimental average molecular weight of the distillate (fraction I) analyzed by using GCxGC/(+)EI TOF was determined using Equation (4.2). (Expected ion m/z based on spectral library matches were used for the AVG MW determination in this equation).

$$\text{AVG MW experimental} = \frac{\sum(\text{Ion m/z} \times \text{GC peak area})}{\sum \text{GC peak area}} \quad (4.2)$$



The experimental average molecular weight of fractions analyzed by (+)APCI/N<sub>2</sub> /CS<sub>2</sub> LQIT-orbitrap was determined using Equation (4.3). (Molecular ion m/z were used for the MW determination in this equation)

$$\text{AVG MW experimental} = \frac{\sum(\text{Ion m/z} \times \text{Abundance})}{\sum \text{Abundance}} \quad (4.3)$$

The experimental average molecular weight of samples analyzed by (+)APCI/O<sub>2</sub> /hexane LQIT-orbitrap was determined using Equation (4.4). [M-H]<sup>+</sup> ions were generated and therefore, (ion m/z+1) was used in this equation.

$$\text{Avg MW experimental} = \frac{\sum((\text{Ion m/z} + 1) \times \text{Abundance})}{\sum \text{Abundance}} \quad (4.4)$$

The experimental average molecular weight of samples analyzed by (+)APCI/N<sub>2</sub>/hexane, methanol LQIT-orbitrap MS was determined using Equation (4.5). [M+H]<sup>+</sup> ions are generated and therefore, (ion m/z-1) was used in this equation.

$$\text{Avg MW experimental} = \frac{\sum((\text{Ion m/z} - 1) \times \text{Abundance})}{\sum \text{Abundance}} \quad (4.5)$$

The average molecular weight of fractionated crude oil can be obtained from the average molecular weights of individual fractions and their gravimetric weights by using below Equation (4.6).

$$\text{Avg MW of fractionated oil} = \frac{\sum(\text{Avg MW of individual fractions} \times \text{Gravimetric weight \%})}{\sum \text{Gravimetric weight \%}} \quad (4.6)$$

The percentage distribution of individual compound classes in whole crude oil was determined from the compound class data obtained from individual fractions and their gravimetric weights by using below Equation (4.7).

$$\% \text{ Compound class distribution in whole crude oil} = \frac{\sum((\text{distribution for individual fractions}) \times \text{weight \%})}{100} \quad (4.7)$$

The theoretical Avg MW for all model compound mixtures studied was calculated using below Equation (4.8).

$$\text{Avg MW theoretical} = \frac{\sum((\text{MW}) \times \text{Concentration})}{\sum \text{Concentration}} \quad (4.8)$$

#### 4.4 FTIR Analysis

FTIR measurements were performed on all the separated crude oil fractions with a Nicolet 6700 FTIR spectrometer (Thermo Scientific). The FTIR spectra were collected using a liquid N<sub>2</sub> cooled MCT (HgCdTe) detector. The scans involved wave numbers from 4000 up to 650 cm<sup>-1</sup> with a resolution of 2 cm<sup>-1</sup> and 64 scans co-added per sample. The spectrum of each fraction was corrected against the background spectrum obtained from the clean, dry cell. Attenuated total reflectance (ATR-FTIR) measurements were made using two different methods. For liquid fractions with sufficient volume of 0.5 mL, a 10-bounce horizontal ATR cell (Pike Technologies, Madison, WI) was used. The internal reflection element (IRE) used was a ZnSe crystal with dimensions of 73 mm by 7 mm and an angle of incidence of 45°. The total volume of the cell is 2 ml. For viscous fractions or semi-solid materials (*e.g.*, asphaltenes), a single bounce diamond ATR cell (GladiATR™ Pike Technologies) was used.

#### 4.5 Results and Discussion

In order to illustrate some of the problems associated with detection of all compounds in crude oil by mass spectrometry without prior separation, a simple equimolar mixture containing typical crude oil components, *i.e.*, two alkylaromatic compounds (n-decylbenzene, n-hexylbenzene), an alkane (pentadecane), two cycloalkanes (cycloheptane, methylcyclopentane), an alkene (1-decene) and an alkyne (1-hexyne), was analyzed by using APCI and APPI. This mixture cannot be ionized

using the traditional ESI, APCI and APPI solvent systems, water and/or methanol, as the hydrocarbons are not soluble in these solvents. CS<sub>2</sub> has been successfully used in the past as a solvent for APCI of hydrocarbon mixtures.<sup>8</sup> Therefore, the model compound mixture was dissolved in CS<sub>2</sub> and analyzed by using both APCI/N<sub>2</sub>/CS<sub>2</sub> (N<sub>2</sub> was used as the nebulizing gas) and APPI/N<sub>2</sub>/CS<sub>2</sub> ionization methods in an LQIT-orbitrap MS. Figure 4.1 shows the APCI/N<sub>2</sub>/CS<sub>2</sub> mass spectrum of the model mixture.

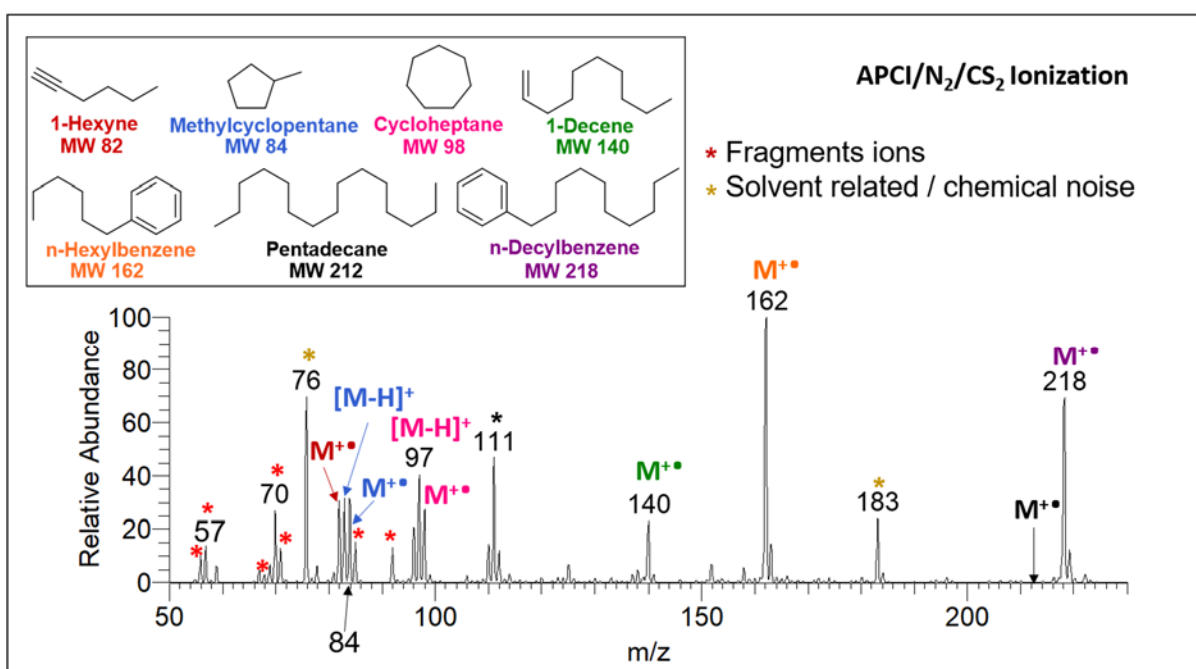


Figure 4.1 APCI/N<sub>2</sub>/CS<sub>2</sub> mass spectrum of an equimolar mixture (1 mM) of seven nonpolar model compounds measured using an injection flow rate of 5 μL/min. Linear alkane and alkene yielded several fragment ions, including those of m/z 57, 70, 71 and 85. Cycloalkanes generated molecular ions (M<sup>+•</sup>) as well as [M-H]<sup>+</sup> ions. Alkylaromatic compounds and the alkyne generated predominantly stable molecular ions.

Compounds in this mixture were also analyzed individually by using APCI/N<sub>2</sub>/CS<sub>2</sub> to identify the ions (fragment ions and intact molecular ions) produced by each individual compound. The

linear alkane fragmented completely upon ionization, generating fragment ions of  $m/z$  57, 71 and 85 and no visible molecular ions, which makes detection of this analyte challenging. The alkyne generated stable molecular ions as well as minor fragment ions of  $m/z$  67. The alkene also produced both stable molecular ions as well as fragment ions of  $m/z$  57 and 70. However, the fragmentation was extensive, with some fragment ions having an equal abundance as the molecular ions. The alkylaromatic compounds were observed to generate mostly stable molecular ions, with minimal fragmentation to form ions of  $m/z$  92. The cycloalkanes generated stable molecular ions, molecular ions that had lost a hydrogen atom and fragment ions of  $m/z$  56, which complicates data analysis. APPI/ $N_2/CS_2$  produced similar results (Figure 4.2).

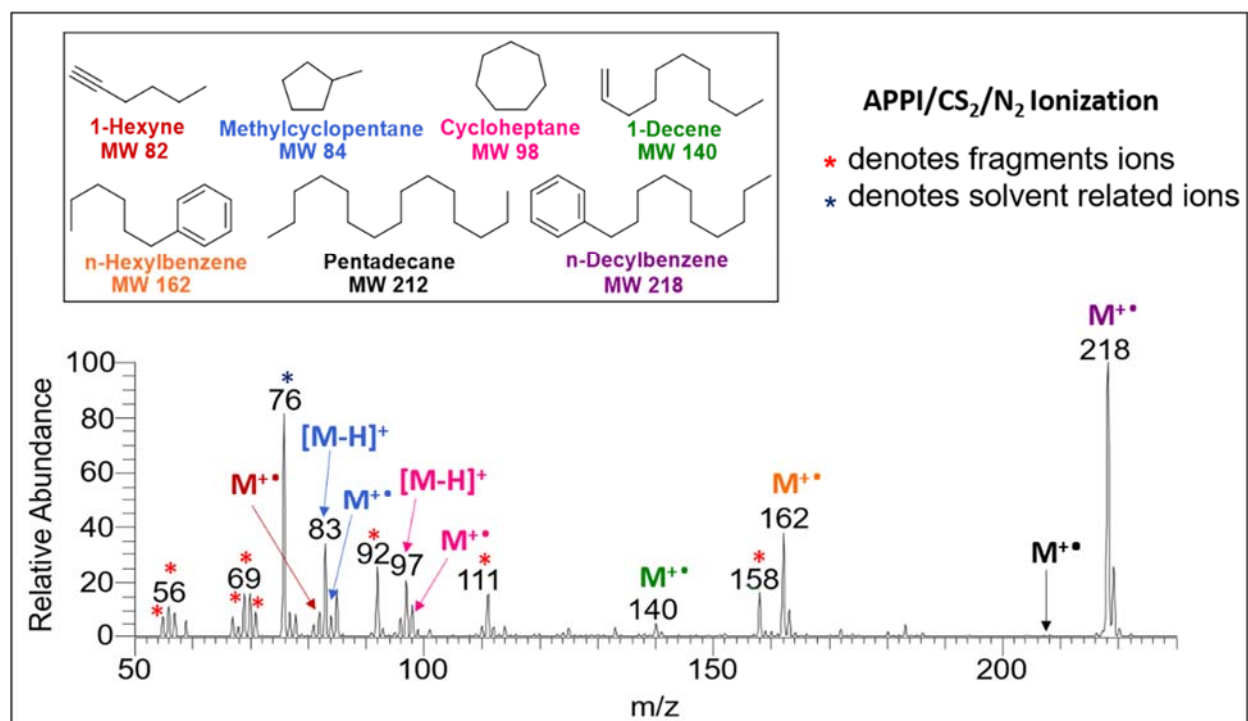


Figure 4.2 APPI/ $N_2/CS_2$  mass spectrum of an equimolar mixture comprising of seven model compounds obtained at an injection flow rate of 5  $\mu$ L/min and a tube lens voltage of 50 V.

In conclusion, the mass spectrum shows more fragment ions than molecular ions, and the molecular ions of different compounds have widely differing relative abundances. Some molecular ions fragment only to a small extent while others fragment extensively. One of the compounds did not produce stable molecular ions at all and hence cannot be easily detected in a mixture. Accurate characterization of the mixture based on these data is not possible. However, if this sample was first separated into different chemical classes, then an ideal ionization method could be selected and optimized for the mass spectrometric analysis of each fraction. This is the approach presented here for the analysis of crude oil.

The methods selected here for the separation of crude oil into six fractions are discussed first. Then, the bulk characterization of each fraction by using FTIR spectroscopy is detailed to determine the classes of compounds in each fraction. This information was used to select appropriate model compounds for each fraction that were then used to develop the optimal analysis method for each fraction.

#### 4.5.1 Separation of Crude Oil

Distillation, precipitation, auto column fractionation and solid phase extraction were used to separate the compounds in the crude oil into six fractions based on their differences in volatility, solubility, and polarity. A schematic for the complete separation process is presented in Figure 4.3.

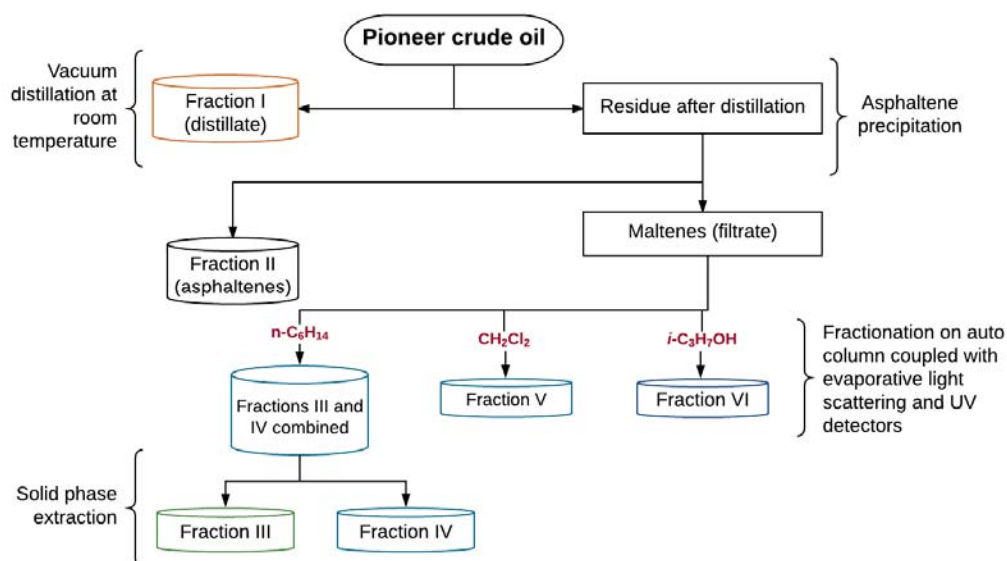


Figure 4.3 DPF scheme for separation of crude oil into six fractions I - VI.

As the first step, the most volatile compounds in the crude oil were separated by room-temperature vacuum distillation from the nonvolatile portion (residue) to generate fraction 1. The remaining residue was separated into asphaltenes (fraction II) and maltenes (all remaining fractions) through precipitation of the asphaltenes by using n-hexane as described in the literature.<sup>15</sup> Maltenes were chromatographically separated into three fractions (n-hexane-eluted fraction (corresponding to fractions III and IV) and fractions V and VI) based on their differences in polarity. This was accomplished by using an auto column coupled with evaporative light scattering (ELSD) and UV detectors and the solvents n-hexane ( $n\text{-C}_6\text{H}_{14}$ ), dichloromethane ( $\text{CH}_2\text{Cl}_2$ ) and isopropanol ( $i\text{-C}_3\text{H}_7\text{OH}$ ), used in this order. Figure 4.4 shows a typical auto column chromatogram of maltenes.

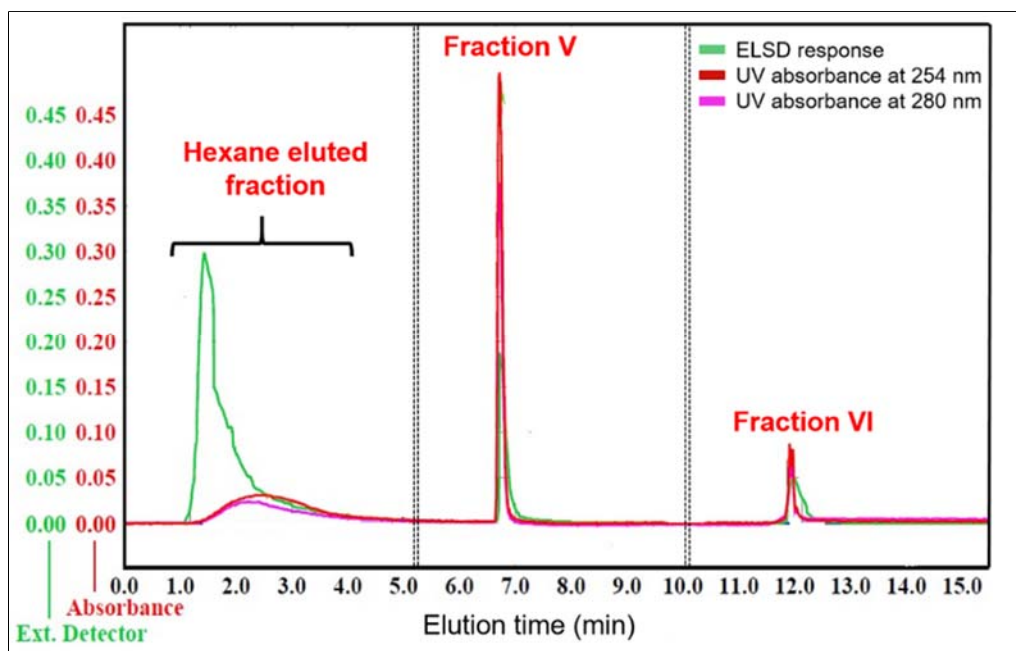


Figure 4.4 Auto column-ELSD/UV chromatogram of maltenes, indicating the separation of maltenes into three fractions. The presence of both ELSD and UV signals in the later eluting part of the n-hexane-eluted fraction indicates co-elution of aromatic compounds along with aliphatic compounds (no UV absorption).

The presence of both ELSD and UV signals in the later eluting part of the hexane-eluted fraction (Figure 4.4) indicated co-elution of two different analyte classes, aliphatic (no UV absorption) and aromatic hydrocarbons. To test this hypothesis, this fraction was analyzed using GCxGC/(EI)TOF MS. Indeed, based on the total ion current GC/GC chromatogram (Figure 4.5A), the n-C<sub>6</sub>H<sub>14</sub>-eluted fraction is a co-eluted mixture of heavy saturated (cyclic, linear and branched) and light aromatic hydrocarbons. Therefore, an additional separation step was necessary. The saturated and aromatic hydrocarbon classes in the n-hexane-eluted fraction were separated via solid phase extraction to produce fractions III (heavy saturated hydrocarbons) and IV (light aromatic hydrocarbons), thus bringing the total number of maltene fractions from three to four (the last two being fractions V and VI eluted by dichloromethane and isopropanol, respectively). The

success of the solid phase extraction was evaluated by using GCxGC/(EI)TOF MS to analyze fraction III (Figure 4.5B). This analysis revealed a small percentage (~9% based on GC peak areas) of aromatic hydrocarbon carryover into the saturated hydrocarbon fraction (III), which could not be avoided.



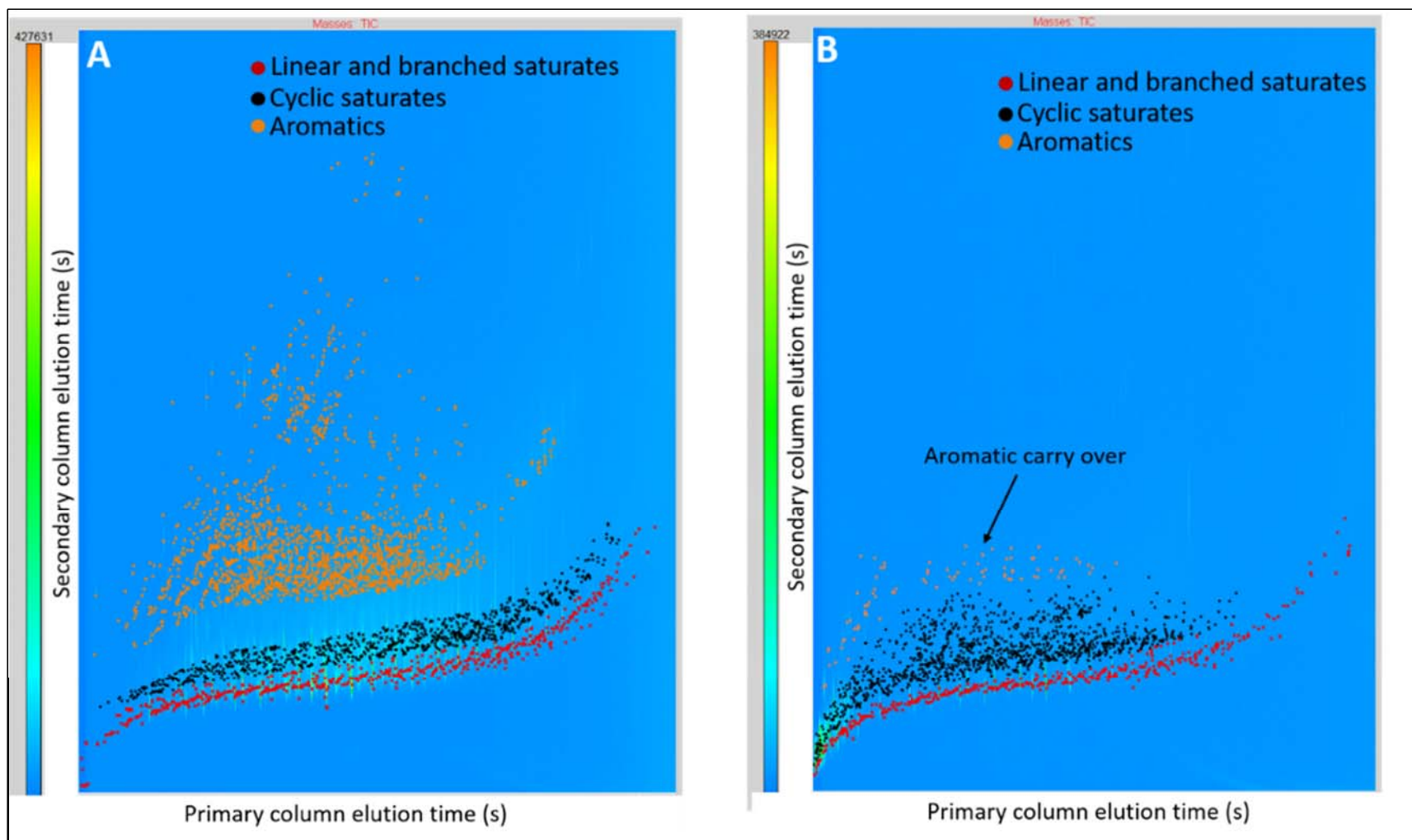


Figure 4.5 Total ion chromatogram measured using GCxGC/((+)EI)TOF for A) n-C<sub>6</sub>H<sub>14</sub>-eluted compounds (fractions III and IV), and B) heavy saturated compounds (fraction III) separated from n-C<sub>6</sub>H<sub>14</sub>-eluted compounds by using solid phase extraction. Linear and branched saturated, aromatic and cyclic saturated compounds are color coded. A small percentage (8%) of carryover of aromatic compounds into the heavy saturated compounds was observed even after solid phase extraction.

After the separation of the crude oil into six fractions, each fraction was gravimetrically weighted. The gravimetric weight percentages of the fractions I, II, III, IV, V and VI are 8%, 1%, 44%, 21%, 9% and 8%, respectively (Table 4.6). The separation method can achieve about 92% sample recovery. Before high-resolution mass spectral analysis of the individual fractions, they were studied by using FTIR spectroscopy to determine the bulk chemical nature of each individual fraction, such as polarity and the extent of aromaticity.

Table 4.6 Gravimetric weight percent distribution of crude oil fractions obtained using DPF separation method.

	<b>Trial 1</b> <b>(%)</b>	<b>Trial 2</b> <b>(%)</b>	<b>Trial 3</b> <b>(%)</b>	<b>Average</b> <b>(%)</b>	<b>Standard deviation</b>
<b>Fraction I</b>	8.6	7.2	8.2	8.0	± 0.7
<b>Fraction II</b>	1.1	1.7	0.9	1.2	± 0.4
<b>Fraction III</b>	42.7	46.3	43.9	44.3	± 1.8
<b>Fraction IV</b>	23.0	18.9	21.7	21.2	± 2.1
<b>Fraction V</b>	9.3	10.2	8.5	9.3	± 0.9
<b>Fraction VI</b>	6.7	8.3	8.7	7.9	± 1.1
<b>Total Recovery</b>	91.4	92.6	91.9	92.0	

It should be noted here that minor amounts of polymers and surfactants, if present in the crude oil due to contamination, eluted from the auto column when a fourth solvent, methanol, was used after isopropanol elution. Analysis of this fraction using (+)ESI allowed for the ionization and detection of these contaminants (Figure 4.6A). ESI mass spectrum of methanol eluted fraction obtained from pristine crude oil did not show these compounds (Figure 4.6B).

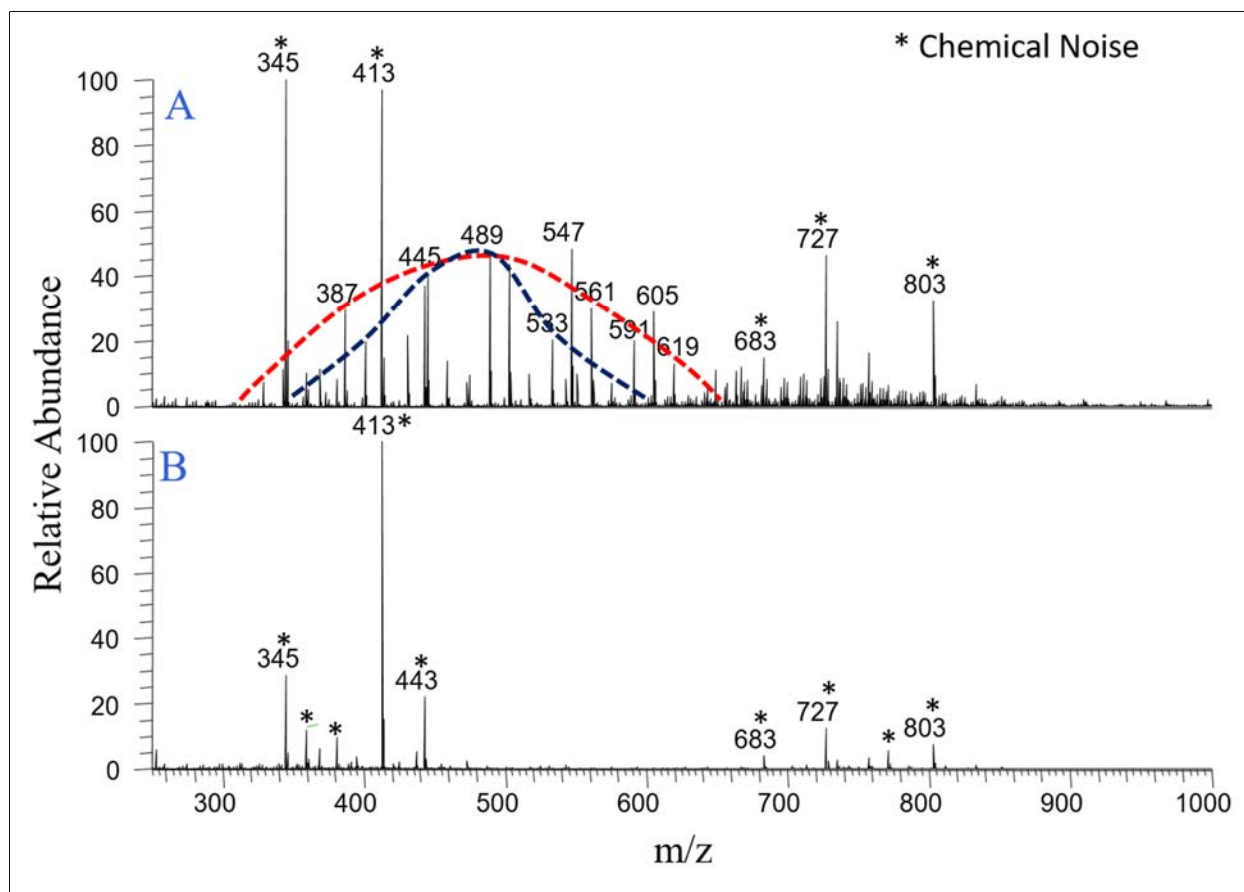


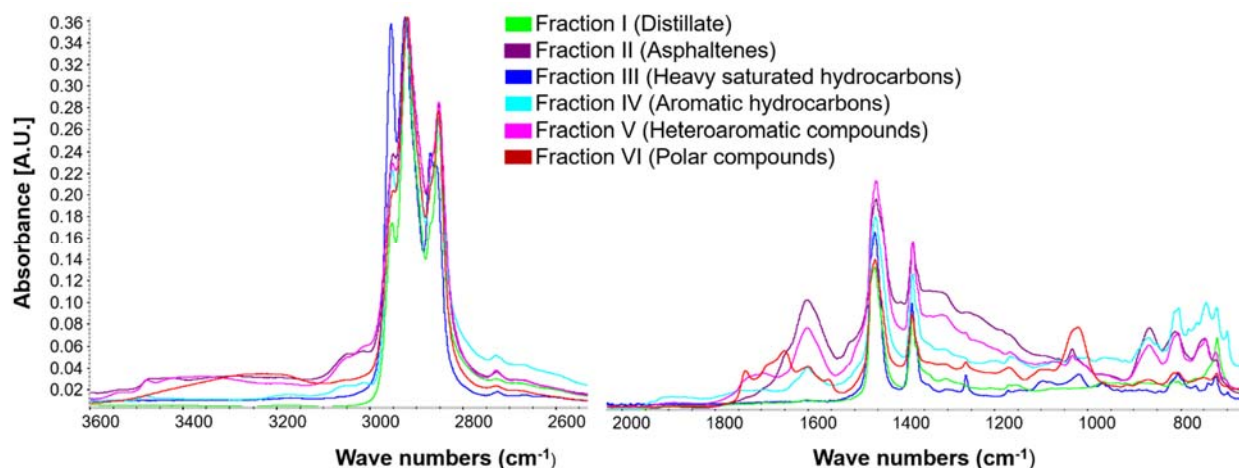
Figure 4.6 A) (+) ESI mass spectrum of methanol eluted fraction of maltenes indicating the presence of polymers in a contaminated crude oil sample. The red dotted line indicates polypropoxylates (repeating unit 58 Da) and the blue dotted line indicates polyethoxylates (repeating unit 44 Da). B) (+) ESI mass spectrum of methanol eluted fraction of a pristine non-contaminated crude oil. This mass spectrum indicates that no compounds other than contaminants eluted upon methanol elution.

#### 4.5.2 Characterization of Individual Fractions by FTIR Spectroscopy

All the FTIR band absorptions and the corresponding functional groups are summarized in Table 4.7. FTIR spectra measured from wave numbers 3600 up to 2200  $\text{cm}^{-1}$  and from 2000 up to 600  $\text{cm}^{-1}$  for all crude oil fractions are given in Figure 4.7.

Table 4.7 FTIR absorption bands and their functional group assignments.

Functional group	Absorption band (cm <sup>-1</sup> )
=C-H aromatic stretch	3020-3100
CH <sub>3</sub> asymmetric and symmetric stretch	2950 and 2872
CH <sub>2</sub> asymmetric and symmetric stretch	2920 and 2830
C=O stretch	1700
NH <sub>2</sub> bending vibrations	1650-1550
C=C stretch	1600
CH <sub>3</sub> or CH <sub>2</sub> deformations	1460
CH <sub>3</sub> deformation	1380
C-O stretch	970-1250
Aromatic C-H deformation (“oop” bands)	900-730

Figure 4.7 FTIR spectra from 3600-2600 cm<sup>-1</sup> and 2000-600 cm<sup>-1</sup> measured for the crude oil fractions.

The strong bands at 2952, 2921, and 2852 cm<sup>-1</sup> correspond to CH<sub>3</sub> and CH<sub>2</sub> aliphatic stretching vibrations and the absorption bands at 1456 and 1376 cm<sup>-1</sup> correspond to CH<sub>3</sub> and CH<sub>2</sub> aliphatic bending vibrations (deformation bands). These absorptions were seen for all the fractions. The ratio between the intensities of some characteristic absorption bands can be used to investigate the bulk characteristic of the fractions. For example, the ratio between the intensities of the -CH<sub>3</sub> (2952

$\text{cm}^{-1}$ ) and  $-\text{CH}_2$  ( $2921 \text{ cm}^{-1}$ ) asymmetric vibration bands for fraction I (distillate) is close to one, which may indicate significant branching. The bands at  $3050 \text{ cm}^{-1}$  ( $=\text{C}-\text{H}$  aromatic stretching vibrations),  $1600 \text{ cm}^{-1}$  (aromatic  $\text{C}=\text{C}$  stretching vibrations) and the out-of-plane (oop)  $\text{C}-\text{H}$  deformation bands at  $900-730 \text{ cm}^{-1}$  (aromatic  $\text{C}-\text{H}$  in-plane and out-of-plane bending vibrations) are characteristic of an aromatic functionality. These bands were observed for fraction II (asphaltenes), fraction IV (aromatic compounds) and fraction V (heteroaromatic compounds). The extent of aromaticity in these fractions was evaluated by considering the ratio between the bands corresponding to aromatic  $\text{C}=\text{C}$  stretching ( $1600 \text{ cm}^{-1}$ ) and aliphatic  $\text{C}-\text{H}$  deformation ( $1460 \text{ cm}^{-1}$ ). The aromatic character is more pronounced in fraction II (asphaltenes), followed by fraction V (heteroaromatic compounds) and fraction IV (aromatic compounds). The fraction VI (polar compounds) showed little aromatic character. The  $\text{C}=\text{O}$  stretching band around  $1700 \text{ cm}^{-1}$  was seen for fraction II (asphaltenes) and fraction VI (polar compounds). The band around  $1030 \text{ cm}^{-1}$  can be assigned to  $\text{C}-\text{O}$  stretching vibrations of either ethers, alcohols or sulfoxides. While these bands were pronounced for fraction VI (polar compounds), only tiny bands corresponding to them were observed for fraction II (asphaltenes) and fraction V (heteroaromatic compounds) of crude oil. The band around  $1650-1550 \text{ cm}^{-1}$  that was seen only for fraction VI (polar compounds) corresponds to  $\text{NH}_2$  scissoring vibrations. To summarize, the spectra measured for fractions I and III indicated the presence of saturated compounds. Spectral analysis of asphaltenes (fraction II) and heteroaromatic compounds (fraction V) revealed the presence of heteroatoms and significant aromatic signatures and only differed in the extent of aromaticity. Analysis of polar compounds (fraction VI) indicated the presence of heteroatoms with minimal signs of aromaticity. Spectral analysis of aromatic hydrocarbons (fraction IV) showed aromatic signatures and the presence of alkyl chains.

To summarize, the spectra measured for the distillate (fraction I) and for the heavy saturated hydrocarbons (fraction III) indicated the predominant presence of saturated hydrocarbons in both fractions. Spectral analysis of the asphaltenes (fraction II) revealed the presence of heteroatoms and significant aromaticity, as expected. The spectrum measured for light aromatic hydrocarbons (fraction IV) indicated the presence of only alkyl aromatic compounds. The spectrum of dichloromethane eluted compounds (fraction V) revealed the presence of heteroatoms and significant aromaticity similar to asphaltenes (fraction II). This fraction is therefore referred to as heteroaromatic compounds from now on. The isopropanol-eluted compounds (fraction VI) were found to contain heteroatoms and have minimal aromaticity. This fraction will be referred to as polar compounds from now on. This bulk information obtained from the FTIR spectral analysis was used to select model compounds to represent the compound types present in the different fractions in order to identify or develop an optimal analysis method for each fraction.

#### 4.5.3 Identification of an Ionization Method for Each Individual Fraction

Based on the FTIR results, the distillate (fraction I) contains saturated hydrocarbons. As this fraction is volatile, compounds in it were separated and analyzed using GCxGC/electron ionization (EI) high-resolution time-of-flight (TOF) MS. EI is a universal ionization method (can ionize all organic compounds) and it provides library-searchable, highly reproducible mass spectra, which allowed for the identification of many of the compounds. The suitability of this method for the semi-quantitative analysis of volatile saturated hydrocarbons has been evaluated earlier by using model compound mixtures.<sup>18</sup> The most abundant compounds identified in this fraction are alkanes and cycloalkanes containing 7–10 carbons.

The remaining five nonvolatile fractions were analyzed using methods other than GCxGC/MS as this method can be used only for relatively volatile compounds. FTIR spectral analysis of

fractions II (asphaltenes), IV (light aromatic compounds) and V (heteroaromatic compounds) revealed the predominant presence of aromatic compounds. The APCI/N<sub>2</sub>/CS<sub>2</sub> method is well suited for the ionization of this type of compounds as it has been reported<sup>8</sup> to ionize different types of aromatic analytes at nearly equal efficiency via predominant formation of stable molecular ions without substantial fragmentation (see Figure 4.8). Therefore, compounds in the fractions II, IV and V were ionized by using this method. Other ionization methods, such as APCI/N<sub>2</sub>/toluene and APCI/N<sub>2</sub>/methanol, were also examined. However, they were found to be less successful than the APCI/N<sub>2</sub>/CS<sub>2</sub> ionization method (see Figure 4.8).

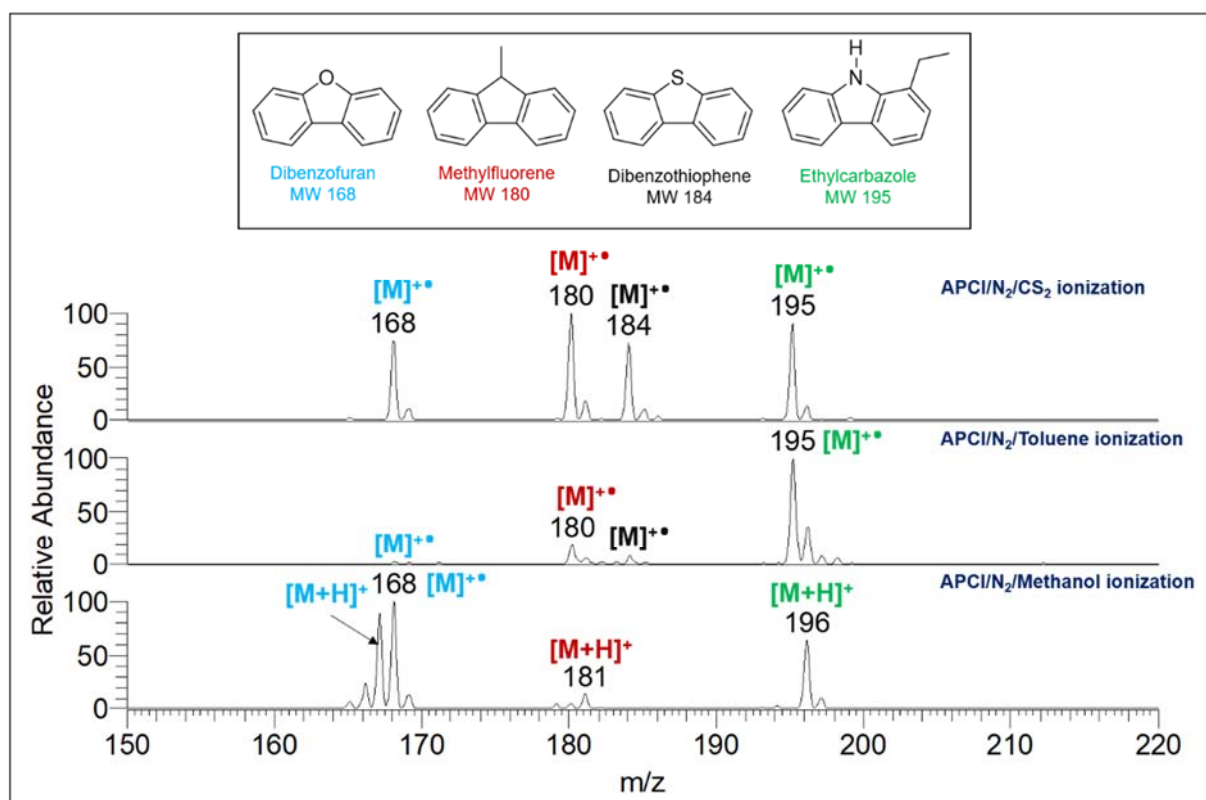


Figure 4.8 APCI/N<sub>2</sub>/CS<sub>2</sub>, APCI/N<sub>2</sub>/toluene and APCI/N<sub>2</sub>/methanol mass spectra of an equimolar mixture (1 mM) containing aromatic and heteroaromatic model compounds. While APCI/N<sub>2</sub>/CS<sub>2</sub> successfully ionized all the four model compounds in the model mixture at roughly equal efficiencies, the other two methods could not replicate the same.

Though APCI/N<sub>2</sub>/CS<sub>2</sub> method has been demonstrated to be successful in ionizing polyaromatic model compounds with long alkyl chains without substantial fragmentation,<sup>8</sup> ionization of monoaromatic model compounds with long alkyl chains (n-phenyldecane, n-phenyldodecane and n-heptadecylbenzene) was observed here to result in the formation of a fragment ion of m/z 92 (toluene radical cation) (see Figure 4.9). All three compounds studied generate this fragment ion.

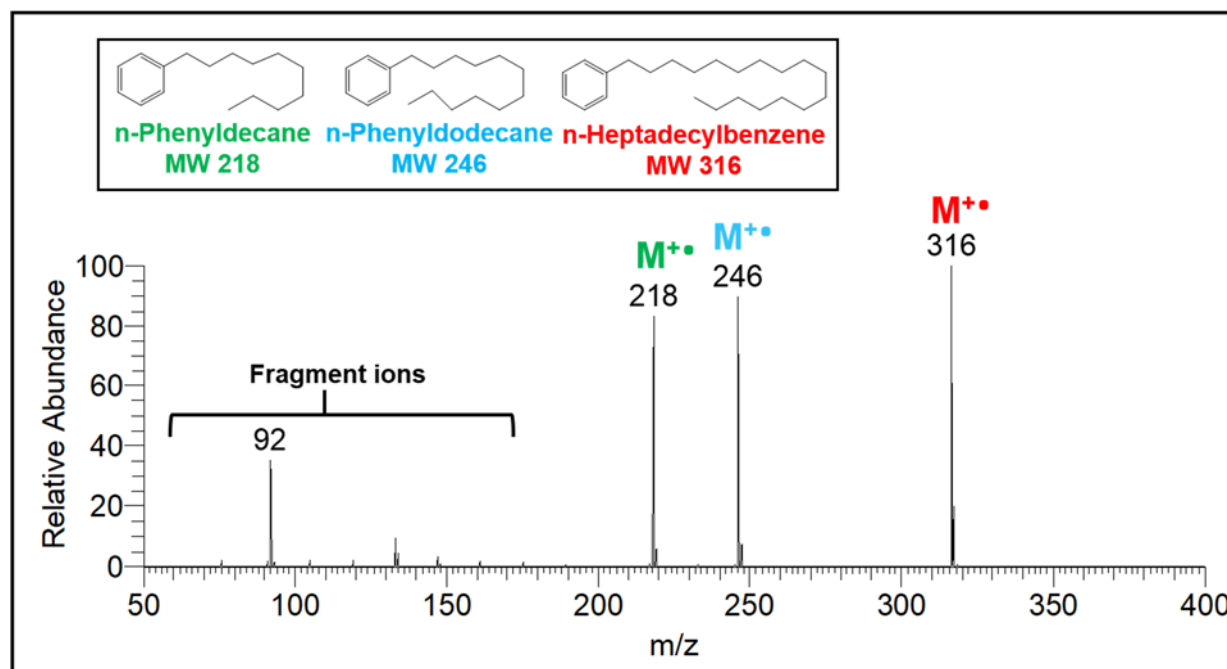


Figure 4.9 APCI/N<sub>2</sub>/CS<sub>2</sub> mass spectrum of an equimolar mixture of three aromatic compounds containing long alkyl chains.

The APCI/N<sub>2</sub>/CS<sub>2</sub> ionization method discussed above is inappropriate for the analysis of heavy saturated hydrocarbons (fraction III) based on a study of an equimolar mixture containing cholestane (a cyclic alkane), squalene (a branched alkane), and pentatriacontane (a linear alkane) (Figure 4.10B). This method generates stable molecular ions for the cyclic alkane but [M-H]<sup>+</sup> ions for the linear and branched alkanes. Also, the cyclic alkane is ionized at substantially greater



efficiency than the linear and branched alkanes. In addition, considerable fragmentation was observed (~22%) especially for linear and branched alkanes. Field ionization is a soft ionization method most commonly employed by the petroleum industry for the ionization of heavy saturated hydrocarbons.<sup>19</sup> However, this ionization method suffers from poor reproducibility.<sup>20</sup> Therefore, the heavy saturated hydrocarbons (fraction III) were instead ionized by using an alternative APCI method. APCI with oxygen as the nebulizer gas and n-hexane as the solvent (APCI/O<sub>2</sub>/n-hexane) has been reported<sup>20</sup> to produce comparable results to FI in ionizing large saturated hydrocarbons. Figure 4.10A shows that the APCI/O<sub>2</sub>/n-hexane method generates stable [M-H]<sup>+</sup> ions via hydride abstraction with minimal fragmentation (< 4-6 %) and with a similar ionization efficiency for cholestane, squalene, and pentatriacontane.

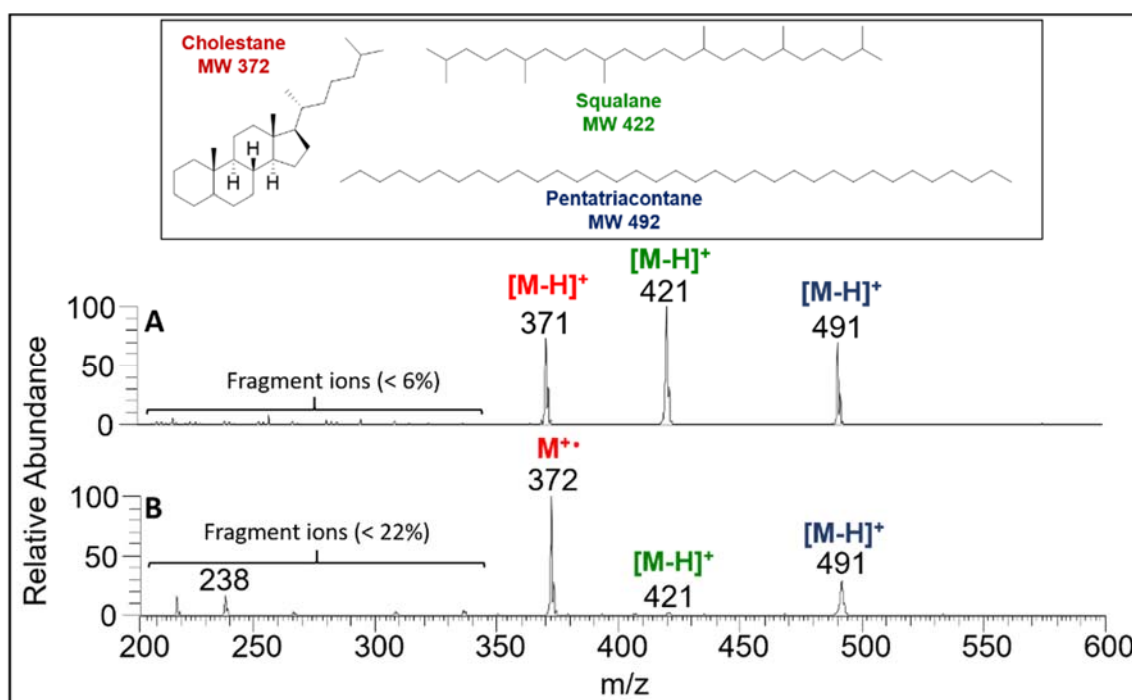


Figure 4.10 (A) APCI/O<sub>2</sub>/n-hexane mass spectrum measured at an injection flow rate of 5  $\mu\text{L min}^{-1}$  and tube lens voltage of 20 V and (B) APCI/N<sub>2</sub>/CS<sub>2</sub> mass spectrum measured at an injection flow rate of 5  $\mu\text{L min}^{-1}$  and tube lens voltage of 30 V for an equimolar mixture (1 mM) comprised of saturated hydrocarbon model compounds (no ions were observed below m/z 200).

Based on the FTIR results fraction VI (polar compounds) contains mostly heteroatom-containing non-aromatic compounds. Analysis of an equimolar mixture of nonaromatic compounds with different heteroatoms (n-butylamine, n-hexylamine, 5-nonanone and diisopropyl sulfide) by using the APCI/N<sub>2</sub>/CS<sub>2</sub> method revealed generation of more than one ion type for each component except for the amines in Figure 4.11, which makes this method unsuitable for fraction VI.

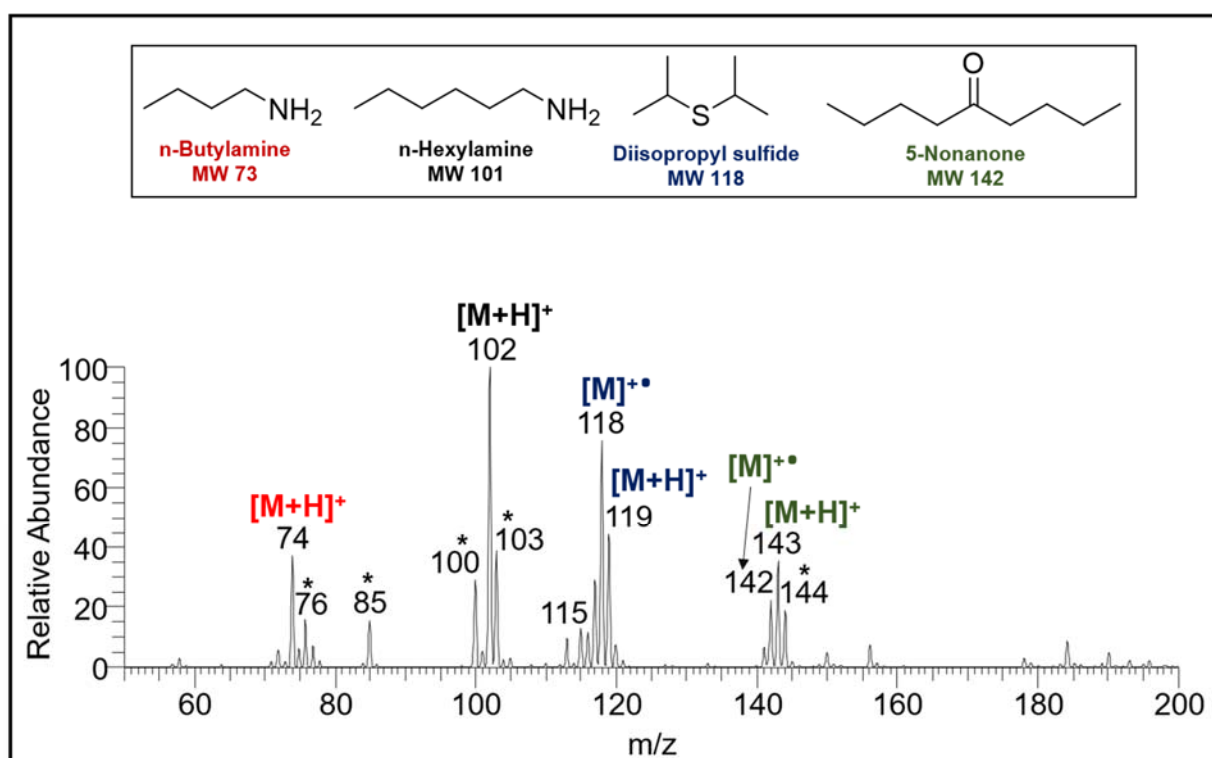


Figure 4.11 APCI/N<sub>2</sub>/CS<sub>2</sub> mass spectrum of an equimolar mixture (1 mM) of nonaromatic heteroatom containing model compounds obtained at an injection flow rate of 5  $\mu$ L/min and a tube lens voltage of 50 V. While amines produced only protonated analyte ion, other analytes produced more than one ion type per analyte (\*denotes chemical noise peaks).

As these analytes should be easy to protonate, the traditional APCI/N<sub>2</sub>/methanol method was explored. Unfortunately, polar compounds (fraction VI) derived from crude oil are not completely soluble in methanol. Therefore, the fraction was first dissolved in a small amount of n-hexane (approx. 15-25% of final volume) followed by dissolution in methanol (approx. 75-85% of final volume). Interestingly, while pure hexane and methanol are not miscible with each other, they are completely miscible in the presence of the polar compounds isolated from the crude oil. Figure 4.12 shows the mass spectrum obtained for the model compound mixture (n-butylamine, n-hexylamine, 5-nonanone and diisopropyl sulfide) by using the (+)APCI/N<sub>2</sub>/hexane, methanol ionization method. Only protonated compounds with reasonably similar relative abundances were observed. It is important to note that at higher injection flow rates (> 20 μL min<sup>-1</sup>) and/or higher concentrations (> 5 mM), competition for ionization and adduct formation was observed, leading to more than one type of ion for each compound (Figure 4.13). The optimized ionization conditions required for ideal analysis of polar compounds (fraction VI) are provided in Table 4.5.

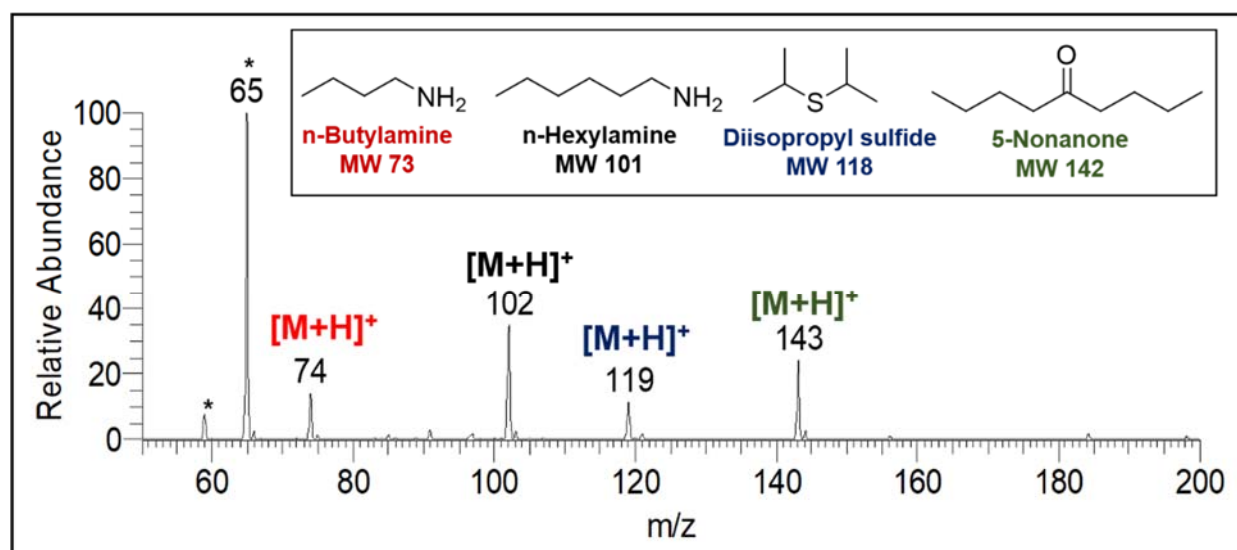


Figure 4.12 APCI/N<sub>2</sub>/n-hexane, methanol mass spectrum of an equimolar mixture (1 mM) of nonaromatic polar compounds measured at an injection flow rate of 1 μL min<sup>-1</sup> and tube lens voltage of 50 V (\* denotes solvent peaks).

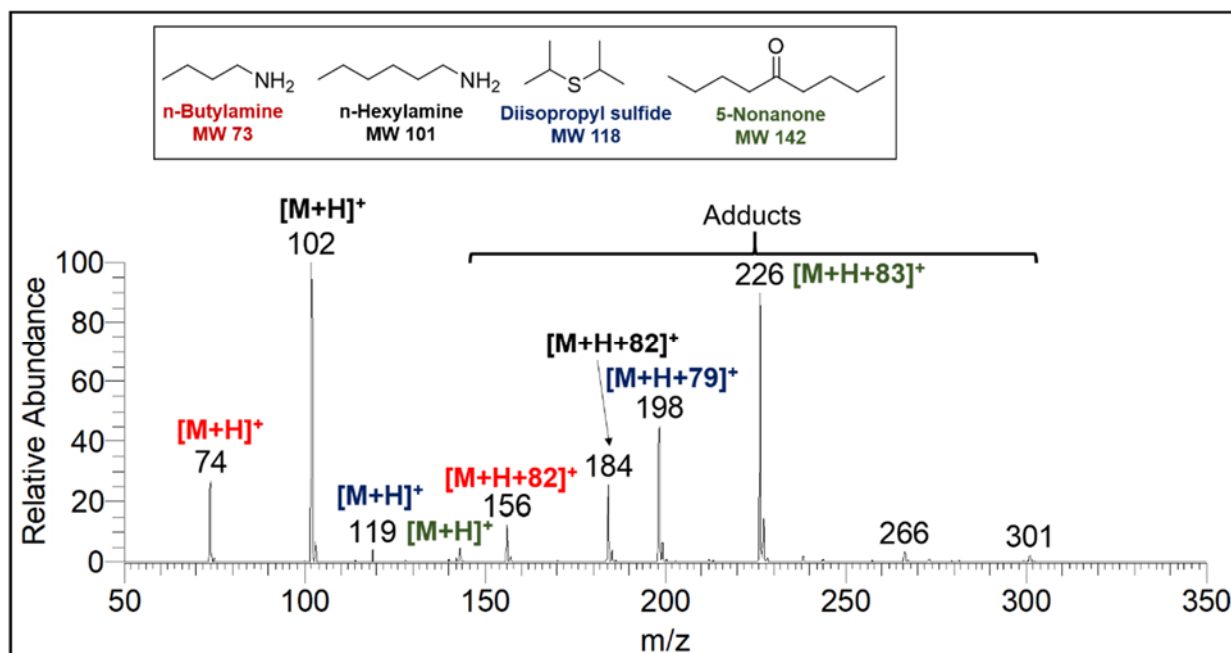


Figure 4.13 APCI/N<sub>2</sub>/hexane, methanol mass spectrum of an equimolar mixture (0.1 mM) of nonaromatic heteroatom containing model compounds obtained at a flow rate of 10  $\mu\text{L}/\text{min}$  and a tube lens voltage of 50 V. Adduct formation was observed at higher flow rates ( $>5 \mu\text{L}/\text{min}$ ).

#### 4.5.4 Characterization of Crude Oil Fractions by Using High-resolution Mass Spectrometry

The high-resolution mass spectrometry instruments and ionization methods that were selected for the analysis of the individual crude oil fractions based on model compound studies are summarized in Figure 4.14.

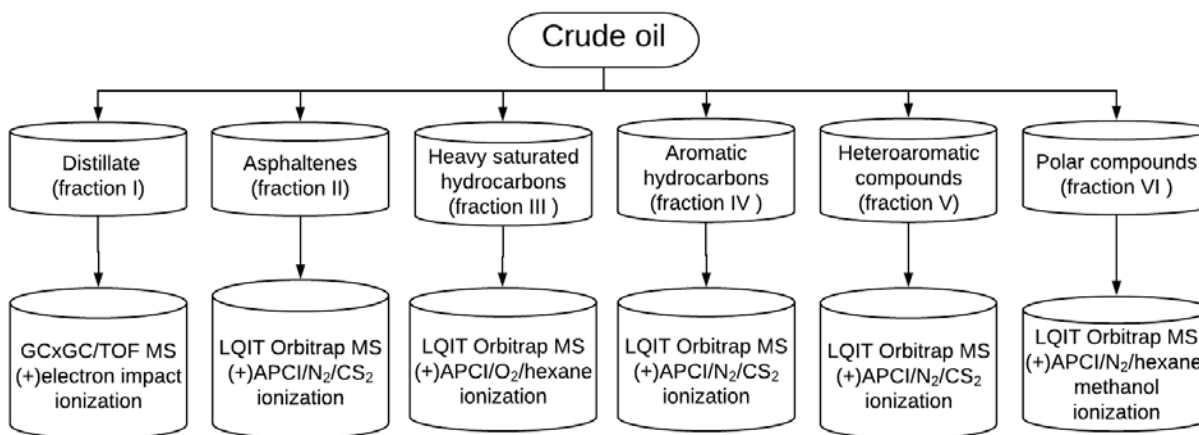


Figure 4.14 Instruments and ionization methods used for high-resolution mass spectral analysis of the six fractions of crude oil.

Based on the total ion-chromatogram (Figure 4.15A) obtained for the distillate (fraction I) by using a high-resolution GCxGC/((+)EI)TOF mass spectrometer (for the conditions, see Table 4.3) the majority of its components are cyclic and acyclic saturated hydrocarbons with a small percentage of small aromatic hydrocarbons. An earlier examination of equimolar model compound mixtures containing cyclic and acyclic saturated hydrocarbons and aromatic hydrocarbons (same compound classes as in the distillate) by using the same mass spectrometer revealed similar instrumental average relative response factors for the cyclic and acyclic saturated hydrocarbons are similar.<sup>18</sup> However, aromatic hydrocarbons were observed to show 30-40% higher response

than saturated hydrocarbons.<sup>18</sup> Since most compounds in the distillate (fraction I) are saturated hydrocarbons, this method should yield semi-quantitative information for the distillate.

Figure 4.15B shows the (+)APCI mass spectra obtained for the five nonvolatile crude oil fractions by using high-resolution LQIT Orbitrap mass spectrometers (for conditions, see Table 4.5). The data obtained under these optimized conditions are semi-quantitative and provide the MW values and elemental compositions for most of the compounds in the fractions. Analysis of these data is discussed below.

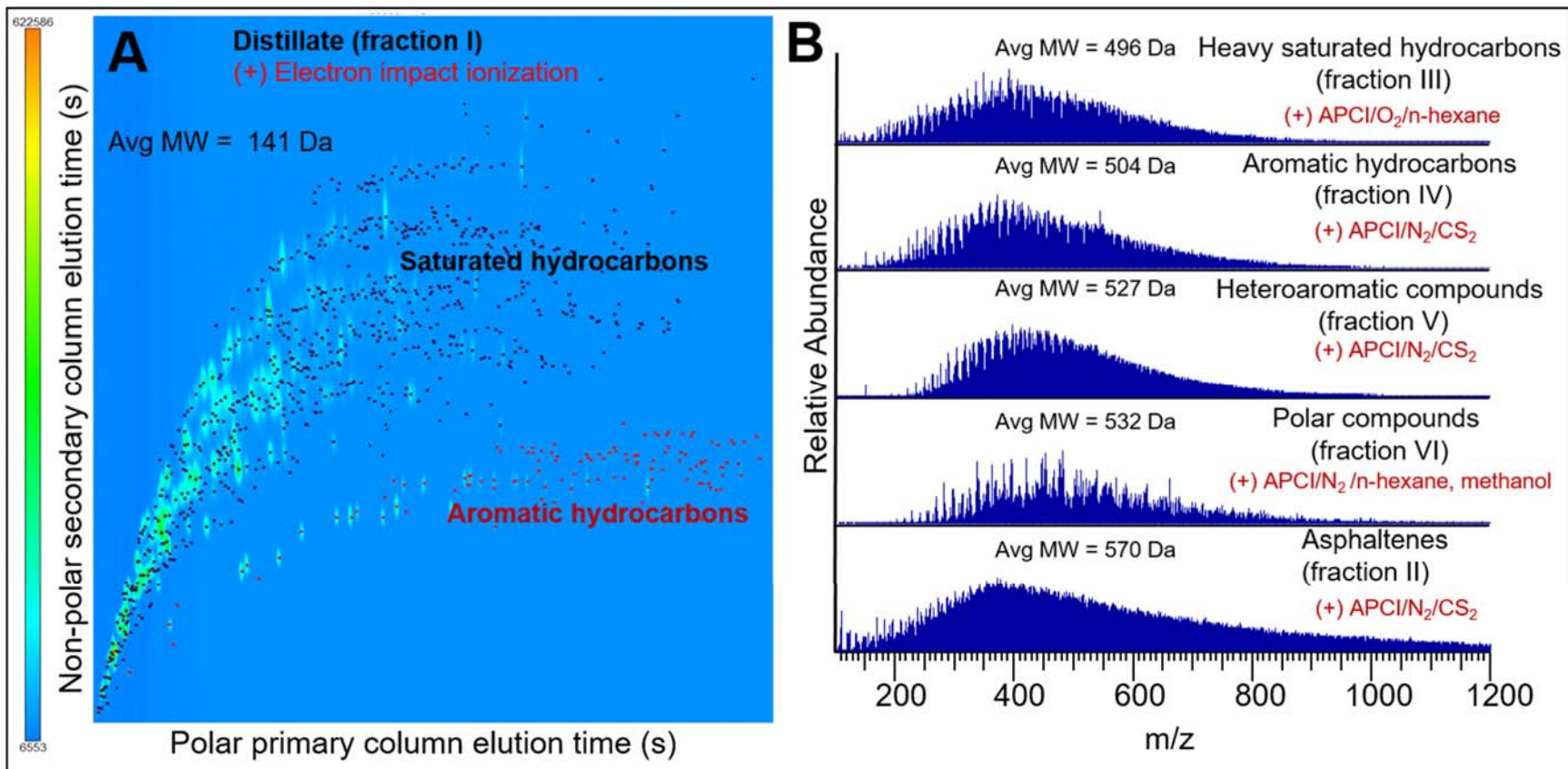


Figure 4.15 A) GCxGC/((+)EI)TOF total ion chromatogram for the distillate (fraction I) of the crude oil. The aromatic hydrocarbons are color coded in red and saturated hydrocarbons in black. B) Positive ion mode APCI mass spectra obtained for the five nonvolatile crude oil fractions (fractions II–VI). Avg MW denotes the weighted average molecular weight (discussed below).

#### 4.5.4.1 Average Molecular Weight (Avg MW) of the Crude Oil

In order to test the accuracy of the optimized mass spectrometry methods discussed above for the determination of the average molecular weights (Avg MW) of the crude oil fractions and ultimately the crude oil itself, the experimental Avg MW was determined for the three model compound mixtures discussed above by using the optimized methods (Table 4.8). Similarly, results have been reported for the equimolar model compound mixture containing volatile hydrocarbons (n-decane, n-dodecane, n-propylcyclohexane, isopropylbenzene and n-butylbenzene) analyzed previously by using the same GCxGC/((+)EI)TOF mass spectrometer (Table 4.8).<sup>18</sup> The experimental Avg MW, theoretical Avg MW and experimental errors for all the model mixtures are summarized in Table 4.8. From these data, it is evident that the determination of the average molecular weights for the model compound mixtures was quite accurate (the error for four of the mixtures was  $\leq 3\%$ ; the greatest error, 7 %, was observed for the mixture containing alkyl benzenes with long alkyl chains). These findings are summarized in Table 4.8.



Table 4.8 Experimental errors in Avg MW obtained using optimized ionization methods for five different model compound mixtures.

	Molecular weight	Ionization mode and method and type of ions generated	Experimental Avg MW	Theoretical Avg MW	Experimental error (%)
<b>1. Small Cyclic, Linear and Aromatic Compounds<sup>[18]</sup></b>					
n-Propylcyclohexane	126	(+)electron impact ionization Molecular ions [M <sup>+</sup> ]	137 Da <sup>a, [18]</sup>	138 Da <sup>b</sup>	1%
n-Dodecane	170				
Isopropylbenzene	120				
n-Decane	142				
n-Butylbenzene	134				
<b>2. Aromatic and Heteroaromatic Compounds</b>					
Dibenzofuran	168	(+)APCI/N <sub>2</sub> /CS <sub>2</sub> Molecular ions [M <sup>+</sup> ]	181 Da <sup>c</sup>	181 Da <sup>b</sup>	0%
Methylfluorene	180				
Dibenzothiophene	184				
Ethyl carbazole	195				
<b>3. Alkyl Aromatic Compounds</b>					
1-Phenyldecane	218	(+)APCI/N <sub>2</sub> /CS <sub>2</sub> Molecular ions [M <sup>+</sup> ]	243 Da <sup>c</sup>	260 Da <sup>b</sup>	7%
1-Phenyldodecane	246				
Heptadecyl benzene	316				
<b>4. Cyclic, Linear And Branched Saturated Compounds</b>					
Cholestane	372	(+)APCI/O <sub>2</sub> / hexane Pseudo molecular ions [M-H] <sup>+</sup>	423 Da <sup>d</sup>	428 Da <sup>b</sup>	1%
Squalane	422				
Pentatriacontane	492				
<b>5. Polar Compounds</b>					
n-Butylamine	73	(+)APCI/hexane, methanol/N <sub>2</sub> Protonated ions [M+H] <sup>+</sup>	112 Da <sup>c</sup>	109 Da <sup>b</sup>	3%
n-Hexylamine	101				
Diisopropyl sulfide	118				
5-Nonanone	142				

<sup>a</sup>Calculated using Eq. 4.2

<sup>b</sup>Calculated using Eq. 4.8

<sup>c</sup>Calculated using Eq. 4.3

<sup>d</sup>Calculated using Eq. 4.4

<sup>e</sup>Calculated using Eq. 4.5

The Avg MW for all the crude oil fractions (I, II, III, IV, V and VI) analyzed by using the optimized mass spectrometric methods are summarized in Table 4.9. Interestingly, the Avg MW for all the fractions excluding the distillate (fraction I) ranged between 496 to 570 Da.

Table 4.9 Avg MW of crude oil determined from the Avg MW of individual fractions (determined using Equations 4.2 – 4.6) and their percent gravimetric weights.

Fractions of crude oil	Avg MW (Da)	Weight (%)
Fraction I (distillate)	141	8
Fraction II (asphaltenes)	570	1
Fraction III (heavy saturated hydrocarbons)	496	45
Fraction IV (aromatic hydrocarbons)	504	20
Fraction V (heteroaromatic compounds)	527	9
Fraction VI (polar compounds)	532	6
Avg MW of fractionated crude oil	473	100

Although it has been convincingly proven earlier (for example, see Figure 4.1) that direct analysis of crude oil without prior separation is far from ideal, a mass spectrum was measured for the unfractionated crude oil by using the APCI/N<sub>2</sub>/CS<sub>2</sub> ionization method for comparison purposes (Figure 4.16).

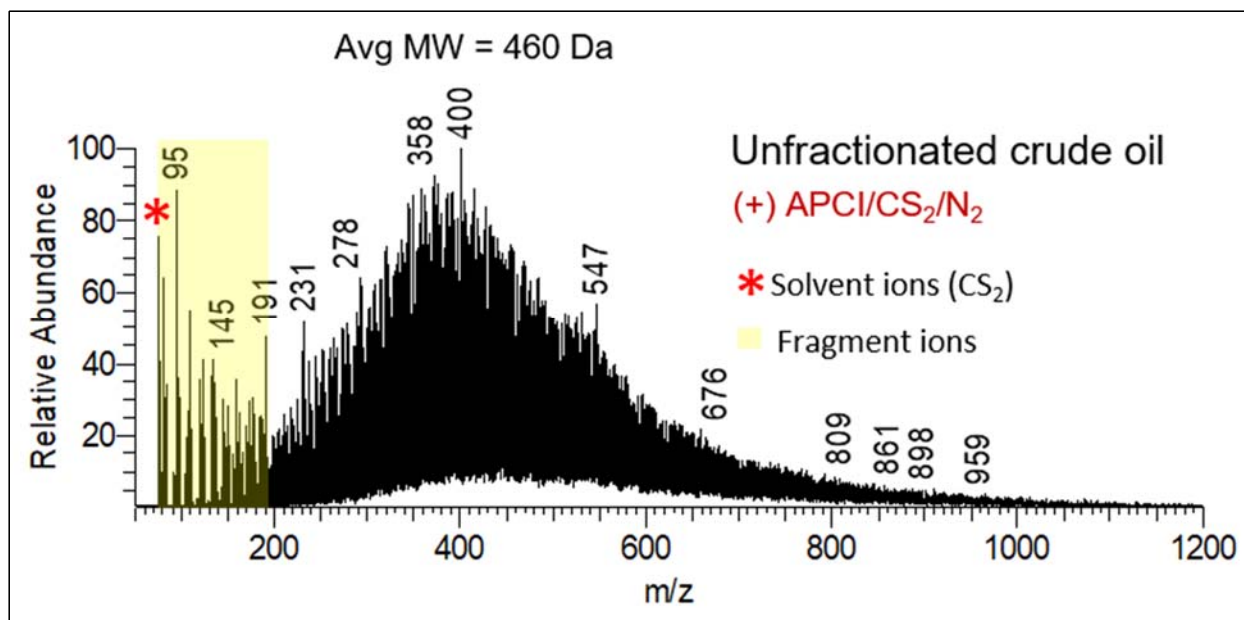


Figure 4.16 APCI/N<sub>2</sub>/CS<sub>2</sub> mass spectrum of unfractionated crude oil obtained at an injection flow rate of 5  $\mu$ L/min and a tube lens voltage of 50 V. Avg MW denotes the weighted average molecular weight (All the ions observed in the mass spectrum were considered to determine the molecular weight).

The Avg MW of the unfractionated crude oil determined based on this mass spectrum was 460 Da (obtained using Equation 4.3). This value is close to that measured for the fractionated crude oil (473 Da; Table 1) in spite of the fact that the APCI/N<sub>2</sub>/CS<sub>2</sub> ionization method completely fragments acyclic saturated hydrocarbons (see Figure 1). The similarity of these values may be explained based on the similar Avg MW values measured for the individual fractions except for the distillate (fraction I), and the relatively low weight percent of this fraction. This may not be true for other crude oils. A study comparing the compositions and Avg MWs of crude oils with different origins is underway.

#### 4.5.4.2 Molecular Profiling of Crude Oil

High-resolution MS data were employed to assign elemental compositions and ring and double bond (RDB) equivalence values for ionized compounds derived from the different crude oil fractions. RDB equivalence plots provide information on the degree of unsaturation and number of rings in the compounds, specifically, the number of alicyclic and aromatic rings and double and triple bonds.

##### 4.5.4.2.1 RDB Equivalence Plots

Figure 4.17 shows the RDB equivalence versus carbon number (RDB equivalence plots) for ionized compounds derived from the six different fractions of the crude oil. Ions containing the heteroatoms N, O and/or S are color coded in the figure for visual differentiation.

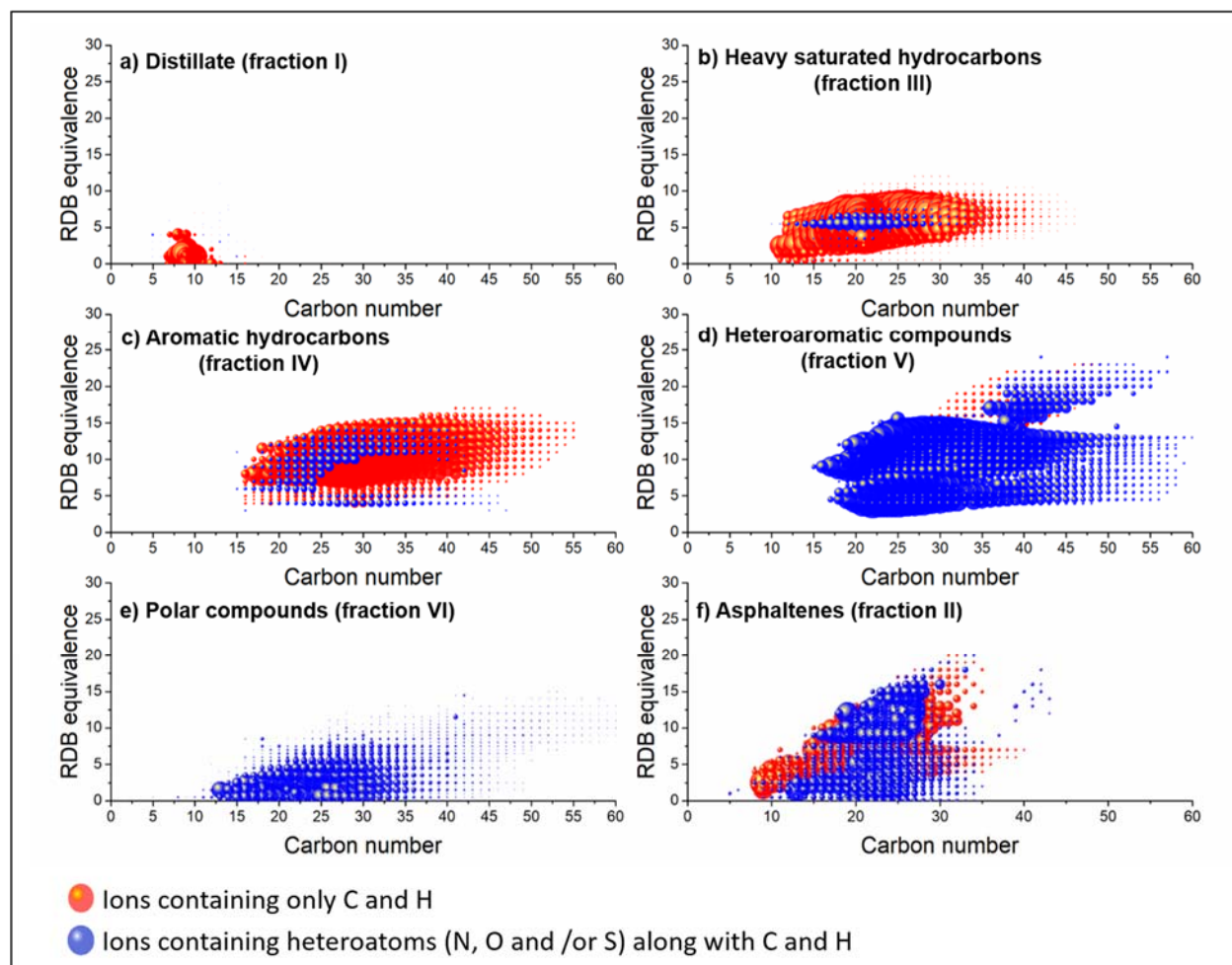


Figure 4.17 Color-mapped bubble plots of the ring and double bond (RDB) equivalence versus carbon number for ionized compounds derived from the six crude oil fractions that were separated and characterized by using the DPF MS method. Bubble size indicates the relative abundance of the ions.

Based on these data, most of the hydrocarbons in the distillate (fraction I) are saturated, and some contain ring structures. Further, a small number of aromatic compounds (with  $RDB \geq 4$ ) were detected, in agreement with the mass spectrometry data discussed above (Figure 4.15A). Most of the compounds in this fraction contain 7-10 carbons and have RDB values of either one or two (minimal degree of unsaturation).

The RDB equivalence plot for heavy saturated hydrocarbons (fraction III) surprisingly indicated the presence of compounds with large RDB values (up to 8; Figure 4.17). This could be due to the presence of aliphatic or aromatic rings, or double or triple bonds. However, since the FTIR data for fraction III revealed no aromatic, alkene or alkyne signatures (Figure 4.7), the large RDB values can be attributed to the presence of compounds containing 1-8 saturated rings. Most of the compounds in this fraction contain 10-35 carbons. Finally, some compounds in fraction III contain a heteroatom, specifically, sulfur (see discussion on compound class distributions below).

Most compounds in the aromatic hydrocarbon group (fraction IV) contain 15-45 carbons. No aliphatic compounds were detected as all the RDB values are greater or equal to four as expected based on FTIR analysis. However, some heteroatom containing compounds were observed and are discussed in the next section.

Most compounds in the heteroaromatic and polar compound groups (fractions V and VI) contain heteroatoms, but these two fractions differ drastically from each other in their carbon number and extent of aromaticity (Figure 4.17). The majority of the compounds in fraction V contain 15-50 carbons while the compounds in fraction VI only contain 12-35 carbons. While the heteroaromatic compound group contains both aromatic compounds ( $RDB \geq 4$ ) and nonaromatic compounds ( $RDB < 4$ ), the majority of the compounds in the polar compound class are nonaromatic ( $RDB < 4$ ). These observations are in agreement with the FTIR results obtained for these fractions.

Asphaltenes (fraction II) contain not only aromatic and heteroaromatic compounds but also compounds that are not aromatic ( $DBE < 4$ ). The compounds in asphaltenes contain 8-35 carbons.

#### 4.5.4.2.2 Compound Class Distributions

Assigning accurate elemental compositions for ionized compounds is critical for the accurate estimation of compound class distributions. However, when analyzing mixtures as complex as crude oil, this requires much greater resolution and mass accuracy than available on the orbitrap (100,000 resolution) and TOF instruments (50,000 resolution) used in this research.<sup>21-24</sup> However, after DPF separation of the crude oil into six fractions based on the volatility, solubility and polarity of the compounds, much simpler mixtures are generated and the compounds in each mixture have similar properties. This makes assigning elemental compositions much easier when using lower resolution instruments.

Elemental composition data thus obtained for ionized compounds derived from the different crude oil fractions can be utilized to classify the compounds into different compound classes further. Figure 4.18 (Table 4.10) shows compound class distributions and their relative abundances for the six fractions.

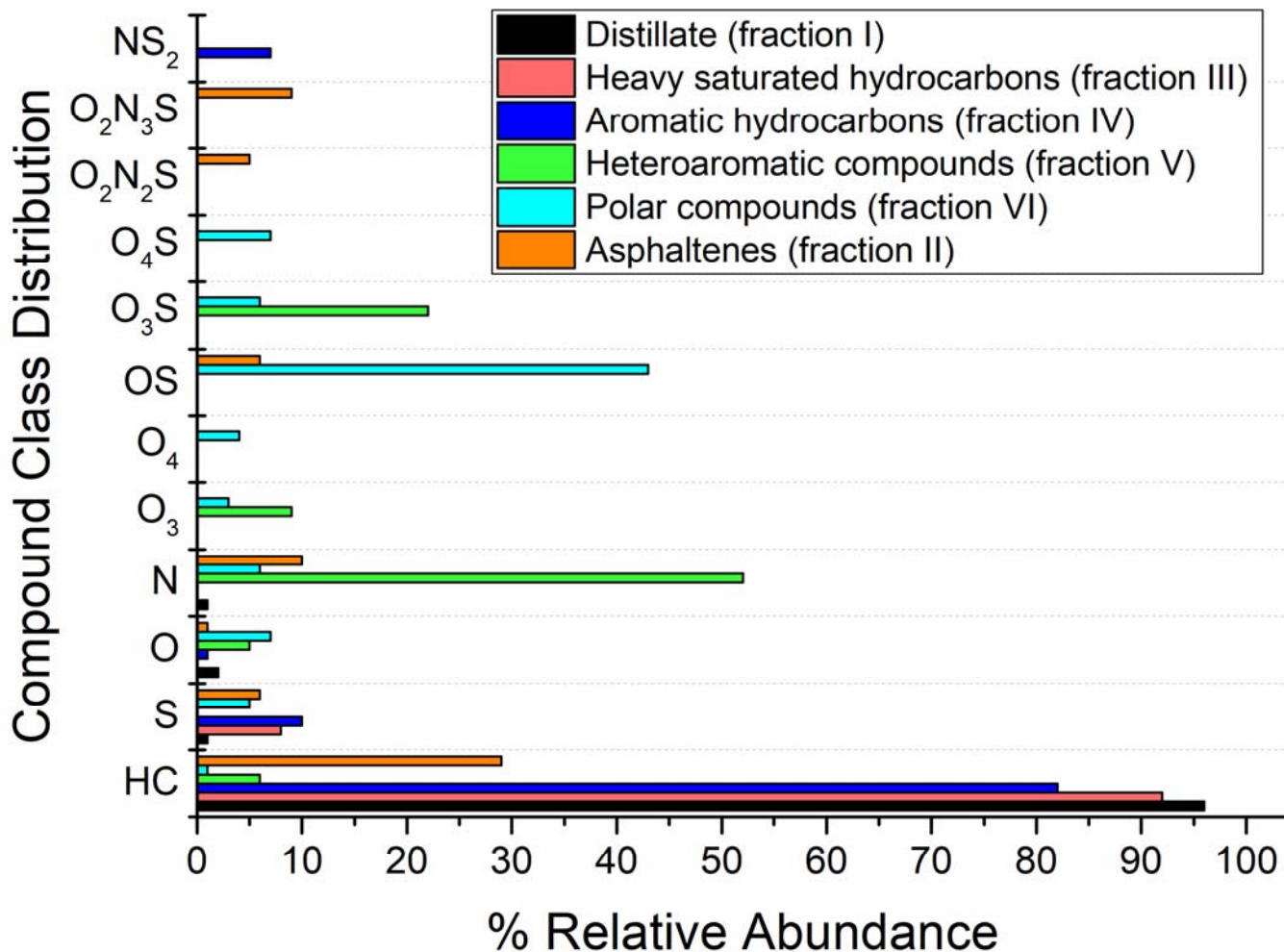


Figure 4.18 Compound class distributions and their percentage relative abundances for crude oil fractions separated and analyzed by using the DPF MS method. The y-axis indicates the assigned elemental compositions by using abbreviations such as NS<sub>2</sub>, which implies compounds containing one nitrogen and two sulfur atoms, in addition to hydrogen and carbon atoms.



Table 4.10. Compound class percentage distributions derived from high-resolution mass spectral data for the six fractions and their gravimetric weight percentages as well as the compound class distributions (highlighted in yellow) for the crude oil.

DPF MS fractions	Distillate (fraction I)	Heavy saturated hydrocarbons (fraction III)	Aromatic hydrocarbons (fraction IV)	Heteroaromatic compounds (fraction V)	Polar Compounds (fraction VI)	Asphaltenes (fraction II)	
Gravimetric weight percentages	8	44	21	9	8	1	
<b>Compound class</b>							<b>Compound class percentage distributions</b>
<b>HC</b>	96	92	82	6	1	40	76
<b>S<sub>1</sub></b>	1	8	10	0	5	1	7
<b>O<sub>1</sub></b>	2	0	1	5	7	5	1
<b>N<sub>1</sub></b>	1	0	0	52	6	6	6
<b>O<sub>2</sub></b>	0	0	0	0	0	0	0
<b>O<sub>3</sub></b>	0	0	0	9	3	34	1
<b>O<sub>4</sub></b>	0	0	0	0	4	5	0
<b>O<sub>6</sub></b>	0	0	0	0	0	0	0
<b>O<sub>1</sub>S<sub>1</sub></b>	0	0	0	0	43	0	3
<b>SO<sub>3</sub></b>	0	0	0	22	6	0	3
<b>O<sub>4</sub>S</b>	0	0	0	0	7	0	0
<b>O<sub>2</sub>N<sub>2</sub></b>	0	0	0	0	0	0	0
<b>O<sub>1</sub>N<sub>1</sub></b>	0	0	0	1	2	2	0
<b>O<sub>2</sub>N<sub>2</sub>S</b>	0	0	0	0	0	0	0
<b>NS<sub>2</sub></b>	0	0	7	0	0	0	2
<b>Total</b>							99

The percentage relative abundance of the hydrocarbon (HC) class was found to be different for each fraction, being the greatest for the distillate (fraction I) and the smallest for the polar compounds (fraction VI). The asphaltenes (fraction II) contain a relatively large number of compounds with a variety of different heteroatoms. While N atoms and SO<sub>3</sub> groups were most abundant in heteroaromatic compounds (fraction V), SO, O and SO<sub>4</sub> atoms/groups are most abundant in polar compounds (fraction VI). Interestingly, some compounds in the aromatic hydrocarbon fraction were found to contain not only S but also NS<sub>2</sub>. To summarize, all the fractions are drastically different in their compound class distributions and their relative abundances.

From the gravimetric weight percentage of individual fractions and their compound class distributions, the weight percentage distribution of individual compound classes in the whole crude oil can be obtained by using Equation 4.7. Figure 4.19 (Table 4.10, highlighted in yellow) shows the summarized weight percentage distributions for the different compound classes consolidated from the data obtained for the individual fractions. These data provide a simplified picture on the presence of different compound classes and their abundances in the whole crude oil. Based on these consolidated results, this crude oil consists of about 12% sulfur-containing compounds (S, OS, and O<sub>3</sub>S). It can also be deduced that this crude oil is very low (3%) in oxygen content (O, O<sub>3</sub>, and O<sub>4</sub>).

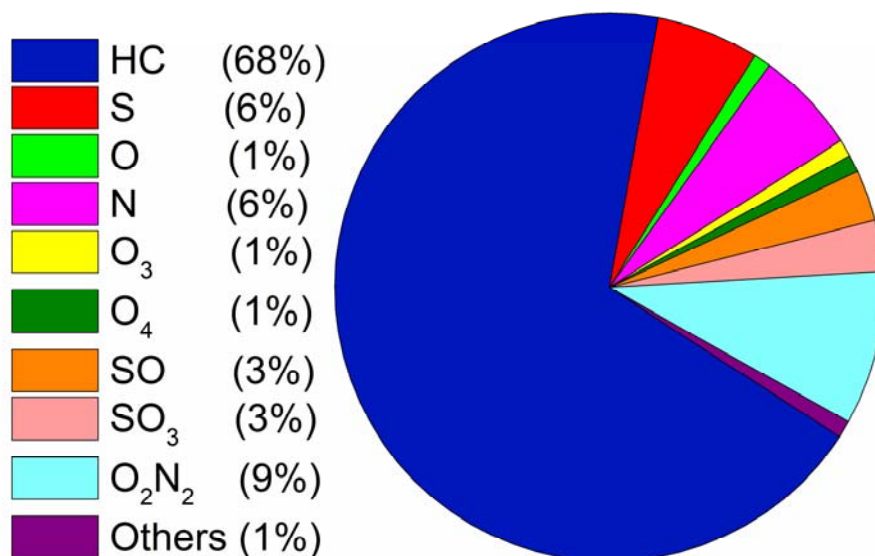


Figure 4.19 Weight percentages of compound classes in crude oil, consolidated from the data obtained for individual fractions.

Further information on individual fractions can be obtained by exploiting the tandem MS capabilities of the LQIT/orbitrap mass spectrometer. This mass spectrometer allows the isolation of a group of isomeric and isobaric ions of a given  $m/z$ -value followed by collision-activated dissociation (CAD) in the ion trap. The resulting MS/MS CAD spectra can provide structural information on crude oil components, such as the number of carbons in alkyl groups and the size of the aromatic cores in asphaltenes<sup>25,26</sup>.

Figure 4.20 shows the CAD mass spectra obtained by using the same “normalized” CAD energy (25 arbitrary units) for molecular ions of  $m/z$  400 (generated upon (+) APCI/N<sub>2</sub>/CS<sub>2</sub> ionization) derived from three different fractions (fractions II, IV and V).

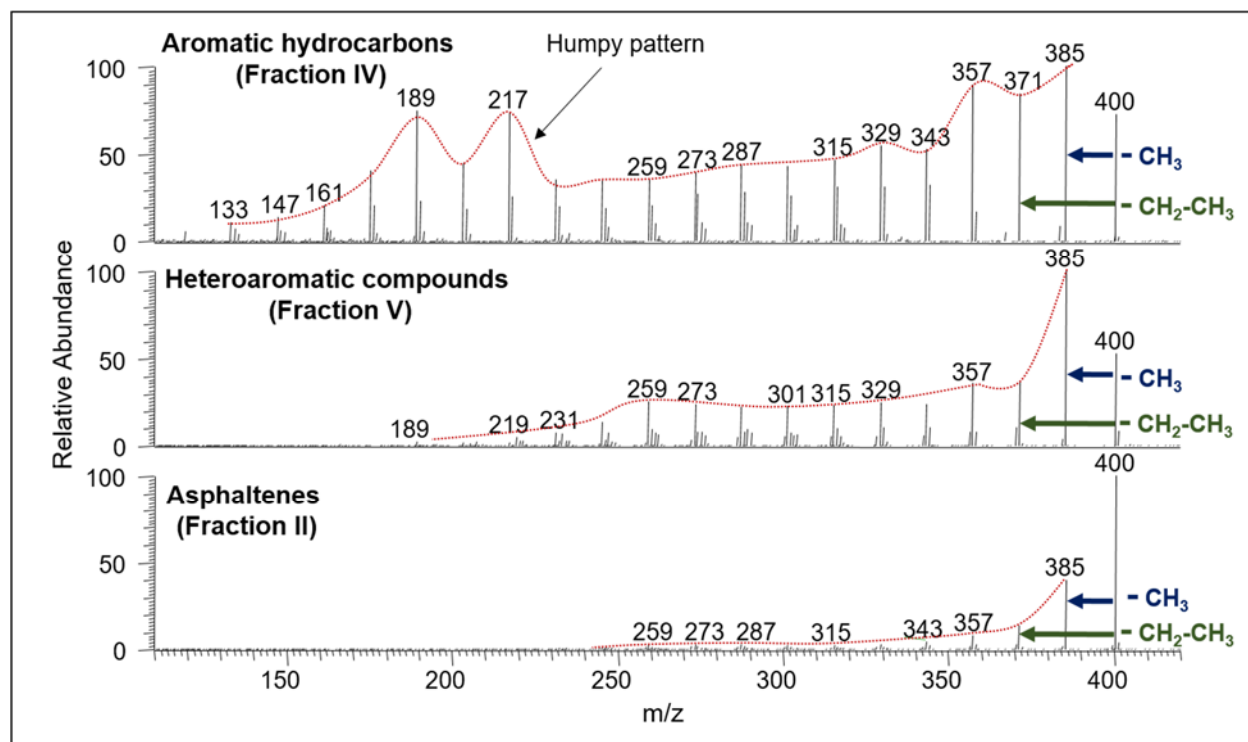


Figure 4.20 CAD mass spectra obtained by using the same “normalized” CAD energy (25 arbitrary units) for the radical cation of  $m/z$  400 derived from three different fractions of the crude oil. The different fragmentation patterns are highlighted using a red dotted line.

The fragmentation patterns (indicated by red dotted lines) observed for these ions indicate that they are very different from each other. The decay patterns observed for the ions derived from the asphaltenes are consistent with the fragmentation patterns reported for asphaltenes,<sup>8</sup> indicating large aromatic cores and short alkyl chains (fastest fragmentations involving elimination of methyl and ethyl radicals). On the other hand, the ions derived from the aromatic hydrocarbon fraction contain small aromatic cores and long alkyl chains. Fragmentation of the ions derived from the heteroaromatic fraction indicates the presence of fairly long alkyl chains in these compounds, information that was not obtained from any of the experiments discussed above.

Figure 4.21 shows more examples of the fragmentation patterns observed for ionized heteroaromatic compounds and asphaltenes (fractions II and V). Figure 4.22 shows representative

CAD mass spectra of protonated compounds derived from the polar compounds fraction. These protonated compounds fragment via unique losses of polar molecules, such as water and formaldehyde, thus confirming the presence of polar functional groups.

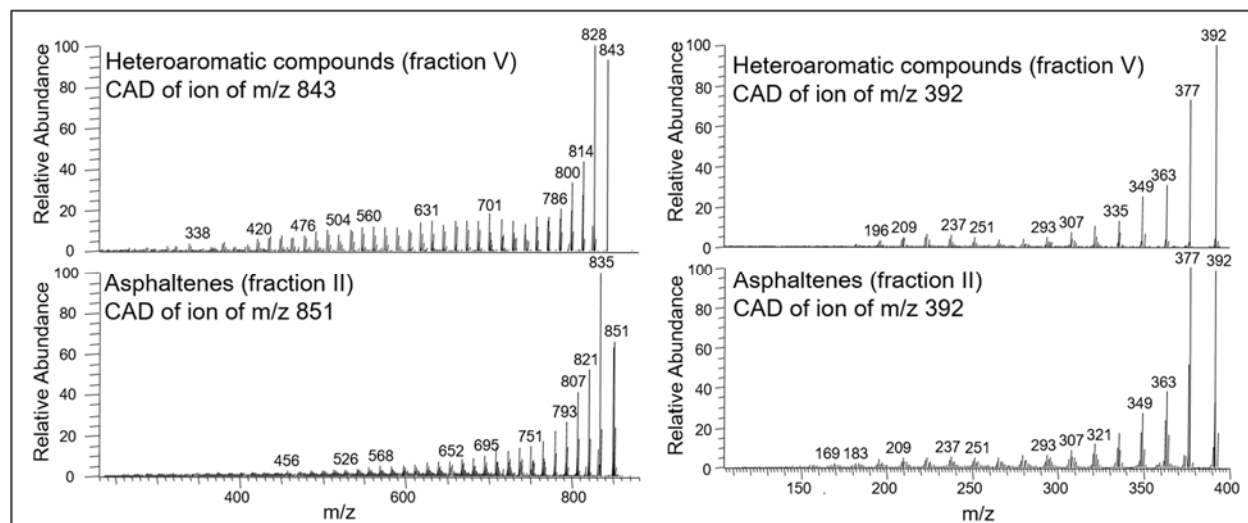


Figure 4.21 CAD mass spectra of different ions derived from the heteroaromatic compounds and asphaltene fractions, highlighting the similarity in fragmentation patterns.

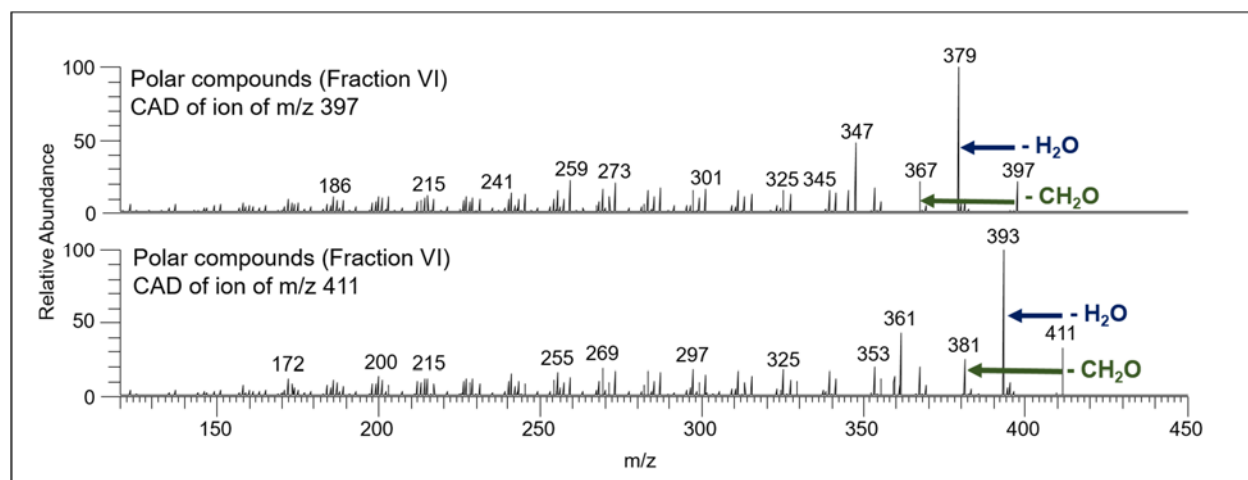


Figure 4.22 CAD mass spectra of ions of  $m/z$  397 and 411 (protonated molecules) derived from polar compounds (fraction VI), indicating characteristic losses of polar molecules, such as water and formaldehyde.

## 4.6 Conclusions

A separation and characterization method entitled Distillation Precipitation Fractionation Mass Spectrometry (DPF-MS) is introduced here for the analysis of crude oil at the molecular level. This method involves separation of the crude oil into six fractions. These fractions are the distillate (fraction I) mostly containing volatile saturated hydrocarbons but also light aromatic hydrocarbons, asphaltenes (fraction II) containing predominantly aromatic and heteroaromatic compounds, heavy saturated hydrocarbons (fraction III) containing cyclic, branched and linear hydrocarbons, aromatic hydrocarbons (fraction III) containing predominantly alkylaromatic compounds, heteroaromatic compounds (fraction V) and polar compounds (fraction VI) containing non-aromatic polar compounds. High-resolution mass spectrometry instruments, specifically, GCxGC/TOF and LQIT/orbitrap mass spectrometers, were used for the molecular level characterization of each individual fraction. An optimized ionization method was developed for each fraction to ionize all of its components with similar efficiency and to generate only one type of ions, either molecular ions or protonated molecules or cations formed upon hydride abstraction. While (+) EI ionization method coupled with GCxGC/TOF was utilized for the characterization of the volatile distillate (fraction I), (+) APCI approaches with different nebulization gases and solvent systems were identified for each nonvolatile fraction (fractions II, III, IV, V, VI).

DPF-MS provides semi-quantitative molecular level information (elemental compositions and molecular weights) that can be further processed to obtain accurate average molecular weight, ring and double bond equivalence values and percentage abundances of different compound classes in the different crude oil fractions. This method excels over previous methods by including the mass balance for each fraction, thus allowing for data consolidation (data obtained from different fractions consolidated into one data set), which provides an accurate overall analysis of

the crude oil, including average molecular weight, heteroatom content, and the weight percentage of different compound classes.

#### 4.7 References

- (1) Denekas, M. O.; Mattax, C. C.; Davis, G. T. Effects of Crude Oil Components on Rock Wettability; Society of Petroleum Engineers: Kansas City, 1959; pp 330–333.
- (2) Tang, G.-Q.; Morrow, N. R. Influence of Brine Composition and Fines Migration on Crude Oil/Brine/Rock Interactions and Oil Recovery. *J. Pet. Sci. Eng.* **1999**, *24* (2), 99–111.
- (3) Walters, C. C. Oil–Oil and Oil–Source Rock Correlation. In *Geochemistry*; Springer Netherlands: Dordrecht, 1998; pp 442–444.
- (4) Schneider, D. F. Select the Right Hydrocarbon Molecular Weight Correlation. *Chem. Eng. Prog. N. Y.* **1998**, *94* (12), 40.
- (5) Marshall, A. G.; Rodgers, R. P. Petroleomics: The Next Grand Challenge for Chemical Analysis. *Acc. Chem. Res.* **2004**, *37* (1), 53–59.
- (6) Bae, E.; Na, J.-G.; Chung, S. H.; Kim, H. S.; Kim, S. Identification of About 30 000 Chemical Components in Shale Oils by Electrospray Ionization (ESI) and Atmospheric Pressure Photoionization (APPI) Coupled with 15 T Fourier Transform Ion Cyclotron Resonance Mass Spectrometry (FT-ICR MS) and a Comparison to Conventional Oil. *Energy Fuels* **2010**, *24* (4), 2563–2569.
- (7) Purcell, J. M.; Hendrickson, C. L.; Rodgers, R. P.; Marshall, A. G. Atmospheric Pressure Photoionization Fourier Transform Ion Cyclotron Resonance Mass Spectrometry for Complex Mixture Analysis. *Anal. Chem.* **2006**, *78* (16), 5906–5912.
- (8) Owen, B. C.; Gao, J.; Borton, D. J.; Amundson, L. M.; Gray, M.; Kenttämä, H. I.; Archibold, E. F.; Tan, X.; Azyat, K.; Tykwinski, R. Carbon Disulfide Reagent Allows the Characterization of Nonpolar Analytes by Atmospheric Pressure Chemical Ionization Mass Spectrometry. *Rapid Commun. Mass Spectrom.* **2011**, *25* (14), 1924–1928.
- (9) Chiaberge, S.; Fiorani, T.; Savoini, A.; Bionda, A.; Ramello, S.; Pastori, M.; Cesti, P. Classification of Crude Oil Samples Through Statistical Analysis of APPI FTICR Mass Spectra. *Fuel Process. Technol.* **2013**, *106*, 181–185.
- (10) Rodgers, R. P.; Marshall, A. G. Petroleomics: Advanced Characterization of Petroleum-Derived Materials by Fourier Transform Ion Cyclotron Resonance Mass Spectrometry (FT-ICR MS). In *Asphaltenes, Heavy Oils, and Petroleomics*; Mullins, O. C., Sheu, E. Y., Hammami, A., Marshall, A. G., Eds.; Springer New York, 2007; pp 63–93.
- (11) Pakarinen, J. M. H.; Teräväinen, M. J.; Pirskanen, A.; Wickström, K.; Vainiotalo, P. A Positive-Ion Electrospray Ionization Fourier Transform Ion Cyclotron Resonance Mass Spectrometry Study of Russian and North Sea Crude Oils and Their Six Distillation Fractions. *Energy Fuels* **2007**, *21* (6), 3369–3374.
- (12) Zhu, X.; Shi, Q.; Zhang, Y.; Pan, N.; Xu, C.; Chung, K. H.; Zhao, S. Characterization of Nitrogen Compounds in Coker Heavy Gas Oil and Its Subfractions by Liquid Chromatographic Separation Followed by Fourier Transform Ion Cyclotron Resonance Mass Spectrometry. *Energy Fuels* **2011**, *25* (1), 281–287.



- (13) Klein, G. C.; Angström, A.; Rodgers, R. P.; Marshall, A. G. Use of Saturates/Aromatics/Resins/Asphaltenes (SARA) Fractionation To Determine Matrix Effects in Crude Oil Analysis by Electrospray Ionization Fourier Transform Ion Cyclotron Resonance Mass Spectrometry. *Energy Fuels* **2006**, *20* (2), 668–672.
- (14) Liu, P.; Shi, Q.; Chung, K. H.; Zhang, Y.; Pan, N.; Zhao, S.; Xu, C. Molecular Characterization of Sulfur Compounds in Venezuela Crude Oil and Its SARA Fractions by Electrospray Ionization Fourier Transform Ion Cyclotron Resonance Mass Spectrometry. *Energy Fuels* **2010**, *24* (9), 5089–5096.
- (15) Buenrostro-Gonzalez, E.; Lira-Galeana, C.; Gil-Villegas, A.; Wu, J. Asphaltene Precipitation in Crude Oils: Theory and Experiments. *AIChE J.* **2004**, *50* (10), 2552–2570.
- (16) Yang, Z.; Yang, C.; Wang, Z.; Hollebhone, B.; Landriault, M.; Brown, C. E. Oil Fingerprinting Analysis Using Commercial Solid Phase Extraction (SPE) Cartridge and Gas Chromatography-Mass Spectrometry (GC-MS). *Anal. Methods* **2011**, *3* (3), 628–635.
- (17) Alzaga, R.; Montuori, P.; Ortiz, L.; Bayona, J. M.; Albaigés, J. Fast Solid-Phase Extraction–Gas Chromatography–Mass Spectrometry Procedure for Oil Fingerprinting: Application to the Prestige Oil Spill. *J. Chromatogr. A* **2004**, *1025* (1), 133–138.
- (18) Luning Prak, D. J.; Romanczyk, M.; Wehde, K. E.; Ye, S.; McLaughlin, M.; Luning Prak, P. J.; Foley, M. P.; Kenttämä, H. I.; Trulove, P. C.; Kilaz, G.; et al. Analysis of Catalytic Hydrothermal Conversion Jet Fuel and Surrogate Mixture Formulation: Components, Properties, and Combustion. *Energy Fuels* **2017**.
- (19) Liang, Z.; Hsu, C. S. Molecular Speciation of Saturates by On-Line Liquid Chromatography–Field Ionization Mass Spectrometry. *Energy Fuels* **1998**, *12* (3), 637–643.
- (20) Jin, C.; Viidanoja, J.; Li, M.; Zhang, Y.; Ikonen, E.; Kenttämä, H. I.; Root, A.; Romanczyk, M.; Manheim, J.; Dziekonski, E. Comparison of Atmospheric Pressure Chemical Ionization and Field Ionization Mass Spectrometry for the Analysis of Large Saturated Hydrocarbons. *Anal. Chem.* **2016**, *88* (21), 10592–10598.
- (21) Wang, Y.; Gu, M. The Concept of Spectral Accuracy for MS. *Anal. Chem.* **2010**, *82* (17), 7055–7062.
- (22) Kind, T.; Fiehn, O. Metabolomic Database Annotations Via Query of Elemental Compositions: Mass Accuracy Is Insufficient Even at Less Than 1 Ppm. *BMC Bioinformatics* **2006**, *7*, 234.
- (23) Khodjanizyazova, S.; Nazari, M.; Garrard, K. P.; Matos, M. P. V.; Jackson, G. P.; Muddiman, D. C. Characterization of the Spectral Accuracy of an Orbitrap Mass Analyzer Using Isotope Ratio Mass Spectrometry. *Anal. Chem.* **2017**.
- (24) G. Marshall, A.; T. Blakney, G.; Chen, T.; K. Kaiser, N.; M. McKenna, A.; P. Rodgers, R.; M. Ruddy, B.; Xian, F. Mass Resolution and Mass Accuracy: How Much Is Enough? *Mass Spectrom.* **2013**, *2* (Spec Iss).

(25) Jarrell, T. M.; Jin, C.; Riedeman, J. S.; Owen, B. C.; Tan, X.; Scherer, A.; Tykwinski, R. R.; Gray, M. R.; Slater, P.; Kenttämä, H. I. Elucidation of Structural Information Achievable for Asphaltenes Via Collision-Activated Dissociation of Their Molecular Ions in MSn Experiments: A Model Compound Study. *Fuel* **2014**, *133*, 106–114.

(26) Borton, D.; Pinkston, D. S.; Hurt, M. R.; Tan, X.; Azyat, K.; Scherer, A.; Tykwinski, R.; Gray, M.; Qian, K.; Kenttämä, H. I. Molecular Structures of Asphaltenes Based on the Dissociation Reactions of Their Ions in Mass Spectrometry. *Energy Fuels* **2010**, *24* (10), 5548–5559.

## **CHAPTER 5. METHOD DEVELOPMENT FOR THE IDENTIFICATION AND QUANTITATION OF TRACERS IN OIL RESERVOIR BRINE BY USING SOLID-PHASE EXTRACTION FOLLOWED BY HIGH PERFORMANCE LIQUID CHROMATOGRAPHY/TANDEM MASS SPECTROMETRY**

### 5.1 Introduction

During enhanced oil recovery (EOR), expensive chemicals, such as surfactants and polymers, are injected into the oil reservoir to improve the sweep efficiency and oil recovery.<sup>1-6</sup> To evaluate and optimize the application of these chemicals, information such as residual oil saturation, reservoir flow performance and other properties of the reservoir are desired.<sup>7</sup> Different varieties of tracers are chosen by the oil industry based on the kind of information desired. The information can be obtained by the injection of suitable inert tracers into the injector well along with other EOR chemicals, followed by monitoring these tracers in the frequently sampled produced fluids. Since the tracers are injected at very low concentrations and are further diluted while flowing through large reservoirs, monitoring them in the produced fluids is a huge analytical challenge and requires sensitive analytical methods. The sensitivity of the analytical method determines the initial quantity of tracer needed to be added to the oil well and therefore the total cost of the tracer experiment.

Our collaborators at Pioneer oil company have used a water tracer, 2-fluorobenzoic acid (2-FBA), for modeling their reservoirs inter-well connectivity and flood patterns. In the past, several analytical methods, such as gas chromatography (GC) coupled with mass spectrometry<sup>8,9</sup> and high-performance (HPLC) or ultra-high-performance liquid chromatography (UPLC) coupled with mass spectrometry<sup>10-12</sup> and HPLC coupled with photometric detectors,<sup>13</sup> have been reported to achieve low limits of detection (LOD) for fluorobenzoic acids. The lowest detection limit (down

to 0.01 ppb) has been reported for a GC-MS method.<sup>8,9</sup> This method achieved higher sensitivity compared to other reported analytical methods by using a 24-hour long, tedious sample preparation procedure involving matrix removal and sample derivatization.

The objective of the work discussed here was to shorten the sample preparation time by developing an alternative but equally sensitive method using a Thermo Surveyor HPLC system coupled with an LQIT mass spectrometer. To preconcentrate the fluorobenzoic acid and to remove salt and organic matrix, a solid phase extraction cartridge was used for sample preparation before HPLC-MS/MS analysis of the sample.

## 5.2 Experimental

### 5.2.1 Sample Collection and Storage

Reservoir brine samples from four different production wells collected at different times were obtained from Pioneer oil company in 500 mL sealed containers. These samples contained both organic (oil) and aqueous (brine) phases. About 250 mL of the aqueous aliquot was separated from the organic phase by using a separatory funnel and was transferred to a glass flask. The pH of this aqueous aliquot was adjusted to 2 – 3 by using formic acid. The aliquot was refrigerated prior to analysis. Under these conditions, the samples were assumed to be stable for at least 30 days. Reservoir brine samples were also collected from the production wells, just before the addition of tracer and these samples are referred to as reservoir brine blank samples in this chapter. These samples are also treated and stored similarly to reservoir brine samples.

### 5.2.2 Chemicals, Reagents, and Solvents

The standards used were 2-fluorobenzoic acid purchased from Sigma-Aldrich (2-FBA, purity > 97%, CAS: 455-29-4), 2-fluorobenzoic-d<sub>4</sub> acid purchased from CDN isotopes (2-DFBA, purity > 98.6% D, CAS: 646502-89-8), 2-chlorobenzoic acid purchased from Sigma-Aldrich (2-CBA, purity > 98%, CAS: 118-91-2), and formic acid purchased from Sigma-Aldrich (purity ≥ 95%). The solvents used were acetonitrile (Proteochem, LC/MS grade, purity 99.9%), and water (Proteochem, LC/MS grade).

### 5.2.3 Instrumentation

Experiments were conducted using a surveyor HPLC coupled with a photodiode array (PDA) detector and Thermo Scientific LTQ linear quadrupole ion trap (LQIT) mass spectrometer. The HPLC separations were performed on Zorbax SB-Phenyl 4.6 x 250 mm column with 5 μm particles under gradient conditions, and the PDA detection for all analytes was performed at 214 nm wavelength with a filter bandwidth of 9 nm.

The mass spectrometric analysis was performed in negative ionization mode by using with electrospray ionization (ESI) probe. The positioning of the ESI probe (distance from the ESI source to ion transfer capillary) was optimized in x, y and z directions to achieve a stable signal. ESI source conditions used for this experiment were as follows: 3 kV spray voltage, 40 (arbitrary units) of sheath gas flow rate (N<sub>2</sub>), 20 (arbitrary units) of auxiliary gas flow rate (N<sub>2</sub>), and 300 °C capillary temperature. The ion optics were optimized for 2-fluorobenzoic acid by using the auto-tune feature of the LTQ Tune plus software interface. During multiple reactions monitoring experiments, the advanced scan feature of the LTQ tune software interface was used to isolate ions and perform CAD as discussed in Chapter 2. The ion isolation and activation parameters were: an isolation width of 2 units, an activation q value of 0.25 and an activation time of 30 ms.

## 5.2.4 Materials

Oasis HLB plus cartridges (540 mg, 60  $\mu\text{m}$ , Part No.186004134, Waters, USA) were used for solid phase extraction. Separations were performed using a Zorbax SB-Phenyl HPLC column (4.6 x 250 mm, 5-micron).

## 5.3 Procedures

### 5.3.1 Sample Preparation

The 250-mL reservoir well sample aliquots (pH adjusted) were spiked with an internal standard, 2-fluorobenzoic- $\text{d}_4$  acid (50 ng/mL). The samples were subjected to extraction in Oasis solid-phase HLB plus extraction cartridges with 540 mg of the sorbent, as described below.

The sorbent in the SPE cartridge was initially conditioned with 10-mL of 75:25 acetonitrile/methanol solvent mixture followed by equilibration with 20-mL of de-ionized water (pH adjusted to 2.5) by rinsing the cartridge. After loading the sample on the sorbent, it was rinsed with 10-mL of de-ionized water (pH adjusted to 2.5) to remove remaining salts and polar compounds. The elution was performed with 10-mL of 75:25 acetonitrile/methanol solvent mixture. After extraction, the eluted solvent was rotovaped to dryness and reconstituted with 500  $\mu\text{L}$  of 60:40 acetonitrile/water. The reconstituted sample was spiked with a second standard, 2-chlorobenzoic acid (10  $\mu\text{g}/\text{mL}$ ). This sample was analyzed by using HPLC/UV/MS developed for the analysis of these samples. The sample preparation workflow is shown in Figure 5.1.

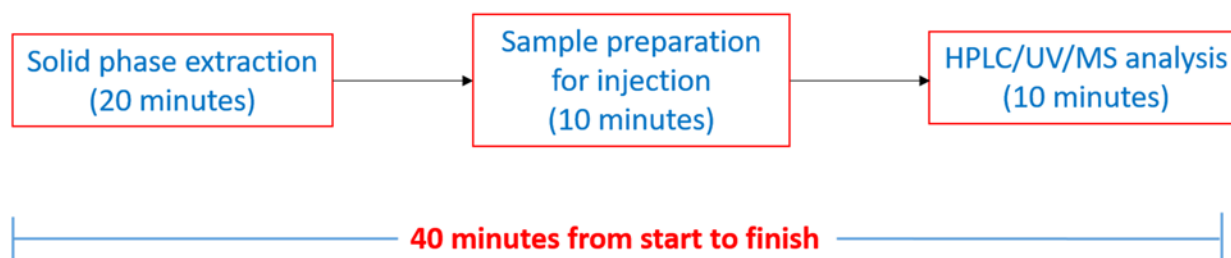


Figure 5.1 Sample preparation and analysis workflow

### 5.3.2 HPLC and MS<sup>n</sup> Analysis Conditions

A 200  $\mu\text{L}$  aliquot of the reconstituted sample was transferred into LC vial for HPLC-MS/MS analysis. The mobile phase A was LCMS grade water doped with 0.05% formic acid, and the mobile phase B was LCMS grade acetonitrile doped with 0.05% formic acid. The column and autosampler were maintained at room temperature. A full loop injection volume (25  $\mu\text{L}$ ) of the sample solution was injected onto the column. The gradient conditions used for the separation are shown in Table 5.1. Mass spectrometry data acquisition was performed with the electrospray ionization source operating in negative ionization mode under tuned optimal conditions for the ionization of 2-fluorobenzoic acid (detailed in Section 5.2.3)

Table 5.1 Gradient conditions for the HPLC separation (lower flow rate of 0.4 mL/min was used initially to prevent backpressure spike).

<b>Time (min)</b>	<b>A (%)</b>	<b>B (%)</b>	<b>Flow (mL/min)</b>
0.00	40	60	0.4
1.50	40	60	0.7
6.00	5	95	0.7
9.00	5	95	0.7
9.10	40	60	0.7
10.00	40	60	0.7

## 5.4 Results and Discussion

Direct analysis of oil reservoir brine samples (without sample preparation) by combining two different separation mechanisms such as LC and MS<sup>n</sup> multiple reaction monitoring (MRM) allow for 2-fluorobenzoic acid to be isolated from complex mixtures and the resulting selectivity achieved by these methods provides confidence that the correct component is being measured. However, because the analyte of interest, 2-fluorobenzoic acid is usually present in very dilute concentrations in the reservoir brine samples, a pre-concentration sample preparation step using solid-phase extraction (SPE) was considered before LC/MS<sup>n</sup> analysis, to maximize the analyte recovery.

The SPE method was developed to achieve selective extraction of 2-fluorobenzoic acid while removing as many interferences (such as inorganic ions and other organic components) as possible from reservoir brine. The challenge with developing a quantitative method involving solid-phase extraction (SPE) technique is, to account for the variability in sample recovery between different batches of SPE cartridges. This issue was addressed by spiking the sample with a stable isotopically labelled internal standard, 2-fluorobenzoic-d<sub>4</sub> acid during sample preparation. This deuterated analogue not only accounts for the variability occurring during sample recovery but also during ionization, which is caused due to matrix interferences. The accurate and reliable quantitation was achieved by considering the relative response ratios of the deuterated internal standard with its unlabelled analogue.

The other problem encountered during method development is the unpredictable shifts in the retention time for 2-fluorobenzoic acid elution when spiked in different reservoir brine samples. In order to allow for positive identification based on the retention time of 2-fluorobenzoic acid, a chromatographically resolvable second internal standard (2-chlorobenzoic acid) was spiked into



the samples post extraction and before HPLC/MS analysis. This allowed for the identification of 2-fluorobenzoic acid based on its relative retention time. The relative retention time of 2-chlorobenzoic acid with respect to 2-fluorobenzoic acid was observed to be  $0.36 \pm 0.03$  min. The further details of the method development are discussed below.

#### 5.4.1 LC/MS Method Development

Arguably, developing an excellent chromatographic method is very critical to develop a robust LC/MS assay as this affects the selectivity and sensitivity by interfering with the ionization mechanism of the analyte of interest. If the components in the matrix co-elute with the analyte of interest, the response of the analyte measured becomes biased or have poor precision. This phenomenon was popularly known as “matrix effects.” To avoid matrix effects, a reasonably good chromatographic method was developed on a Zorbax SB-Phenyl LC column under gradient conditions (details of the method are discussed in the procedure). This method was evaluated by spiking known concentration of 2-fluorobenzoic acid standard into one of the reservoir brine sample matrices. However, due to significant matrix variability observed between different reservoir wells samples and the variability between samples of the same reservoir well collected at different time points, a clean separation of tracer using the same chromatographic method for all the reservoir samples was not practically possible. The issue associated with the matrix effects was resolved by including pre-sample cleanup using solid phase extraction and the addition of isotopically labelled internal standard to the sample.

#### 5.4.1.1 Extraction Using Solid Phase Extraction

For separating 2-fluorobenzoic acid from interfering sample matrices and for simultaneous preconcentrating, solid phase extraction cartridge was used. Different solid-phase extraction substrates have been reported earlier to enrich fluorobenzoic acids out of aqueous samples.<sup>13,14</sup> For the purposes of our study, Oasis HLB cartridges were selected due to their reported ability to achieve best recoveries of acidic compounds such as 2-fluorobenzoic acid.<sup>8</sup>

The method development for solid phase extraction involves four critical steps namely, 1. wetting and conditioning, 2. sample loading, 3. wash/ rinse and 4. Elution. Each step in the extraction procedure was optimized, and the details of the optimized extraction method are provided in the sample preparation procedure. To ensure optimal target analyte retention, the sample was pretreated before solid phase extraction by adjusting the ionic strength/ pH of the sample below the pKa of 2-fluorobenzoic acid (3.27). Further, to account for the variations in sample recovery, a stable isotopically labelled internal standard (2-fluorobenzoic -d<sub>4</sub> acid) was added to the sample during sample preparation. To elute 2-fluorobenzoic acid effectively from the cartridge, different solvents (water, acetonitrile, methanol) and solvent combinations were evaluated, and the optimal extraction was achieved by using 75:25 acetonitrile/methanol solvent mixture.

The percentage extraction efficiency for 2-fluorobenzoic acid on Oasis HLB cartridge using the developed extraction protocol was calculated by using the equation below.

$$\% \text{ Extraction efficiency} = \frac{\text{concentration of 2-fluorobenzoic acid measured after extraction}}{\text{concentration of 2-fluorobenzoic acid assuming 100\% retention}} \times 100$$

The concentration of 2-fluorobenzoic acid after solid phase extraction can be obtained by multiplying the concentration of known 2-fluorobenzoic acid spiked into the reservoir brine

sample prior to solid phase extraction, with the enrichment factor. The enrichment factor is the volume ratio of the sample volume before extraction and after extraction. For example, in this study, the 2-fluorobenzoic acid was spiked at 50 ng/mL concentration in 250 mL of reservoir brine sample and is subjected to sample extraction procedure detailed in section 5.3.1 . The enriched 2-fluorobenzoic acid was eluted into the collection vial using suitable acetonitrile/methanol solvent mixture, which was further rotovaped and reconstituted in 500  $\mu$ L (0.5 mL) of solvent (final volume) before LCMS analysis. The concentration of 2-fluorobenzoic acid after solid phase extraction was determined to be 10500 ng/mL (10.5 ppm) using LC/MS<sup>n</sup> analysis. The concentration of 2-fluorobenzoic acid assuming 100 % retention is calculated to be 12500 ng/mL (50 ng/mL x 250 mL). The volume ratio (250 mL/0.5 mL) gives an enrichment factor of 500. Therefore, the percentage extraction efficiency for solid phase extraction cartridge was calculated to be about 84% with a relative standard deviation of 3.1% (5 replicate studies).

#### 5.4.1.2 Mass Spectrometer Optimization

After the development of LC method, optimization of mass spectrometer parameters is necessary to achieve excellent sensitivity and reproducibility. There are many parameters that affect the ionization and detection of analytes in a mass spectrometer. However, only the parameters that have a significant impact on quantitation such as positioning of the ESI probe, ESI nebulization conditions, ion de-solvation parameters and ion trap parameters were optimized (the optimized conditions are provided in Section 5.2.3).

### 5.4.1.3 MS/MS Analysis

Selected ion monitoring (SIM) is a mass spectrometric acquisition mode that can be used to selectively scan for the masses of specific ions generated from the analyte of interest. Initially, this approach was used for the selective identification and quantitation of 2-fluorobenzoic acid (Figure 5.2).

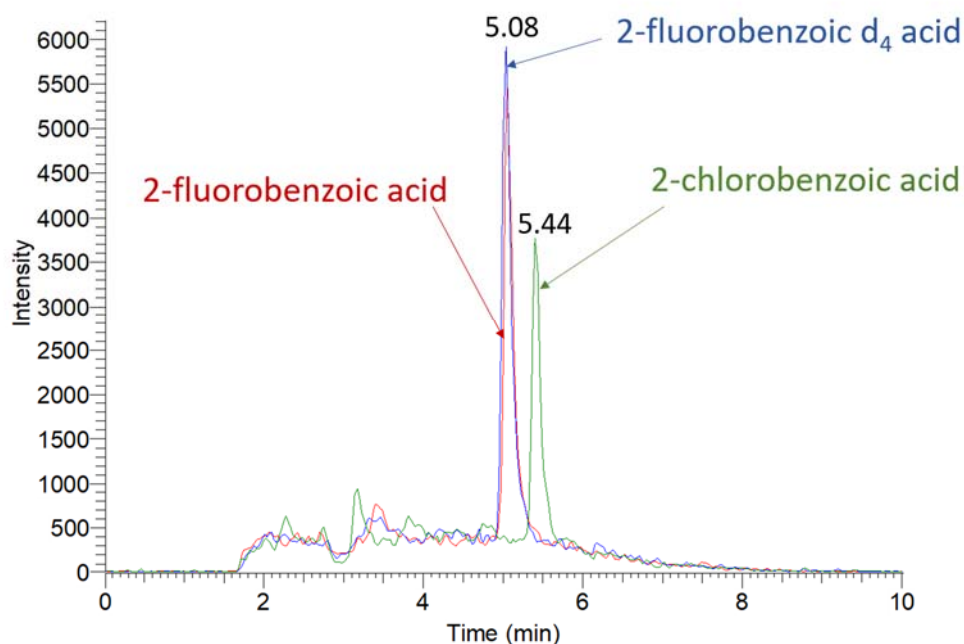


Figure 5.2 The chromatogram corresponding to the selective ion monitoring analysis (of ions of  $m/z$  139, 143 and 155) of reservoir brine blank sample spiked with 2-fluorobenzoic acid ( $m/z$  139), 2-fluorobenzoic- $d_4$  acid ( $m/z$  143) and 2-chlorobenzoic acid ( $m/z$  155) each at  $0.25 \mu\text{g/mL}$  concentration. The selected ion monitoring generated simple chromatograms of selected masses

However, when analyzing the samples collected from few reservoir brine samples, even the use of selective ion monitoring did not eliminate the matrix interference, due to the coelution of isobaric analyte ions. One such example is shown in Figure 5.3A. Although the selective ion monitoring is typically expected to generate a simple chromatogram for selected mass, it generated

complex chromatograms for the reservoir brine samples spiked with 2-fluorobenzoic acid. This is due to the presence of isobaric ions in the sample matrix. In these situations, the automated peak detection and integration algorithm performed improper integration, therefore providing inaccurate quantitation values for 2-fluorobenzoic acid. This problem could be minimized by manual integration while processing the data. To overcome this problem without manual intervention and to achieve more selectivity, a tandem mass spectrometric technique called “multiple reaction monitoring (MRM)” was used. MRM allows the monitoring of specific collision-activated dissociation (CAD) reactions for each analyte of interest. This technique provides the needed confidence that the correct analyte is being monitored. This is typically accomplished by monitoring two reactions, which involves the detection of precursor ions followed by monitoring a specific fragment ion produced from the precursor ion upon CAD. Figure 5.3B shows a chromatogram corresponding to the multiple reaction monitoring analysis of the same sample as discussed in Figure 5.3A. The interference from isobaric ions (as observed in Figure 5.3A) was removed by monitoring the specific fragment ion ( $m/z$  95) produced from ionized 2-fluorobenzoic acid ( $m/z$  139) after CAD.

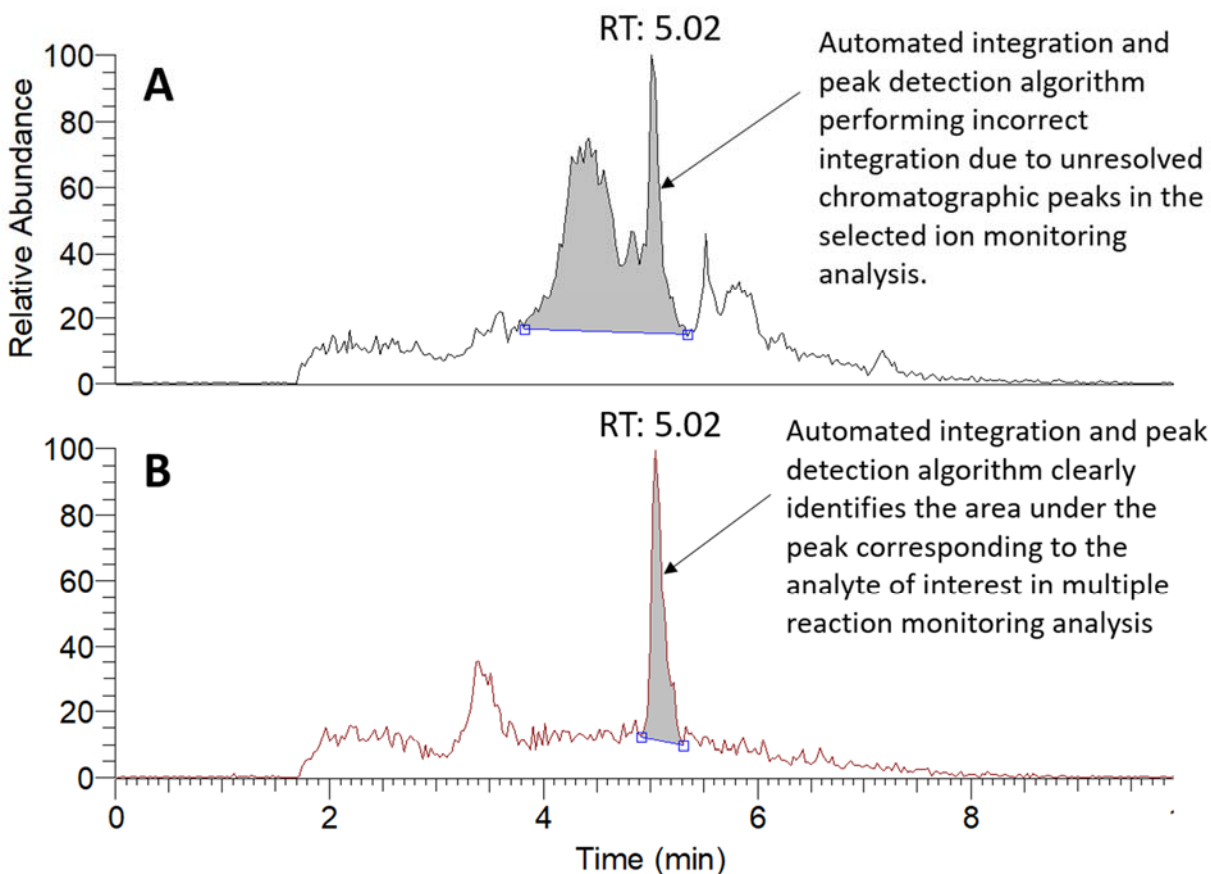


Figure 5.3 A) The chromatogram corresponding to the selective ion monitoring analysis of reservoir brine spiked with 2-fluorobenzoic acid ( $m/z$  139) at  $0.33 \mu\text{g/mL}$  concentration. The chromatogram generated is complicated and the peak eluting at 5.02 minutes corresponds to 2-fluorobenzoic acid and is partially obscured by isobaric ions derived from the matrix B) The chromatogram corresponding to the multiple reaction monitoring analysis of the same sample discussed in part A. Monitoring the specific fragment ion ( $m/z$  95) produced from ionized parent ion ( $m/z$  139) after CAD, clearly shows the peak corresponding to 2-fluorobenzoic acid, by eliminating the interference from co-eluting isobaric ions.

By comparison (Figure 5.3A and B), the multiple reaction monitoring of the reactions clearly shows the peak corresponding to the analyte of interest even in a complex matrix with coeluting isobaric ions. The HPLC method coupled with multiple reaction monitoring tandem mass spectrometric technique developed for 2-fluorobenzoic acid can be considered as having excellent specificity.

#### 5.4.1.3.1 Optimization of MRM Conditions

The ion trap parameters that can be optimized for multiple reaction monitoring reaction include mainly the CAD energy. The degree of fragmentation of each parent ion in the ion trap is dependent on the amount of collision energy provided. The high value for CAD energy was preferred in this experiment in order to fragment the parent ion completely and thereby reduce interference from isobaric interference. For example, At CAD energy of 16, 2-fluorobenzoic acid completely fragmented to produce characteristic fragment ion of m/z 95 and therefore selected as the optimal CAD energy to monitor this reaction. The MRM conditions used for monitoring the reactions for 2-fluorobenzoic acid, 2-fluorobenzoic-d<sub>4</sub> acid, and 2-chlorobenzoic acid are provided in Table 5.2. The parent ion and its corresponding fragment ion monitored for MRM reactions are generally represented as “parent ion → characteristic fragment ion”. The HPLC-MS/MS chromatograms measured under optimized conditions for a reservoir sample spiked with 2-fluorobenzoic acid (139 →95), 2-fluorobenzoic-d<sub>4</sub> acid (143 →95) and 2-chlorobenzoic acid (155 →111) are shown in Figure 5.4.

Table 5.2 Multiple reaction monitoring conditions

	Compound	Precursor ion	Fragment ion	CAD energy	Reactions
1	2-fluorobenzoic acid	139	95	16	139 → 95
2	2-fluorobenzoic-d <sub>4</sub> acid	143	95	16	143 → 95
3	2-chlorobenzoic acid	155	111	20	155 → 111

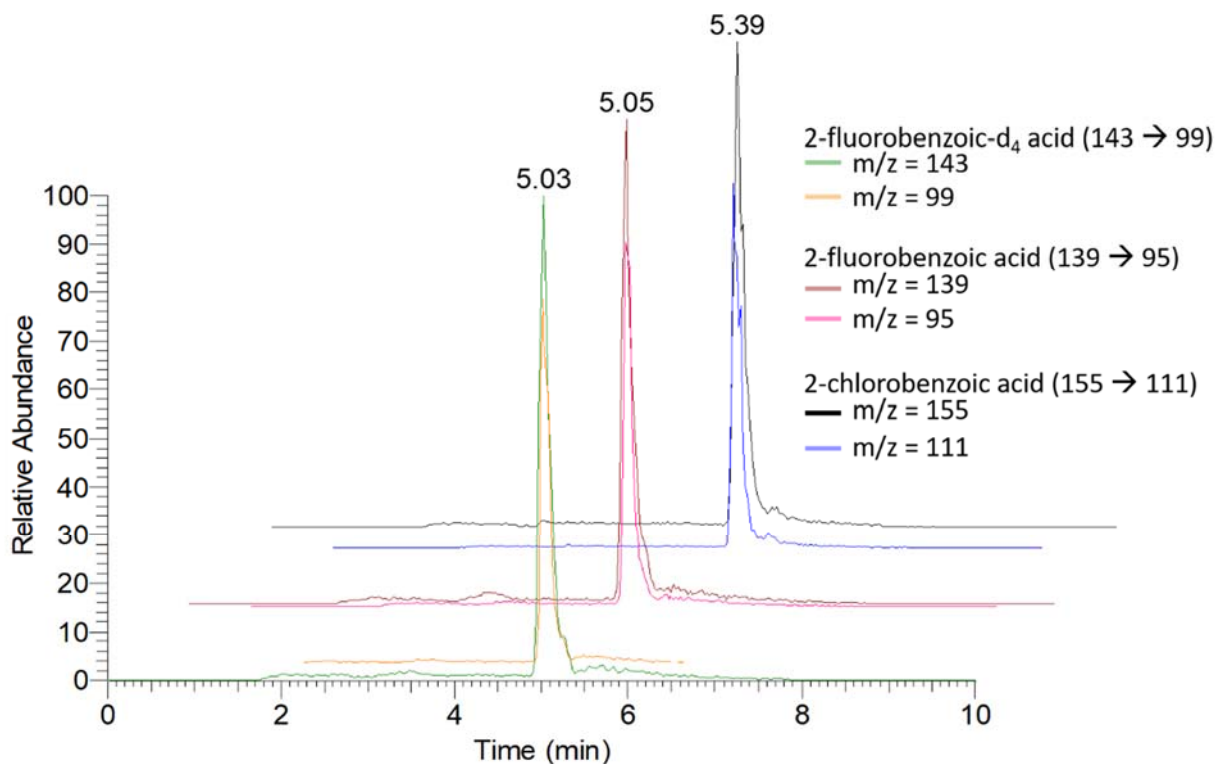


Figure 5.4 The overlay 3D MS/MS chromatograms for a reservoir sample spiked with 2-fluorobenzoic-d<sub>4</sub> acid, 2-fluorobenzoic acid and 2-chlorobenzoic acid at about 5 µg/mL concentrations. Monitoring both the precursor ion and the fragment ion associated with the precursor ion makes the method more sensitive and selective compared to selected ion monitoring.

#### 5.4.2 Method Assessment

The developed analytical methods sensitivity is dependent on the combination of factors such as a) extraction efficiency of the cartridge, b) LC conditions and c) mass spectrometer response. The detection and quantitation limits were established for this method based on the signal-to-noise (S/N) ratio at a particular concentration upon LCMS analysis. The detection limit was defined in this method as the concentration of 2-fluorobenzoic acid that will achieve a S/N ratio of three and quantitation limits for this method was reported as the concentration of 2-fluorobenzoic acid that will achieve a S/N ratio of ten. Since the mass spectrometer shows linear



response over a certain concentration range before reaching saturation, either at the detector or in the ion source, the linear dynamic range for this method must be evaluated. In this method, the stable isotopically labelled internal standard (2-fluorobenzoic-d<sub>4</sub> acid) was spiked into the samples and standards to achieve accurate quantitation by accounting for the variability in sample preparation, LC injection and matrix effects. Therefore, the relative response factor for 2-fluorobenzoic acid to its deuterated analogue must be determined.

In order to establish above-discussed limits for this method, Direct analysis of reservoir brine blank samples spiked with a range of known concentrations (0.16, 0.25, 0.33, 1.6, 3.3, 5.0, 8.3, 16.6, 33.3 and 66.6 ppm) of 2-fluorobenzoic acid and its deuterated analogue were performed. Two calibration curves were plotted for these concentrations, by plotting the peak areas of the fragment ions (m/z 95 and m/z 99) derived upon CAD from parent ion of 2-fluorobenzoic acid (m/z 139) and its deuterated analogue (m/z 143). The calibration curves showed good linearity for both 2-fluorobenzoic acid and its isotope analogue ( $r^2 > 0.99$ ) in the concentration range of 0.16 ppm up to 33.3 ppm (Figure 5.5). The equations of the form  $y = mx + c$  was utilized for the calibration, where  $x$  = concentration of the standards in ppm and  $y$  = peak area of the characteristic fragments m/z 95 and m/z 99 obtained from 2-fluorobenzoic acid and its deuterated analogue respectively. The relative response factor for 2-fluorobenzoic acid and its isotope analog was determined to be about one from their slopes by using the equation shown below.

$$\text{Relative response factor} = \frac{\text{slope of 2-fluorobenzoic-d}_4\text{acid}}{\text{slope of 2-fluorobenzoic acid}}$$

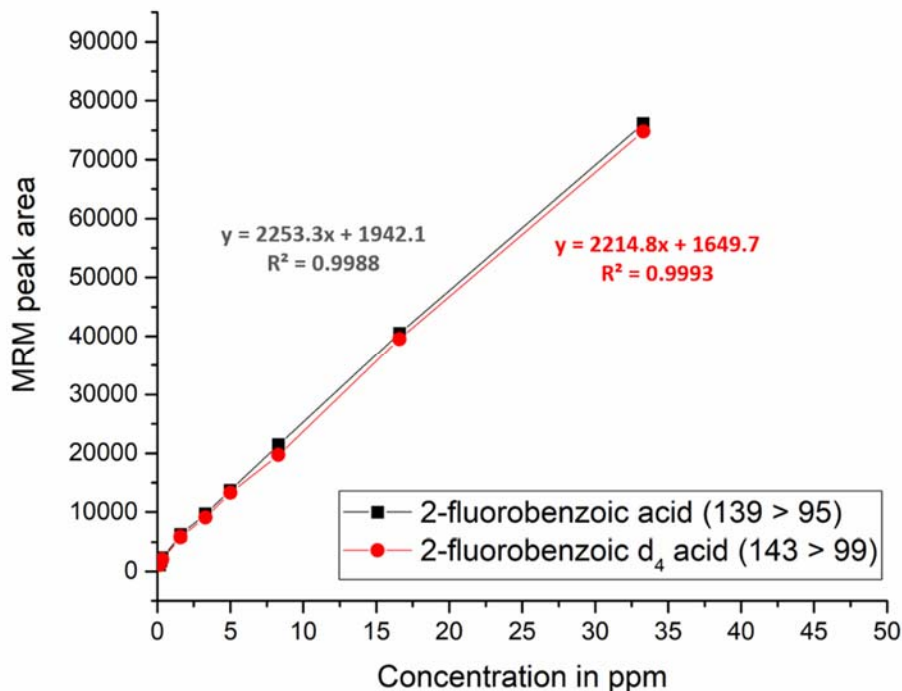


Figure 5.5 Calibration curve for 2-fluorobenzoic acid and 2-fluorobenzoic-d<sub>4</sub> acid. The calibration curve equations for seven different concentrations of standards are provided in the figure.

Using this data, the instrument detection limit was determined to be 160 ppb, since the S/N ratio is greater than three above this concentration. However, this detection limit which is measured by direct analysis of the sample does not consider the solid-phase extraction step, which results in sample pre-concentration/sample enrichment. To measure these practical limits, 250-mL reservoir brine blank samples were spiked with a range of known concentrations (0.5, 0.66, 3.2, 6.6, 10, 16.6, 33.2 and 66.4 ppb) of 2-fluorobenzoic acid and its deuterated analogue was subjected to solid-phase extraction and other sample steps as described in Section 5.3.1. These standards were analyzed by using HPLC/MS<sup>n</sup> method developed, and the calibration curves were plotted similarly as described above. The practical method detection limit was determined to be 3.2 ppb, and the quantitation limit was established to be 10 ppb for 2-fluorobenzoic acid.

### 5.4.3 Results for Oil Reservoir Brine Samples

The levels of 2-fluorobenzoic acid were quantitated in various oil reservoir well samples obtained from Pioneer oil company. A chromatograms showing the peaks corresponding to the specific fragment ions produced upon CAD of ionized parent ions of 2-fluorobenzoic acid, 2-fluorobenzoic-d4 acid and 2-chlorobenzoic acid and UV absorption spectrum of a reservoir well sample (no 12) collected from one of the Pioneer oil wells after 92 days of tracer injection is shown in Figure 5.6 as an example. Using HPLC/ MS<sup>n</sup> analytical method coupled with solid-phase extraction, the concentration of the tracer in this reservoir oil well was determined to be 15.2 ppb. All the samples were prepared as discussed in Section 5.3.1 and the relative responses of 2-fluorobenzoic acid if detected were compared to the known concentration of its deuterated analogue for quantitation. The results of other oil wells are presented in Table 5.3.

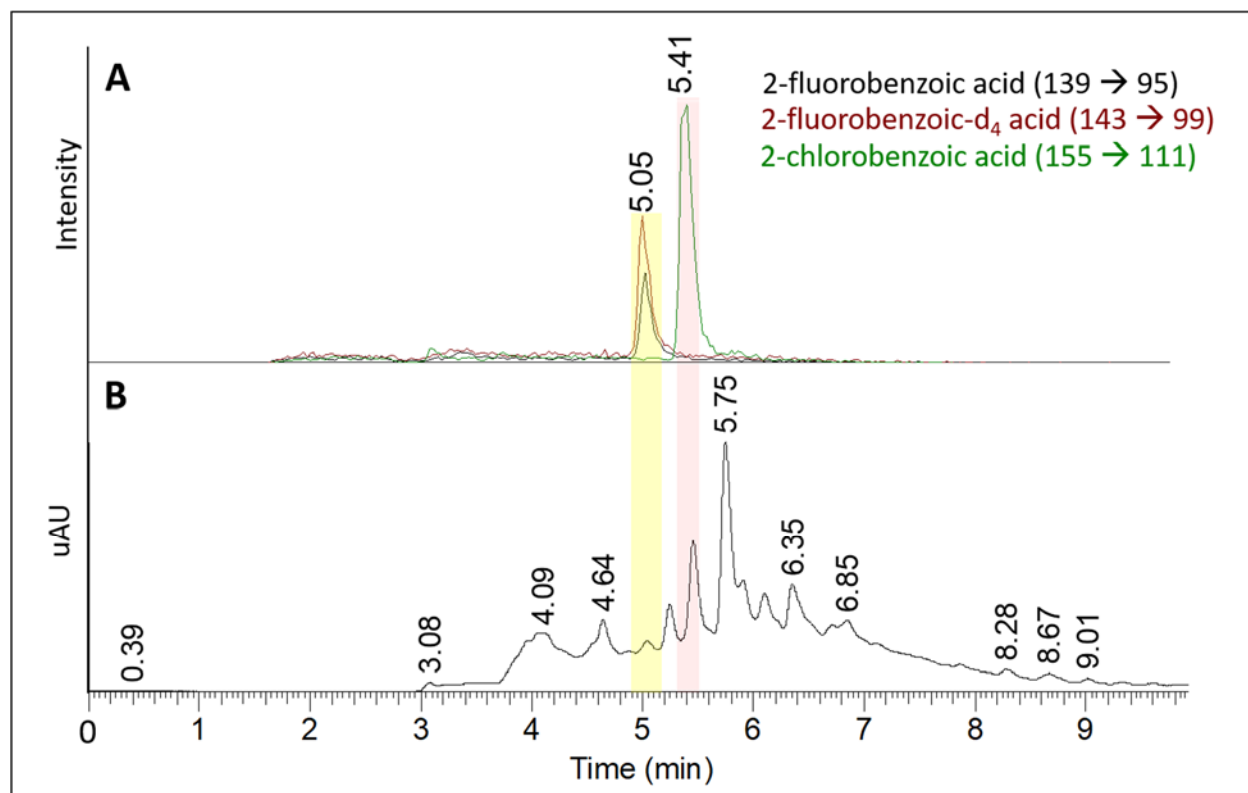


Figure 5.6 Chromatogram of oil reservoir brine sample (no 12) spiked with two internal standards. A) The chromatogram showing the MRM transitions of 2-fluorobenzoic acid, 2-fluorobenzoic-d<sub>4</sub> acid, and 2-chlorobenzoic acid B) The UV absorption spectrum of the sample at 214 nm wavelength. The peaks corresponding to the tracer and the internal standards is obscured in the matrix of other UV absorbing compounds present in the matrix, not allowing for identification or quantitation.

Table 5.3 Results on levels of 2-fluorobenzoic acids in ppb (ng/mL) in the analyzed samples.

Sample number	Production Well number	Days After Injection (days)	2-FBA PPB Purdue
1	1	12	0
2	1	33	0
3	1	61	0
4	1	75	0
5	1	96	Detected but below quantitation limit
6	1	110	Detected but below quantitation limit
7	1	124	Detected but below quantitation limit
8	2	12	0
9	2	33	0
10	2	61	0
11	2	75	0
12	2	96	15.2
13	2	110	14.9
14	2	124	42
15	3	12	0
16	3	33	0
17	3	61	0
18	3	75	0
18	3	96	0
20	3	110	Detected but below quantitation limit
21	3	124	Detected but below quantitation limit
22	4	12	0
23	4	33	0
24	4	61	0
25	4	75	0
26	4	96	0
27	4	110	Detected but below quantitation limit
28	4	124	Detected but below quantitation limit

## 5.5 Conclusions

The development of a method based on a solid-phase extraction followed by HPLC tandem mass spectrometry is described in this chapter for the quantitation of 2-fluorobenzoic acid in oil reservoir brine samples. The method achieved a 500-fold enrichment of 2-fluorobenzoic acid for reservoir brine samples after solid phase extraction with Oasis HLB cartridges. The extraction efficiencies for these cartridges were found to be 84 % with a relative standard deviation of 3.1%. After extraction, the samples were analyzed for the tracer, 2-fluorobenzoic acid by LC and MS<sup>n</sup> multiple reaction monitoring (MRM). This method allows for 2-fluorobenzoic acid to be isolated from complex mixtures and the resulting selectivity achieved by LC/MS<sup>n</sup> methods provide confidence that the correct component is being measured. The addition of deuterated analogue of 2-fluorobenzoic acid to the samples during sample preparation, not only accounts for the variability in sample extraction and recovery but also accounts for variability in ionization caused due to matrix effects and therefore allows for accurate quantitation of tracer. The practical detection limits for this method were determined to be 3.2 ppb, and the quantitation limits are at 10 ppb in reservoir brine sample matrices. Although this method could not achieve the sensitivity of the previously published work on GC-MS,<sup>9</sup> this method provides a high throughput capability by eliminating the tedious sample derivation and sample preparation steps. The method developed here is 36 times faster than the reported GC-MS method.<sup>9</sup> Further improvements in the detection limits can be achieved by using UPLC and more sensitive mass spectrometers. The method was used for the identification and quantitation of tracers in oil reservoir brine samples.

## 5.6 References

- (1) Denney, D. Alkaline/Surfactant/Polymer Flood: Single-Well Chemical-Tracer Tests - Design, Implementation, and Performance. *J. Pet. Technol.* **2011**, *63* (06), 86–88.
- (2) Hernandez, C.; Chacon, L.; Anselmi, L.; Angulo, R.; Manrique, E.; Romero, E.; de Audemard, N.; Carlisle, C. Single Well Chemical Tracer Test to Determine ASP Injection Efficiency at Lagomar VLA-6/9/21 Area, C4 Member, Lake Maracaibo, Venezuela; Society of Petroleum Engineers, 2002.
- (3) Taber, J. J.; Martin, F. D.; Seright, R. S. EOR Screening Criteria Revisited - Part 1: Introduction to Screening Criteria and Enhanced Recovery Field Projects. *SPE Reserv. Eng.* **1997**, *12* (03), 189–198.
- (4) Taber, J. J.; Martin, F. D.; Seright, R. S. EOR Screening Criteria Revisited—Part 2: Applications and Impact of Oil Prices. *SPE Reserv. Eng.* **1997**, *12* (03), 199–206.
- (5) Zainal, S.; Manap, A. A. A.; Hamid, P. A.; Othman, M.; Chong, M. B. O.; Yahaya, A. W.; Darman, N. B.; Mat Sai, R. Offshore Chemical EOR: The Role of an Innovative Laboratory Program in Managing Result Uncertainty to Ensure the Success of a Pilot Field Implementation; Society of Petroleum Engineers, 2008.
- (6) Zwart, A. H. de; Batenburg, D. W. van; Stoll, M.; Al-Harthi, S. Numerical Interpretation of Single Well Chemical Tracer Tests for ASP Injection; 2011.
- (7) Guan, L.; Du, Y.; Johnson, S.; Choudhary, M. Advances of Interwell Tracer Analysis in the Petroleum Industry. *J. Can. Pet. Technol.* **2005**, *44* (5).
- (8) Müller, K.; Seubert, A. Ultra Trace Determination of Fluorobenzoic Acids in Tap and Reservoir Water Using Solid-Phase Extraction and Gas Chromatography–mass Spectrometry. *J. Chromatogr. A* **2012**, *1260*, 9–15.
- (9) Müller, K.; Seubert, A. Ultra Trace Determination of Fluorobenzoic Acids in Reservoir and Ground Water Using Isotope Dilution Gas Chromatography Mass Spectrometry. *Isotopes Environ. Health Stud.* **2014**, *50* (2), 277–284.
- (10) Juhler, R. K.; Mortensen, A. P. Analysing Fluorobenzoate Tracers in Groundwater Samples Using Liquid Chromatography–tandem Mass Spectrometry: A Tool for Leaching Studies and Hydrology. *J. Chromatogr. A* **2002**, *957* (1), 11–16.
- (11) Serres-Piole, C.; Moradi-Tehrani, N.; Lobinski, R.; Preud'homme, H. Direct Sensitive Simultaneous Determination of Fluorinated Benzoic Acids in Oil Reservoir Waters by Ultra High-Performance Liquid Chromatography–Tandem Mass Spectrometry. *J. Chromatogr. A* **2011**, *1218* (34), 5872–5877.
- (12) Müller, K.; Seubert, A. Separation and Determination of Fluorobenzoic Acids Using Ion Chromatography–electrospray Mass Spectrometry. *J. Chromatogr. A* **2012**, *1270*, 96–103.

- (13) Galdiga, C. U.; Greibrokk, T. Trace Analysis of Fluorinated Aromatic Carboxylic Acids in Aqueous Reservoir Fluids by HPLC. *J. Liq. Chromatogr. Relat. Technol.* **1998**, *21* (6), 855–868.
- (14) Weigel, S.; Kallenborn, R.; Hühnerfuss, H. Simultaneous Solid-Phase Extraction of Acidic, Neutral and Basic Pharmaceuticals from Aqueous Samples at Ambient (Neutral) PH and Their Determination by Gas Chromatography–mass Spectrometry. *J. Chromatogr. A* **2004**, *1023* (2), 183–195.



## VITA

Ravikiran Yerabolu was born in Nellore, Andhra Pradesh, India on May 31<sup>st</sup>, 1987. From an early age, he was always very excited about science and technology. He decided on pursuing Pharmacy as an undergraduate at MGR Medical University and found himself engaged especially in the fields of chemistry and biochemistry. He graduated with a perfect 4.0 GPA and received “Outstanding Student Award” for four consecutive years, a prestigious award given to one outstanding student every year for their overall performance. Over the four years of his undergraduate career and after working as a Chemist for a year in Penn Bio-chemicals, India, his aptitude for research had increased, and he decided to pursue further education. In January 2011, he enrolled in Governors State University, Illinois, for a master’s program in Analytical chemistry. Shortly after graduating, he accepted a position at Teva Pharmaceuticals, New York, where he developed and validated analytical methods for approval/licensing as a part of new drug application submissions to Food and Drug Administration. After working in the industry for a short time, he decided to make his future in the field of Analytical Chemistry, especially Mass Spectrometry. To pursue his interests, Ravi applied for a Ph.D. program at Purdue University, knowing the school's fantastic reputation in the field of Mass Spectrometry. Once accepted, he launched himself into the Ph.D. program and joined Professor Hilikka I Kenttämä group, where he worked in collaboration with companies such as AstraZeneca, Merck, and Pioneer Oil, toward developing advanced analytical methodologies for the characterization of complex mixtures. During his time at Purdue University, Ravi also met the love of his life, Veda, who was also pursuing her Ph.D. at Purdue University. They got married on October 1<sup>st</sup>, 2017 and are very excited to start their new future together. In February 2018, Ravi successfully defended his dissertation and was granted his Ph.D.

## PUBLICATIONS

1. Huaming Sheng, Weijuan Tang, **Ravikiran Yerabolu**, John Kong, Peggy Williams, Minli Zhang, Hilikka I. Kenttämää,\* Mass Spectrometric Identification of the *N*-Monosubstituted *N*-Hydroxylamino Functionality in Protonated Analytes via Ion/molecule Reactions in Tandem Mass Spectrometry, *Rapid Commun. Mass Spectrom.* **2015**, *29*, 730-734.
2. Huaming Sheng, Weijuan Tang, **Ravikiran Yerabolu**, Joann Max, Raghavendar R. Kotha, James S. Riedeman, Minli Zhang, Hilikka I. Kenttämää,\* Identification of *N*-Oxide and Sulfoxide Functionalities in Protonated Drug Metabolites by Using Ion-molecule Reactions Followed by Collisionally Activated Dissociation in a Linear Quadrupole Ion Trap Mass Spectrometer, *J. Org. Chem.* **2016**, *81*, 575-586.
3. Weijuan Tang, Huaming Sheng, John Kong, **Ravikiran Yerabolu**, Hanyu Zhu, Minli Zhang, Hilikka I. Kenttämää,\* Gas-phase Ion/Molecule Reactions for the Identification of Sulfone Functionalities in Protonated Analytes in a Linear Quadrupole Ion Trap Mass Spectrometer, *Rapid Commun. Mass Spectrom.* **2016**, *30*, 1435-1441.
4. James Riedeman, Tiffany Jarrell, Chunfen Jin, Huaming Sheng, **Ravikiran Yerabolu**, John Kong, Hilikka I. Kenttämää,\* Ion/Molecule Reactions of Dimethylamine with Protonated Analytes Facilitate the Identification of Tertiary *N*-Oxide Functionalities in a Linear Quadrupole Ion Trap Mass Spectrometer, *Int. J. Mass Spectrom.* **2017**.
5. Priya Murria, Celeb k. Miskin, Robert Boyne, Laurance T. Cain, **Ravikiran Yerabolu**, Evan C. Wegener, Jeffrey T. Miller, Hilikka I. Kenttämää, Rakesh Agrawal,\* Speciation of CuCl and CuCl<sub>2</sub> Thiol-Amine Solutions and Characterization of Resulting Drop Cast Thin Films: Implications for Device Fabrication, *Inorg. Chem.*, **2017** Accepted. DOI: [10.1021/acs.inorgchem.7b01359](https://doi.org/10.1021/acs.inorgchem.7b01359).

*Rapid Commun. Mass Spectrom.* 2015, 29, 730–734  
(wileyonlinelibrary.com) DOI: 10.1002/rcm.7154

## Mass spectrometric identification of the *N*-monosubstituted *N*-hydroxylamino functionality in protonated analytes via ion/molecule reactions in tandem mass spectrometry

Huaming Sheng<sup>1</sup>, Weijuan Tang<sup>1</sup>, Ravikiran Yerabolu<sup>1</sup>, John Y. Kong<sup>1</sup>, Peggy E. Williams<sup>1</sup>, Minli Zhang<sup>2</sup> and Hilkka I. Kenttämä<sup>1\*</sup>

<sup>1</sup>Purdue University, Department of Chemistry, West Lafayette, IN 47907, USA

<sup>2</sup>AstraZeneca, Boston, MA 02130, USA

**RATIONALE:** *N*-Monosubstituted hydroxylamines correspond to an important class of metabolites for many bioactive molecules. In this study, a tandem mass spectrometric method based on ion/molecule reactions was developed for the identification of compounds with the *N*-monosubstituted hydroxylamino functionality.

**METHODS:** The diagnostic ion/molecule reaction occurs between protonated analytes with 2-methoxypropene (MOP) inside a linear quadrupole ion trap mass spectrometer.

**RESULTS:** Most protonated compounds with *N*-monosubstituted and disubstituted hydroxylamino and oxime functional groups react with MOP via proton transfer and formation of a stable adduct in a linear quadrupole ion trap mass spectrometer. However, only protonated compounds with *N*-monosubstituted hydroxylamino groups form the characteristic MOP adduct–MeOH product. Possible mechanisms of this reaction are discussed.

**CONCLUSIONS:** A method based on functional group-selective ion/molecule reactions in a linear quadrupole ion trap mass spectrometer has been demonstrated to allow the identification of protonated compounds with the *N*-monosubstituted hydroxylamino functionality. Only *N*-monosubstituted hydroxylamines react with MOP via formation of an adduct that has eliminated methanol. Copyright © 2015 John Wiley & Sons, Ltd.

*N*-Monosubstituted hydroxylamines correspond to an important class of metabolites common for many bioactive molecules containing primary amino or nitro functionalities, such as the anti-tumor prodrug CB 1954, Dapsone, and sulfamethoxazole.<sup>[1–6]</sup> Hydroxylamine metabolites often display completely different bioactivities than their parent compounds. For example, Dapsone's hydroxylamine metabolite is reported to cause adverse effects, such as methemoglobinemia and hemolysis.<sup>[7]</sup> On the other hand, sulfamethoxazole's hydroxylamine metabolite shows even greater bioactivity than sulfamethoxazole itself.<sup>[8]</sup> Hence, it is essential to identify these *N*-hydroxylamine metabolites. However, the small quantity and unstable nature of these *N*-hydroxylamine drug metabolites make it challenging to characterize these compounds by using conventional analytical methods, such as nuclear magnetic resonance (NMR) or Fourier transform infrared (FT-IR) spectroscopy, in highly complex plasma.<sup>[9]</sup> Moreover, no characteristic fragmentation behavior has been found for ionized hydroxylamine metabolites in tandem mass spectrometry (MS/MS) experiments based on collision-induced dissociation (CID).<sup>[2,10]</sup> MS/MS methods based on ion/molecule reactions of ionized analytes hold great promise for being able to provide information useful in the

identification of specific functional groups.<sup>[11–15]</sup> Our group has successfully developed such methods for the identification of many different functionalities in protonated analytes.<sup>[12–20]</sup> In the work presented here, gas-phase ion/molecule reactions of 2-methoxypropene (MOP) are demonstrated to allow the identification of the protonated *N*-monosubstituted hydroxylamine functionality in a linear quadrupole ion trap.

## EXPERIMENTAL

### Chemicals

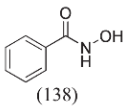
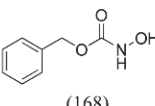
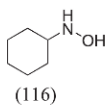
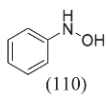
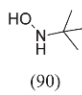
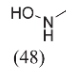
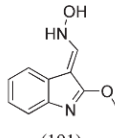
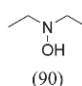
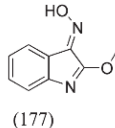
The indole hydroxylamine and oxime derivatives (Table 1) were provided by AstraZeneca. All other chemicals were purchased from Sigma-Aldrich. Their purities were ≥98%. All chemicals were used without further purification.

### Instrumentation

All mass spectrometry experiments were performed using a Thermo Scientific LTQ linear quadrupole ion trap (LQIT) equipped with an electrospray ionization (ESI) source. Sample solutions were prepared in methanol at analyte concentrations ranging from 0.01 up to 1 mg/mL. An integrated syringe driver directly infused the solutions into the ESI source at a rate of 20 μL/min. In the ESI source (operated in positive ion mode), the vaporizer and capillary temperatures were set at 400 °C and 265 °C, respectively.

\* Correspondence to: H. I. Kenttämä, Purdue University, Department of Chemistry, West Lafayette, IN 47907, USA.  
E-mail: hilkka@purdue.edu

**Table 1.** Reactions of MOP ( $PA^a = 214$  kcal/mol), their efficiencies, and different reaction pathway branching ratios for protonated hydroxylamines

Reagent ( $m/z$ of $[M+H]^+$ )	PA (kcal/mol)	Observed reactions <sup>b</sup> and their branching ratios <sup>c</sup>	Reaction efficiency <sup>d</sup>	
 (138)	211.7 <sup>a</sup>	Proton transfer (73) <b>Adduct-MeOH (188)</b> Adduct (210)	87% 12% 1%	35%
 (168)	–	Proton transfer (73) <b>Adduct-MeOH (208)</b> Adduct (240)	63% 4% 23%	3%
 (116)	216.0 <sup>a</sup>	Proton transfer (73) <b>Adduct-MeOH (156)</b> Adduct (188)	51% 25% 24%	5%
 (110)	204.6 <sup>a</sup>	Proton transfer (73) <b>Adduct-MeOH (150)</b> Adduct (182)	81% 13% 6%	10%
 (90)	–	Proton transfer (73) <b>Adduct-MeOH (130)</b>	73% 27%	22%
 (48)	–	Proton transfer (73) <b>Adduct-MeOH (130)</b>	97% 3%	93%
 (191)	–	Proton transfer (73) <b>Adduct-MeOH (231)</b> Adduct (263)	1% 15% 84%	0.02%
 (90)	218.6 <sup>e</sup>	Adduct (162) Proton transfer (73)	85% 15%	0.2%
 (177)	–	Proton transfer (73) Adduct (249)	89% 11%	4.5%

<sup>a</sup>Sheng *et al.*<sup>[19]</sup>  
<sup>b</sup>The  $m/z$ -value of the reaction product is given after the reaction in parentheses.  
<sup>c</sup>Fraction that each product ion contributes to the total product ion distribution.  
<sup>d</sup>Estimated precision  $\pm 10\%$ ; estimated accuracy  $\pm 50\%$ .  
<sup>e</sup>Sheng *et al.*<sup>[20]</sup>

The sheath gas ( $N_2$ ) flow was maintained at about 30 arbitrary units. The voltages for the ion optics were optimized for each analyte by using the tune feature of the LTQ Tune Plus interface. The normal detection mass range was from  $m/z$  50 up to 500. However, a low detection mass range ( $m/z$  20–200) was used for the kinetic study of the reactions of protonated methanol with the reagent (MOP). The manifold used to introduce reagents into the helium buffer gas line was first described by Gronert.<sup>[21,22]</sup> A diagram of the exact manifold used in this research was published by Habicht *et al.*<sup>[13]</sup> MOP was introduced into the manifold via a syringe pump at the rate of 10  $\mu$ L/h. A known amount of He (0.8 L/h) was used to dilute MOP. The syringe port and surrounding area were heated to  $\sim 70$  °C to ensure evaporation of MOP. Before entering the trap, the He/reagent mixture was split using two Granville-Phillips leak valves, instead of the standard flow splitter. This allowed a better control over the amount of the mixture introduced into the instrument. One leak valve was set to establish a helium pressure of  $\sim 3$  mTorr in the ion trap by allowing  $\sim 2$  mL/min of the mixture into the trap,<sup>[23]</sup> while the other leak valve controlled the amount of flow diverted to waste. A typical nominal pressure of MOP in the trap during the experiments was  $0.68 \times 10^{-5}$  Torr. After the experiments were completed each day, the manifold was isolated from the instrument and placed under vacuum to remove any remaining reagent.

### Kinetics

After the analytes had been ionized by protonation in the ESI source as described above, the protonated analytes were isolated by ejecting all unwanted ions from the trap. An isolation window of 2  $m/z$ -units was employed. The isolated ions were allowed to react for variable time periods (varying residence times in the ion trap) with the reagent MOP introduced as described above. During ion/molecule reactions, the neutral reagent is always present at a constant pressure and its concentration is in excess of that of the ion of interest. Hence, these reactions follow pseudo-first-order kinetics. The reaction efficiencies ( $\text{Eff.} = k_{\text{reaction}}/k_{\text{collision}}$  = the fraction of ion/molecule collisions that results in the formation of products) were determined by measuring each reaction's rate (IM) and the rate of the highly exothermic proton-transfer reaction (PT) between protonated methanol and the reagent (MOP) under identical conditions in the same day. The rates were measured by determining the relative abundances of the reactant ion and product ions as a function of reaction time. The slope of the decay of the abundance of the reactant ion in a semi-logarithmic plot of the ion abundances as a function of time gives the rate constant  $k$  multiplied by the concentration of the neutral reagent. Assuming that the exothermic proton-transfer reaction (PT) between protonated methanol and the reagent (MOP) proceeds at collision rate ( $k_{\text{collision}}$ ; this can be calculated by using a parameterized trajectory theory,<sup>[24]</sup> the efficiencies of the ion/molecule reactions can be obtained by using Eqn. (1). This equation is based on the ratio of the slopes of the two reactions studied ( $k_{\text{reaction}}[\text{MOP}] = \text{slope}(\text{IM})$  and  $k_{\text{collision}}[\text{MOP}] = \text{slope}(\text{PT})$ ;  $[\text{MOP}] = \text{MOP concentration}$ ). It is also based on the plots of the natural logarithm of the relative abundance of the

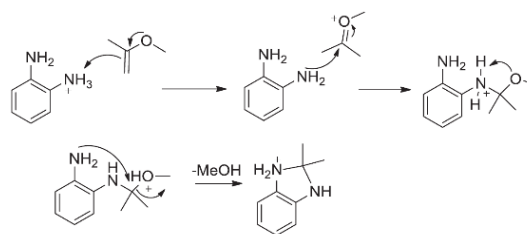
reactant ion versus reaction time for the ion/molecule (IM) and exothermic proton transfer (PT) reactions (thus eliminating the need to know  $[\text{MOP}]$ ), masses of the ion ( $M_i$ ), neutral reagent ( $M_n$ ), and methanol ( $M_{(\text{PT})}$ ), and the pressure read by an ion gauge for the neutral reagent during the ion/molecule reaction ( $P_{n(\text{IM})}$ ) and the proton-transfer reaction ( $P_{n(\text{PT})}$ ).

$$\text{Efficiency} = \frac{\text{slope}(\text{IM})}{\text{slope}(\text{PT})} * \left( \frac{M_i(M_{(\text{PT})} + M_n)}{M_{(\text{PT})}(M_i + M_n)} \right)^{1/2} * \left( \frac{P_{n(\text{PT})}}{P_{n(\text{IM})}} \right) * 100 \quad (1)$$

### RESULTS

In previous reports, the reactivity of MOP (proton affinity (PA) = 214 kcal/mol)<sup>[20]</sup> was screened toward protonated compounds with various functional groups, such as sulfone, sulfoxide, *N*-oxide, carboxylic acid, keto, amino and hydroxy.<sup>[17,18,20]</sup> MOP was found to form an abundant stable adduct with protonated *N*-oxides, sulfoxides and diamines (all with PA  $\sim 220$  kcal/mol), which is useful for their identification.<sup>[17,18,20]</sup> Moreover, adduct-MeOH was the only major product observed when MOP was allowed to react with protonated *o*-phenylenediamine but not for *m*-phenylenediamine and *p*-phenylenediamine. Scheme 1 shows a proposed mechanism that involves proton transfer followed by two nucleophilic attacks by the amino functionalities to the quaternary carbon center of MOP, which leads to the loss of a methanol molecule.<sup>[17]</sup>

In the present study, reactions of protonated *N*-monosubstituted hydroxylamines with MOP are compared to those of many other analytes (Tables 1 and 2) in order to explore whether MOP can be used to differentiate *N*-monosubstituted hydroxylamines from other compounds. As shown in Table 2, proton transfer is the major reaction for analytes (e.g., dimethyl sulfone, phenol) whose PA is 15–20 kcal/mol lower than the PA of MOP. The MOP adduct becomes more abundant than proton transfer product ions when the PA of the analyte (e.g., pyridine *N*-oxide, butylamine) is 5–10 kcal/mol higher than that of MOP. Since most hydroxylamines have a lower PA (205–215 kcal/mol) than MOP, proton transfer is the major reaction. The MOP adduct was also observed for most of these compounds. Interestingly, only protonated compounds with an *N*-monosubstituted hydroxylamine functionality



**Scheme 1.** Published<sup>[17]</sup> mechanism for the reaction of protonated *o*-phenylenediamine with MOP.

The sheath gas ( $N_2$ ) flow was maintained at about 30 arbitrary units. The voltages for the ion optics were optimized for each analyte by using the tune feature of the LTQ Tune Plus interface. The normal detection mass range was from  $m/z$  50 up to 500. However, a low detection mass range ( $m/z$  20–200) was used for the kinetic study of the reactions of protonated methanol with the reagent (MOP). The manifold used to introduce reagents into the helium buffer gas line was first described by Gronert.<sup>[21,22]</sup> A diagram of the exact manifold used in this research was published by Habicht *et al.*<sup>[13]</sup> MOP was introduced into the manifold via a syringe pump at the rate of 10  $\mu$ L/h. A known amount of He (0.8 L/h) was used to dilute MOP. The syringe port and surrounding area were heated to  $\sim 70$  °C to ensure evaporation of MOP. Before entering the trap, the He/reagent mixture was split using two Granville-Phillips leak valves, instead of the standard flow splitter. This allowed a better control over the amount of the mixture introduced into the instrument. One leak valve was set to establish a helium pressure of  $\sim 3$  mTorr in the ion trap by allowing  $\sim 2$  mL/min of the mixture into the trap,<sup>[23]</sup> while the other leak valve controlled the amount of flow diverted to waste. A typical nominal pressure of MOP in the trap during the experiments was  $0.68 \times 10^{-5}$  Torr. After the experiments were completed each day, the manifold was isolated from the instrument and placed under vacuum to remove any remaining reagent.

### Kinetics

After the analytes had been ionized by protonation in the ESI source as described above, the protonated analytes were isolated by ejecting all unwanted ions from the trap. An isolation window of 2  $m/z$ -units was employed. The isolated ions were allowed to react for variable time periods (varying residence times in the ion trap) with the reagent MOP introduced as described above. During ion/molecule reactions, the neutral reagent is always present at a constant pressure and its concentration is in excess of that of the ion of interest. Hence, these reactions follow pseudo-first-order kinetics. The reaction efficiencies ( $\text{Eff.} = k_{\text{reaction}}/k_{\text{collision}} =$  the fraction of ion/molecule collisions that results in the formation of products) were determined by measuring each reaction's rate (IM) and the rate of the highly exothermic proton-transfer reaction (PT) between protonated methanol and the reagent (MOP) under identical conditions in the same day. The rates were measured by determining the relative abundances of the reactant ion and product ions as a function of reaction time. The slope of the decay of the abundance of the reactant ion in a semi-logarithmic plot of the ion abundances as a function of time gives the rate constant  $k$  multiplied by the concentration of the neutral reagent. Assuming that the exothermic proton-transfer reaction (PT) between protonated methanol and the reagent (MOP) proceeds at collision rate ( $k_{\text{collision}}$ ; this can be calculated by using a parameterized trajectory theory<sup>[24]</sup>), the efficiencies of the ion/molecule reactions can be obtained by using Eqn. (1). This equation is based on the ratio of the slopes of the two reactions studied ( $k_{\text{reaction}}[\text{MOP}] = \text{slope (IM)}$  and  $k_{\text{collision}}[\text{MOP}] = \text{slope (PT)}$ ;  $[\text{MOP}] = \text{MOP concentration}$ ). It is also based on the plots of the natural logarithm of the relative abundance of the

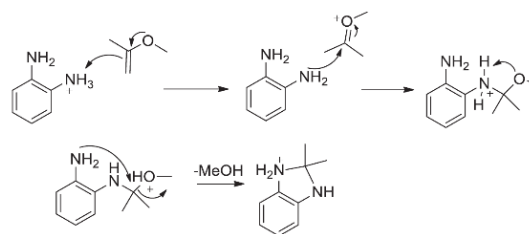
reactant ion versus reaction time for the ion/molecule (IM) and exothermic proton transfer (PT) reactions (thus eliminating the need to know  $[\text{MOP}]$ ), masses of the ion ( $M_i$ ), neutral reagent ( $M_n$ ), and methanol ( $M_{(\text{PT})}$ ), and the pressure read by an ion gauge for the neutral reagent during the ion/molecule reaction ( $P_{n(\text{IM})}$ ) and the proton-transfer reaction ( $P_{n(\text{PT})}$ ).

$$\text{Efficiency} = \frac{\text{slope(IM)}}{\text{slope(PT)}} * \left( \frac{M_i(M_{(\text{PT})} + M_n)}{M_{(\text{PT})}(M_i + M_n)} \right)^{1/2} * \left( \frac{P_{n(\text{PT})}}{P_{n(\text{IM})}} \right) * 100 \quad (1)$$

### RESULTS

In previous reports, the reactivity of MOP (proton affinity (PA) = 214 kcal/mol)<sup>[20]</sup> was screened toward protonated compounds with various functional groups, such as sulfone, sulfoxide, *N*-oxide, carboxylic acid, keto, amino and hydroxy.<sup>[17,18,20]</sup> MOP was found to form an abundant stable adduct with protonated *N*-oxides, sulfoxides and diamines (all with PA  $\sim 220$  kcal/mol), which is useful for their identification.<sup>[17,18,20]</sup> Moreover, adduct-MeOH was the only major product observed when MOP was allowed to react with protonated *o*-phenylenediamine but not for *m*-phenylenediamine and *p*-phenylenediamine. Scheme 1 shows a proposed mechanism that involves proton transfer followed by two nucleophilic attacks by the amino functionalities to the quaternary carbon center of MOP, which leads to the loss of a methanol molecule.<sup>[17]</sup>

In the present study, reactions of protonated *N*-monosubstituted hydroxylamines with MOP are compared to those of many other analytes (Tables 1 and 2) in order to explore whether MOP can be used to differentiate *N*-monosubstituted hydroxylamines from other compounds. As shown in Table 2, proton transfer is the major reaction for analytes (e.g., dimethyl sulfone, phenol) whose PA is 15–20 kcal/mol lower than the PA of MOP. The MOP adduct becomes more abundant than proton transfer product ions when the PA of the analyte (e.g., pyridine *N*-oxide, butylamine) is 5–10 kcal/mol higher than that of MOP. Since most hydroxylamines have a lower PA (205–215 kcal/mol) than MOP, proton transfer is the major reaction. The MOP adduct was also observed for most of these compounds. Interestingly, only protonated compounds with an *N*-monosubstituted hydroxylamine functionality

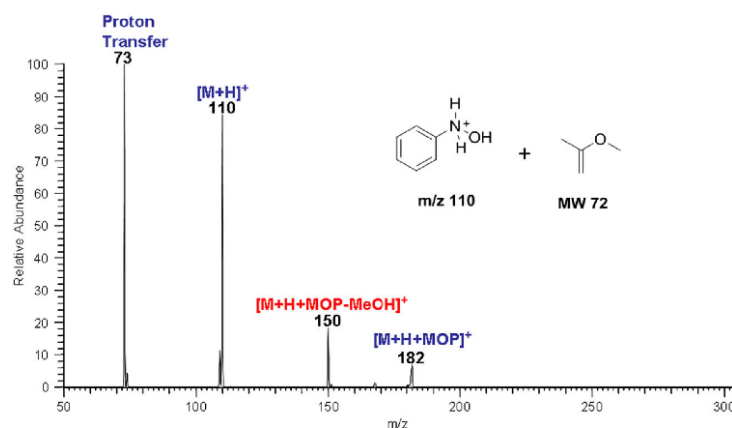


**Scheme 1.** Published<sup>[17]</sup> mechanism for the reaction of protonated *o*-phenylenediamine with MOP.

**Table 2.** Reactions of MOP ( $PA^a = 214$  kcal/mol), their efficiencies and branching ratios of different reaction pathways for a protonated carboxylic acid, sulfone, sulfoxide, ketone, *N*-oxide, phenol and amine<sup>[20]</sup>

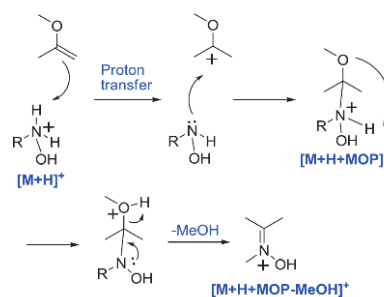
Reagent ( $m/z$ of $[M+H]^+$ )	$PA^b$ (kcal/mol)	Observed reactions and their branching ratios <sup>c</sup>	Reaction efficiency <sup>d</sup>
Benzoic acid (123)	203.2	Proton transfer 100%	42%
Butyl sulfoxide (163)	220.1	Proton transfer 1% Addition 99%	3%
Dimethyl sulfone (95)	193.5	Proton transfer 100%	67%
Acetone (59)	196.7	Proton transfer 100%	67%
Pyridine <i>N</i> -oxide (96)	219.2	Proton transfer 1% Addition 99%	0.4%
Phenol (95)	195.5	Proton transfer 98% Addition 2%	9%
Butylamine (74)	220.2	Proton transfer 98% Addition 2%	0.3%
Butanol (75)	188.8	Proton transfer 100%	87%

<sup>a</sup>Duan *et al.*<sup>[18]</sup>  
<sup>b</sup>Sheng *et al.*<sup>[20]</sup>  
<sup>c</sup>Fraction that each product ion contributes to the total product ion distribution.  
<sup>d</sup>Estimated precision  $\pm 10\%$ ; estimated accuracy  $\pm 50\%$ .



**Figure 1.** A mass spectrum measured after 200 ms reaction of protonated phenylhydroxylamine ( $m/z$  110) with MOP. The most abundant product ion ( $m/z$  73) corresponds to proton transfer reaction. The other two product ions correspond to adduct-MeOH ( $m/z$  150) and MOP adduct ( $m/z$  182).

show the MOP adduct-MeOH product (Fig. 1) among all studied compounds. Some compounds, such as protonated *N*-methylhydroxylamine and *N*-*tert*-butylhydroxylamine, only show the adduct-MeOH product besides the proton transfer product. A possible mechanism for the formation of adduct-MeOH is shown in Scheme 2. The first step involves proton transfer from protonated hydroxylamine to MOP followed by the nucleophilic attack by the nitrogen atom to form the MOP adduct. Another proton transfer from the protonated nitrogen atom to the methoxy group occurs within this ion/molecule complex followed by the nucleophilic attack by the nitrogen atom to form an oxime-like adduct-MeOH product. The presence of a hydrogen atom on the nitrogen atom is crucial for the second proton transfer to occur, leading to the MeOH loss. This is confirmed by the fact that no adduct-MeOH was observed for *N*-disubstituted hydroxylamines and oximes since these compounds do not possess an NH group. This characteristic adduct-MeOH reaction can be used to distinguish *N*-monosubstituted hydroxylamines from *N*-disubstituted



**Scheme 2.** Proposed reaction mechanisms for the formation of a stable MOP adduct and elimination of methanol from an unstable MOP adduct upon reaction of protonated *N*-monosubstituted *N*-hydroxylamines with MOP.

*N*-hydroxylamines, oximes, as well as compounds with functional groups such as sulfone, sulfoxide, *N*-oxide, carboxylic acid, keto, amino and hydroxy.

## CONCLUSIONS

The ability to use functional group-selective ion/molecule reactions in a linear quadrupole ion trap mass spectrometer to identify protonated compounds with the *N*-monosubstituted *N*-hydroxylamine functionality has been demonstrated. Most protonated *N*-monosubstituted *N*-hydroxylamine model compounds were found to react with MOP via proton transfer and formation of an adduct and a diagnostic adduct-MeOH product. A hydrogen atom bound to the nitrogen atom was found to be crucial for the formation of the adduct-MeOH product. *N,N*-Disubstituted hydroxylamines, oximes, sulfones, sulfoxides, *N*-oxides, carboxylic acids, ketones, amines and alcohols mainly yield MOP adducts and/or proton transfer product ions. The results obtained suggest that this method is applicable to the rapid identification of *N*-monosubstituted hydroxylamines.

## Acknowledgement

AstraZeneca is thanked for financial support.

## REFERENCES

- [1] G. Gamboa da Costa, R. Singh, V. M. Arlt, A. Mirza, M. Richards, T. Takamura-Enya, H. H. Schmeiser, P. B. Farmer, D. H. Phillips. Quantification of 3-nitrobenzanthrone-DNA adducts using online column-switching HPLC-electrospray tandem mass spectrometry. *Chem. Res. Toxicol.* **2009**, *22*, 1860.
- [2] R. R. Miller, G. A. Doss, R. A. Stearns. Identification of a hydroxylamine glucuronide metabolite of an oral hypoglycemic agent. *Drug Metab. Dispos.* **2004**, *32*, 178.
- [3] F. Angelelli, M. Aschi, F. Cacace, F. Pepi, G. de Petris. Gas-phase reactivity of hydroxylamine toward charged electrophiles. A mass spectrometric and computational study of the protonation and methylation of H<sub>2</sub>NOH. *J. Phys. Chem.* **1995**, *99*, 6551.
- [4] S. X. Peng, M. J. Strojnowski, J. K. Hu, B. J. Smith, T. H. Eichhold, K. R. Wehmeyer, S. Pikul, N. G. Almstead. Gas chromatographic-mass spectrometric analysis of hydroxylamine for monitoring the metabolic hydrolysis of metalloprotease inhibitors in rat and human liver microsomes. *J. Chromatogr. B Biomed. Sci. Appl.* **1999**, *724*, 181.
- [5] M. D. Coleman. Dapsone toxicity: some current perspectives. *Gen. Pharmacol.* **1995**, *26*, 1461.
- [6] N. A. Helsby, D. M. Ferry, A. V. Patterson, S. M. Pullen, W. R. Wilson. 2-Amino metabolites are key mediators of CB 1954 and SN 23862 bystander effects in nitroreductase GDEPT. *Br. J. Cancer* **2004**, *90*, 1084.
- [7] M. D. Tingle, R. Mahmud, J. L. Maggs, M. Pirmohamed, B. K. Park. The hydroxylamine of sulfamethoxazole synergizes with FK506 and cyclosporin A, inhibiting T-cell proliferation. *J. Pharmacol. Exp. Ther.* **1997**, *283*, 817.
- [8] D. A. Hess, I. A. Bird, W. Y. Almawi, M. J. Rieder. The hydroxylamine of sulfamethoxazole synergizes with FK506 and cyclosporin A, inhibiting T-cell proliferation. *J. Pharmacol. Exp. Ther.* **1997**, *281*, 540.
- [9] Y. Ye, H. Liu, P. Horvatovich, W. Chan. Liquid chromatography-electrospray ionization tandem mass spectrometric analysis of 2-alkylcyclobutanones in irradiated chicken by precolumn derivatization with hydroxylamine. *J. Agric. Food Chem.* **2013**, *61*, 5758.
- [10] L. Debrauwer, D. Zalko, G. Bories, J. Tulliez. Electrospray ionization mass spectrometric study of *N*-oxidation products of clenbuterol. *Rapid Commun. Mass Spectrom.* **1997**, *11*, 1089.
- [11] S. Osburn, V. Ryzhov. Ion-molecule reactions: analytical and structural tool. *Anal. Chem.* **2013**, *85*, 769.
- [12] R. J. Eismín, M. Fu, S. Yem, F. Widjaja, H. I. Kenttämäa. Identification of epoxide functionalities in protonated monofunctional analytes by using ion/molecule reactions and collision-activated dissociation in different ion trap tandem mass spectrometers. *J. Am. Soc. Mass Spectrom.* **2012**, *23*, 12.
- [13] S. C. Habicht, N. R. Vinueza, E. F. Archibold, P. Duan, H. I. Kenttämäa. Identification of the carboxylic acid functionality by using electrospray ionization and ion-molecule reactions in a modified linear quadrupole ion trap mass spectrometer. *Anal. Chem.* **2008**, *80*, 3416.
- [14] K. M. Campbell, M. A. Watkins, S. Li, M. N. Fiddler, B. Winger, H. I. Kenttämäa. Functional group selective ion/molecule reactions: mass spectrometric identification of the amido functionality in protonated monofunctional compounds. *J. Org. Chem.* **2007**, *72*, 3159.
- [15] J. Somuramasami, P. Duan, L. Amundson, E. Archibold, B. Winger, H. I. Kenttämäa. Differentiation of protonated aromatic regioisomers related to lignin by reactions with trimethylborate in a Fourier transform ion cyclotron resonance mass spectrometer. *J. Am. Soc. Mass Spectrom.* **2011**, *22*, 1040.
- [16] M. Fu, R. J. Eismín, P. Duan, S. Li, H. I. Kenttämäa. Ion-molecule reactions facilitate the identification and differentiation of primary, secondary and tertiary amino functionalities in protonated monofunctional analytes in mass spectrometry. *Int. J. Mass Spectrom.* **2009**, *282*, 77.
- [17] M. Fu, P. Duan, S. Li, S. C. Habicht, D. S. Pinkston, N. R. Vinueza, H. I. Kenttämäa. Regioselective ion-molecule reactions for the mass spectrometric differentiation of protonated isomeric aromatic diamines. *Analyst* **2008**, *133*, 452.
- [18] P. Duan, M. Fu, T. A. Gillespie, B. E. Winger, H. I. Kenttämäa. Identification of aliphatic and aromatic tertiary *N*-oxide functionalities in protonated analytes via ion/molecule and dissociation reactions in an FT-ICR mass spectrometer. *J. Org. Chem.* **2009**, *74*, 1114.
- [19] H. Sheng, P. E. Williams, W. Tang, M. Zhang, H. I. Kenttämäa. Identification of the sulfone functionality in protonated analytes via ion/molecule reactions in a linear quadrupole ion trap mass spectrometer. *J. Org. Chem.* **2014**, *79*, 2883.
- [20] H. Sheng, P. E. Williams, W. Tang, M. Zhang, H. I. Kenttämäa. Identification of the sulfoxide functionality in protonated analytes via ion/molecule reactions in linear quadrupole ion trap mass spectrometry. *Analyst* **2014**, *139*, 4296.
- [21] S. Gronert. Estimation of effective ion temperatures in a quadrupole ion trap. *J. Am. Soc. Mass Spectrom.* **1998**, *9*, 845.
- [22] S. Gronert. Quadrupole ion trap studies of fundamental organic reactions. *Mass Spectrom. Rev.* **2005**, *24*, 100.
- [23] J. C. Schwartz, M. W. Senko, J. E. Syka. A two-dimensional quadrupole ion trap mass spectrometer. *J. Am. Soc. Mass Spectrom.* **2002**, *13*, 659.
- [24] T. Su, W. J. Chesnavich. Parametrization of the ion-polar molecule collision rate constant by trajectory calculations. *J. Chem. Phys.* **1982**, *76*, 5183.



# Identification of *N*-Oxide and Sulfoxide Functionalities in Protonated Drug Metabolites by Using Ion–Molecule Reactions Followed by Collisionally Activated Dissociation in a Linear Quadrupole Ion Trap Mass Spectrometer

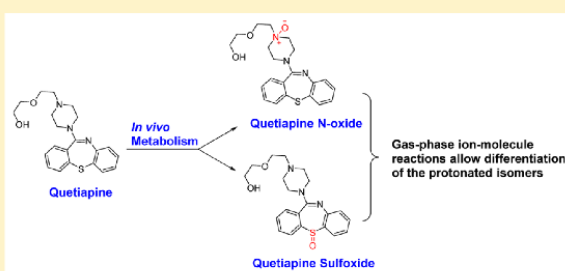
Huaming Sheng,<sup>†</sup> Weijuan Tang,<sup>†</sup> Ravikiran Yerabolu,<sup>†</sup> Joann Max,<sup>†</sup> Raghavendhar R. Kotha,<sup>†</sup> James S. Riedeman,<sup>†</sup> John J. Nash,<sup>†</sup> Minli Zhang,<sup>‡</sup> and Hilkka. I. Kenttämäa<sup>\*,†</sup>

<sup>†</sup>Purdue University, Department of Chemistry, West Lafayette, Indiana 47907, United States

<sup>‡</sup>AstraZeneca, Boston, Massachusetts 02130, United States

## Supporting Information

**ABSTRACT:** The *in vivo* oxidation of sulfur and nitrogen atoms in many drugs into sulfoxide and *N*-oxide functionalities is a common biotransformation process. Unfortunately, the unambiguous identification of these metabolites can be challenging. In the present study, ion–molecule reactions of tris(dimethylamino)borane followed by collisionally activated dissociation (CAD) in an ion trap mass spectrometer are demonstrated to allow the identification of *N*-oxide and sulfoxide functionalities in protonated polyfunctional drug metabolites. Only ions with *N*-oxide or sulfoxide functionality formed diagnostic adducts that had lost dimethyl amine (DMA). This was demonstrated even for an analyte that contains a substantially more basic functionality than the functional group of interest. CAD of the diagnostic product ions (*M*) resulted mainly in type A (*M* – DMA) and B fragment ions (*M* – HO–B(N(CH<sub>3</sub>)<sub>2</sub>)<sub>2</sub>) for *N*-oxides, but sulfoxides also formed diagnostic C ions (*M* – O=BN(CH<sub>3</sub>)<sub>2</sub>), thus allowing differentiation of the functionalities. Some protonated analytes yielded abundant TDMAB adducts that had lost *two* DMA molecules instead of just one. This provides information on the environment of the *N*-oxide and sulfoxide functionalities. Quantum chemical calculations were performed to explore the mechanisms of the above-mentioned reactions. The method can be implemented on HPLC for real drug analysis.



## INTRODUCTION

In phase I oxidative metabolism, *N*-oxides and sulfoxides are common metabolites for many sulfur and nitrogen containing heterocyclic drugs<sup>1,2</sup> (for examples of *N*-oxide metabolites,<sup>3</sup> see Figure 1). Fast structural elucidation of these metabolites is essential for the drug discovery process since the metabolites may have profoundly altered functional parameters from those of the drugs, such as adverse biological activity, different clearance rates, and enhanced toxicity.<sup>4–7</sup> Hence, it is crucial to establish methods that allow the unambiguous identification of compounds containing these two functionalities, especially in drugs that contain both sulfur and nitrogen atoms. However, most analytical methods still face challenges in the identification of *N*-oxide and sulfoxide functionalities in molecules in complex mixtures.<sup>8–10</sup>

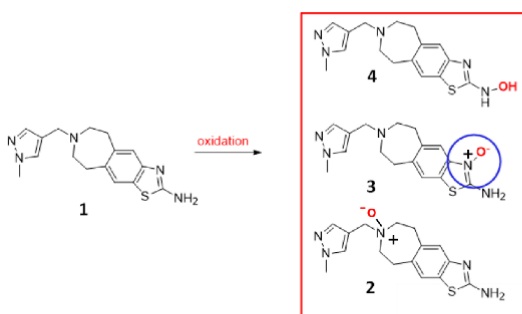
Although NMR is invaluable in the identification of C-hydroxylation metabolites, the low natural abundances of <sup>15</sup>N (0.37%) and <sup>33</sup>S (0.74%) limit the use of NMR in the detection of N- and S-containing oxidation products.<sup>11,12</sup> Moreover, the metabolite of interest must exist in sufficient quantities and be purified for structure determination by NMR.<sup>13</sup>

Tandem mass spectrometry based on collisionally activated dissociation (CAD) coupled with high-performance liquid chromatography (HPLC/MS/MS) is widely used to identify drug metabolites. However, in many cases, sulfoxide, *N*-oxide, and common C-hydroxylation metabolites have the same molecular weight. Moreover, due to the lack of specific fragmentation patterns for ionized *N*-oxides (for an example, see Figure S1) and sulfoxides upon CAD,<sup>14–16</sup> it is challenging to unambiguously identify these functionalities and to differentiate them from C-hydroxylation metabolites.

Tandem mass spectrometric methods based on ion–molecule reactions hold great promise for being able to provide information useful in the identification of specific functional groups in small organic molecules and in differentiation of isomers.<sup>17–28</sup> This can be carried out on analytes as they elute from an HPLC.<sup>29,30</sup> However, most of these past studies focused on simple monofunctional analytes instead of real polyfunctional drug metabolites. Furthermore, no ion–

Received: October 17, 2015

Published: December 11, 2015



**Figure 1.** Three possible isomeric oxidation metabolites (2–4) of 2-aminothiazolo-benzazepine (2-ATBA), 7-[(1-methyl-1*H*-pyrazol-4-yl)methyl]-6,7,8,9-tetrahydro-*SH*-[1,3]thiazolo[4,5-*h*][3]benzazepin-2-amine (1).<sup>3</sup> The *N*-oxides were identified as being formed in human, rat, dog, and monkey microsomes.

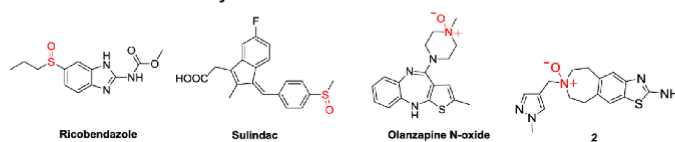
molecule reactions have been reported that could be used to differentiate protonated tertiary *N*-oxides from sulfoxides. In the present study, gas-phase ion/molecule reactions of tris(dimethylamino)borane (TDMAB) followed by CAD are demonstrated to allow the unambiguous identification of protonated sulfoxide and *N*-oxide functionalities in polyfunc-

tional drug metabolites. The applicability of the method on a real drug sample was demonstrated by the identification of an *N*-oxide metabolite isolated from dog liver microsomes.

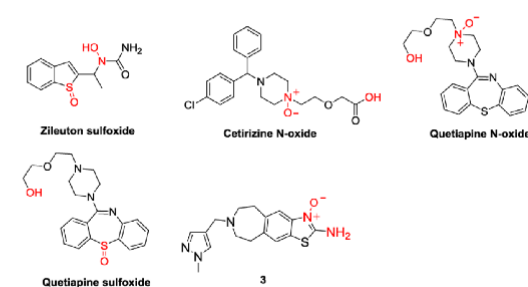
## RESULTS AND DISCUSSION

**Reactions of TDMAB with Protonated Drug Metabolites ( $MS^2$  Experiments).** Protonated monofunctional *N*-oxide, pyridine, and amide model compounds have been reported previously to react with TDMAB via facile formation of a TDMAB adduct that has lost a neutral dimethylamine (DMA) molecule (TDMAB adduct – DMA) in  $MS^2$  experiments (see the top of Figure 3 for the ion–molecule reaction and a representative  $MS^2$  spectrum below the mechanism).<sup>24</sup> The same was observed here for the first time for simple sulfoxides (see Table S1 in Supporting Information). Analogous reactivity has *not* been observed for monofunctional compounds containing other functionalities, including sulfide, sulfone, amino, imino, hydroxy, carboxylic acid, and carboxylic ester groups.<sup>24</sup> In this study, formation of a TDMAB adduct followed by elimination of DMA was found to be the major reaction only for protonated polyfunctional drug metabolites containing either an *N*-oxide or a sulfoxide functionality (Figure 2; Table 1). Some *N*-oxides and sulfoxides underwent addition to TDMAB followed by elimination of two DMA molecules instead (discussed later). Other protonated polyfunctional

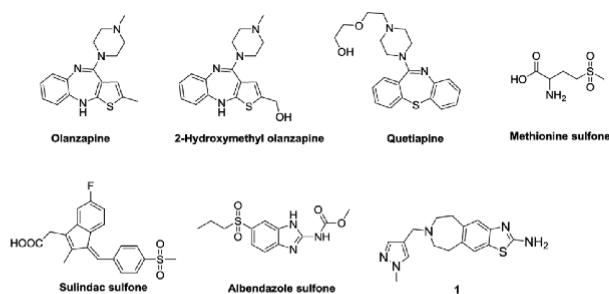
### A. Molecules that show only TDMAB adduct - DMA:



### B. Molecules that show both TDMAB adduct - DMA and TDMAB adduct - 2 DMA:


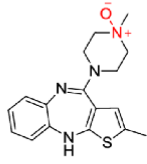

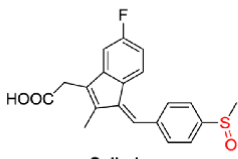
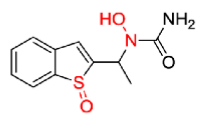


### C. Molecules that do not react with TDMAB or show very minor TDMAB adduct - DMA:



**Figure 2.** Drugs and drug metabolites used in this study. The functional groups that are involved in the formation of TDMAB adducts that have lost a DMA molecule and TDMAB adducts that have lost two DMA molecules (discussed later in this paper) are marked in red.

**Table 1.** Observed Product Ions Formed upon Reactions of TDMAB (T) with Protonated Cetirizine N-Oxide, Olanzapine N-Oxide, Ricobendazole, Sulindac and Zileuton Sulfoxide (all referred to as M below) and Their Relative Abundances (MS<sup>2</sup> experiments) as well as the Compositions and Relative Abundances of the CAD Products of the TDMAB Adducts That Had Lost a DMA Molecule (MH<sup>+</sup> + T – DMA, also referred to as N below) (MS<sup>3</sup> experiments) (the color coding matches that in Figure 3)

Analyte (M)	Observed product ions and their relative abundances (MS <sup>2</sup> )	CAD products of MH <sup>+</sup> + T – DMA (N) and their relative abundances (MS <sup>3</sup> )
 Cetirizine N-oxide	<p>MH<sup>+</sup> + T – 2 DMA (<i>m/z</i> 458) 45%</p> <p>MH<sup>+</sup> + T – DMA (<i>m/z</i> 503) 41%</p> <p>MH<sup>+</sup> + DMA<sup>a</sup> (<i>m/z</i> 450) 14%</p>	<p>N – DMA (<i>m/z</i> 458) (A) 60%</p> <p>N – HOB(N(CH<sub>3</sub>)<sub>2</sub>)<sub>2</sub> (<i>m/z</i> 387) (B) 100%</p>
 Olanzapine N-oxide	<p>MH<sup>+</sup> + T – DMA (<i>m/z</i> 427) 100%</p>	<p>N – DMA (<i>m/z</i> 382) (A) 10%</p> <p>N – HOB(N(CH<sub>3</sub>)<sub>2</sub>)<sub>2</sub> (<i>m/z</i> 311) (B) 100%</p>
 Ricobendazole	<p>MH<sup>+</sup> + T – DMA (<i>m/z</i> 380) 62%</p> <p>MH<sup>+</sup> + DMA<sup>a</sup> (<i>m/z</i> 327) 38%</p>	<p>N – DMA (<i>m/z</i> 335) (A) 100%</p> <p>N – HOB(N(CH<sub>3</sub>)<sub>2</sub>)<sub>2</sub> (<i>m/z</i> 264) (B) 80%</p> <p>N – O=BN(CH<sub>3</sub>)<sub>2</sub> (<i>m/z</i> 309) (C) 30%</p> <p>N – H<sub>2</sub>O – B(N(CH<sub>3</sub>)<sub>2</sub>)<sub>2</sub><sup>+</sup> (<i>m/z</i> 263) 20%</p> <p>T + H<sup>+</sup> (<i>m/z</i> 144) 10%</p>
 Sulindac	<p>MH<sup>+</sup> + T – DMA (<i>m/z</i> 455) 88%</p> <p>MH<sup>+</sup> (<i>m/z</i> 357) 5%</p> <p>MH<sup>+</sup> + DMA<sup>a</sup> (<i>m/z</i> 402) 4%</p> <p>MH<sup>+</sup> + T (<i>m/z</i> 500) 3%</p>	<p>N – DMA (<i>m/z</i> 410) (A) 20%</p> <p>N – HOB(N(CH<sub>3</sub>)<sub>2</sub>)<sub>2</sub> (<i>m/z</i> 339) (B) 50%</p> <p>N – O=BN(CH<sub>3</sub>)<sub>2</sub> (<i>m/z</i> 384) (C) 100%</p>
 Zileuton Sulfoxide	<p>MH<sup>+</sup> + DMA<sup>a</sup> (<i>m/z</i> 298) 59%</p> <p>MH<sup>+</sup> + T – DMA (<i>m/z</i> 351) 36%</p> <p>MH<sup>+</sup> + T – 2 DMA (<i>m/z</i> 306) 5%</p>	<p>N – DMA (<i>m/z</i> 306) (A) 100%</p> <p>N – O=BN(CH<sub>3</sub>)<sub>2</sub> (<i>m/z</i> 280) (C) 10%</p>

<sup>a</sup>The formation of a DMA adduct upon reaction with TDMAB may occur as shown in Figure S2.

compounds studied (without sulfoxide or N-oxide functional groups) did not rapidly undergo either reaction (Figure 2; Table 2).

The likely mechanisms for the formation of TDMAB adducts that have lost a neutral DMA molecule for protonated N-oxides and sulfoxides are shown in Figure 3. As proposed in the literature for N-oxides,<sup>24</sup> the mechanisms involve initial proton transfer from protonated N-oxide or sulfoxide to the amino moiety of TDMAB followed by nucleophilic addition of an

oxygen atom of the N-oxide or sulfoxide group to the boron center. The proton affinity (PA) of TDMAB is 230 kcal/mol,<sup>24</sup> which is close to the PAs of N-oxide<sup>24</sup> (~230 kcal/mol) and sulfoxide<sup>27</sup> (~220 kcal/mol) functionalities in simple analytes. Hence, proton transfer can occur between simple protonated N-oxides or sulfoxides and TDMAB, eventually leading to the formation of TDMAB adducts that have lost a DMA molecule.

The selectivity of TDMAB toward protonated N-oxides and sulfoxides in simple monofunctional analytes may be partially

**Table 2.** Observed Product Ions and Their Relative Abundances for Reactions of Protonated Olanzapine, 2-Hydroxymethylolanzapine, Quetiapine, Methionine Sulfone, Sulindac Sulfone, and Albendazole Sulfone (all referred to as M below) (for structures, see Figure 2) with TDMAB (T) (MS<sup>2</sup> experiments)

Analyte (M)	Observed product ions and their relative abundances (MS <sup>2</sup> )	
Olanzapine	No Product	
2-Hydroxymethylolanzapine	No Product	
Quetiapine	No Product	
Methionine sulfone	MH <sup>+</sup> + DMA <sup>a</sup> ( <i>m/z</i> 227)	86%
	T + H <sup>+</sup> ( <i>m/z</i> 144)	14%
	MH <sup>+</sup> + DMA <sup>a</sup> ( <i>m/z</i> 418)	35%
Sulindac sulfone	T + H <sup>+</sup> ( <i>m/z</i> 144)	34%
	MH <sup>+</sup> + T ( <i>m/z</i> 516)	26%
	MH <sup>+</sup> + T – DMA ( <i>m/z</i> 471)	5%
	MH <sup>+</sup> + DMA <sup>a</sup> ( <i>m/z</i> 343)	69%
Albendazole sulfone	MH <sup>+</sup> + T ( <i>m/z</i> 441)	20%
	T + H <sup>+</sup> ( <i>m/z</i> 144)	7%
	MH <sup>+</sup> + T – DMA ( <i>m/z</i> 396)	4%

<sup>a</sup>The formation of a DMA adduct upon reaction with TDMAB may occur as shown in Figure S2.

rationalized based on the PAs of the analyte molecules. TDMAB (PA = 230 kcal/mol) readily deprotonates protonated analyte molecules with PAs lower than that of TDMAB, including all analytes with only oxygen-containing functionalities, to yield protonated TDMAB.<sup>24</sup> Protonated sulfones (PAs range from 190–212 kcal/mol<sup>26</sup>) have PAs fairly close to that of TDMAB but lower. Hence, they react with TDMAB to form protonated TDMAB and a stable adduct (Figure 2; Table 2; two sulfones also gave a very small amount of TDMAB adducts that had lost a DMA molecule). As mentioned above, PAs of *N*-oxide<sup>24</sup> (~230 kcal/mol) and sulfoxide<sup>27</sup> functionalities (~220 kcal/mol) in simple compounds are greater than those of sulfones and close to that of TDMAB. This enables formation of a long-lived collision complex after proton transfer, as the proton transfer is not highly exothermic, which would lead to immediate separation of the proton transfer products. Within the long-lived collision complex, nucleophilic addition by the *N*-oxide<sup>24</sup> or sulfoxide analyte (Table S1) to the boron center of protonated TDMAB can occur and lead to elimination of a DMA molecule as shown in Figure 3.

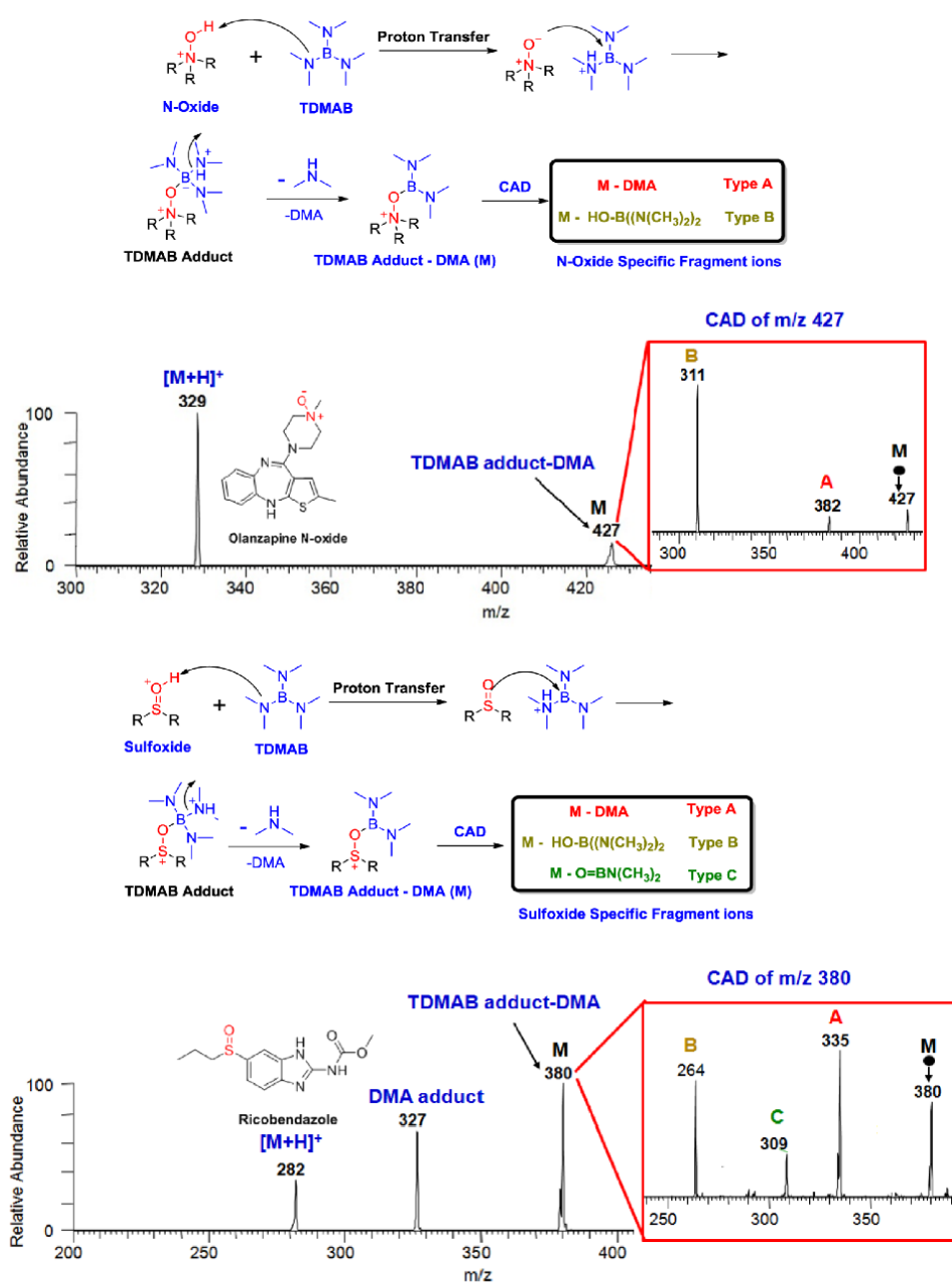
In order to explore whether the above-mentioned rationale also applies to polyfunctional molecules, quantum chemical calculations were carried out to estimate the PAs of several functionalities in most of the polyfunctional molecules studied (Figures S3–S8), i.e., ricobendazole, albendazole sulfone, quetiapine, quetiapine sulfoxide, quetiapine *N*-oxide, olanzapine, olanzapine *N*-oxide, 2-hydroxymethylolanzapine, cetirizine *N*-oxide, sulindac, sulindac sulfone, methionine sulfone, and compounds 2, 3, and 4 (for structures of these three compounds, see Figure 1). The PAs calculated for all only oxygen- or only sulfur-containing functionalities are less than 210 kcal/mol, as expected. Also as expected, sulfone functionalities were calculated to have similar or slightly greater PAs (199–213 kcal/mol) but still well below that of TDMAB (PA = 230 kcal/mol). Hence, observation of protonated TDMAB and a stable TDMAB adduct for sulindac sulfone, which contains only oxygen- and/or sulfur-containing function-

alities, is not surprising (Table 2). For methionine sulfone and albendazole sulfone, the most basic site is not the sulfone group but a primary amino group and an imino group, respectively. The PAs of these groups (both 222 kcal/mol; Figures S3 and S8) are well below that of TDMAB, which explains the observation of protonated TDMAB and a stable TDMAB adduct also for these protonated molecules (Table 2).

In the other extreme, some analytes, such as quetiapine, olanzapine and hydroxymethylolanzapine, contain a highly basic imino or amino group (the PAs of the most basic tertiary amino groups are 240, 246, and 249 kcal/mol, respectively; Figure S4) that cannot be deprotonated by TDMAB to initiate the diagnostic reaction sequence. Hence, it is not surprising that no reactions were observed for such analytes (quetiapine, olanzapine, and 2-hydroxymethylolanzapine; Table 2).

The diagnostic reactivity (formation of TDMAB adducts that have lost a DMA molecule) dominated only for compounds containing a sulfoxide or an *N*-oxide functionality. The calculated PAs of the sulfoxide functionalities (219, 224, 230, and 234 kcal/mol) and one *N*-oxide functionality (231 kcal/mol) in the polyfunctional compounds studied (Figures S3–S8) were found to be similar to those of related simple monofunctional compounds. In most cases, these also are the most basic functionalities in the compounds and thus most likely to be protonated. Hence, it is not surprising that similar reactivity toward TDMAB (Table 1) was observed as in the case of simple monofunctional molecules containing a sulfoxide (Table S1) or an *N*-oxide<sup>24</sup> functionality. Upon interaction with TDMAB, deprotonation of the protonated *N*-oxide or sulfoxide functionality occurs and the diagnostic product ion is formed, as shown in Figure 3.

However, the PAs of the *N*-oxide functionalities in olanzapine *N*-oxide (240 kcal/mol; Figure S4), cetirizine *N*-oxide (245 kcal/mol; Figure S5), and quetiapine *N*-oxide (248 kcal/mol; Figure 4) are very high, likely due to intramolecular hydrogen bond formation with nearby functionalities for two of these analytes (the hydroxyl group 27O in quetiapine *N*-oxide (Figure 4, bottom) and the carbonyl group 26O in cetirizine *N*-oxide (Figure S5)). TDMAB should not be able to abstract a proton from these protonated *N*-oxide groups. In spite of this, the diagnostic TDMAB adducts that had lost a DMA molecule were formed for protonated quetiapine (Table 3), olanzapine and cetirizine *N*-oxides (Table 1). These findings strongly suggest that the two protonated analytes (ionized by ESI from methanol solution) carry the proton not only on the most basic site (*N*-oxide) but also on sites with PAs less or equal to that of TDMAB (230 kcal/mol). These sites include a tertiary amino group in quetiapine *N*-oxide (PA = 218 kcal/mol; Figure 4), in olanzapine *N*-oxide (PA = 215 kcal/mol; Figure 4) and in cetirizine *N*-oxide (PA = 223 kcal/mol; Figure S5). The ability of the less basic functionalities to compete for the proton upon ESI may be partially rationalized by the finding that the *N*-oxide functionalities in neutral quetiapine and cetirizine *N*-oxides are already involved in stabilizing hydrogen bonding (Figures 3 (top) and S5) and hence may not be accessible for protonation. However, it should be also noted that protonation of other functionalities besides the most basic one upon ESI is not entirely unknown. Gaseous protonated 4-aminobenzoic acid has been reported to carry the proton either the carbonyl group (favored by 8 kcal/mol in the gas phase) or both the carbonyl group and the amino group, depending on the solvent(s) used.<sup>31a–c</sup> Similarly, 4-hydroxybenzoic acid has been found to be deprotonated on the phenol and/or carboxylic acid

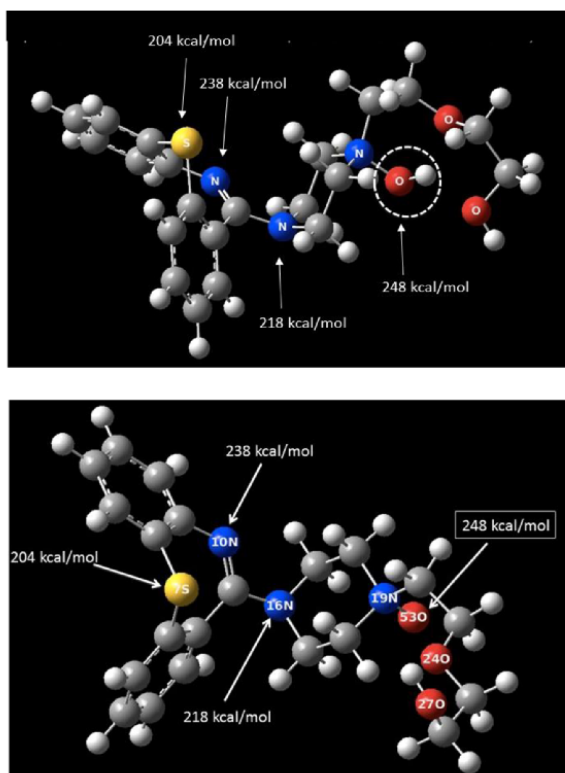


**Figure 3.** Likely mechanisms leading to the formation of TDMAB adducts that have lost a DMA molecule for protonated N-oxides<sup>24</sup> and sulfoxides, MS<sup>2</sup> spectra showing the products of above reactions, and MS<sup>3</sup> CAD mass spectra of the TDMAB adducts that have lost a DMA molecule, illustrated using olanzapine N-oxide (top) and ricobendazole (bottom). Only sulfoxides yield the diagnostic type C fragment ions in the MS<sup>3</sup> experiment.

sites depending on ESI conditions, in spite of the fact that the phenoxide anion is more stable by 8 kcal/mol in the gas phase.<sup>31d</sup>

Further support for the possibility that the polyfunctional analytes studied here can carry the proton at several sites after ESI is provided by examination of the behavior of one of the sulfoxide-containing analytes. For quetiapine sulfoxide, the sulfoxide group (PA = 234 kcal/mol) is not the most basic site,

as for the other sulfoxides studied; a tertiary amino group and an imino group have substantially greater PAs (245 and 242 kcal/mol, respectively; Figure S4). If this analyte was solely protonated at the most basic amino or imino functionalities, TDMAB could not deprotonate the protonated molecule. However, protonated quetiapine sulfoxide was found to yield the diagnostic TDMAB adduct that had lost a DMA molecule (and a TDMAB adduct that had lost two DMA molecules)



**Figure 4.** PAs of the most basic functionalities are indicated for the optimized quetiapine *N*-oxide protonated on the *N*-oxide functionality (highlighted with a circle; top) and for the optimized neutral *N*-oxide (bottom; B3LYP/6-31G++(d,p) level of theory). In both structures, the *N*-oxide moiety is involved in hydrogen bonding with the terminal hydroxyl functionality.

(Table 3). Hence, after ESI, this compound must carry a proton at several sites, including the less basic tertiary amino and/or the sulfoxide functionalities (PA = 225 and 234 kcal/mol, respectively; Figure S4).

While the above-mentioned PA considerations help in understanding the behavior of several analytes studied here, they cannot fully explain the selectivity observed for TDMAB. For example, some nitrogen functionalities other than *N*-oxide have PAs close to those of sulfoxides and *N*-oxides, such as, for example, the less basic tertiary amino group (220 kcal/mol) in quetiapine (Figure S4). If this molecule was protonated at this site (in addition to the most basic tertiary amino group with PA = 240 kcal/mol), TDMAB should be able to deprotonate it and form the diagnostic product. However, protonated quetiapine does not form the diagnostic TDMAB adduct that has lost a DMA molecule (Table 2). In agreement with this finding, amines with PAs ranging from 227 up to 242 kcal/mol have been reported to either transfer a proton to TDMAB or be unreactive but not produce TDMAB adducts that have lost a DMA molecule.<sup>24</sup> TDMAB is able to deprotonate protonated amines with PAs below 230 kcal/mol; however, no TDMAB adducts that have lost a DMA molecule were observed for these compounds.

The lack of reactivity of amines toward protonated TDMAB within a collision complex after proton transfer is likely due to their small dipole moments (e.g., those of methyl and triethyl

amines are only 1.31 and 0.61 D<sup>32a,b</sup>), which results in only low solvation energy for the proton transfer complex.<sup>33</sup> Hence, the complex is more likely to dissociate to proton transfer products or lose energy upon collisions with helium buffer gas to yield a stable adduct rather than undergo further reactions. On the other hand, the dipole moments of *N*-oxides (that of pyridine *N*-oxide is 4.13 D<sup>31c</sup>) and sulfoxides (that of dimethyl sulfoxide is 3.96 D<sup>31c</sup>) are large. Hence, the proton transfer collision complexes of protonated TDMAB with *N*-oxides and sulfoxides are better stabilized toward dissociation and have longer lifetimes than those of amines, which allows for further reactions within the collision complex after proton transfer.

**Collisionally Activated Dissociation (CAD) of the Diagnostic Product Ions (MS<sup>3</sup> Experiments).** Isolation of the TDMAB adducts that had lost a DMA molecule followed by CAD (MS<sup>3</sup> experiments) can be used to differentiate *N*-oxide and sulfoxide containing drug metabolites from each other. For both sulfoxides and *N*-oxides, CAD of the diagnostic ion proceeds through the elimination of a DMA molecule and a HOB(N(CH<sub>3</sub>)<sub>2</sub>)<sub>2</sub> molecule to produce type A and type B fragment ions, respectively (Figure 3; Table 1). However, sulfoxides also produce diagnostic type C fragment ions via elimination of (CH<sub>3</sub>)<sub>2</sub>N–B=O (Figure 3).

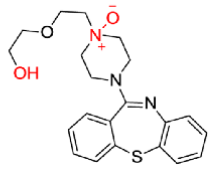
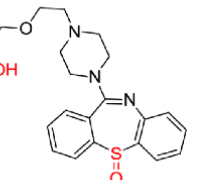
Quantum chemical calculations were used to examine the mechanisms of formation of type A and B fragment ions by using a simple *N*-oxide model compound (Figure 5, left). For type A fragment ions, a six-membered transition state leads to elimination of a DMA molecule. The barrier for formation of type B fragment ions via a different six-membered transition state is calculated to be lower than that for type A ions, in agreement with their relative abundances: type B fragment ions usually dominate (Figure 3; Table 1). These ions are formed via elimination of zwitterionic O=B<sup>−</sup>(N(CH<sub>3</sub>)<sub>2</sub>)(NH<sup>+</sup>(CH<sub>3</sub>)<sub>2</sub>) (Figure 5, bottom left). Based on these calculations, the likely mechanisms for the formation of type A and B fragment ions from the TDMAB adducts that have lost a DMA molecule for protonated olanzapine *N*-oxide are shown in Figure S7.

Further calculations were performed to explore the mechanism of formation of the diagnostic type C fragment ions for sulfoxides by using a simple sulfoxide model compound. A four-membered transition state was found to lead to these fragment ions (Figure 5, right). An analogous mechanism is not possible for *N*-oxides, which explains why they do not form type C fragment ions. Based on calculations, CAD of the TDMAB adduct of sulindac that has lost a DMA molecule likely occurs as shown in Figure 6.

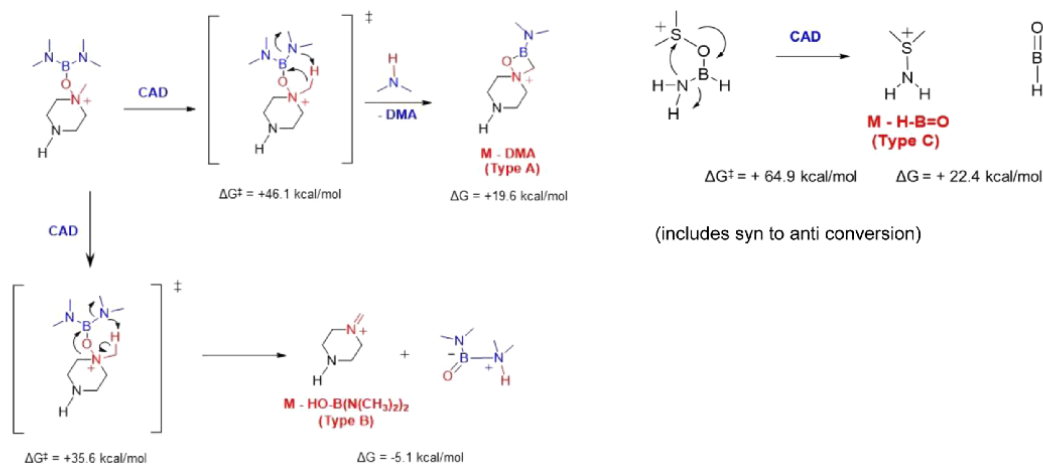
It is interesting to note that CAD of the TDMAB adducts of protonated monofunctional sulfoxide model compounds that have lost a DMA molecule did not show the above-mentioned characteristic fragment ions (Table S1), with the exception of losses of DMA molecules. None of their fragment ions were formed by elimination of a boron containing molecule, as type B and C fragment ions. Instead, they produced either B(N(CH<sub>3</sub>)<sub>2</sub>)<sub>2</sub><sup>+</sup> or H<sub>2</sub>OB(N(CH<sub>3</sub>)<sub>2</sub>)<sub>2</sub><sup>+</sup> fragment ions, likely because the *N*-containing part of the fragmenting ion is able to stabilize the charge better than the sulfoxide-containing part due to its small size. Hence, it is obvious that polyfunctional analytes with an *N*-oxide or sulfoxide functionality can behave very differently from simple compounds.

The formation of type A and B fragment ions via the mechanisms discussed above requires the presence of a hydrogen atom at an atom (carbon for all the compounds discussed above) bound to the sulfoxide or *N*-oxide

**Table 3.** Observed Ion–molecule Reaction Product Ions and Their Relative Abundances as well as the Compositions and Relative Abundances of the CAD Products of TDMAB Adduct – 2 DMA ( $MH^+ + T - 2DMA$ , also referred to as **N** below) Formed in Reactions of Protonated Quetiapine *N*-Oxide and Quetiapine Sulfoxide (referred to as **M** below) with TDMAB (**T**)

Analyte ( <b>M</b> )	Observed product ions and their relative abundances	CAD of <b>M + T - 2 DMA</b> ( <b>N</b> ) and the relative abundances of fragment ions
 Quetiapine <i>N</i> -oxide	$MH^+ + T - 2DMA$ ( $m/z$ 453) 95% $MH^+ + DMA^a$ ( $m/z$ 445) 3% $MH^+ + T - DMA$ ( $m/z$ 498) 2%	$N - DMA$ ( $m/z$ 453) 100% $N - O = BN(CH_3)_2 - \triangle$ ( $m/z$ 383) 40%
 Quetiapine Sulfoxide	$MH^+ + T - 2DMA$ ( $m/z$ 453) 86% $MH^+ + DMA^a$ ( $m/z$ 445) 12% $MH^+ + T - DMA$ ( $m/z$ 498) 2%	$N - O = BN(CH_3)_2 - \triangle$ ( $m/z$ 383) 100%

<sup>a</sup>The formation of a DMA adduct upon reaction with TDMAB may occur as shown in Figure S2.



**Figure 5.** Calculated free energies of activation and free energy changes for reactions producing type A and B (left) and type C (right) fragment ions for simple model compounds ( $M06-2X/6-311++G(d,p)/M06-2X/6-311++G(d,p)$  level of theory).

functionality. Hence, it is not surprising that no type B ions were observed for zileuton sulfoxide that contains no hydrogen atoms at carbon in the  $\alpha$ -position to the sulfoxide group. However, type A fragment ions were nevertheless observed. A possible mechanism for the formation of these ions is shown in Figure 7.

**Formation of TDMAB Adducts That Have Lost Two DMA Molecules upon Reactions of Some Protonated Drug Metabolites with TDMAB ( $MS^2$  Experiments).** Some protonated drug metabolites containing a sulfoxide or *N*-oxide functionality, *i.e.*, cetirizine *N*-oxide, quetiapine *N*-oxide, and

quetiapine sulfoxide, showed abundant products due to elimination of not just one but *two* DMA molecules from their TDMAB adducts (TDMAB adduct – 2 DMA; Tables 1 and 3). These products were not observed for analytes without a sulfoxide or *N*-oxide functionality. For protonated quetiapine *N*-oxide and sulfoxide, TDMAB adducts that have lost two DMA molecules are the major product ions (Table 3).

A possible mechanism for the formation of TDMAB adducts of protonated quetiapine that have lost two DMA molecules is shown in Figure 8. After the formation of the TDMAB adduct that has lost one DMA molecule as described above, a hydroxyl

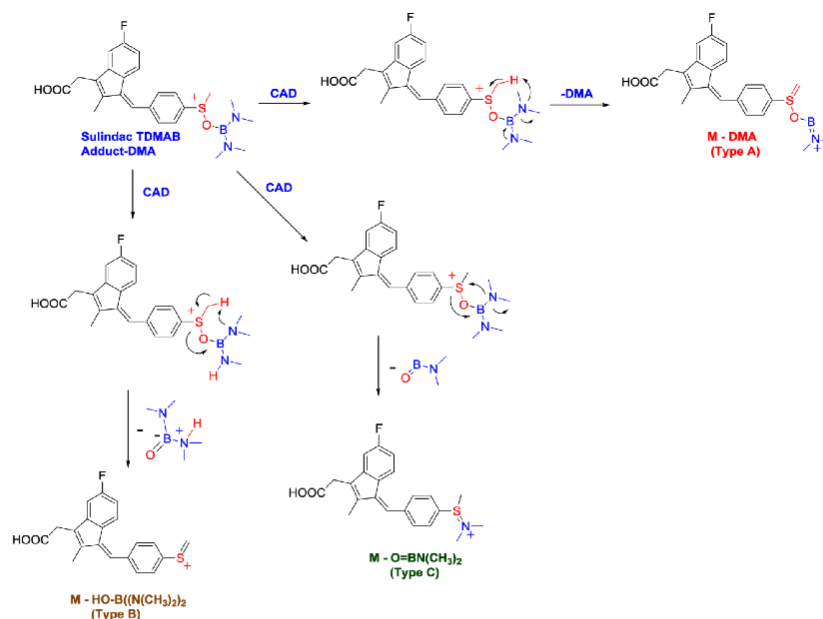


Figure 6. Proposed mechanisms for the formation of type A, B, and C fragment ions from TDMAB adduct of sulindac that has lost a DMA molecule.

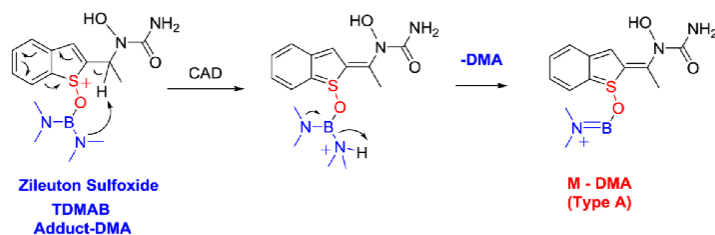


Figure 7. Proposed mechanism for the formation of type A fragment ions upon CAD of TDMAB adduct of zileuton sulfoxide that has lost a DMA molecule.

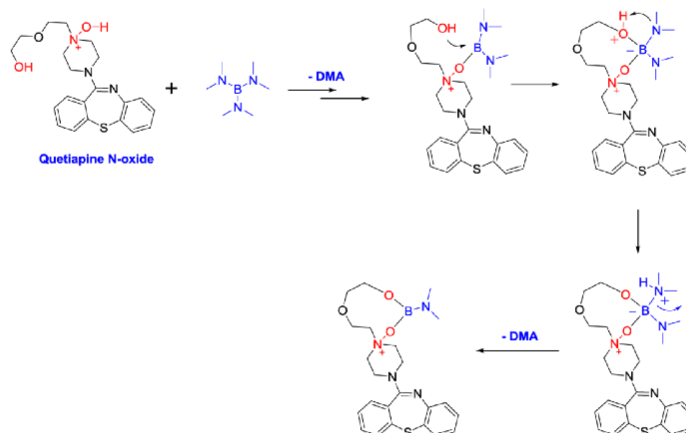
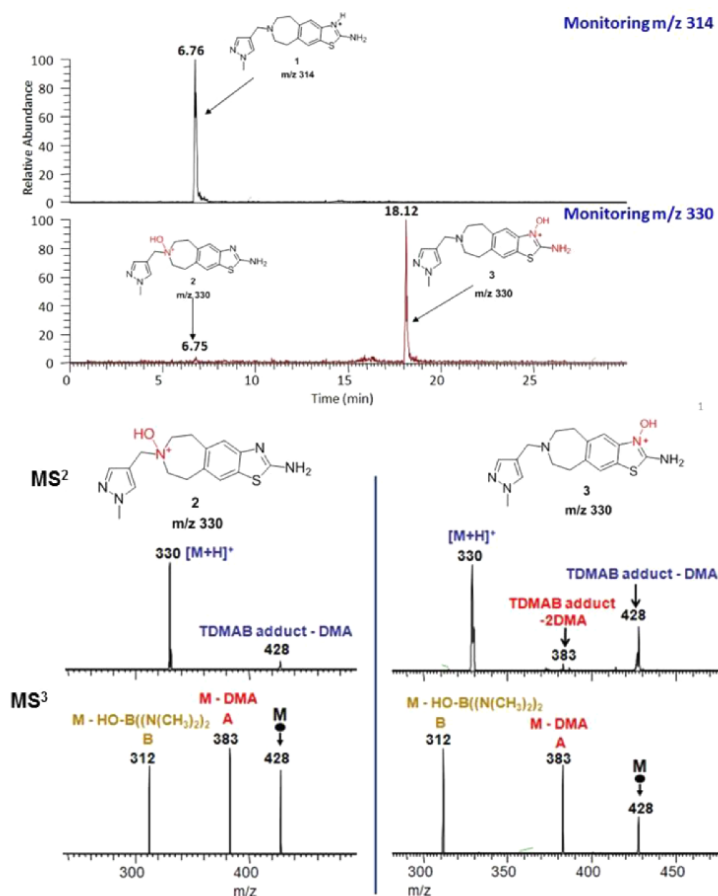


Figure 8. Proposed mechanism for the formation of the TDMAB adducts that have lost two DMA molecules for protonated quetiapine N-oxide.

group in the side chain is likely to add to the boron center, followed by proton transfer and elimination of a second DMA molecule. Formation of analogous product ions by protonated

cetirizine N-oxide and zileuton sulfoxide (Table 1) can be explained in a similar manner by involving nucleophilic attack by their carboxylic acid and hydroxylamino functionalities,





**Figure 9.** Selected ion chromatograms for ions of  $m/z$  314 and 330 for HPLC separation (phenyl column) of the dog liver metabolite mixture containing compounds 1–3 (top) and the MS<sup>2</sup> and MS<sup>3</sup> spectra measured for compounds 2 and 3 ionized by ESI as they eluted from the column (bottom).

respectively. Surprisingly, protonated quetiapine sulfoxide also formed this product ion in spite of not containing a nearby nucleophilic group. It is possible that the hydroxyl functionality in the remote alkyl chain can reach over to the boron atom bound to the sulfoxide group and react as shown in Figure 8 to form TDMAB adducts that have lost two DMA molecules with the calculated structure shown in Figure S8. Support for the structures of the TDMAB adducts that have lost two DMA molecules for quetiapine *N*-oxide and sulfoxide was obtained by CAD (Figure S11). Based on these results, the observation of TDMAB adducts that have lost two DMA molecules indicates the presence of a sulfoxide or an *N*-oxide functionality with a nearby nucleophilic group or a nucleophilic group that has access to these functionalities.

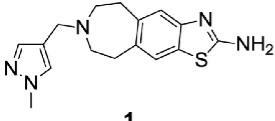
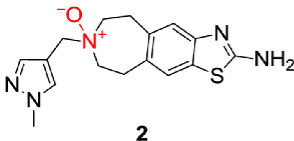
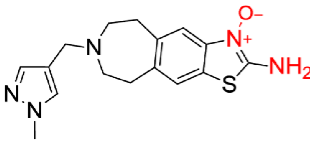
**Identification of a Drug Metabolite Isolated from Dog Liver Microsomes.** The MS<sup>3</sup> method described above was used to confirm the identification<sup>3</sup> of the drug metabolite 3 shown in Figure 1, an oxidized metabolite of 2-aminothiazolo-benzazepine (1). The mass spectrometric characterization of 3 was challenging since CAD only indicated that the oxidation occurred on the thiazole ring.<sup>3</sup> Hence, it was impossible to determine whether the oxidation site was one of the two

nitrogen atoms or the sulfur atom in the thiazole ring (Figure 1; Figure S1). Moreover, compound 3 is labile, which prevented its purification and the synthesis of the metabolite standard. Tandem mass spectrometry and ion–molecule reactions selective for hydroxylamines and *N*-oxides were used<sup>3</sup> to rule out the hydroxylamine metabolite. Solution reactions were used to rule out the sulfoxide functionality, thus identifying the unknown as the *N*-oxide 3. Hence, compound 3 provides a great test case for the proposed MS<sup>3</sup> method that, based on the above-mentioned studies on pure compounds, can be used to differentiate between *N*-oxide and sulfoxide functionalities in polyfunctional analytes.

Since compound 3 was obtained as a mixture that contains 1–3 as well as other metabolites,<sup>3</sup> an HPLC method was first developed to separate 3 from other metabolites. A phenyl column (Figure 9, top) was found to completely separate 3 from the azepine *N*-oxide 2 whereas a C18 column could not separate these two compounds (Figure S12).

The mass spectrometry results are summarized in Table 4 and Figure 9. The protonated drug molecule 1 did not react with TDMAB, in agreement with the lack of sulfoxide or *N*-oxide functionalities in this compound. The protonated azepine

**Table 4.** Observed Ion–Molecule Reaction Product Ions Formed in Reactions of Protonated 1–3 (referred to as **M** below) with TDMAB (**T**) and Their Relative Abundances as well as the Compositions and Relative Abundances of the CAD Products of the TDMAB Adducts That Had Lost a DMA Molecule ( $MH^+ + T - DMA$ , also referred to as **N** below)

Analyte ( <b>M</b> )	Observed product ions and their relative abundances ( $MS^2$ )	CAD of TDMAB adduct – DMA ( <b>N</b> ) and the relative abundances of CAD fragment ions ( $MS^3$ )
 <b>1</b>	No Products	-----
 <b>2</b>	$MH^+ + T - DMA$ ( $m/z$ 428) 100%	<b>N – DMA</b> ( $m/z$ 383) (A) 100% <b>N – HOB(N(CH<sub>3</sub>)<sub>2</sub>)<sub>2</sub></b> ( $m/z$ 312) (B) 85%
 <b>3</b>	$MH^+ + T - DMA$ ( $m/z$ 428) 83% $MH^+ + T - 2 DMA$ ( $m/z$ 383) 12% $MH^+ + DMA$ <sup>a</sup> ( $m/z$ 375) 5%	<b>N – DMA</b> ( $m/z$ 383) (A) 80% <b>N – HOB(N(CH<sub>3</sub>)<sub>2</sub>)<sub>2</sub></b> ( $m/z$ 312) (B) 100%

<sup>a</sup>The formation of a DMA adduct upon reaction with TDMAB may occur as shown in Figure S2.

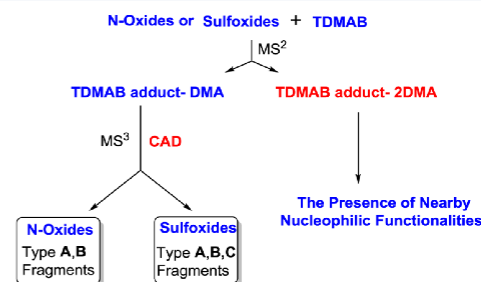
*N*-oxide reference compound **2** and the unknown metabolite **3** showed the TDMAB adducts that had lost one DMA molecule to be indicative of the presence of a sulfoxide or an *N*-oxide functionality. However, protonated compound **3** also showed the TDMAB adduct that had lost two DMA molecules (Table 4), indicative of an *N*-oxide or sulfoxide with a nearby nucleophilic functionality. This was expected if the oxidized functionality was in the thiazole ring, as suggested earlier based on solution reactions.<sup>3</sup>

Differentiation between sulfoxide and *N*-oxide metabolites was performed using CAD. The TDMAB adducts that had lost a DMA molecule formed from both compounds **2** and **3** gave the typical type A and B fragment ions, as expected. Most importantly, no type C fragment ions diagnostic for a sulfoxide was formed, demonstrating that the unknown compound **3** contains an *N*-oxide functionality. Likely mechanisms for the formation of the TDMAB adducts that have lost a DMA molecule (and those that have lost two DMA molecules) and their CAD reactions are shown in Figures S13 and S14 for **3**. They are analogous to the mechanisms discussed above for pure compounds. In conclusion, the unknown compound was identified as the thiazole *N*-oxide **3** by using HPLC/MS<sup>3</sup> experiments based on ion–molecule reactions and CAD.

## CONCLUSIONS

In this study, ion–molecule reactions with TDMAB followed by CAD were demonstrated to allow the identification and differentiation of protonated *N*-oxide and sulfoxide containing

drug metabolites in a linear quadrupole ion trap mass spectrometer (Figure 10). Only protonated polyfunctional



**Figure 10.** A general scheme for structural characterization of *N*-oxides and sulfoxides by MS<sup>3</sup> experiments employing ion–molecule reactions with TDMAB and CAD.

compounds containing either an *N*-oxide or a sulfoxide functionality showed abundant TDMAB adducts that had lost a DMA molecule (or two DMA molecules) when allowed to react with TDMAB in the gas phase (MS<sup>2</sup> experiments). CAD of the TDMAB adducts that had lost a DMA molecule gave type A and B fragment ions for both sulfoxides and *N*-oxides (MS<sup>3</sup> experiments). However, only sulfoxides yielded diagnostic type C fragment ions, which distinguishes these two functionalities. The formation of TDMAB adducts that have

lost two DMA molecules for some *N*-oxides and sulfoxides in the MS<sup>2</sup> experiments was found to indicate the presence of a nucleophilic group with access to the *N*-oxide or sulfoxide functionality, thus providing information on the chemical environment of these two functional groups (Figure 10). Finally, the ion–molecule reaction/CAD MS<sup>3</sup> method was successfully applied in the identification of a drug metabolite in dog liver microsomes by using HPLC/tandem mass spectrometry.

The results obtained in above studies demonstrated that protonated multifunctional compounds, such as drug metabolites, can carry the proton at several different sites with unequal PAs after evaporation by ESI from methanol solution. Hence, identification of a functionality is possible even when this is not the most basic functionality in the gaseous compound.

## EXPERIMENTAL SECTION

**Materials.** Ricobendazole, albendazole, and zioleuton sulfoxide were purchased from Santa Cruz Biotechnology (Dallas, Texas, USA); sulindac and sulindac sulfone were purchased from ENZO Life Sciences (Farmingdale, New York, USA); olanzapine *N*-oxide, 2-hydroxymethylolanzapine, quetiapine, quetiapine *N*-oxide, quetiapine sulfoxide, and cetzirizine *N*-oxide were purchased from Toronto Research Chemicals (Toronto, Ontario, Canada); and olanzapine, methionine sulfone, and tris(dimethylamino)borane (TDMAB) were purchased from Sigma-Aldrich (St. Louis, Missouri, USA). High-performance liquid chromatography–mass spectrometry (HPLC/MS) grade water, methanol, and acetonitrile were purchased from Fisher Scientific (Pittsburgh, PA, USA). All chemicals were used without further purification. A Zorbax SB-C18 column (4.6 mm × 250 mm, 5 μm particle size) and a Zorbax SB-Phenyl column (4.6 mm × 250 mm, 5 μm particle size) were purchased from Agilent Technologies (Santa Clara, CA). Compounds 1–3 were provided by AstraZeneca. Compound 1 is the parent drug compound. Compound 2 is a synthesized azepine *N*-oxide metabolite of 1. Compound 3 is the major (unknown) metabolite formed upon incubation of 1 in dog liver microsomes.<sup>3</sup>

**Sample Preparation.** Stock solutions of all the above-mentioned analytes were prepared at a final concentration of 0.1 mM in methanol. For HPLC/MS analysis, all analytes were dissolved in acetonitrile to achieve a final volume of 1 mL and an analyte concentration of 0.01 mM.

**Instrumentation.** All mass spectrometry experiments were performed using a Thermo Scientific LTQ linear quadrupole ion trap (LQIT) equipped with an ESI source. An integrated syringe drive was used to directly infuse the analyte solutions into the ESI source at a rate of 20 μL/min. All analytes were ionized via (+) ESI. The (+) ESI conditions were as follows: 3.5–4 kV spray voltage, sheath and auxiliary gas (N<sub>2</sub>) flow of 20 and 10 (arbitrary units), and a heated ion transfer capillary/mass spectrometer inlet temperature of 275 °C. The voltages for the ion optics were optimized for each analyte by using the tune feature of the LTQ Tune Plus interface. The protonated, isolated analytes were allowed to react with the reagent TDMAB in the ion trap for 50 up to 500 ms; however, up to 1000 ms were used in cases where no reactions were observed.

The manifold used to introduce reagents into the helium buffer gas line was first described by Gronert.<sup>34,35</sup> A diagram of the exact manifold used in this research was published by Habicht et al.<sup>19</sup> TDMAB was introduced into the manifold via a syringe pump at a flow rate of 20 μL/h. A known amount of He (1.5 L/h) was used to dilute TDMAB. The syringe port and surrounding area were heated to ~90 °C to ensure evaporation of TDMAB. Before entering the trap, the He/reagent mixture was split using two Granville-Phillips leak valves, instead of the standard flow splitter. This allowed better control over the amount of the mixture introduced into the instrument. One leak valve was set to establish a helium pressure of ~3 m Torr in the ion trap by allowing ~2 mL/min of the mixture into the trap<sup>36</sup> while the other leak valve controlled the amount of flow diverted to waste. A

typical nominal pressure of TDMAB in the trap during the experiments was  $0.68 \times 10^{-5}$  Torr. After the experiments were completed each day, the manifold was isolated from the instrument and placed under vacuum to remove any remaining reagent.

In collisionally activated dissociation (CAD) experiments, the advanced scan features of the LTQ Tune Plus interface were used to isolate the ions by using an *m/z* window of 2 units. At a *q* value of 0.25, the ions were subjected to CAD by using helium as the collision gas for an activation time of 30 ms. “Normalized collision energies” were varied from 20% up to 40%.

The detection mass range was from *m/z* 50 up to 500. All mass spectra acquired were an average of at least 20 spectra. Xcalibur 2.0 software was used for processing of all data produced.

**High Performance Liquid Chromatography/Tandem Mass Spectrometry.** The reference compounds 1 and 2 and the dog liver metabolite mixture of 1 (obtained as described in the literature<sup>3</sup>) were introduced into the HPLC/MS via an autosampler as a full-loop injection volume for high reproducibility. The flow rate was 0.5 mL/min. Solutions containing 0.1% (v/v) formic acid in water (A) and 0.1% formic acid (v/v) in acetonitrile (B) were used as the mobile phase solvents. Formic acid was chosen to encourage positive ion production. The nonlinear gradient used was as follows: 0.0 min, 95% A and 5% B; 10.0 min, 80% A and 20% B; 18.0 min, 55% A and 45% B; 25.0 min, 3% A and 97% B; 26.0 min, 3% A and 97% B; 26.1 min, 95% A and 5% B; 30.0 min, 95% A and 5% B. The column was located in a thermostated compartment where the temperature was maintained at 30 °C. Mass spectrometric analysis of the HPLC eluent was performed using single ion monitoring for ions of *m/z* 314 (protonated 1) and *m/z* 330 (protonated 2 and 3). Ions with the *m/z* values 314 and *m/z* 330 were selected for further isolation and MS<sup>2</sup> experiments involving CAD. For MS<sup>2</sup> experiments, an ion isolation window of 2 *m/z* was used prior to ion fragmentation at a *q* value of 0.25 for 30 ms at a normalized collision energy of 35% (arbitrary units).

**Computational Studies.** The Gaussian 03 suite of programs was used for all calculations.<sup>37</sup> Proton affinities were calculated at the B3LYP/6-31G++(d,p) level of theory. All the neutral and protonated molecules' lowest energy conformers were identified using the Maestro 7.0 Macro-model conformational search. The free energies of activation and reaction were calculated at the M06-2X/6-311++G(d,p)/M06-2X/6-311++G(d,p) level of theory.

## ASSOCIATED CONTENT

### Supporting Information

The Supporting Information is available free of charge on the ACS Publications website at DOI: 10.1021/acs.joc.5b02409.

Minimum energy geometry data (ZIP)

Additional information on the proton affinity and potential energy surface calculations of some molecules, HPLC chromatogram of C18 column for separation of the mixture of 3 and the ion–molecule reaction results of TDMAB with some simple sulfoxide model compounds (PDF)

## AUTHOR INFORMATION

### Corresponding Author

\*E-mail: hilkka@purdue.edu.

### Notes

The authors declare no competing financial interest.

## ACKNOWLEDGMENTS

The authors thank AstraZeneca for their financial support.

## REFERENCES

- (1) (a) Crettol, S.; Petrovic, N.; Murray, M. *Curr. Pharm. Des.* **2010**, *16*, 204–219. (b) Zuniga, F. L.; Loi, D.; Ling, K. H.; Tang-Liu, D. D. *Expert Opin. Drug Metab. Toxicol.* **2012**, *8*, 467–485.
- (2) Chen, X.; Hussain, S.; Parveen, S.; Zhang, S.; Yang, Y.; Zhu, C. *Curr. Med. Chem.* **2012**, *19*, 3578–3604.
- (3) Zhang, M.; Eismín, R.; Kenttämäa, H. I.; Xiong, H.; Wu, Y.; Burdette, D.; Urbanek, R. *Drug Metab. Dispos.* **2015**, *43*, 358–366.
- (4) Bright, T. V.; Dalton, F.; Elder, V. L.; Murphy, C. D.; O'Connor, N. K.; Sandford, G. *Org. Biomol. Chem.* **2013**, *11*, 1135–1142.
- (5) St. Jean, D. J., Jr.; Fotsch, C. *J. Med. Chem.* **2012**, *55*, 6002–6020.
- (6) Park, B. K.; Boobis, A.; Clarke, S.; Goldring, C. E. P.; Jones, D.; Kenna, J. G.; Lambert, C.; Laverty, H. G.; Naisbitt, D. J.; Nelson, S.; Nicoll-Griffith, D. A.; Obach, R. S.; Routledge, P.; Smith, D. A.; Tweedie, D. J.; Vermeulen, N.; Williams, D. P.; Wilson, I. D.; Baillie, T. A. *Nat. Rev. Drug Discovery* **2011**, *10*, 292–306.
- (7) Kalgutkar, A. S.; Gardner, I.; Obach, R. S.; Shaffer, C. L.; Callegari, E.; Henne, K. R.; Mutlib, A. E.; Dalvie, D. K.; Lee, J. S.; Nakai, Y.; O'Donnell, J. P.; Boer, J.; Harriman, S. P. *Curr. Drug Metab.* **2005**, *6*, 161–225.
- (8) Caslavská, J.; Thormann, W. *J. Chromatogr. A* **2011**, *1218*, 588–601.
- (9) Bhawe, D. P.; Muse, W. B., 3rd; Carroll, K. S. *Infect. Disord.: Drug Targets* **2007**, *7*, 140–158.
- (10) Dibbern, D. A., Jr.; Montanaro, A. *Ann. Allergy, Asthma, Immunol.* **2008**, *100*, 91–100.
- (11) Prakash, C.; Shaffer, C. L.; Nedderman, A. *Mass Spectrom. Rev.* **2007**, *26*, 340–369.
- (12) Palmnas, M. S.A.; Vogel, H. J. *Metabolites* **2013**, *3*, 373–396.
- (13) Lenz, E. M. *Methods Mol. Biol.* **2011**, *708*, 299–319.
- (14) Froelich, J. M.; Reid, G. E. *J. Am. Soc. Mass Spectrom.* **2007**, *18*, 1690–1705.
- (15) Reid, G. E.; Roberts, K. D.; Kapp, E. A.; Simpson, R. I. *J. Proteome Res.* **2004**, *3*, 751–759.
- (16) Jiang, X.; Smith, J. B.; Abraham, E. C. *J. Mass Spectrom.* **1996**, *31*, 1309–1310.
- (17) Osburn, S.; Ryzhov, V. *Anal. Chem.* **2013**, *85*, 769–778.
- (18) Eismín, R. J.; Fu, M.; Yem, S.; Widjaja, F.; Kenttämäa, H. I. *J. Am. Soc. Mass Spectrom.* **2012**, *23*, 12–22.
- (19) Habicht, S. C.; Vinueza, N. R.; Archibold, E. F.; Duan, P.; Kenttämäa, H. I. *Anal. Chem.* **2008**, *80*, 3416–3421.
- (20) Campbell, K. M.; Watkins, M. A.; Li, S.; Fiddler, M. N.; Winger, B.; Kenttämäa, H. I. *J. Org. Chem.* **2007**, *72*, 3159–3165.
- (21) Somuramasami, J.; Duan, P.; Amundson, L.; Archibold, E.; Winger, B.; Kenttämäa, H. I. *J. Am. Soc. Mass Spectrom.* **2011**, *22*, 1040–1051.
- (22) Fu, M.; Eismín, R. J.; Duan, P.; Li, S.; Kenttämäa, H. I. *Int. J. Mass Spectrom.* **2009**, *282*, 77–84.
- (23) Fu, M.; Duan, P.; Li, S.; Habicht, S. C.; Pinkston, D. S.; Vinueza, N. R.; Kenttämäa, H. I. *Analyst* **2008**, *133*, 452–454.
- (24) Duan, P.; Fu, M.; Gillespie, T. A.; Winger, E.; Kenttämäa, H. I. *J. Org. Chem.* **2009**, *74*, 1114–1123.
- (25) Duan, P.; Gillespie, T. A.; Winger, B. E.; Kenttämäa, H. I. *J. Org. Chem.* **2008**, *73*, 4888–4894.
- (26) Sheng, H.; Williams, P. E.; Tang, W.; Riedeman, J. S.; Zhang, M.; Kenttämäa, H. I. *J. Org. Chem.* **2014**, *79*, 2883–2889.
- (27) Sheng, H.; Williams, P. E.; Tang, W.; Zhang, M.; Kenttämäa, H. I. *Analyst* **2014**, *139*, 4296–4302.
- (28) Sheng, H.; Tang, W.; Yerabolu, R.; Kong, J. Y.; Williams, P. E.; Zhang, M.; Kenttämäa, H. I. *Rapid Commun. Mass Spectrom.* **2015**, *29*, 730–734.
- (29) Habicht, S. C.; Vinueza, N. R.; Amundson, L. M.; Kenttämäa, H. I. *J. Am. Soc. Mass Spectrom.* **2011**, *22*, 520–530.
- (30) Habicht, S. C.; Duan, P.; Vinueza, N. R.; Fu, M.; Kenttämäa, H. I. *J. Pharm. Biomed. Anal.* **2010**, *51*, 805–811.
- (31) (a) Tian, Z.; Kass, S. R. *Angew. Chem., Int. Ed.* **2009**, *48*, 1321–1323. (b) Schmidt, J.; Meyer, M. K.; Spector, I.; Kass, S. R. *J. Phys. Chem. A* **2011**, *115*, 7625–7632. (c) Campbell, J. L.; Le Blanc, J. C. Y.; Schneider, B. B. *Anal. Chem.* **2012**, *84*, 7857–7864. (d) Schröder, D.; Buděšínský, M.; Roithová, J. *J. Am. Chem. Soc.* **2012**, *134*, 15897–15905.
- (32) (a) Nelson, R. D., Lide, D. R., Maryott, A. A. *National Standard Reference Data Series-National Bureau of Standards 10*. Washington, DC, 20402 (retrieved May 10, 2015). (b) Pople, J. A.; Gordon, M. J. *Am. Chem. Soc.* **1967**, *89*, 4253–4261. (c) Brown, R. D.; Burden, F. R.; Garland, W. *Chem. Phys. Lett.* **1970**, *7*, 461–462.
- (33) Bowers, M. T. *Gas Phase Ion Chemistry*, Vol. 1; Academic Press: 1979.
- (34) Gronert, S. *J. Am. Soc. Mass Spectrom.* **1998**, *9*, 845–848.
- (35) Gronert, S. *Mass Spectrom. Rev.* **2005**, *24*, 100–120.
- (36) Schwartz, J. C.; Senko, M. W.; Syka, J. E. *J. Am. Soc. Mass Spectrom.* **2002**, *13*, 659–669.
- (37) Frisch, M. J.; Trucks, G. W.; Schlegel, H. B.; Scuseria, G. E.; Robb, M. A.; Cheeseman, J. R.; Montgomery, Jr., J. A.; Vreven, T.; Kudin, K. N.; Burant, J. C.; Millam, J. M.; Iyengar, S. S.; Tomasi, J.; Barone, V.; Mennucci, B.; Cossi, M.; Scalmani, G.; Rega, N.; Petersson, G. A.; Nakatsuji, H.; Hada, M.; Ehara, M.; Toyota, K.; Fukuda, R.; Hasegawa, J.; Ishida, M.; Nakajima, T.; Honda, Y.; Kitao, O.; Nakai, H.; Klene, M.; Li, X.; Knox, J. E.; Hratchian, H. P.; Cross, J. B.; Bakken, V.; Adamo, C.; Jaramillo, J.; Gomperts, R.; Stratmann, R. E.; Yazyev, O.; Austin, A. J.; Cammi, R.; Pomelli, C.; Ochterski, J. W.; Ayala, P. Y.; Morokuma, K.; Voth, G. A.; Salvador, P.; Dannenberg, J. J.; Zakrzewski, V. G.; Dapprich, S.; Daniels, A. D.; Strain, M. C.; Farkas, O.; Malick, D. K.; Rabuck, A. D.; Raghavachari, K.; Foresman, J. B.; Ortiz, J. V.; Cui, Q.; Baboul, A. G.; Clifford, S.; Cioslowski, J.; Stefanov, B. B.; Liu, G.; Liashenko, A.; Piskorz, P.; Komaromi, I.; Martin, R. L.; Fox, D. J.; Keith, T.; Al-Laham, M. A.; Peng, C. Y.; Nanayakkara, A.; Challacombe, M.; Gill, P. M. W.; Johnson, B.; Chen, W.; Wong, M. W.; Gonzalez, C.; Pople, J. A. *Gaussian 03*, Revision C.02; Gaussian, Inc.: Wallingford, CT, 2004.

## Gas-phase ion–molecule reactions for the identification of the sulfone functionality in protonated analytes in a linear quadrupole ion trap mass spectrometer

Weijuan Tang<sup>1,3†</sup>, Huaming Sheng<sup>1,4‡</sup>, John Y. Kong<sup>1</sup>, Ravikiran Yerabolu<sup>1</sup>, Hanyu Zhu<sup>1</sup>, Joann Max<sup>1</sup>, Minli Zhang<sup>2</sup> and Hilka I. Kenttämaa<sup>1\*</sup>

<sup>1</sup>Department of Chemistry, Purdue University, West Lafayette, IN 47907, USA

<sup>2</sup>AstraZeneca, Waltham, MA 02541, USA

<sup>3</sup>DuPont, 200 Powder Mill Rd., Wilmington, DE 19843, USA

<sup>4</sup>Merck, 125 E Lincoln Ave, Rahway, NJ 07065, USA

**RATIONALE:** The oxidation of sulfur atoms is an important biotransformation pathway for many sulfur-containing drugs. In order to rapidly identify the sulfone functionality in drug metabolites, a tandem mass spectrometric method based on ion–molecule reactions was developed.

**METHODS:** A phosphorus-containing reagent, trimethyl phosphite (TMP), was allowed to react with protonated analytes with various functionalities in a linear quadrupole ion trap mass spectrometer. The reaction products and reaction efficiencies were measured.

**RESULTS:** Only protonated sulfone model compounds were found to react with TMP to form a characteristic [TMP adduct–MeOH] product ion. All other protonated compounds investigated, with functionalities such as sulfoxide, N-oxide, hydroxylamino, keto, carboxylic acid, and aliphatic and aromatic amino, only react with TMP via proton transfer and/or addition. The specificity of the reaction was further demonstrated by using a sulfoxide-containing anti-inflammatory drug, sulindac, as well as its metabolite sulindac sulfone.

**CONCLUSIONS:** A method based on functional group-selective ion–molecule reactions in a linear quadrupole ion trap mass spectrometer has been demonstrated for the identification of the sulfone functionality in protonated analytes. A characteristic [TMP adduct–MeOH] product ion was only formed for the protonated sulfone analytes. The applicability of the TMP reagent in identifying sulfone functionalities in drug metabolites was also demonstrated. Copyright © 2016 John Wiley & Sons, Ltd.

Rapid identification of drug metabolites, degradation products, and impurities is crucial in the drug discovery and development process since some of them are toxic.<sup>[1–3]</sup> Analytical techniques, such as nuclear magnetic resonance (NMR) spectroscopy, Fourier transform infrared (FT-IR) spectroscopy, and X-ray crystallography, can be utilized to obtain information on functional groups and elemental connectivity in an analyte.<sup>[4–6]</sup> However, compounds that are present in only small quantities in complex mixtures are difficult to identify using the above methods.

Tandem mass spectrometry (MS/MS) has evolved to be a powerful technique for mixture analysis due to its high sensitivity, selectivity and speed.<sup>[7,8]</sup> Single-stage mass spectrometry (MS) can provide the molecular mass and

elemental composition of the ionized analytes, while MS/MS utilizing collision-induced dissociation (CID) can provide structural information for ionized unknown analytes.<sup>[9]</sup> When the functionalities of ionized analytes cannot be definitively determined by CID alone, an alternative MS<sup>n</sup> technique based on ion–molecule reactions can be utilized to obtain structural information.<sup>[10]</sup> We have successfully developed methods based on ion–molecule reactions to identify various functional groups in ionized analytes.<sup>[11–21]</sup> Several neutral reagents have been investigated extensively, including boron- and oxygen-containing organic reagents with good leaving groups.<sup>[11–21]</sup> However, phosphorus-containing neutral reagents have been rarely studied. The only report to have appeared thus far focused on the identification of the amino functionality as well as differentiation of primary, secondary and tertiary protonated amino functionalities by using diethyl methylphosphonate and hexamethylphosphoramide.<sup>[22]</sup> In this case, proton transfer and adduct formation are the two major reaction pathways.<sup>[22]</sup>

Oxidized sulfur functionalities, such as sulfone and sulfoxide, are common in drug metabolites.<sup>[23]</sup> Only a few MS/MS studies based on CID of ionized sulfones and

\* Correspondence to: H. I. Kenttämaa, Department of Chemistry, Purdue University, West Lafayette, IN 47907, USA.  
E-mail: hilka@purdue.edu

† Present address: DuPont, Garnet Valley, PA 19060, USA.

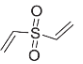
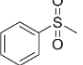
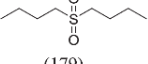
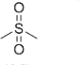
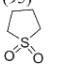
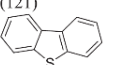
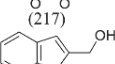
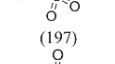
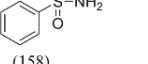
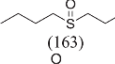
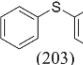

‡ Present address: Merck, 125 E Lincoln Ave, Rahway, NJ 07065, USA.

sulfoxides have been published. None of them showed sulfone- or sulfoxide-specific fragmentation patterns.<sup>[24–27]</sup> In an effort to enable identification of sulfur-containing functionalities in drug metabolites, we recently reported a boron-containing reagent (trimethyl borate, TMB) that allows the identification of protonated sulfone analytes<sup>[19]</sup> and an oxygen-containing reagent (2-methoxypropene, MOP) for the identification of protonated sulfoxide analytes.<sup>[20]</sup> TMB was found to yield a diagnostic product

ion, adduct–Me<sub>2</sub>O, upon reaction with protonated sulfone analytes while MOP was found to yield stable adducts for protonated sulfoxides and N-oxides. Sulfoxides can be identified based on their higher reaction efficiencies.

While the above results are encouraging, more than one reagent is desirable for the correct identification of each functionality in order to avoid problems caused by false positive and negative results. In this study, a phosphorus-containing reagent, trimethyl phosphite (TMP), was examined

**Table 1.** Reaction products (*m/z* values and branching ratios) and efficiencies for the reactions of protonated sulfones and sulfoxides with TMP (PA = 222.2 kcal/mol)<sup>[33]</sup>

Reagent ( <i>m/z</i> of [M+H] <sup>+</sup> )	PA (kcal/mol)	Product ions ( <i>m/z</i> ) and their branching ratios		Reaction efficiency
 (119)	206.3 <sup>[19]</sup>	Protonated TMP (125) <b>Adduct - MeOH (309)</b>	72% <b>28%</b>	90%
 (157)	201.4 <sup>[19]</sup>	Protonated TMP (125) <b>Adduct - MeOH (249)</b>	74% <b>26%</b>	76%
 (179)	203.7 <sup>[19]</sup>	Protonated TMP (125) <b>Adduct - MeOH (271)</b>	98% <b>2%</b>	94%
 (95)	194.6 <sup>a</sup>	Protonated TMP (125) <b>Adduct - MeOH (187)</b>	75% <b>25%</b>	98%
 (121)	198.3 <sup>[19]</sup>	Protonated TMP (125) <b>Adduct - MeOH (213)</b>	71% <b>29%</b>	90%
 (217)	205.0 <sup>[19]</sup>	Protonated TMP (125) <b>Adduct - MeOH (309)</b>	94% <b>6%</b>	59%
 (197)	200.9 <sup>a</sup>	Protonated TMP (125) <b>Adduct - MeOH (289)</b> Adduct (321)	29% <b>7%</b> 64%	58%
 (158)	202.9 <sup>a</sup>	Protonated TMP (125) <b>Adduct - MeOH (250)</b> Adduct (282)	96% <b>3%</b> 1%	89%
 (163)	220.1 <sup>[19]</sup>	Protonated TMP (125) Adduct (287)	96% 4%	87%
 (203)	222.5 <sup>[19]</sup>	Protonated TMP (125) Adduct (327)	95% 5%	73%
 (79)	211.3 <sup>[33]</sup> 210.5 <sup>a</sup>	Protonated TMP (125) Adduct (203)	98% 2%	101%
 (166)	227.9 <sup>a</sup>	Protonated TMP (125) Adduct (290)	1% 99%	3%

<sup>a</sup>Calculated at the B3LYP/6-31G++(d,p) level of theory.

## Identification of the sulfone functionality

as a potential additional reagent for the identification of sulfur-containing functionalities. It was found to form characteristic [TMP adduct–MeOH] ions only upon reactions with protonated sulfone analytes. Thus, it can be used for differentiation of sulfone functionalities from many other functional groups, including sulfoxide, hydroxylamino, N-oxide, aniline, amino, keto and carboxylic acid. The reaction specificity was further demonstrated by studying a sulfoxide-containing anti-inflammatory drug, sulindac, as well as its metabolite, sulindac sulfone.

## EXPERIMENTAL

## Chemicals

All chemicals were purchased from Sigma-Aldrich (St. Louis, MO, USA). Their purities were  $\geq 98\%$ . All chemicals were used without further purification.

## Instrumentation

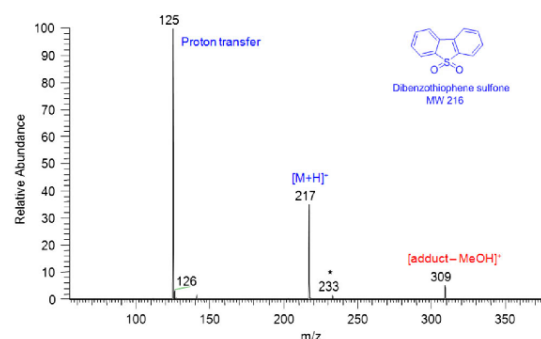
All mass spectrometry experiments were performed using an LTQ linear quadrupole ion trap (LQIT; Thermo Scientific, Waltham, MA, USA) equipped with an atmospheric pressure chemical ionization (APCI) source. The analytes were dissolved in methanol with a final concentration of 0.01–1 mg/mL. The sample solutions were introduced into the mass spectrometer by direct infusion at a flow rate of 20  $\mu\text{L}/\text{min}$  by using a syringe drive. The APCI source was operated in positive ion mode. The temperatures for the vaporizer and transfer capillary were set at 300  $^{\circ}\text{C}$  and 275  $^{\circ}\text{C}$ , respectively. Nitrogen was used as the sheath gas and auxiliary gas, with the flow rate maintained at 30 and 10 arbitrary units, respectively. The voltages for the ion optics were optimized for each individual analyte by using the tune feature of the LTQ Tune Plus interface. The normal mass range ( $m/z$  50–500) was used for all the experiments, while the low mass range ( $m/z$  20–200) was used for examination of the exothermic proton-transfer reaction between protonated methanol and the reagent (TMP). The type of manifold used to introduce the reagent was first described by Gronert.<sup>[28,29]</sup> A diagram of the exact manifold used in this research was published by Habicht *et al.*<sup>[13]</sup> This manifold setup passes the gas through the He splitter of the LQIT. TMP was introduced into the manifold via a syringe pump at 10  $\mu\text{L}/\text{h}$ . A known flow rate of helium gas (0.8 L/h) was used to carry TMP into the mass spectrometer. The syringe port and surrounding area were heated to  $\sim 70$   $^{\circ}\text{C}$  to ensure evaporation of TMP.<sup>[30]</sup> A leak valve (Granville-Phillips, Chelmsford, MA, USA) was used to control the amount of the reagent introduced into the instrument, while another leak valve (Granville-Phillips) controlled the amount of helium diverted to waste.<sup>[31]</sup> A typical nominal pressure (read-out on the ion gauge) of TMP in the ion trap during the experiments was  $0.6 \times 10^{-5}$  Torr.

## Kinetics

After the analytes had been ionized by protonation in the APCI source, the protonated analytes were selected using an isolation window of 2  $m/z$  units. The isolated ions were

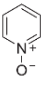
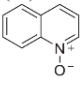
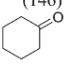
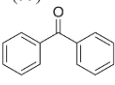
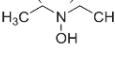
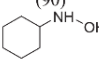
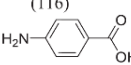
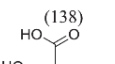
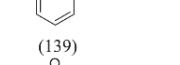
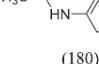
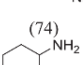
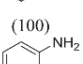
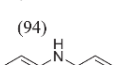
allowed to react with the reagent TMP for variable periods of time. In the course of ion–molecule reactions, the concentration of the neutral reagent is in great excess of that of the ion of interest. Therefore, the pressure of TMP can be considered as a constant, and the reactions follow pseudo-first-order kinetics. The reaction efficiency corresponds to the fraction of ion–molecule collisions that leads to the formation of products. The reaction efficiency,  $k_{\text{reaction}}/k_{\text{collision}}$ , was calculated by measuring the rate of each ion–molecule reaction (IM) and the rate of the highly exothermic proton-transfer reaction (PT) between protonated methanol and the reagent (TMP) under identical conditions. The above rates were measured by determining the relative abundances of the reactant ion and product ions as a function of reaction time. In a semi-logarithmic plot of the ion abundances as a function of time, the decay slope of the reactant ion corresponds to the rate constant,  $k$ , multiplied by the neutral reagent's concentration. Assuming that the exothermic proton-transfer reaction (PT) between protonated methanol and TMP proceeds at collision rate  $k_{\text{collision}}$  (this can be calculated by using a parameterized trajectory theory<sup>[32]</sup>), the efficiencies of the ion–molecule reactions can be obtained by using Eqn. (1). The reaction efficiency is based on the ratio of the slopes of the two reactions studied, i.e.,  $k_{\text{reaction}}[\text{TMP}] = \text{slope}(\text{IM})$ ,  $k_{\text{collision}}[\text{TMP}] = \text{slope}(\text{PT})$ , wherein  $[\text{TMP}] = \text{TMP concentration}$ . It is obvious that there is no need to measure the concentration of TMP as it cancels out in the calculation. In addition, the reaction efficiency is dependent on the masses of the ion ( $M_i$ ), the reagent ( $M_n$ ), and methanol ( $M_{(\text{PT})}$ ), as well as on the pressure read by an ion gauge for the reagent during the ion–molecule reaction ( $P_{n(\text{IM})}$ ) and the proton-transfer reaction ( $P_{n(\text{PT})}$ ).

$$\text{Efficiency} = \frac{\text{slope}(\text{IM})}{\text{slope}(\text{PT})} \times \left( \frac{M_i M_{(\text{PT})} + M_n}{M_{(\text{PT})} (M_i + M_n)} \right)^{1/2} \times \left( \frac{P_{n(\text{PT})}}{P_{n(\text{IM})}} \right) \times 100 \quad (1)$$



**Figure 1.** A mass spectrum measured after 100 ms reaction of protonated dibenzothiophene sulfone with TMP in the LQIT instrument (\*secondary product of protonated TMP corresponding to a protonated TMP dimer that has lost a methane molecule).

**Table 2.** Reaction products (*m/z* values and branching ratios) and efficiencies for reactions between protonated N-oxides, ketones, hydroxylamines, carboxylic acids, and aliphatic and aromatic amines with TMP (PA = 222.2 kcal/mol<sup>[33]</sup>)

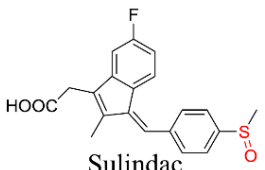
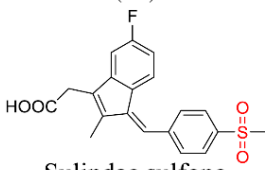
Reagent ( <i>m/z</i> of [M+H] <sup>+</sup> )	PA (kcal/mol)	Product ions ( <i>m/z</i> ) and their branching ratios	Reaction efficiency	
 (96)	220.6 <sup>[33]</sup> 217.7 <sup>a</sup>	Protonated TMP (125) Adduct (220) <sup>a</sup>	98% 2%	94%
	225.3 <sup>[33]</sup>	Protonated TMP (125) Adduct (270)	66% 34%	10%
 (146)	201 <sup>[33]</sup>	Protonated TMP (125)	100%	110%
 (99)	210.0 <sup>[33]</sup>	Protonated TMP (125) Adduct (307)	98% 2%	91%
 (183)	218.6 <sup>[33]</sup>	Protonated TMP (125) Adduct (214)	97% 3%	87%
 (90)	215.9 <sup>[33]</sup>	Protonated TMP (125) Adduct (240)	95% 5%	94%
 (116)	206.7 <sup>[33]</sup>	Protonated TMP (125)	100%	71%
 (138)	200.7 <sup>a</sup>	Protonated TMP (125)	100%	78%
 (139)	207.5 <sup>a</sup>	Protonated TMP (125) Adduct (304)	98% 2%	95%
 (180)	220.2 <sup>[33]</sup>	Protonated TMP (125) Adduct (198)	95% 5%	30%
 (74)	223.3 <sup>[33]</sup>	Protonated TMP (125) Adduct (224)	94% 6%	86%
 (100)	210.9 <sup>[33]</sup> 209.0 <sup>a</sup>	Protonated TMP (125)	100%	53%
 (94)	214.4 <sup>a</sup>	Protonated TMP (125) Adduct (294)	97% 3%	46%
(170)				

<sup>a</sup>Calculated at the B3LYP/6-31G++(d,p) level of theory.



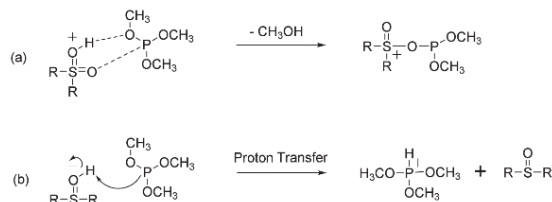
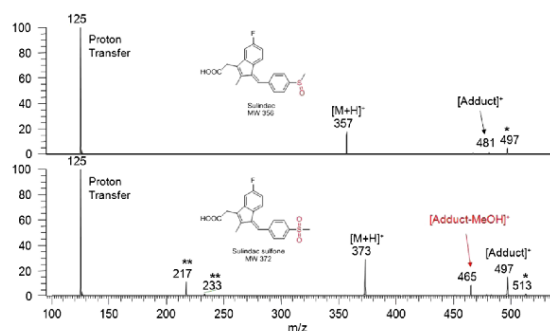
## Identification of the sulfone functionality

**Table 3.** Reaction products ( $m/z$  values and branching ratios) and efficiencies for reactions of protonated sulindac and sulindac sulfone with TMP (PA = 222.2 kcal/mol<sup>[33]</sup>)

Reagent ( $m/z$ of [M+H] <sup>+</sup> )	PA <sup>[34]</sup> (kcal/mol)	Product ions ( $m/z$ ) and their branching ratios	Reaction efficiency
 Sulindac (373)	224	Protonated TMP (125) 89% Adduct (481) 11%	53%
 Sulindac sulfone (373)	203	Protonated TMP (125) 75% Adduct - MeOH (465) 9% Adduct (497) 16%	78%

## RESULTS AND DISCUSSION

In an effort to search for additional reagents that would allow the mass spectrometric identification of sulfur-containing functionalities in protonated analytes via ion–molecule reactions, trimethyl phosphite (TMP) was selected because its proton affinity (PA) (220 kcal/mol<sup>[33]</sup>) is close to that of sulfoxides (~220 kcal/mol<sup>[19]</sup>) and higher than that of sulfones (~205 kcal/mol<sup>[19]</sup>). This should allow the TMP to deprotonate protonated sulfoxides and sulfones, which is usually the first step in functional-group-selective ion–molecule reactions.<sup>[11–22]</sup> As shown in Table 1, proton transfer was the major reaction for both protonated sulfones and protonated sulfoxides. However, protonated sulfones showed characteristic [TMP adduct–MeOH] product ions. A mass spectrum measured after 100 ms reaction of protonated

**Scheme 1.** Proposed mechanisms for (a) the formation of a stable [TMP adduct–MeOH] product ion upon reaction of only protonated sulfones with TMP and (b) proton transfer upon reaction of protonated sulfoxides with TMP.**Figure 2.** Mass spectra measured after 300 ms reaction of protonated sulindac (top) and sulindac sulfone (bottom) with TMP in the LQIT (\*adducts with trimethylphosphate, a minor impurity in TMP; \*\* secondary products of protonated TMP corresponding to the protonated TMP dimer that has lost a methane or methanol molecule).

dibenzothiophene sulfone with TMP is shown in Fig. 1 as an example. The most abundant product ion ( $m/z$  125) is formed by proton transfer. The other product ion ( $m/z$  309) corresponds to [TMP adduct–MeOH].

In order to probe the selectivity of the above reaction for protonated sulfones, TMP was allowed to react with other protonated analytes containing various functional groups, such as N-oxide, hydroxylamino, keto, carboxylic acid, and aliphatic and aromatic amino. The reaction products and efficiencies are summarized in Table 2. The main reaction was proton transfer, and minor addition reactions were also observed for some protonated analytes, yet no [TMP adduct–MeOH] product ion was observed.

In order to test whether the above reactivity would also be observed for multifunctional analytes, the reactions of protonated sulindac and its oxidation metabolite, sulindac sulfone, with TMP were examined. Only sulindac sulfone showed the [TMP adduct–MeOH] product ion (Table 3). The mass spectra measured after 300 ms reaction of protonated sulindac and sulindac sulfone with TMP are shown in Fig. 2. This result demonstrates the utility of this method for the identification of the sulfone functionality in drug metabolites.

Based on above observations, a mechanism is proposed for the formation of the [TMP adduct–MeOH] ion for protonated sulfones in Scheme 1(a). The selectivity of TMP toward sulfones is rationalized by a cyclic six-membered transition state that only protonated sulfones can form with TMP. Through this transition state, a proton is transferred to a less basic methoxy group as opposed to the most basic phosphorus center, resulting in the formation of the [TMP adduct–MeOH] product ion by displacement of a methanol molecule. For the other protonated functionalities, such as sulfoxide and N-oxide, the proton is probably transferred to the most basic site, the phosphorus center, since these functional groups cannot form the six-membered transition states possible for sulfones (Scheme 1(b)).

## CONCLUSIONS

A method based on a functional-group-selective ion–molecule reaction in a linear quadrupole ion trap mass spectrometer has been demonstrated for the identification of the sulfone functionality in protonated analytes. A phosphorus-containing reagent, trimethyl phosphite (TMP), can form characteristic [TMP adduct–MeOH] product ions only when allowed to react with protonated sulfone analytes. All other protonated compounds investigated in this study, with functionalities such as sulfoxide, N-oxide, hydroxylamino, keto, carboxylic acid, and aliphatic or aromatic amino, react with TMP via proton transfer and/or addition. The selectivity of TMP toward protonated sulfones is rationalized by a favorable six-membered transition state that other analytes cannot form. The results obtained for sulindac and sulindac sulfone suggest that this method allows the identification of sulfone functional groups in drug metabolites even in the presence of other functionalities.

## Acknowledgement

We thank AstraZeneca for financial support.

## REFERENCES

- [1] F. I. Zuniga, D. Loi, K. H. Ling, D. D. Tang-Liu. Idiosyncratic reactions and metabolism of sulfur-containing drugs. *Expert Opin. Drug Metab. Toxicol.* **2012**, *8*, 467.
- [2] X. Chen, S. Hussain, S. Parveen, S. Zhang, Y. Yang, C. Zhu. Sulfonyl group-containing compounds in the design of potential drugs for the treatment of diabetes and its complications. *Curr. Med. Chem.* **2012**, *19*, 3578.
- [3] M. D. Coleman. *Human Drug Metabolism, An Introduction*, (2nd edn.). John Wiley, Chichester, **2010**.
- [4] J. Caslavská, W. Thormann. Stereoselective determination of drugs and metabolites in body fluids, tissues and microsomal preparations by capillary electrophoresis (2000–2010). *J. Chromatogr. A* **2011**, *1218*, 588.
- [5] D. P. Bhawe, W. B. Muse 3rd, K. S. Carroll. Drug targets in mycobacterial sulfur metabolism. *Infect. Disord. Drug Targets* **2007**, *7*, 140.
- [6] D. A. Dibbern, A. Montanaro. Allergies to sulfonamide antibiotics and sulfur-containing drugs. *Ann. Allergy Asthma Immunol.* **2008**, *100*, 91.
- [7] S. A. McLuckey, J. M. Wells. Mass analysis at the advent of the 21st century. *Chem. Rev.* **2001**, *101*, 571.
- [8] R. H. Perry, R. G. Cooks, R. J. Knoll. Orbitrap mass spectrometry: instrumentation, ion motion and applications. *Mass Spectrom. Rev.* **2008**, *27*, 661.
- [9] R. G. Cooks, K. L. Busch, G. L. Glish. Mass spectrometry: analytical capabilities and potentials. *Science* **1983**, *222*, 273.
- [10] S. Osburn, V. Ryzhov. Ion–molecule reactions: Analytical and structural tool. *Anal. Chem.* **2013**, *85*, 769.
- [11] M. A. Watkins, B. E. Winger, R. C. Shea, H. I. Kenttämäa. Ion–molecule reactions for the characterization of polyols and polyol mixtures by ESI/FT-ICR mass spectrometry. *Anal. Chem.* **2005**, *77*, 1385.
- [12] K. M. Campbell, M. A. Watkins, S. Li, M. N. Fiddler, B. Winger, H. I. Kenttämäa. Functional group selective ion/molecule reactions: mass spectrometric identification of the amido functionality in protonated monofunctional compounds. *J. Org. Chem.* **2007**, *72*, 3159.
- [13] S. C. Habicht, N. R. Vinueza, E. F. Archibold, P. Duan, H. I. Kenttämäa. Identification of the carboxylic acid functionality by using electrospray ionization and ion–molecule reactions in a modified linear quadrupole ion trap mass spectrometer. *Anal. Chem.* **2008**, *80*, 3416.
- [14] M. Fu, P. Duan, S. Li, S. C. Habicht, D. S. Pinkston, N. R. Vinueza, H. I. Kenttämäa. Regioselective ion–molecule reactions for the mass spectrometric differentiation of protonated isomeric aromatic diamines. *Analyst* **2008**, *133*, 452.
- [15] P. Duan, T. A. Gillespie, B. E. Winger, H. I. Kenttämäa. Identification of the aromatic tertiary N-oxide functionality in protonated analytes via ion/molecule reactions in mass spectrometers. *J. Org. Chem.* **2008**, *73*, 4888.
- [16] P. Duan, M. Fu, T. A. Gillespie, B. E. Winger, H. I. Kenttämäa. Identification of aliphatic and aromatic tertiary N-oxide functionalities in protonated analytes via ion/molecule and dissociation reactions in an FT-ICR mass spectrometer. *J. Org. Chem.* **2009**, *74*, 1114.
- [17] J. Somuramasami, P. Duan, L. Amundson, E. Archibold, B. Winger, H. I. Kenttämäa. Differentiation of protonated aromatic regioisomers related to lignin by reactions with trimethylborate in a Fourier transform ion cyclotron resonance mass spectrometer. *J. Am. Soc. Mass Spectrom.* **2011**, *22*, 1040.
- [18] R. J. Eismín, M. Fu, S. Yem, F. Widjaja, H. I. Kenttämäa. Identification of epoxide functionalities in protonated monofunctional analytes by using ion/molecule reactions and collision-activated dissociation in different ion trap tandem mass spectrometers. *J. Am. Soc. Mass Spectrom.* **2012**, *23*, 12.
- [19] H. Sheng, P. E. Williams, W. Tang, J. S. Riedeman, M. Zhang, H. I. Kenttämäa. Identification of the sulfone functionality in protonated analytes via ion/molecule reactions in a linear quadrupole ion trap mass spectrometer. *J. Org. Chem.* **2014**, *79*, 2883.
- [20] H. Sheng, P. E. Williams, W. Tang, M. Zhang, H. I. Kenttämäa. Identification of the sulfoxide functionality in protonated analytes via ion/molecule reactions in linear quadrupole ion trap mass spectrometry. *Analyst* **2014**, *139*, 4296.
- [21] H. Sheng, W. Tang, R. Yerabolu, J. Y. Kong, P. E. Williams, M. Zhang, H. I. Kenttämäa. Mass spectrometric identification of the N-monosubstituted N-hydroxylamino functionality in protonated analytes via ion/molecule reactions in tandem mass spectrometry. *Rapid Commun. Mass Spectrom.* **2015**, *29*, 730.
- [22] M. Fu, R. J. Eismín, P. Duan, S. Li, H. I. Kenttämäa. Ion–molecule reactions facilitate the identification and differentiation of primary, secondary and tertiary amino functionalities in protonated monofunctional analytes in mass spectrometry. *Int. J. Mass Spectrom.* **2009**, *282*, 77.

- [23] H. L. Holland. Biotransformation of organic sulfides. *Nat. Prod. Rep.* **2001**, *18*, 171.
- [24] J. A. Hibbs, F. B. Jariwala, C. S. Weisbecker, A. B. Attygalle. Gas-phase fragmentations of anions derived from N-phenyl benzenesulfonamides. *J. Am. Soc. Mass Spectrom.* **2013**, *24*, 1280.
- [25] W. Lam, R. Ramanathan. In electrospray ionization source hydrogen/deuterium exchange LC-MS and LC-MS/MS for characterization of metabolites. *J. Am. Soc. Mass Spectrom.* **2002**, *13*, 345.
- [26] X. Jiang, J. B. Smith, E. C. Abraham. Identification of a MS-MS fragment diagnostic for methionine sulfoxide. *J. Mass Spectrom.* **1996**, *31*, 1309.
- [27] J. M. Froelich, G. E. Reid. Mechanisms for the proton mobility-dependent gas-phase fragmentation reactions of S-alkyl cysteine sulfoxide-containing peptide ions. *J. Am. Soc. Mass Spectrom.* **2007**, *18*, 1690.
- [28] S. Gronert. Estimation of effective ion temperatures in a quadrupole ion trap. *J. Am. Soc. Mass Spectrom.* **1998**, *9*, 845.
- [29] S. Gronert. Quadrupole ion trap studies of fundamental organic reactions. *Mass Spectrom. Rev.* **2005**, *24*, 100.
- [30] N. V. K. Dutt, A. P. Kahol, P. Jyothiraju. Vapor pressure of trimethyl phosphite and triethylamine. *J. Chem. Eng. Data* **1982**, *27*, 369.
- [31] J. C. Schwartz, M. W. Senko, J. E. Syka. A two-dimensional quadrupole ion trap mass spectrometer. *J. Am. Soc. Mass Spectrom.* **2002**, *13*, 659.
- [32] T. Su, W. J. Chesnavich. Parametrization of the ion-polar molecule collision rate constant by trajectory calculations. *J. Chem. Phys.* **1982**, *76*, 5183.
- [33] NIST Standard Reference Database 1A. Available: <http://webbook.nist.gov/>.
- [34] H. Sheng, W. Tang, R. Yerabolu, J. Max, R. R. Kotha, J. S. Riedeman, J. J. Nash, M. Zhang, H. I. Kenttämä. Identification of N-oxide and sulfoxide functionalities in protonated drug metabolites by using ion-molecule reactions followed by collisionally activated dissociation in a linear quadrupole ion trap mass spectrometer. *J. Org. Chem.* **2016**, *81*, 575.



Contents lists available at ScienceDirect

## International Journal of Mass Spectrometry

journal homepage: [www.elsevier.com/locate/ijms](http://www.elsevier.com/locate/ijms)

## Full Length Article

Ion/molecule reactions of dimethylamine with protonated analytes facilitate the identification of tertiary *N*-oxide functionalities in a linear quadrupole ion trap mass spectrometerJames S. Riedeman<sup>a</sup>, Tiffany M. Jarrell<sup>b</sup>, Chunfen Jin<sup>c</sup>, Huaming Sheng<sup>b</sup>, Ravikiran Yerabolu<sup>c</sup>, John Kong<sup>c</sup>, Hilkka I. Kenttämä<sup>a,\*</sup><sup>a</sup> Global Analytical, Procter & Gamble, Winton Hill Business Center, 6280 Center Hill Avenue, Cincinnati, OH 45224, United States<sup>b</sup> Analytical Research & Development, Merck Research Laboratory, Rahway, NJ 07076, United States<sup>c</sup> Department of Chemistry, Purdue University, 560 Oval Drive, West Lafayette, IN 47907, United States

## ARTICLE INFO

## Article history:

Received 18 March 2017

Received in revised form 8 July 2017

Accepted 28 July 2017

Available online xxx

## Keywords:

Dimethylamine  
Ion–molecule reactions  
Tertiary *N*-oxides  
Functional group selective  
Ion trap mass spectrometry

## ABSTRACT

A method is presented for the rapid identification of tertiary aliphatic and aromatic *N*-oxide functionalities in protonated analytes *via* ion–molecule reactions with dimethylamine (DMA) in a linear quadrupole ion trap mass spectrometer (LQIT). DMA was leaked into the trapping region of the mass spectrometer and allowed to react with protonated analytes (ionized by electrospray ionization) for 500 ms, after which all ions were detected. Protonated analytes with the tertiary *N*-oxide functionality react with DMA to yield exclusively product ions with *m/z*-values that are 45 units greater than that of the protonated analyte, corresponding to a stable DMA adduct. Collision-activated dissociation of the adduct ions suggests that formation of a hydrogen bond between DMA and the protonated analytes is responsible for the formation of the stable adduct. Hydrogen bond energies were calculated for several adducts at the B3LYP/6-31++G(d,p) level of theory (including correction for basis-set superposition error) to define the potential energy wells for the formation of [M+H+DMA]<sup>+</sup> adduct ions. The relative enthalpies calculated for the [M+H+DMA]<sup>+</sup> adduct ions were found to be lower than those of the products resulting from proton transfer from protonated tertiary *N*-oxides and one aromatic ketone, ketoprofen, to DMA. On the other hand, a protonated primary *N*-oxide, nitrosobenzene, exclusively reacts *via* proton transfer with DMA, which was calculated to be more exothermic than formation of an adduct ion. Collisional cooling was found to be crucial to the formation of an adduct ion for analytes with proton affinities lower than that of DMA. Ion–molecule reactions of protonated 4-nitro-2-picoline *N*-oxide (PA = 206 kcal mol<sup>-1</sup>) with DMA (PA = 222 kcal mol<sup>-1</sup>) in an FT-ICR at ultra-high vacuum with no buffer gas resulted solely in proton transfer to DMA. Finally, examination of the reactions of DMA with protonated clozapine and clozapine-4'-*N*-oxide demonstrated that DMA can be used to identify the *N*-oxide functionality in the presence of other basic functionalities. Compared to other reagents reported for the identification of tertiary *N*-oxide functionalities *via* ion–molecule reactions in a mass spectrometer, DMA is the only one volatile enough to be used in a multi-ported pulsed valve system designed for rapid introduction of several reagents, each diagnostic for a different functionality, for characterization of analytes as they elute from an HPLC.

© 2017 Elsevier B.V. All rights reserved.

## 1. Introduction

Methods for the rapid detection of *N*-oxide functionalities in unknown molecules in complex mixtures are of great current interest for several reasons. For example, the oxidation of the amino functional group is a common metabolic pathway for

many nitrogen-containing pharmaceuticals [1,2]. In some cases, the degradation products containing the *N*-oxide functionality have been shown to be genotoxic [3,4]. Further, amine-based surfactants persisting in the environment are known to form *N*-oxides upon aerobic biodegradation [5]. These *N*-oxides have been found to be particularly toxic to photobacteria and crustacea living in aquatic ecosystems [5].

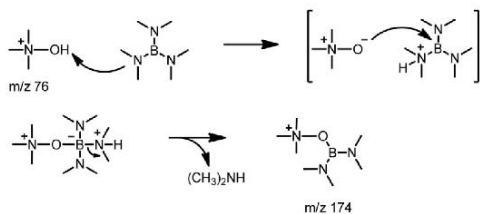
NMR and FT-IR are viable techniques for the identification of unknown compounds but require fairly pure samples. NMR detects <sup>15</sup>N but its natural abundance is only 0.37% of that of <sup>14</sup>N, which

\* Corresponding author.

E-mail address: [hilkka@purdue.edu](mailto:hilkka@purdue.edu) (H.I. Kenttämä).<http://dx.doi.org/10.1016/j.ijms.2017.07.020>

1387–3806/© 2017 Elsevier B.V. All rights reserved.

Please cite this article in press as: J.S. Riedeman, et al., Ion/molecule reactions of dimethylamine with protonated analytes facilitate the identification of tertiary *N*-oxide functionalities in a linear quadrupole ion trap mass spectrometer, *Int. J. Mass Spectrom.* (2017), <http://dx.doi.org/10.1016/j.ijms.2017.07.020>



**Scheme 1.** Diagnostic reaction between protonated tertiary *N*-oxides with TDMAB.

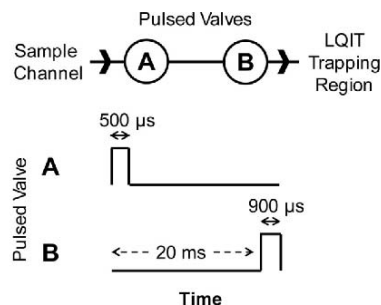
makes this a very insensitive technique for the detection of *N*-oxides. FT-IR has a good sensitivity but cannot distinguish tertiary *N*-oxides from primary *N*-oxides in a mixture [6]. On the other hand, tandem mass spectrometry has excellent sensitivity and can be used to analyze complex mixtures without prior purification [7,8]. Collision-activated dissociation (CAD) commonly employed in tandem mass spectrometry experiments has been used extensively to probe the structures of ionized compounds directly in complex mixtures. However, CAD of protonated *N*-oxides does not, in general, produce functional group-specific fragmentation that can be used to distinguish protonated *N*-oxides from other ionized nitrogen-containing compounds [9].

Tandem mass spectrometric methods based on ion-molecule reactions have been demonstrated to be particularly useful for the identification of specific functional groups in ionized analytes [10–18]. For example, aliphatic and aromatic tertiary *N*-oxide functionalities with high proton affinities [12] (220–240 kcal mol<sup>-1</sup>) can be identified in protonated analytes via their reactions with tris(dimethylamino)borane (TDMAB) (Scheme 1) in a Fourier-transform ion cyclotron resonance (FT-ICR) mass spectrometer [12]. The diagnostic reaction involves a proton transfer/nucleophilic substitution mechanism and forms a boron-derivatized *N*-oxide (TDMAB adduct – (CH<sub>3</sub>)<sub>2</sub>NH) [12]. This method has been adapted to a linear quadrupole ion trap (LQIT) mass spectrometer equipped with an external reagent-mixing manifold that allows TDMAB to be introduced through the helium buffer gas inlet into the ion trap [15]. The major limitation of this reagent inlet system is that it only allows the use of one reagent at a time (and hence examination of just one functionality). In order to enable the examination of the presence of several functionalities in analytes eluting from an HPLC, a multi-ported pulsed valve system was developed for the rapid introduction of several reagents into the mass spectrometer [19]. This reagent introduction system requires the reagents to be volatile so that they can be rapidly introduced and also promptly pumped out before the introduction of the next reagent. Unfortunately, the high boiling point of TDMAB (147–148 °C) makes this reagent incompatible with the pulsed valve system. Thus, a more volatile reagent, dimethylamine (DMA), was tested for the identification of tertiary *N*-oxides. Its boiling point is an order of magnitude lower (7–9 °C) than that of TDMAB.

## 2. Experimental

### 2.1. Chemicals

*N*-Oxides (>95%), dimethylamine (>99%) as a pressurized gas in a cylinder, and ketoprofen (≥98%) were purchased from Sigma-Aldrich. Acetonitrile and methanol were purchased from OmniSolv (99.9%). Ethanol was purchased from Koptec (>99%). Ethyl acetate and diethyl ether were purchased from Macron (≥99%). Propionaldehyde was purchased from Alfa Aesar (97%). All chemicals were used without further purification.



**Fig. 1.** Schematic of the pulsed valve set-up (top) and an event timeline for each pulsed valve during an experimental sequence (bottom). The pulse width of pulsed valve A (500 μs) was the time the pulsed valve was open. When pulsed valve A was opened, DMA flowed from the sample channel into the space between pulsed valves A and B. The pulse width of B (900 μs) was the time this pulsed valve was open to the LQIT. The dashed arrow represents the delay from the start of the sequence to the time when the pulsed valve B opened.

### 2.2. LQIT mass spectrometry experiments

Mass spectrometric data for all experiments, apart from one (see Section 2.4), were collected using a Thermo Scientific linear quadrupole ion trap (LQIT) mass spectrometer (LTQ, Thermo Scientific, San Jose, CA, USA) utilizing an electrospray ionization (ESI) source operating in positive-ion mode. The ion trapping region of the instrument was maintained at a nominal pressure of about 10<sup>-5</sup> Torr by a triple-inlet turbomolecular pump, as measured by an ion gauge (Granville-PhillipsR 342™ mini ion gauge). Samples were dissolved in methanol (1 mg/mL) and introduced into the ESI source via a syringe pump at a flow rate of 10 μL/min. A tee connector combined 50/50 (v/v) methanol/water from a Finnigan Surveyor MS Pump Plus with the sample at a flow rate of 200 μL/min to facilitate formation of a stable ESI spray. Ion source conditions were as follows: 275 °C capillary temperature, N<sub>2</sub> sheath gas flow of 60 (arbitrary units), N<sub>2</sub> auxiliary gas flow of 30 (arbitrary units), 2 kV spray voltage, 18 V capillary voltage, and 50 V tube lens voltage. The automated tuning feature of the instrument was used to optimize the ion optics for ions (from *m/z* 50 up to *m/z* 500). Experiments were performed utilizing the scan features of the LTQ Tune Plus interface (Xcalibur 2.1 version). Analyte ions were isolated using a 2 *m/z*-unit window with a *q* value of 0.25 and then allowed to react with DMA for 500 ms before all ions were ejected from the trap and detected. The scan with the maximum signal in the total ion chromatogram (TIC) was used for determining the product ion abundance relative to that of the protonated analyte ([M+H]<sup>+</sup>). Subsequent experiments were performed only after enough time had passed for DMA to be fully evacuated from the mass spectrometer's vacuum region (approximately 20 s, see Section 3).

### 2.3. Reagent introduction using pulsed valves

DMA reagent was introduced into the ion trapping region of the LQIT by using two Series 9 pulsed valves, each with an exit orifice of 0.060 inches (Parker Hannifin Corp., Cleveland, OH), as described previously [19]. Approximately 1 ccm (STP) of gaseous DMA was introduced via a gas regulator through a rubber hose and a needle inserted through a rubber septum into the pulsed valve sample channel (Fig. 1). DMA was introduced into the ion trap by first opening the pulsed valve connected to the sample channel (i.e., pulsed valve A, Fig. 1) for 500 μs to allow the reagent to flow into the space between the pulsed valves (i.e., between A and B). Next, the pulsed valve interfacing with the LQIT (i.e., pulsed valve B) was opened for 900 μs to let the reagent enter the mass spectrometer.

A 20 ms delay was set between the opening events of pulsed valves A and B.

#### 2.4. FT-ICR mass spectrometry experiment

Ion-molecule reactions between DMA and protonated 4-nitro-2-picoline *N*-oxide were carried out at ultra-high vacuum ( $\sim 10^{-9}$  Torr) in a dual cell 3 T Fourier transform ion cyclotron resonance mass spectrometer (FT-ICR) [20]. The instrument was an Extrel Model FTMS 2001 operated by an IonSpec Omega2XP data station. 4-Nitro-2-picoline *N*-oxide was introduced into one side of the dual cell via a manual solids probe (heated at 80 °C) and ionized by EI (electron energy: 25 eV, emission current: 6  $\mu$ A, ionization time: 100 ms). Chemical ionization of the *N*-oxide to yield protonated molecules (*M*+*H*) was achieved via reactions between molecular ions of the *N*-oxide and the neutral *N*-oxide by a process described as self-chemical ionization (self-CI) [21]. The product ions were transferred into the other “clean” side of the dual cell through a 2 mm hole in the conductance limiting plate by grounding the plate for 124  $\mu$ s. A 1 s delay after transfer was provided to allow ions to cool via IR emission [22] before reactions with DMA. Stored waveform inverse Fourier transform [23] (SWIFT) excitation pulses were used to eject all ions except protonated 4-nitro-2-picoline *N*-oxide. The isolated protonated *N*-oxide was allowed to react with DMA introduced via a variable leak valve. Protonated *N*-oxide and DMA were allowed to interact for 500 ms before all ions were excited and detected. Nominal pressure in both cells was maintained at  $5.9 \times 10^{-8}$  Torr and monitored by ionization gauges on both sides of the dual cell.

#### 2.5. Computational methods

All geometries and zero-point energies were calculated at the B3LYP/6-31++G(d,p) level of theory by using the Gaussian 09 suite of programs [24]. Frequency calculations were performed to verify all stationary points as energy minima and to provide zero-point vibrational energy corrections. Minimum energy structures do not have imaginary frequencies. Proton affinities were computed as the energy difference between the molecule of interest and the same molecule with one additional proton. This method was found to be reasonably accurate when comparing the difference ( $\Delta$ ) between calculated proton affinities and the experimental values available in literature for 5,5-dimethyl-1-pyrroline *N*-oxide ( $\Delta = 0.23$  kcal mol $^{-1}$ ), pyridine *N*-oxide ( $\Delta = 2.2$  kcal mol $^{-1}$ ), nitrosobenzene ( $\Delta = 2.1$  kcal mol $^{-1}$ ), and trimethylamine *N*-oxide ( $\Delta = 1.5$  kcal mol $^{-1}$ ).

Hydrogen bond energies were calculated using the standard energy difference method [25]. The hydrogen bond energy between a hydrogen bond donor (D) and acceptor (A) is calculated by

$$\Delta E_{HB}^{CP}(AD) = E_{AD}^{AD} - E_A^{AD} - E_D^{AD} \quad (1)$$

where  $\Delta E_{HB}^{CP}(AD)$  is the hydrogen bond energy including counterpoise correction for basis set superposition error (BSSE), *AD* (subscript) represents the set of Cartesian coordinates defining the structure of the adduct ion,  $E_{AD}^{AD}$  is the energy of the adduct formed from a hydrogen bond acceptor A and a hydrogen bond donor D, and  $E_A^{AD}$  and  $E_D^{AD}$  are the energies of A and D molecules calculated using the basis set of the adduct AD (acceptor/donor), respectively. The subscripts A and D in  $E_A^{AD}$  and  $E_D^{AD}$  denote the Cartesian coordinates that define the geometry of acceptor (A) and donor (D). The superscript AD in  $E_A^{AD}$ ,  $E_D^{AD}$  and  $E_{AD}^{AD}$  denotes the basis set used for the optimization of acceptor, donor, and acceptor/donor (hydrogen bond) adduct, respectively. The BSSE arises from the artificial energy stabilization of donor and acceptor as they approach each other in the adduct ion. During energy minimization, each molecule in the adduct ion utilizes extra basis functions from the other, thus

artificially lowering its own energy. To correct for this error, the counterpoise procedure was used [26]. As an example, to calculate the energy of a specific hydrogen bond donor D in an adduct ion, all the basis functions of the hydrogen bond acceptor A at the atomic positions of A are made available to D while ignoring the charges of electrons and nuclei on A. The BSSE is evaluated by taking the difference

$$E_{BSSE}(D) = E_D^{AD} - E_D^D \quad (2)$$

where  $E_{BSSE}(D)$  is the artificial stabilization afforded to D by the additional basis sets of A in the adduct ion.  $E_A^{AD}$  and  $E_D^{AD}$  are the energies of the acceptor (A) and donor (D) molecules, as described earlier. The same procedure was applied to molecule A.

### 3. Results and discussion

Reactivity of protonated primary and tertiary *N*-oxides and other protonated heteroatom-containing molecules toward dimethylamine (DMA) was examined in a linear quadrupole ion trap (LQIT). In order to understand the observed reactivity, acidities and hydrogen-bond energies were calculated for a number of protonated analytes and their DMA adducts. Finally, the residence time of DMA in the trapping region of the mass spectrometer was examined to test for the potential utility of DMA in HPLC/tandem mass spectrometric analysis incorporating multiple neutral reagents introduced consecutively via pulsed valves during an HPLC analysis.

#### 3.1. Reactivity of protonated *N*-oxides toward dimethylamine (DMA)

Protonated analytes were introduced into the ion trap via ESI. DMA was introduced into the ion trap through a pair of pulsed valves (A and B in Fig. 1). Trapped ions were allowed to interact with DMA for 500 ms before all ions were ejected and detected. DMA was found to react with all protonated aliphatic and aromatic tertiary *N*-oxide analytes (M) by efficient formation of a stable adduct ( $[M+H+DMA]^+$ ; Table 1) with a *m/z*-value 45 units greater than that of the analyte ion (Fig. 2). This was not observed for most other protonated analytes (Table 2; these analytes are discussed later).

Protonated primary *N*-oxide nitrosobenzene (1° *N*-oxide; Table 1, entry 1) showed no adduct formation. This finding suggests that DMA may be useful as a diagnostic reagent for distinguishing tertiary *N*-oxides from primary *N*-oxides and other analytes.

In previous studies of the reactivity of TDMAB toward protonated tertiary *N*-oxides, CAD of the diagnostic adduct – CH<sub>3</sub>OH products provided structural information useful for identification of the adduct structure [10]. However, CAD of the DMA adducts of protonated tertiary *N*-oxide analytes results in the loss of DMA to yield the protonated analyte and/or protonated DMA. Hence, no structural information is obtained from this experiment. The most plausible explanation for this fragmentation is that the structure of the DMA adduct involves a hydrogen bond between the protonated analyte and DMA (Scheme 2, top).

The wide range of PAs of the analytes (206–242 kcal mol $^{-1}$ ) that form a stable adduct with DMA (PA = 222 kcal mol $^{-1}$ ) indicates that adduct formation is not very sensitive to the PA of the analyte (Tables 1 and 2, entry 10). However, analytes having proton affinities more than 20 kcal mol $^{-1}$  below that of DMA react by proton transfer exclusively (Table 2; Scheme 2, bottom). In order to better understand the relationship between the strength of the hydrogen bond between DMA and the protonated analytes and the formation of a stable adduct, the hydrogen bond energies of several adducts were estimated. A strong hydrogen bond may explain the observed reactivity of DMA with tertiary *N*-oxides. The energy of a typical hydrogen bond is generally less than 12 kcal mol $^{-1}$  for neutral molecules but has been shown previously to be greater

**Table 1**

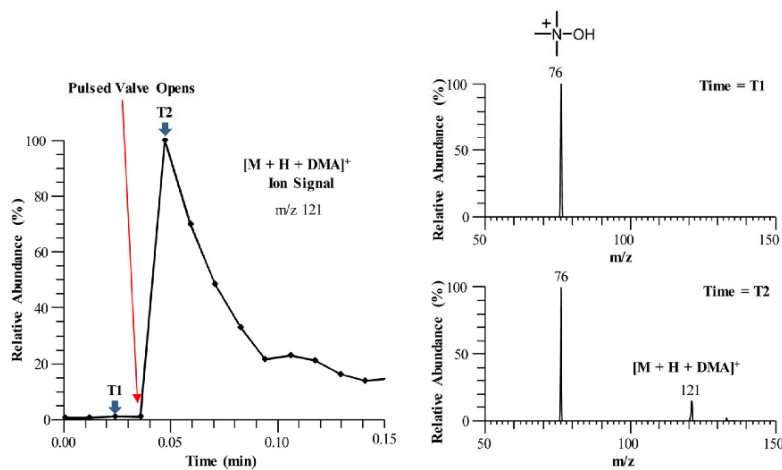
*N*-Oxides, Their PAs (in kcal mol<sup>-1</sup>), Observed Reactions (Reaction Time = 500 ms) of Their Protonated Forms with DMA (Reagent Pressure Was the Same for All Experiments; PA<sup>a</sup> = 222 kcal mol<sup>-1</sup>), and the Abundance of Products Formed (Relative to the Protonated Analyte [M+H]<sup>+</sup>) in a Linear Quadrupole Ion Trap Mass Spectrometer.

Analyte (M)	( <i>m/z</i> of [M+H] <sup>+</sup> )	Proton Affinity (PA) (kcal mol <sup>-1</sup> )	Observed Reaction (abundance %)
	108	204.0 <sup>a</sup>	Proton transfer to DMA (55)
	122	219.4 <sup>b</sup>	[M + H] <sup>+</sup> + DMA (85)
	114	221.2 <sup>c</sup>	[M + H] <sup>+</sup> + DMA (98)
	343	236.7 <sup>b</sup> (A)	[M + H] <sup>+</sup> + DMA (24)
		220.2 <sup>b</sup> (B)	
		237.3 <sup>b</sup> (C)	
		216.9 <sup>b</sup> (D)	
	254	220.6 <sup>b</sup>	[M + H] <sup>+</sup> + DMA (52)
	96	220.7 <sup>a</sup>	[M + H] <sup>+</sup> + DMA (91)
	146	227.6 <sup>c</sup>	[M + H] <sup>+</sup> + DMA (84)
	162	234.7 <sup>b</sup>	[M + H] <sup>+</sup> + DMA (10)
	76	235.0 <sup>a</sup>	[M + H] <sup>+</sup> + DMA (20)
	110	225.5 <sup>c</sup>	[M + H] <sup>+</sup> + DMA (41)
	155	206.3 <sup>b</sup>	[M + H] <sup>+</sup> + DMA (45)
	258	242.0 <sup>b</sup>	[M + H] <sup>+</sup> + DMA (89)

<sup>a</sup>PA value from Ref. [27].

<sup>b</sup>Calculated at the B3LYP/6-31++G(d,p) level of theory.

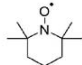
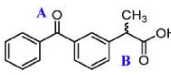
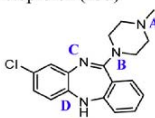
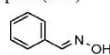
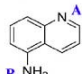
<sup>c</sup>PA value from [12].



**Fig. 2.** The ion signal (extracted ion chromatogram) for the adduct ion [M+H+DMA]<sup>+</sup> for trimethylamine *N*-oxide (M) as a function of time before and after DMA was introduced into the LQIT (left). At time T1, before DMA had entered the trapping region of the instrument, only protonated trimethylamine *N*-oxide (*m/z* 76) was visible in the mass spectrum (top right). At time T2, the pulsed valve had opened, allowing DMA to enter the trapping region of the instrument, which enabled the formation of a stable adduct ion with *m/z* value 45 units greater (*m/z* 121) than the *m/z* value of protonated trimethylamine *N*-oxide (bottom right). This ion signal gradually tapered in abundance as DMA was pumped away by the vacuum system.

**Table 2**

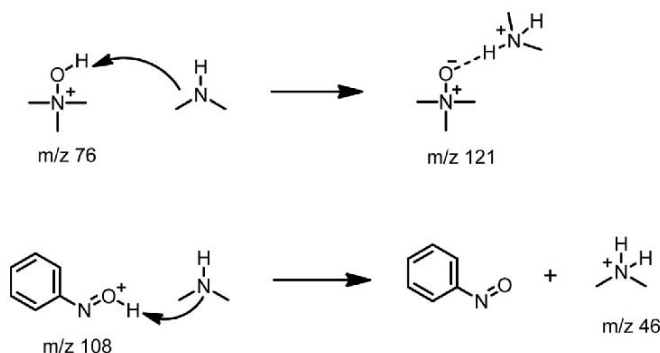
Reactions Observed (Reaction Time = 500 ms) for Various Protonated Analytes Possessing Different PAs with DMA (Reagent Pressure was Consistent for All Experiments; PA<sup>a</sup> = 222 kcal mol<sup>-1</sup>) and the Abundance of Products Formed (Relative to the Protonated Analyte [M+H]<sup>+</sup>) in a Linear Quadrupole Ion Trap Mass Spectrometer.

Analyte (m/z of [M+H] <sup>+</sup> )	Proton Affinity (PA) (kcal mol <sup>-1</sup> )	Observed Reaction (abundance %)
Ethyl acetate (89)	200.0 <sup>a</sup>	Proton transfer to DMA (28)
Acetonitrile (42)	186.0 <sup>a</sup>	Proton transfer to DMA (63)
Ethanol (47)	186.0 <sup>a</sup>	Proton transfer to DMA (74)
Diethyl ether (75)	198.0 <sup>a</sup>	Proton transfer to DMA (81)
Acetone (59)	194.0 <sup>a</sup>	Proton transfer to DMA (97)
Propionaldehyde (59)	187.9 <sup>a</sup>	Proton transfer to DMA (15)
Hexanoic acid (117)	188.2 <sup>b</sup>	Proton transfer to DMA (33)
Heptanoic acid (131)	188.2 <sup>b</sup>	Proton transfer to DMA (49)
 TEMPO (157)	210.9 <sup>a</sup>	[M + H] <sup>+</sup> + DMA (3)
 Ketoprofen (255)	212.0 <sup>b</sup> (A) 199.6 <sup>b</sup> (B)	[M + H] <sup>+</sup> + DMA (60) <sup>c</sup>
 Clozapine (327)	228.4 <sup>b</sup> (A) 223.9 <sup>b</sup> (B) 239.4 <sup>b</sup> (C) 218.1 <sup>b</sup> (D)	No observed reaction <sup>c</sup>
 Benzaldehyde oxime (122)	210.2 <sup>b</sup>	Proton transfer to DMA (41)
Pyridine (80)	222.3 <sup>a</sup>	[M + H] <sup>+</sup> + DMA (1)
 5-Aminoquinoline (145)	231.5 <sup>b</sup> (A) 210.7 <sup>b</sup> (B)	[M + H] <sup>+</sup> + DMA (5)

<sup>a</sup>PA value from Ref. [27].

<sup>b</sup>Calculated at the B3LYP/6-31++G(d,p) level of theory.

<sup>c</sup>Low mass cut-off of the instrument prevented observation of ions of m/z <50.



**Scheme 2.** Reactions of protonated tertiary *N*-oxides and nitrosobenzene with DMA.



than 30 kcal mol<sup>-1</sup> for several negatively charged hydrogen bond acceptors such as *N*-oxides [28].

Hydrogen bond energies ( $\Delta E_{HB}^{CP}$ ; the energy released as a result of hydrogen bond formation) for various [M+H+DMA]<sup>+</sup> adduct ions (Table 3) were calculated using density functional theory (DFT) at the B3LYP/6-31++G(d,p) level of theory. These hydrogen bond energies were compared to the differences in the proton affinities ( $\Delta PA$ ) between the analytes and DMA to determine whether hydrogen bond formation is more energetically favorable than proton transfer for reactions where adduct formation was observed. Values of  $\Delta PA$  that are negative indicate an exothermic proton transfer reaction between the protonated analyte and DMA in Table 3.

The adduct ion was found to be lower on the potential energy surface than the proton transfer product for all protonated analytes that react with DMA to produce a stable adduct. The results are best represented visually by the use of the Brauman potential energy diagram [29] as shown in Fig. 3. The geometries of all adduct ions minimized to complex C upon optimization in DFT calculations, even for analytes with proton affinities greater than that of DMA, such as trimethylamine *N*-oxide (PA<sup>19</sup> = 235 kcal mol<sup>-1</sup>) and clozapine-4'-*N*-oxide (PA = 236.7 kcal mol<sup>-1</sup>). This finding indicates either a single-well potential energy surface or possibly a shallow barrier between intermediates B and C, a common observation for strongly hydrogen bond donor/acceptor pairs [28,30]. Further, this finding suggests that the energy of complex B is higher than that of C if such a minimum exists on the potential energy surface. Formation of a stable adduct ion was only observed when the transition from C to D is endothermic, which is easily determined from the difference  $\Delta PA - \Delta E_{HB}^{CP}$  as shown in Table 3. Positive values indicate that hydrogen bond formation is energetically more favorable than proton transfer.

Formation of a stable adduct ion (intermediate C, Fig. 3) for tertiary *N*-oxides suggests that there is considerable collisional cooling of the ions with helium buffer gas [31] in the linear quadrupole ion trap. Otherwise, all reactions with a negative  $\Delta PA$  value would occur via proton transfer. Additionally, some of the hydrogen bond formation energy may be lost as a result of radiative cooling (spontaneous emission of infrared photons) [32]. In order to evaluate the influence collisional cooling has on adduct formation, reactions between protonated 4-nitro-2-picoline *N*-oxide (PA = 206 kcal mol<sup>-1</sup>) (Table 1, entry 11) and DMA were examined in a dual-cell 3T Fourier-transform ion cyclotron resonance (FT-ICR) mass spectrometer in ultra-high vacuum and in the absence of any buffer gas.  $\Delta PA$  (PA<sub>analyte</sub> - PA<sub>DMA</sub>) for this reaction is negative. Thus, adduct formation in the FT-ICR would indicate that radiative cooling expels enough energy to stabilize the adduct ion and collisional cooling would not be crucial for stabilization of the adduct. The FT-ICR experiment was carried out by protonating 4-nitro-2-picoline *N*-oxide in one of the two cells in the FT-ICR followed by transfer of the protonated *N*-oxide ions into the other cell to react with DMA. For this experiment only proton transfer to DMA was observed. Hence, collisional cooling appears to be necessary for stable adduct formation for analytes having PA less than that of DMA.

The final step in the proton transfer reaction pathway, formation of proton transfer products D from intermediate C (Fig. 3), was found to be endothermic for all protonated analytes that yield a stable adduct with DMA (Table 3). On the other hand, when the dissociation of intermediate C to yield proton transfer products D is exothermic, an adduct was not observed ( $\Delta PA - \Delta E_{HB}^{CP} < 0$ ). For example, proton transfer is the only reaction observed for protonated nitrosobenzene, a primary *N*-oxide, likely due to the proton transfer products (D, Fig. 3b) being more energetically favorable than hydrogen bound adduct (intermediate C, Fig. 3b) by 4.6 kcal mol<sup>-1</sup> (Table 3, entry 2, left). On the other hand, all

protonated analytes with an endothermic C → D transition formed stable adducts with DMA and did not yield proton transfer products, with the exception of one. The transition from intermediate C to D for TEMPO (Fig. 3c) was calculated to be endothermic ( $\Delta E_{HB}^{CP} - \Delta PA = 3.9$  kcal mol<sup>-1</sup>), which suggests that adduct formation should dominate. However, the abundance of adduct ([M+H+DMA]<sup>+</sup>) was only 3% relative to the precursor ([M+H]<sup>+</sup>, reaction time = 500 ms; Table 2, entry 9). Low rate for this particular reaction is likely the result of steric hindrance due to the four methyl groups adjacent to the nitroxyl functionality (Table 3, entry 3).

The reactivity of protonated clozapine and clozapine-4'-*N*-oxide toward DMA was also examined (Table 1, entry 4 and Table 2, entry 11). Clozapine is an atypical antipsychotic drug for the treatment of schizophrenia symptoms and is particularly beneficial because of its efficacy on treatment-resistant patients [33]. Clozapine-4'-*N*-oxide is a metabolite of clozapine that has been found to be completely inactive, thus its presence in the drug ultimately reduces the plasma concentration of the active drug clozapine after ingestion [34,35]. Therefore, it is important to be able to identify clozapine-4'-*N*-oxide in drug samples. The presence of the tertiary *N*-oxide functionality in protonated clozapine-4'-*N*-oxide (but not in protonated clozapine) is clearly revealed by its reaction with DMA resulting in the appearance of a product ion with a *m/z* value 45 units greater than that of the analyte ion (Table 1, entry 4).

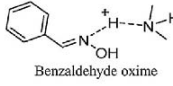
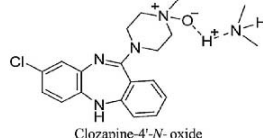
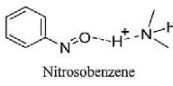
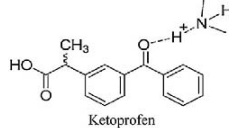
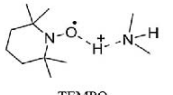

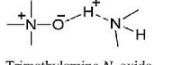
### 3.2. Reactivity of DMA toward other types of protonated analytes

The specificity of reactions of DMA was further investigated by examining its reactivity toward protonated O- and N-containing analytes that do not contain the *N*-oxide functionality (Table 2). Exclusive proton transfer was observed for most analytes. However, protonated ketoprofen reacted with DMA by formation of a stable adduct (Table 2, entry 10). The potential energy surface shown in Fig. 3 indicates that adduct formation is energetically more favorable than proton transfer by 2.5 kcal mol<sup>-1</sup> for this analyte, which is in agreement with the observed reactivity. Isolation of the [M+H+DMA]<sup>+</sup> complex (protonated ketoprofen + DMA) was attempted in order to subject the ion to CAD for structure determination but the adduct was found to be too unstable to be isolated. This finding indicates a low barrier to dissociation for the [M+H+DMA]<sup>+</sup> complex. The endothermicity of transition C → D is calculated to be only 2.5 kcal mol<sup>-1</sup> for this analyte (Table 3) and hence may be too low to prevent formation of D during the isolation event (upon which the isolated ion usually gains some energy). However, the low-mass cut off of the instrument prevents observation of the proton transfer product (protonated DMA) so a proton transfer reaction was not confirmed experimentally. Protonated clozapine showed no reactivity toward DMA (Table 2, entry 11). However, the low-mass cut-off of the instrument also prevented the observation of the proton transfer reaction for this system. Protonated basic analytes, such as pyridine and 5-aminoquinoline, did form a stable adduct with DMA but the abundance of the adduct (relative to the protonated analyte [M+H]<sup>+</sup>) was low ( $\leq 5\%$  relative to [M+H]<sup>+</sup> at 500 ms) compared to the abundances of the adducts observed for protonated *N*-oxides (Table 1).

### 3.3. Residence time of DMA in the ion trap

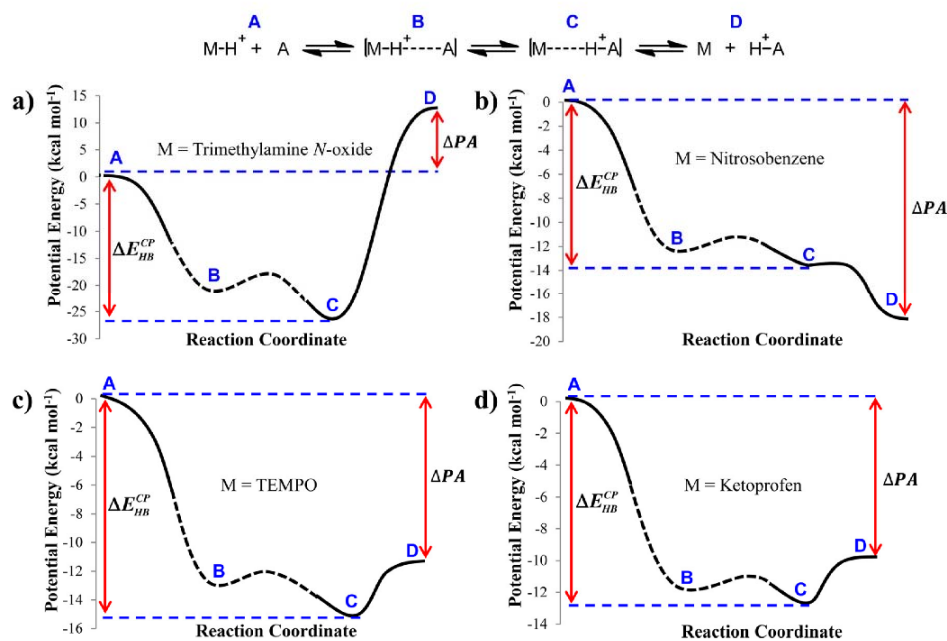
Unwanted ion-molecule reactions may persist for long time periods after introducing reagents with low boiling points into the ion trapping region of a mass spectrometer. Thus, the residence time of DMA in the trapping region of the mass spectrometer was experimentally determined. In order to measure this, DMA was introduced into the trapping region of the LQIT by using the pulsed valve system and allowed to react with protonated methanol dimer

**Table 3**  
Calculated Hydrogen Bond Energies ( $\Delta E_{HB}^{CP}$ ), Calculated Proton Affinity Differences ( $\Delta PA = \text{proton affinity of analyte} - \text{proton affinity of DMA}$ ), and Free Energy Changes for the Conversion of Intermediate C to D ( $\Delta PA - \Delta E_{HB}^{CP}$ ) for Various  $[M+H+DMA]^+$  Adducts Ions.

$[M+H+DMA]^+$ Complex	$\Delta PA^a$ (kcal mol <sup>-1</sup> )	$\Delta E_{HB}^{CP b}$ (kcal mol <sup>-1</sup> )	$\Delta PA - \Delta E_{HB}^{CP}$ (kcal mol <sup>-1</sup> )	$[M+H+DMA]^+$ Complex	$\Delta PA$ (kcal mol <sup>-1</sup> )	$\Delta E_{HB}^{CP}$ (kcal mol <sup>-1</sup> )	$\Delta PA - \Delta E_{HB}^{CP}$ (kcal mol <sup>-1</sup> )
 Benzaldehyde oxime	-11.8	6.3	-5.5	 Clozapine 4'-N-oxide	14.7	26.1	40.8
 Nitrosobenzene	-18.0	13.4	-4.6	 Ketoprofen	-10.0	12.5	2.5
 TEMPO	-11.1	15.0	3.9	 Acetonitrile	-36.0	13.8	-22.2
 Trimethylamine N-oxide	13.0	25.0	38.0				

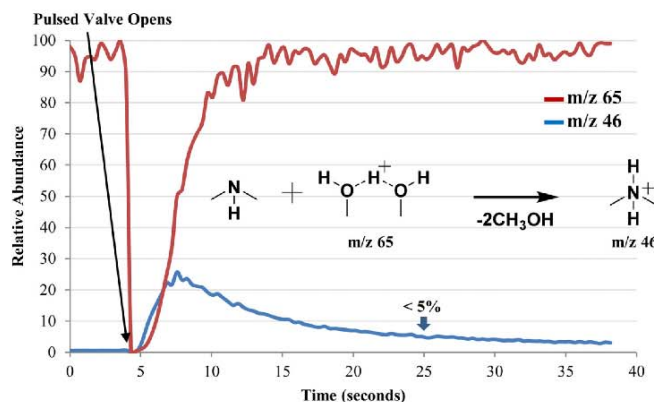
<sup>a</sup>  $\Delta PA = \text{proton affinity of analyte (M)} - \text{proton affinity of DMA}$ , calculated at the B3LYP/6-31++G(d,p) level of theory.

<sup>b</sup> Calculated at the B3LYP/6-31++G(d,p).



**Fig. 3.** Potential energy profiles for proton transfer to DMA from protonated trimethylamine *N*-oxide (top left), nitrosobenzene (top right), TEMPO (bottom left), and ketoprofen (bottom right). The unknown portion of the energy profile is represented by a dashed line. The hydrogen bond energy,  $\Delta E_{HB}^{CP}$ , was calculated at the B3LYP/6-31++G(d,p) level of theory by using the counterpoise procedure. Proton affinities were calculated at the B3LYP/6-31++G(d,p) level of theory.  $\Delta PA$  was calculated as the difference in the proton affinity of DMA and the analyte (M).

Please cite this article in press as: J.S. Riedeman, et al., Ion/molecule reactions of dimethylamine with protonated analytes facilitate the identification of tertiary *N*-oxide functionalities in a linear quadrupole ion trap mass spectrometer, *Int. J. Mass Spectrom.* (2017), <http://dx.doi.org/10.1016/j.ijms.2017.07.020>



**Fig. 4.** Selected ion monitoring of protonated methanol dimer and DMA during the proton transfer reaction in the LQIT. When the pulsed valve closest to the LQIT opens, DMA enters the trapping region of the instrument and reacts with protonated methanol dimer by abstracting a proton. This is evident from the sharp decrease in the abundance of protonated methanol dimer ( $m/z$  65) with a simultaneous increase in the abundance of protonated DMA ( $m/z$  46). After 19.8 s the abundance of protonated DMA fell below 5% abundance relative to protonated methanol dimer indicating nearly complete removal of DMA by the vacuum system.

(generated by ESI operating in positive mode) while the instrument scanned continuously. Protonated methanol dimer reacts with DMA by proton transfer only. As seen in Fig. 4, the abundance of protonated DMA rises while the abundance of protonated methanol dimer decreases simultaneously. The abundance of protonated DMA fell below 5% relative to protonated methanol dimer after about 20 s in the trapping region of the mass spectrometer indicating that most of the DMA had been pumped away by the vacuum system of the mass spectrometer.

#### 4. Conclusions

A selective ion-molecule reaction, exclusive formation of a stable adduct upon reaction with dimethylamine (DMA), has been identified for protonated tertiary aliphatic and aromatic *N*-oxides and one aromatic ketone (ketoprofen) in a linear quadrupole ion trap mass spectrometer. The structure of this adduct is proposed to be a hydrogen bond complex of the protonated analyte and DMA. Calculated hydrogen bond energies for the adduct ions were found to explain the reactivity of DMA toward protonated tertiary *N*-oxides and ketoprofen. Formation of a stable gas-phase hydrogen bond complex occurred for analytes whose proton transfer reaction was calculated to be less energetically favorable than adduct formation. In contrast, other protonated O- and N-containing analytes were not observed to react with DMA, react only slowly, or react exclusively by proton transfer to DMA. Thus, the presence of other functionalities does not affect the reactivity of DMA towards the above mentioned *N*-oxides in most cases. Additionally, the PA of these analytes had little influence on their reactivity toward DMA as indicated by the wide range of PAs for tertiary *N*-oxides that, after protonation, form a stable adduct with DMA. However, the above method does not yield additional structural information specific to each analyte upon isolation of the adduct ion followed by CAD. Dissociation of the complex yields the protonated analyte or protonated DMA.

The ability to use DMA to distinguish protonated clozapine from protonated clozapine-4'-*N*-oxide suggests that this approach is applicable to the analysis of drug metabolites with several functionalities. Also, this reagent can be used in many different types of reagent inlet systems since it is volatile and has a short residence time in the vacuum region of a mass spectrometer. This also enables the utilization of this reagent in multi-ported inlet sys-

tems designed for the nearly simultaneous use of several different reagents on a chromatographic time scale [19].

#### Acknowledgments

This work was partially supported as part of the Center for Direct Catalytic Conversion of Biomass to Biofuels (C3Bio), an Energy Frontier Research Center funded by the U.S. Department of Energy, Office of Science, and Office of Basic Energy Sciences under Award Number DE-SC0000997. This grant supported the work of Tiffany Jarrell and Huaming Sheng. The authors would also like to thank AstraZeneca for their generous financial support.

#### References

- [1] M.H. Bickel, *Pharmacol. Rev.* 21 (1969) 325.
- [2] J. Rose, N. Castagnoli, *Med. Res. Rev.* 3 (1983) 73.
- [3] J. Ashby, R.W. Tennant, *Mutat. Res.* 204 (1988) 17.
- [4] J. Ashby, R.W. Tennant, E. Zeiger, S. Stasiewicz, *Mutat. Res.* 223 (1989) 73.
- [5] M.T. García, E. Campos, I. Ribosa, *Chemosphere* 69 (2007) 1574.
- [6] S. Krzywdka, M. Jaskólski, M. Gdaniec, Z. Dega-Szafran, M. Grundwald-Wyspiańska, M. Szafran, Z. Dauter, G. Davies, *J. Mol. Struct.* 375 (1996) 197.
- [7] L.M. Amundson, R.J. Eismín, J.N. Reece, M. Fu, S.C. Habicht, A.B. Mossman, R.C. Shea, H.I. Kenttämä, *Energy Fuels* 25 (2011) 3212.
- [8] T.M. Jarrell, C.L. Marcum, H. Sheng, B.C. Owen, C.J. O'Lenick, H. Maraun, J.J. Bozell, H.I. Kenttämä, *Green Chem.* 16 (2014) 2713.
- [9] G. McRae, C.M. Monreal, *Anal. Bioanal. Chem.* 400 (2011) 2205.
- [10] P. Duan, T.A. Gillespie, B.E. Winger, H.I. Kenttämä, *J. Org. Chem.* 73 (2008) 4888.
- [11] G. Moneti, G. Pieraccini, D. Favretto, P. Traldi, *J. Mass Spectrom.* 34 (1999) 1354.
- [12] P. Duan, M. Fu, T.A. Gillespie, B.E. Winger, H.I. Kenttämä, *J. Org. Chem.* 74 (2009) 1114.
- [13] R.J. Eismín, M. Fu, S. Yem, F. Widjaja, H.I. Kenttämä, *J. Am. Soc. Mass Spectrom.* 23 (2012) 12.
- [14] R. Eismín, M. Fu, S. Yem, F. Widjaja, H. Kenttämä, *J. Am. Soc. Mass Spectrom.* 23 (2012) 12.
- [15] S.C. Habicht, P. Duan, N.R. Vinuesa, M. Fu, H.I. Kenttämä, *J. Pharm. Biomed. Anal.* 51 (2010) 805.
- [16] S.C. Habicht, N.R. Vinuesa, L.M. Amundson, H.I. Kenttämä, *J. Am. Soc. Mass Spectrom.* 22 (2011) 520.
- [17] S. Gronert, *Chem. Rev.* 101 (2001) 329.
- [18] J.S. Brodbelt, *Mass Spectrom. Rev.* 16 (1997) 91.
- [19] T. Jarrell, J. Riedeman, M. Carlsen, R. Replogle, T. Selby, H. Kenttämä, *Anal. Chem.* 86 (2014) 6533.
- [20] J.M. Price, H.I. Kenttämä, *J. Phys. Chem. A* 107 (2003) 8985.
- [21] S. Ghaderi, P.S. Kulkarni, E.B. Ledford, C.L. Wilkins, M.L. Gross, *Anal. Chem.* 53 (1981) 428.
- [22] R.C. Dunbar, *Mass Spectrom. Rev.* 11 (1992) 309.
- [23] J.W. Gauthier, T.R. Trautman, D.B. Jacobson, *Anal. Chim. Acta* 246 (1991) 211.

- [24] M.J. Frisch, G.W. Trucks, H.B. Schlegel, G.E. Scuseria, M.A. Robb, J.R. Cheeseman, G. Scalmani, V. Barone, B. Mennucci, G.A. Petersson, H. Nakatsuji, M. Caricato, X. Li, H.P. Hratchian, A.F. Izmaylov, J. Bloino, G. Zheng, J.L. Sonnenberg, M. Hada, M. Ehara, K. Toyota, R. Fukuda, J. Hasegawa, M. Ishida, T. Nakajima, Y. Honda, O. Kitao, H. Nakai, T.J.A. Vreven, J. Montgomery, J.E. Peralta, F. Ogliaro, M. Bearpark, J.J. Heyd, E. Brothers, K.N. Kudin, V.N. Staroverov, T. Keith, R. Kobayashi, J. Normand, K. Raghavachari, A. Rendell, J.C. Burant, S.S. Iyengar, J. Tomasi, M. Cossi, N. Rega, J.M. Millam, M. Klene, J.E. Knox, J.B. Cross, V. Bakken, C. Adamo, J. Jaramillo, R. Gomperts, R.E. Stratmann, O. Yazyev, A.J. Austin, R. Cammi, C. Pomelli, J.W. Ochterski, R.L. Martin, K. Morokuma, V.G. Zakrzewski, G.A. Voth, P. Salvador, J.J. Dannenberg, S. Dapprich, A.D. Daniels, O. Farkas, J.B. Foresman, J.V. Ortiz, J. Cioslowski, D.J. Fox, Revision C.01 Ed., Gaussian Inc., Wallingford, CT, 2010.
- [25] S. Scheiner, *Hydrogen Bonding: A Theoretical Perspective*, Oxford University Press, New York, 1997.
- [26] S.F. Boys, F. Bernardi, *Mol. Phys.* 19 (1970) 553.
- [27] E.P.L. Hunter, S.G. Lias, *J. Phys. Chem. Ref. Data* 27 (1998) 413.
- [28] J. Chen, M.A. McAllister, J.K. Lee, K.N. Houk, *J. Org. Chem.* 63 (1998) 4611.
- [29] J.J. Brauman, *J. Mass Spectrom.* 30 (1995) 1649.
- [30] J.H. Nelson, L.C. Nathan, R.O. Ragsdale, *J. Am. Chem. Soc.* 90 (1968) 5754.
- [31] G.C. Stafford, P.E. Kelley, J.E.P. Syka, W.E. Reynolds, J.F. Todd, *J. Int. J. Mass Spectrom. Ion Process.* 60 (1984) 85.
- [32] L. Sleno, D.A. Volmer, *J. Mass Spectrom.* 39 (2004) 1091.
- [33] J. Kane, G. Honigfeld, J. Singer, H. Meltzer, *Arch. Gen. Psychiatry* 45 (1988) 789.
- [34] M.C. Olianas, S. Dedoni, R. Ambu, P. Onali, *Eur. J. Pharmacol.* 607 (2009) 96.
- [35] M. Pirmohamed, D. Williams, S. Madden, E. Templeton, B.K. Park, *J. Pharmacol. Exp. Ther.* 272 (1995) 984.

# Speciation of CuCl and CuCl<sub>2</sub> Thiol-Amine Solutions and Characterization of Resulting Films: Implications for Semiconductor Device Fabrication

Priya Murria,<sup>†,§</sup> Caleb K. Miskin,<sup>‡,§</sup> Robert Boyne,<sup>‡</sup> Laurance T. Cain,<sup>†</sup> Ravikiran Yerabolu,<sup>†</sup> Ruihong Zhang,<sup>‡</sup> Evan C. Wegener,<sup>‡</sup> Jeffrey T. Miller,<sup>‡</sup> Hilikka I. Kenttämä,<sup>\*,†</sup> and Rakesh Agrawal<sup>\*,†,§</sup>

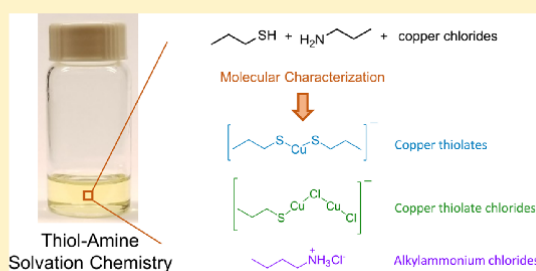
<sup>†</sup>Department of Chemistry, Purdue University, 560 Oval Drive, West Lafayette, Indiana 47907, United States

<sup>‡</sup>Davidson School of Chemical Engineering, Purdue University, 480 Stadium Mall Drive, West Lafayette, Indiana 47907, United States

<sup>§</sup>School of Materials Engineering, Purdue University, West Lafayette, Indiana 47907, United States

## Supporting Information

**ABSTRACT:** Thiol-amine mixtures are an attractive medium for the solution processing of semiconducting thin films because of their remarkable ability to dissolve a variety of metals, metal chalcogenides, metal salts, and chalcogens. However, very little is known about their dissolution chemistry. Electrospray ionization high-resolution tandem mass spectrometry and X-ray absorption spectroscopy were employed to identify the species formed upon dissolution of CuCl and CuCl<sub>2</sub> in 1-propanethiol and *n*-butylamine. Copper was found to be present exclusively in the 1+ oxidation state for both solutions. The copper complexes detected include copper chlorides, copper thiolates, and copper thiolate chlorides. No complexes of copper with amines were observed. Additionally, alkylammonium ions and alkylammonium chloride adducts were observed. These findings suggest that the dissolution is initiated by proton transfer from the thiol to the amine, followed by coordination of the thiolate anions with copper cations. Interestingly, the mass and X-ray absorption spectra of the solutions of CuCl and CuCl<sub>2</sub> in thiol-amine were essentially identical. However, dialkyl disulfides were identified by Raman spectroscopy as an oxidation product only for the copper(II) solution, wherein copper(II) had been reduced to copper(I). Analysis of several thiol-amine pairs suggested that the dissolution mechanism is quite general. Finally, analysis of thin films prepared from these solutions revealed persistent chlorine impurities, in agreement with previous studies. These impurities are explained by the mass spectrometric finding that chloride ligands are not completely displaced by thiolates upon dissolution. These results suggest that precursors other than chlorides will likely be preferred for the generation of high-efficiency copper chalcogenide films, despite the reasonable efficiencies that have been obtained for films generated from chloride precursors in the past.



## INTRODUCTION

Solution processing of electronic materials is an attractive alternative to vacuum-based methods because of its promise of high-throughput, roll-to-roll fabrication at low cost. Processing of inorganic materials in organic solvents is of particular interest as a means to combine the superior electronic properties and stability of inorganic materials with the facile processing of organic solutions.<sup>1,2</sup> Recently, significant work has been performed to advance the so-called molecular precursor route to inorganic thin films.<sup>3</sup> This route involves the dissolution of appropriate precursor salts to form a homogeneous solution, followed by an appropriate coating method, and (usually) subsequent heat treatments to evaporate the residual solvent, remove impurities, and promote the growth of a polycrystalline film of the desired final phase.

Recently, a promising solvent system containing an amine and a thiol was developed for dissolution of a host of metal, metal

chalcogenide, and metal salt precursors that are typically difficult to dissolve.<sup>3–9</sup> The system has found significant use in processing metal chalcogenide solar cells,<sup>9–18</sup> luminescent quantum dots,<sup>9,19,20</sup> nanoparticles,<sup>5,6,20–24</sup> and thermoelectrics,<sup>25</sup> making it a very general solvent system for metal chalcogenide chemistry. However, little is known about the solution chemistry associated with the thiol-amine solvent system. This fundamental understanding is essential in order to further develop the technique. Early work using this solvent system by Liu et al. led to the hypothesis that elemental selenium can be reduced by oxidizing the thiols into disulfides, resulting in oleylamine/selenium complexes.<sup>5</sup> This hypothesis was supported by work carried out by Walker and Agrawal that showed that, once the dissolution was complete, it was possible to remove the thiol

Received: May 30, 2017

Published: November 13, 2017

and disulfide compounds while maintaining selenium in the solution.<sup>6</sup>

Researchers have also attempted to understand the dissolution mechanisms of metals and metal salts other than selenium in thiol-amine solutions. Webber and Brutchey reported that mixing 1,2-ethylenediamine with 1,2-ethanedithiol resulted in a ~15000 times increase in the electrolytic conductivity, indicating significant ion formation.<sup>7</sup> This result was supported by the loss of the signal for the sulfhydryl proton in the <sup>1</sup>H NMR spectrum of a mixture of ethanethiol and 1,2-ethylenediamine and the greatly reduced intensity of the S–H signal in the Raman spectrum of the mixture compared to pure ethanethiol.<sup>8</sup> Buckley et al. recently studied solutions of Sn, SnS, and SnO in 1,2-ethylenediamine and 1,2-ethanedithiol solutions by using <sup>119</sup>Sn NMR and Raman spectroscopy and thermogravimetric analysis–differential scanning calorimetry. The results indicated the formation of a single molecular solute, likely bis(1,2-ethanedithiolate)tin(II).<sup>26</sup> However, much remains unknown concerning the dissolution mechanism, which was recently identified as one of the most pressing scientific needs for this solvent system.<sup>3</sup>

In this work, we used electrospray ionization coupled with high-resolution tandem mass spectrometry, synchrotron X-ray absorption spectroscopy, and Raman spectroscopy for characterization of the compounds in solutions formed upon dissolution of CuCl and CuCl<sub>2</sub> in 1-propanethiol and *n*-butylamine mixtures. These salts were chosen for this study because they are useful precursors for the synthesis of many copper-containing chalcogenides. We further analyzed annealed films prepared from these solutions with and without added sulfur via X-ray diffraction, Raman spectroscopy, and energy-dispersive X-ray spectroscopy to understand how these films evolve upon heating.

## ■ MATERIALS AND METHODS

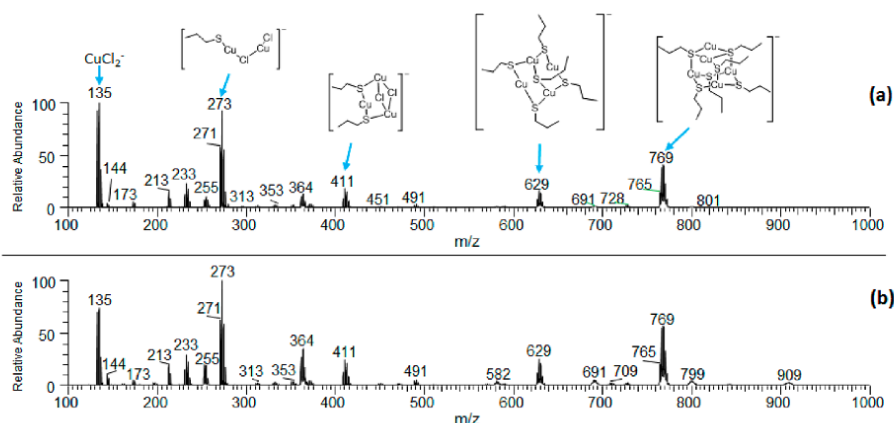
**Materials.** CuCl (≥99.995%), CuCl<sub>2</sub> (anhydrous, ≥99.995%), sulfur (99.98%), 1-propanethiol (PT; 99%), and dipropyl disulfide (DPDS; 98%) were purchased from Sigma-Aldrich. *n*-Butylamine (BA; 99+%), *n*-propylamine (99+%), and ethanethiol (ET; 99+%) were purchased from Acros Organics. Hydrogen chloride (HCl; 37% aqueous solution) was purchased from Macron Chemicals. All chemicals were used without further purification.

**Solution Preparation.** Solutions (10 mM) of CuCl and CuCl<sub>2</sub> were prepared by dissolving each salt in a mixture of BA and PT with a 1:1 molar ratio in a nitrogen glovebox. These solutions were obtained by the addition of BA to the copper salt first, followed by the addition of thiol. The addition of the amine resulted in a partially dissolved, slightly blue-green solution for CuCl and a brilliant royal-blue suspension for CuCl<sub>2</sub>. After the addition of thiol, the salts fully dissolved, and transparent, light-yellow, visually identical solutions were obtained (see Figure S1). A white aerosol, hypothesized to be fine *n*-butylammonium chloride (BACl) particles, was formed in the headspace above these solutions during dissolution. A setup was developed for the air-free injection of these solutions into the mass spectrometer. The setup consists of a 5 mL Hamilton syringe connected to a 500 μL Hamilton syringe via a three-way Hamilton valve and high-purity perfluoroalkoxy tubing. The 5 mL syringe was used as a reservoir syringe for the smaller 500 μL Hamilton syringe. Solutions were aspirated into the syringes inside a nitrogen-filled glovebox and then connected to the ion source of the mass spectrometer, which was constantly being purged with inert gas. The 500 μL syringe was connected to the syringe pump on the mass spectrometer. The three-way valve was then opened to allow injection into the mass spectrometer. The syringes were fabricated such that the fluid contacts only the borosilicate glass, poly(tetrafluoroethylene), or similar chemically inert materials. A schematic of this setup is included in Figure S2. Note that while CuCl and CuCl<sub>2</sub> both dissolve in PT without BA, their behavior in the thiol-amine solution is of interest because these

salts would be dissolved in this manner for metal chalcogenide film preparation. For example, this is the case for the preparation of Cu<sub>2</sub>ZnSn(S,Se)<sub>4</sub> or Cu(In,Ga)Se<sub>2</sub> films, whereas the other precursors require both thiol and amine for dissolution.<sup>10,16</sup>

**Electrospray Ionization High-Resolution Tandem Mass Spectrometry (ESI-MS/MS).** Solutions of CuCl and CuCl<sub>2</sub> in BA and PT were characterized using a Thermo Scientific (Waltham, MA) LTQ Orbitrap XL hybrid mass spectrometer. An electrospray ionization (ESI) source was used for ionization. The solutions were pumped into the ESI source by using a syringe pump at a rate of 5 μL min<sup>-1</sup>. The ESI source conditions were set to the following: 2.2 kV spray voltage, 40 (arbitrary units) flow rate of sheath gas (N<sub>2</sub>), 10 (arbitrary units) flow rate of auxiliary gas (N<sub>2</sub>), and 275 °C capillary temperature. All ion optic voltages were set using the LTQ Tune Plus interface tuning features. MS spectra were collected in both positive- and negative-ion modes. Elemental compositions were obtained via high-resolution mass analysis and further confirmed based on isotopic distribution patterns. Structural assignments of ions were based on collision-activated-dissociation (CAD) MS spectra. CAD experiments involved the isolation of ions of a particular *m/z* value in the ion trap and kinetic excitation of the ions, followed by their fragmentation upon collisions with a helium buffer gas (helium partial pressure in the ion trap ~ 10<sup>-3</sup> Torr). A *q* value of 0.25 and an activation time of 30 ms were employed. The ion isolation window was adjusted such that only ions of the same nominal *m/z* value were isolated while allowing a good signal for the CAD MS spectra. Data processing was performed using *Xcalibur 2.1* software.

**X-ray Absorption Spectroscopy (XAS).** XAS measurements were performed at the Cu Kα edge (8.9790 keV) on the bending magnet beamline of the Materials Research Collaborative Access Team (MRCAT) at the Advanced Photon Source (APS), Argonne National Laboratory. The X-ray ring at the APS has a current of 102 mA, and the beamline has a flux of 5 × 10<sup>10</sup> photons s<sup>-1</sup>. Photon energies were selected using a water-cooled, double-crystal Si(111) monochromator, which was detuned by approximately 50% to reduce harmonic reflections. Measurements were made in transmission step-scan mode, and data points were acquired in three separate regions: a preedge region (from –250 to –50 eV, step size = 10 eV, and dwell time = 0.25 s), the X-ray absorption near-edge structure (XANES) region (from –50 to –30 eV, step size = 5 eV, and dwell time = 0.25 s, and from –30 to +30 eV, step size = 0.4 eV, and dwell time = 0.5 s), and the extended X-ray absorption fine structure (EXAFS) region (from 0 to 12 Å<sup>-1</sup>, step size = 0.05 Å<sup>-1</sup>, and dwell time = 0.5 s and from 12 to 15 Å<sup>-1</sup>, step size = 0.05 Å<sup>-1</sup>, and dwell time = 1.0 s). The ionization chambers were optimized for the maximum current with linear response (~10<sup>10</sup> photons detected s<sup>-1</sup>), with 10% absorption in the incident ion chamber and 70% absorption in the transmission detector. The X-ray beam size was 0.5 × 2.5 mm<sup>2</sup>. Data were collected in transmission mode. A third detector in series simultaneously collected a copper foil reference spectrum with each measurement for energy calibration. Air- and moisture-sensitive reference compounds were loaded into an argon-filled glovebox (10.0 ppm of O<sub>2</sub> and 0.5 ppm of H<sub>2</sub>O). Solid samples were pressed into a cylindrical sample holder consisting of six wells, thereby forming a self-supporting wafer. To achieve an absorbance (μx) of approximately 1.0, solid samples were diluted with silica gel. The sample holder was placed in a quartz reactor tube (1 in. o.d. and 10 in. length) sealed with Kapton windows by two Ultra-Torr fittings through which gas could be flown. To reduce absorption of X-ray photons by the gases in the beam path, the reactor was purged with helium following removal from the glovebox. Solid samples were measured at room temperature under a helium atmosphere. Liquid samples were prepared in a nitrogen-filled glovebox. Polymer cells (Medlin, 50 mm length, 3.1 mm o.d., and 1.9 mm i.d.) were filled with sample and sealed with a VCO face-sealed fitting and Teflon O-ring inside the glovebox. XAS spectra were analyzed using *WinXAS 3.1* software.<sup>27</sup> The data were obtained from –250 eV below the edge to 850 eV above the edge and normalized with linear and cubic fits of the preedge and postedge regions, respectively. The oxidation state of copper in each sample was determined based on the measured XANES edge energy via a comparison of the analogous energy measured for reference materials, copper foil, solid samples of Cu<sub>2</sub>O, CuCl, CuO, and CuCl<sub>2</sub>, and an aqueous Cu(NH<sub>3</sub>)<sub>4</sub>(NO<sub>3</sub>)<sub>2</sub> solution



**Figure 1.** (–)ESI-MS spectra of solutions of (a) CuCl and (b) CuCl<sub>2</sub> in a 1:1 molar BA/PT mixture. It should be noted that, because of the presence of multiple stable isotopes of copper, sulfur, and chlorine, the most abundant ion in any given ion cluster is not a monoisotopic ion.

[prepared by dissolving copper(II) nitrate in an excess 28–30% aqueous ammonium hydroxide solution]. The edge energy of the XANES spectrum was determined from the inflection point in the edge, i.e., the maximum in the first derivative of the XANES spectrum. The preedge energy was determined from the maximum of the preedge peak. The EXAFS coordination parameters were obtained by a least-squares fit in the  $R$  space of the  $k^2$ -weighted Fourier transform data from 3.1 to 10.7 Å<sup>-1</sup>. The first shell fits of the magnitude and imaginary parts were performed between 1.0 and 2.2 Å. Fits were performed by the refinement of coordination numbers, bond distance ( $R$ ), energy shift ( $E_0$ ), and the Debye–Waller factor ( $\Delta\sigma^2$ ). Experimental phase and amplitude fitting functions for Cu–Cl and Cu–S scattering were determined from NiCl<sub>2</sub> (coordination number = 6 at 2.43 Å).

**Computational Methods.** Geometry optimizations were performed using the *Gaussian09* program<sup>28</sup> with the B3PW91 functional and the LANL2DZ basis set. This combination of functional and basis set has been shown to provide reasonable results for copper, with about 3% errors in geometries.<sup>29</sup> All geometry optimizations were followed by a full Hessian calculation to guarantee that the minima had all positive eigenvalues. In order to reduce the computational cost of these calculations, propyl groups were replaced by methyl groups.

**Film Preparation.** Solutions (0.2 M) of CuCl and CuCl<sub>2</sub> in a 1:1 molar ratio of BA/PT were drop-cast onto pieces of soda lime glass, and two sets of films were prepared for each solution. Both sets of films were heated on a hot plate at 80 °C in a nitrogen glovebox until visually dry. One set was further heated to 350 °C at a rate of ~75 °C min<sup>-1</sup> and held at 350 °C for 4 min. To explore the role of added elemental sulfur on the formation of copper chalcogenide films (as is commonly done in device preparation<sup>10</sup>), copper chloride solutions with added sulfur were prepared. This was accomplished by preparing 0.4 M solutions of CuCl and CuCl<sub>2</sub> in 1:1 BA/PT (similar to that described in the *Solution Preparation* section), into which an equal volume of either 0.4 M (molar ratio of S/Cu = 1) or 1.2 M (molar ratio of S/Cu = 3) elemental sulfur solution in 1:1 BA/PT was added. These solutions were drop-cast onto soda lime glass and dried at 80 and 350 °C (as described above). A reference film of BaCl was prepared by adding 1.25 mL of 37% HCl(aq) dropwise into 1.25 mL of BA (*Caution! This should be done slowly as the reaction is very vigorous and results in the formation of a fine white aerosol believed to be BaCl*). This solution was then drop-cast onto glass and dried at 80 °C to remove excess HCl, resulting in a transparent polycrystalline film.

**X-ray Diffraction (XRD).** XRD spectra of the dried films were obtained using a Rigaku Smartlab with a Cu  $K\alpha$  source operating at 40 V and 44 mA. Data were collected in Bragg–Brentano geometry using a step size of 0.05° and a scan speed of 4.0° min<sup>-1</sup>.

**Raman Spectroscopy.** Raman spectra were obtained using a Thermo Scientific DXR2 spectrometer with a 633 nm laser. Spectra

were recorded for the dried films, for neat BA, PT, and DPDS, and for 0.4 M solutions of CuCl and CuCl<sub>2</sub> in 1:1 molar mixtures of BA and PT. Liquid samples were sealed in Hellma Analytics fluorescence quartz cuvettes in a glovebox prior to analysis. The laser power was adjusted between 1 and 8 mW as needed to minimize laser-induced sample damage.

**Energy-Dispersive X-ray Spectroscopy (EDS).** EDS was used to estimate the atomic compositions of the dried films. This was carried out using an FEI Quanta 3D scanning electron microscope operated at an accelerating voltage of 20 kV and equipped with an Oxford INCA Xstream-2 silicon drift detector. Data analysis was performed using Oxford AZtec software. Multiple sites were analyzed for each sample to obtain a representative average, although the sampling was not rigorously randomized and judgment was used to interrogate relevant areas.

## RESULTS AND DISCUSSION

### ESI-MS/MS of CuCl and CuCl<sub>2</sub> Thiol-amine Solutions.

The solutions of CuCl and CuCl<sub>2</sub> in a 1:1 molar mixture of BA and PT were analyzed using both negative- and positive-ion-mode electrospray ionization high-resolution mass spectrometry [(–)ESI and (+)ESI-MS] in order to detect both negative and positive ions, respectively. This ionization method is gentle and does not cause fragmentation of the ions. Figure 1 shows the (–)ESI-MS spectra of the two solutions. The accurate  $m/z$  value was measured for each detected ion in order to determine its elemental composition (Table 1). Furthermore, CAD MS spectra were measured for all major ions (Figures S3–S6) in order to obtain structural information. On the basis of these measurements, the major ions were identified to be complexes of copper(I) with propylthiolates and/or chlorides for both solutions (Figure 1 and Table 1). Quantum-chemical calculations were used to provide support for the proposed structures (Figure S7; the Cartesian coordinates are also shown in the Supporting Information, SI). No complexes of copper and BA were observed in these MS spectra (Table 1). However, BA formed BaCl adducts of variable sizes (i.e., [C<sub>4</sub>H<sub>9</sub>NH<sub>3</sub><sup>+</sup>]<sub>*n*</sub>[Cl<sup>–</sup>]<sub>*n+1*</sub>; Table 1). The elemental compositions and proposed structures for all major ions are shown in Table 1. Solutions of CuCl and CuCl<sub>2</sub> dissolved in other thiol-amine mixtures (butylamine/ET and propylamine/ET) were found to form analogous ions, implying that the dissolution processes were similar (see Figures S8 and S9). Surprisingly, the MS spectra measured for CuCl and CuCl<sub>2</sub> solutions were found to be

Table 1. Elemental Compositions and Proposed Structures for Ions Detected by Using (–)ESI-MS (Figure 1)

Measured $m/z$ of monoisotopic ion (error $\pm$ ppm from expected mass)	Elemental composition	Proposed ion/structure
70.94623 (17.6 ppm)	HCl <sub>2</sub>	$[\text{Cl}-\text{H}-\text{Cl}]^-$
132.86826 (11.3 ppm)	CuCl <sub>2</sub>	$[\text{Cl}-\text{Cu}-\text{Cl}]^-$
144.03566 (10.6 ppm)	C <sub>4</sub> H <sub>12</sub> NCl <sub>2</sub>	$[(\text{C}_4\text{H}_{12}\text{N})^+(\text{Cl})_2]^-$
172.92636 (9.3 ppm)	CuC <sub>3</sub> H <sub>7</sub> ClS	$[\text{Cl}-\text{Cu}-\text{S}-\text{C}_3\text{H}_7]^-$
212.98438 (7.7 ppm)	CuC <sub>6</sub> H <sub>14</sub> S <sub>2</sub>	$[\text{C}_3\text{H}_7\text{S}-\text{Cu}-\text{S}-\text{C}_3\text{H}_7]^-$
230.76678 (6.8 ppm)	Cu <sub>2</sub> Cl <sub>3</sub>	$[\text{Cl}-\text{Cu}-\text{Cl}-\text{Cu}-\text{Cl}]^-$
253.10153 (6.2 ppm)	C <sub>8</sub> H <sub>24</sub> N <sub>2</sub> Cl <sub>3</sub>	$[(\text{C}_4\text{H}_{12}\text{N}^+)_2(\text{Cl})_3]^-$
270.82480 (5.9 ppm)	Cu <sub>2</sub> C <sub>3</sub> H <sub>7</sub> Cl <sub>2</sub> S	$[\text{C}_3\text{H}_7\text{S}-\text{Cu}-\text{Cl}-\text{Cu}-\text{Cl}]^-$
310.88290 (5.5 ppm)	Cu <sub>2</sub> C <sub>6</sub> H <sub>14</sub> ClS <sub>2</sub>	$[\text{C}_3\text{H}_7\text{S}-\text{Cu}-\text{Cl}-\text{Cu}-\text{S}-\text{C}_3\text{H}_7]^-$
328.66528 (4.9 ppm)	Cu <sub>3</sub> Cl <sub>4</sub>	$[\text{Cl}-\text{Cu}-\text{Cl}-\text{Cu}-\text{Cl}-\text{Cu}-\text{Cl}]^-$
350.94098 (5.1 ppm)	Cu <sub>2</sub> C <sub>9</sub> H <sub>21</sub> S <sub>3</sub>	$[\text{C}_3\text{H}_7\text{S}-\text{Cu}-\text{S}-\text{Cu}-\text{S}-\text{C}_3\text{H}_7]^-$
362.16748 (4.7 ppm)	C <sub>12</sub> H <sub>36</sub> N <sub>3</sub> Cl <sub>4</sub>	$[(\text{C}_4\text{H}_{12}\text{N}^+)_3(\text{Cl})_4]^-$
408.78135 (4.2 ppm)	C <sub>6</sub> H <sub>14</sub> Cl <sub>2</sub> Cu <sub>3</sub> S <sub>2</sub>	$[\text{C}_3\text{H}_7\text{S}-\text{Cu}-\text{Cl}-\text{Cu}-\text{Cl}-\text{Cu}-\text{S}-\text{C}_3\text{H}_7]^-$
448.83941 (4.1 ppm)	C <sub>9</sub> H <sub>21</sub> ClCu <sub>3</sub> S <sub>3</sub>	$[\text{C}_3\text{H}_7\text{S}-\text{Cu}-\text{S}-\text{Cu}-\text{Cl}-\text{Cu}-\text{S}-\text{C}_3\text{H}_7]^-$

nearly identical. The reasons for this result are discussed later in this paper.

In order to detect analytes present in the solutions of CuCl and CuCl<sub>2</sub> that cannot be ionized via (–)ESI-MS, (+)ESI-MS was utilized. The (+)ESI-MS spectra measured for the two solutions are shown in Figure 2. Similar to the results obtained using (–)ESI-MS, the two (+)ESI-MS spectra are almost identical. On the basis of high-resolution measurements, most of the detected ions are adducts of butylammonium cations and chloride anions, except that they contain one more butylammonium unit than chloride unit as they carry a net positive charge (Figure 2 and Table 2). In addition, a few ions corresponding to condensation of a butylammonium cation with one or more butylamines,

possibly via the elimination of NH<sub>3</sub> and H<sub>2</sub> molecules, were observed ( $m/z$  114, 128, 199, and 270; Figure 2 and Table 2); the formation mechanism of these ions is not known at this time. It should be noted that the presence of these imines was not indicated by <sup>13</sup>C and <sup>1</sup>H NMR spectroscopy (Figures S10–S13) of the solutions. Therefore, it is likely that these ions are produced in the ion source of the mass spectrometer. Only one ion containing both sulfur and nitrogen was detected ( $m/z$  230; Table 2). The elemental compositions and proposed structures for the major ions observed in (+)ESI-MS spectra are summarized in Table 2. The structures were proposed based on CAD MS spectra. Selected CAD MS spectra are shown in



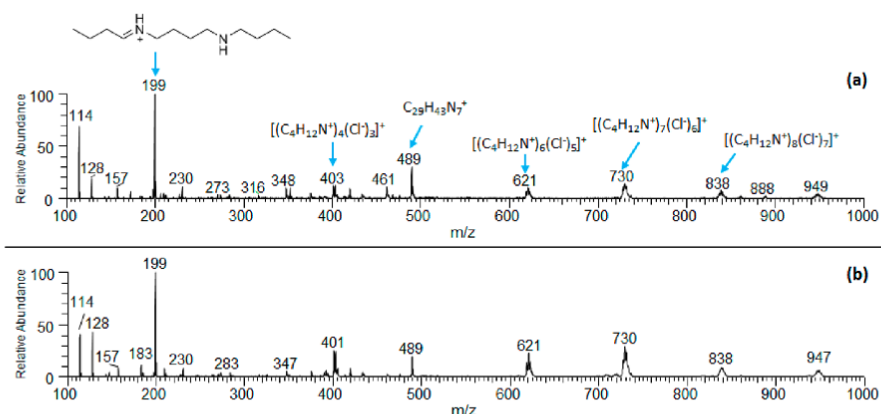


Figure 2. (+)ESI-MS spectra of solutions of (a) CuCl and (b) CuCl<sub>2</sub> in a 1:1 molar BA/PT mixture. It should be noted that, because of the presence of multiple stable isotopes of copper, sulfur, and chlorine, the most abundant ion in any given ion cluster is not a monoisotopic ion.

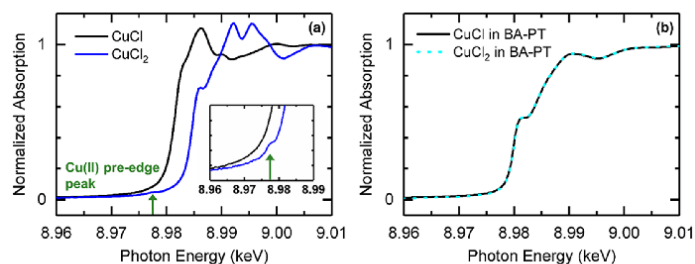
Table 2. Elemental Compositions and Molecular Formulae for Ions Observed in the (+)ESI-MS Spectra Shown in Figure 2

Measured m/z of monoisotopic ion (error $\pm$ ppm from expected mass)	Elemental composition	Proposed ion /structure
74.09586 (-7.6 ppm)	C <sub>4</sub> H <sub>12</sub> N	
114.12701 (-6.3 ppm)	C <sub>7</sub> H <sub>16</sub> N	
128.14258 (-6.2 ppm)	C <sub>8</sub> H <sub>18</sub> N	
147.18465 (-6.3 ppm)	C <sub>8</sub> H <sub>23</sub> N <sub>2</sub>	[(C <sub>4</sub> H <sub>11</sub> N)(C <sub>4</sub> H <sub>12</sub> N)] <sup>+</sup>
183.16116 (-6.0 ppm)	C <sub>8</sub> H <sub>24</sub> N <sub>2</sub> Cl	[(C <sub>4</sub> H <sub>12</sub> N <sup>+</sup> ) <sub>2</sub> (Cl)] <sup>+</sup>
199.21570 (-5.9 ppm)	C <sub>12</sub> H <sub>27</sub> N <sub>2</sub>	
230.19234 (-5.9 ppm)	C <sub>13</sub> H <sub>28</sub> NS	
270.28886 (-5.6 ppm)	C <sub>16</sub> H <sub>36</sub> N <sub>3</sub>	
283.28401 (-5.7 ppm)	C <sub>16</sub> H <sub>35</sub> N <sub>4</sub>	-
401.29156 (-5.8 ppm)	C <sub>16</sub> H <sub>48</sub> N <sub>4</sub> Cl <sub>3</sub>	[(C <sub>4</sub> H <sub>12</sub> N <sup>+</sup> ) <sub>4</sub> (Cl) <sub>3</sub> ] <sup>+</sup>
489.35572 (-3.5 ppm)	C <sub>29</sub> H <sub>43</sub> N <sub>7</sub>	-
619.42165 (-6.3 ppm)	C <sub>24</sub> H <sub>72</sub> N <sub>6</sub> Cl <sub>5</sub>	[(C <sub>4</sub> H <sub>12</sub> N <sup>+</sup> ) <sub>6</sub> (Cl) <sub>5</sub> ] <sup>+</sup>
728.48703 (-6.0 ppm)	C <sub>28</sub> H <sub>84</sub> N <sub>7</sub> Cl <sub>6</sub>	[(C <sub>4</sub> H <sub>12</sub> N <sup>+</sup> ) <sub>7</sub> (Cl) <sub>6</sub> ] <sup>+</sup>

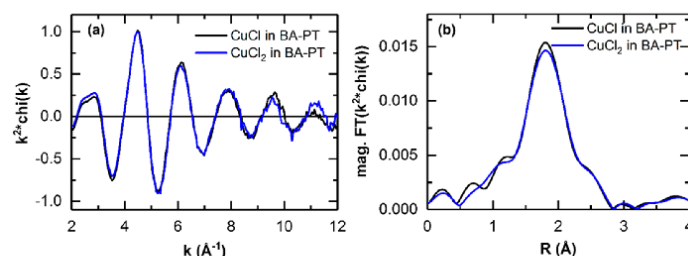
Figures S14–S16. Copper-containing ions were not observed in the (+)ESI-MS spectra.

The above MS analysis suggests that nearly identical mixtures are formed upon dissolution of CuCl and CuCl<sub>2</sub> in the BA/PT mixture. These data further indicate that copper(II) is reduced to copper(I) upon dissolution of CuCl<sub>2</sub> in the BA/PT mixture because only ions containing copper(I) were observed in both solutions. However, MS experiments did not reveal what compound might have been oxidized in this reaction. Disulfides

are the most likely oxidation product formed when copper is reduced in BA/PT solutions because they have been reported to form when selenium is reduced in thiol-amine solutions.<sup>5,6</sup> However, ESI-MS is ineffective in ionizing nonpolar analytes such as disulfides.<sup>30,31</sup> This was tested by examining a solution of CuCl<sub>2</sub> in a BA/PT mixture that was doped with dimethyl disulfide. Dimethyl disulfide was not detected in the ESI-MS spectra. Thus, Raman spectroscopy was used to attempt to detect disulfides in the solutions studied, as discussed below.



**Figure 3.** Copper K-edge XANES measured from 8.96 to 9.01 keV for (a) CuCl (black trace) and CuCl<sub>2</sub> (blue trace) powder standards and (b) solutions of CuCl (black dashed trace) and CuCl<sub>2</sub> (cyan trace) dissolved in 10:1 molar BA/PT mixtures. The inset indicates the copper(II) peak more clearly.



**Figure 4.** (a)  $k^2$ -weighted EXAFS and (b) the magnitude of the Fourier transform of the  $k^2$ -weighted EXAFS of solutions of CuCl (black trace) and CuCl<sub>2</sub> (blue trace) in 10:1 BA/PT.

**XAS of CuCl and CuCl<sub>2</sub> Solutions.** To confirm the oxidation state and local ligand environment of copper in the solutions of CuCl and CuCl<sub>2</sub> in BA/PT, XAS experiments were performed. The XANES spectra for 0.2 M solutions of CuCl and CuCl<sub>2</sub> dissolved in a 10:1 molar BA/PT mixture are shown in Figure 3b. Note that the relative concentration of thiol in the studied solutions was reduced to decrease the absorption of X-ray photons by sulfur. Also, the concentration of dissolved copper was increased to obtain a good signal for copper. The XANES spectra of solutions of CuCl and CuCl<sub>2</sub> in 1:1 BA/PT are very similar to the XANES spectra of solutions of CuCl and CuCl<sub>2</sub> in 10:1 BA/PT, although the signal-to-noise ratio is lower for the copper chlorides in 1:1 BA/PT (Figure S17).

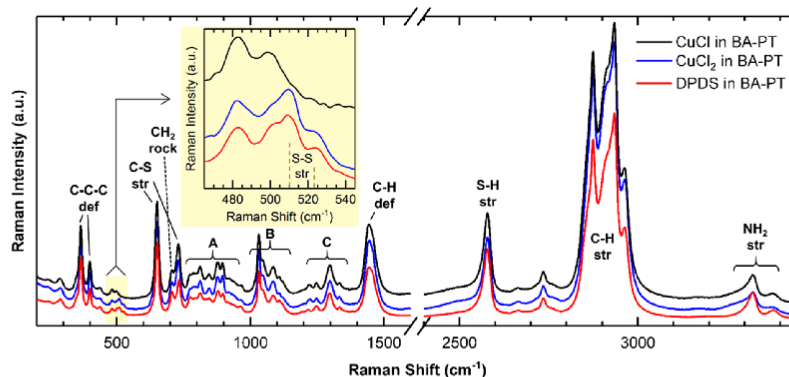
Copper(II) compounds show a characteristic pre-edge signal at 8.9775 keV, as shown in the XANES spectra of the reference compounds CuO, CuCl<sub>2</sub>, and Cu(NH<sub>3</sub>)<sub>4</sub>(NO<sub>3</sub>)<sub>2</sub> (Figure S18). This pre-edge signal corresponds to a dipole-forbidden transition of a 1s core electron of copper(II) to a 3d orbital. This pre-edge signal was not observed for copper(I) compounds because the transition of a 1s electron to the fully filled 3d orbitals is not possible. The XANES energy for copper(I) corresponds to a dipole-allowed transition of an electron from the 1s orbital to a 4p orbital, and it depends on the oxidation state and coordination chemistry of copper. The XANES spectra of pressed powder samples of CuCl and CuCl<sub>2</sub> are shown in Figure 3a. The edge energies of CuCl and CuCl<sub>2</sub> are 8.9816 and 8.9847 keV, respectively. The increase in the edge energy seen for copper(II) is typical for an increase in the oxidation state.

Solutions of CuCl and CuCl<sub>2</sub> in 10:1 BA/PT (Figure 3b) do not show the pre-edge signal corresponding to copper(II) discussed above. Furthermore, the XANES spectra of CuCl and CuCl<sub>2</sub> in the BA/PT solutions are identical, implying that the oxidation state and ligand environment around copper is the same in both solutions. These observations corroborate the MS results: that the oxidation state of copper in these solutions is 1+,

and the ligand environment of copper is the same in both solutions.

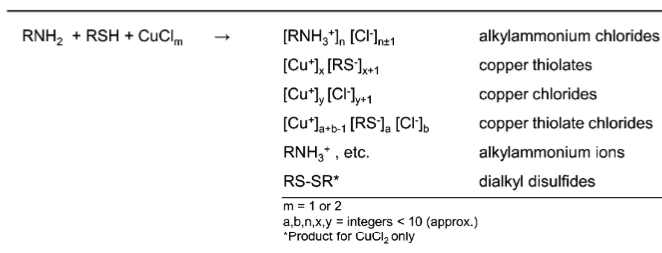
These findings are in agreement with other reports, which suggest that the reduction of copper(II) to copper(I) in the presence of thiolates is a highly favored redox reaction resulting in the oxidation of thiolates to disulfides.<sup>32,33</sup> While copper(II) thiolates were not observed in this study, it is possible to form copper(II) thiolates. In particular, recent work has investigated the equilibrium between copper(II)  $\mu$ -thiolate and copper(I) disulfide structures.<sup>34,35</sup> It was found that careful kinetic controls used to stabilize copper(II)  $\mu$ -thiolate as copper(I) disulfide are thermodynamically preferred.<sup>34</sup> Sterics and small changes in the ligands were found to play an important role in the stabilization of copper(II)  $\mu$ -thiolate.<sup>35</sup>

In order to determine the local coordination environment of copper in the aforementioned solutions, EXAFS data were collected for both solutions. Figure 4a shows the  $k^2$ -weighted EXAFS spectra of 0.2 M solutions of CuCl and CuCl<sub>2</sub> dissolved in a 10:1 molar BA/PT mixture. The spectra of the two samples are identical, implying that copper has the same local coordination environment in both solutions. Figure 4b shows the magnitude of the Fourier transform of the  $k^2$ -weighted EXAFS spectra for the solutions. The peak at 1.81 Å and shoulder at 1.27 Å (phase-uncorrected distances) are due to Cu–Cl and Cu–S scattering. Because chlorine and sulfur differ by one electron, they are indistinguishable by EXAFS. Thus, a total Cu–Cl/S coordination number and average Cu–Cl/S bond distance ( $R$ ) were determined through standard EXAFS fitting procedures (Figures S19 and S20 and Tables S1). The average total Cl/S coordination number for each sample was found to be 3.0 at a distance of 2.29 Å. The error in the coordination number obtained from this method is typically about 20%.<sup>36</sup> The MS results suggested that copper has a coordination number of 2 or 3 (Table 1); thus, the coordination number obtained from XAS substantiates the identities of the compounds determined by MS.



**Figure 5.** Raman spectra measured for 0.4 M solutions of CuCl (black line) and CuCl<sub>2</sub> (blue line) in a 1:1 molar BA/PT mixture. The spectrum of a 0.2 M solution of DPDS in a 1:1 molar BA/PT mixture is also shown for comparison (red line). The similarities between the CuCl<sub>2</sub> and DPDS spectra imply the presence of a disulfide bond in the CuCl<sub>2</sub> sample. The inset shows a detailed view of the highlighted region and locations of typical S–S peaks. Region A (750–1000 cm<sup>-1</sup>): CH<sub>2</sub> and CH<sub>3</sub> rocking and CSH deformations. Region B (1000–1150 cm<sup>-1</sup>): C–C stretching. Region C (1200–1350 cm<sup>-1</sup>): CH<sub>x</sub> bending and wagging.

### Scheme 1. Summary of the Dissolution Chemistry of CuCl and CuCl<sub>2</sub> in Monoamine–Monothiol Solutions



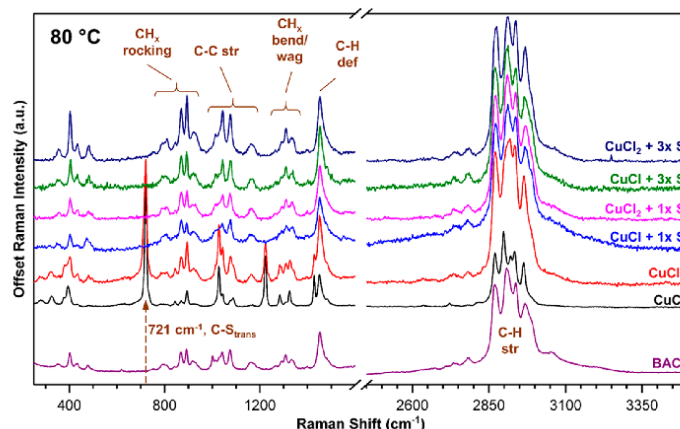
In addition, the lack of Cu–N scattering in EXAFS is in agreement with the lack of observation of complexes of copper and BA in MS data.

**Raman Spectroscopy of CuCl and CuCl<sub>2</sub> Solutions.** As mentioned above, dialkyl disulfides cannot be detected using ESI-MS. However, Raman spectroscopy is adept at detecting –SH, –NH<sub>2</sub>, and S–S functionalities.<sup>37</sup> Figure 5 shows the Raman spectra measured for 0.4 M solutions CuCl and CuCl<sub>2</sub> and 0.2 M solution of DPDS dissolved in a 1:1 molar BA/PT mixture. DPDS was used as a positive control because it is the expected oxidation product formed upon dissolution of CuCl<sub>2</sub> in BA/PT. The concentration of DPDS was chosen to be 0.2 M based on the premise that for every 2 mol of copper(II) reduced, 1 mol of DPDS would be formed (i.e.,  $2\text{Cu}^{2+} + 2\text{RSH} + 2\text{RNH}_2 \rightarrow 2\text{Cu}^+ + \text{R-S-S-R} + 2\text{RNH}_3^+$ ). The spectra measured for solutions of CuCl and CuCl<sub>2</sub> in BA/PT are essentially identical except for a doublet of peaks around 510 and 524 cm<sup>-1</sup> in the spectrum for CuCl<sub>2</sub> (Figure 5). These peaks were also observed for DPDS (Figure 5), and they are characteristic for the S–S bond.<sup>37</sup> The striking similarity between the spectra measured for the CuCl<sub>2</sub> and DPDS solutions supports the formation of DPDS upon dissolution of CuCl<sub>2</sub> in thiol-amine mixtures.

Spectra of neat BA, PT, and DPDS were also obtained (Figure S21) and used to identify the major peaks of interest in Figure 5 in consultation with the available literature.<sup>38,37,39–43</sup> Peaks at 3382 and 3323 cm<sup>-1</sup> indicate the presence of the NH<sub>2</sub> group.<sup>38</sup> The peak at 2578 cm<sup>-1</sup> corresponds to the S–H stretch of the thiol group.<sup>39,40,42,43</sup> The intense peaks in the region of 2850–3000 cm<sup>-1</sup> correspond to C–H stretching.<sup>37,38</sup> The peak at 1442

cm<sup>-1</sup> is attributed to C–H deformations.<sup>37,38</sup> Peaks at 651 and 732 cm<sup>-1</sup> correspond to the C–S bond in the gauche and trans configurations, respectively, and both were observed for these solutions.<sup>40,42,43</sup> Region A in Figure 5 (750–1000 cm<sup>-1</sup>) corresponds predominantly to CH<sub>2</sub> and CH<sub>3</sub> rocking,<sup>37,40–43</sup> although it also contains peaks associated with CSH deformations.<sup>42,43</sup> Region B (1000–1150 cm<sup>-1</sup>) corresponds to C–C stretching.<sup>39,40,43</sup> Region C (1200–1350 cm<sup>-1</sup>) corresponds to CH<sub>x</sub> bending and wagging in vapor-phase IR data for amines and thiols and is the likely contributor here as well.<sup>37,38</sup>

One significant feature in the spectra measured for the BA/PT solutions studied here is the large S–H peak at 2578 cm<sup>-1</sup> (Figure 5). This finding implies that the thiols have not been deprotonated to a large extent, in contrast to earlier studies<sup>7,14</sup> on dithiol/diamine and dithiol/monoamine mixtures. In these previous studies, mixing of dithiols and amines resulted in the formation of ions that caused a ~15000 times increase in the conductivity of the solution and the formation of a crystalline solid product comprised of protonated amines and dithiolates.<sup>7,14</sup> In contrast to these literature results,<sup>7</sup> a crystalline product was not observed for the BA/PT solutions studied here and no significant changes in the conductivity were observed (although a small increase in the conductivity was observed upon dissolution of the copper chloride salts; see Table S2). The lack of strong conductivity, no crystalline product formation, and minimal deprotonation of the thiol (as indicated by Raman spectroscopy) strongly imply that the BA/PT mixture does not undergo proton exchange to a large extent or it only occurs in the



**Figure 6.** Raman spectra of films prepared by drop-casting solutions and drying to 80 °C. The spectra obtained for films with added sulfur are similar to the BACl reference spectrum, while the spectra obtained for the films without added sulfur show distinct features. The peak at 721 cm<sup>-1</sup> is indicative of the C–S bond in the trans conformation when the S atom is bound to metal atoms in the solid state.<sup>39,41</sup>

presence of the metal salt. The greater propensity of the dithiolamine mixtures to form thiolate ions could explain their increased ability to dissolve metals and metal chalcogenides.<sup>7</sup>

To summarize the solution chemistry, dissolution in BA/PT and other monoamine/monothiol solutions can be thought of as an acid/base reaction in which the sulfhydryl proton is transferred to the amine, resulting in nucleophilic thiolate anions and alkylammonium ions. This occurs spontaneously in dithiolamine solutions<sup>7</sup> but does not appear to occur to a great extent in monoamine–monothiol solutions. However, in the presence of CuCl or CuCl<sub>2</sub>, alkylammonium ions and thiolates are formed for the monoamine–monothiol mixtures, as evidenced by the detected copper thiolate and copper thiolate chloride ions in ESI-MS experiments. In the case of CuCl<sub>2</sub>, copper(II) is reduced to copper(I), resulting in the formation of dialkyl disulfides. The dissolution process is summarized in Scheme 1.

The fact that chloride is not completely displaced by the thiolate groups upon dissolution of CuCl and CuCl<sub>2</sub> in BA/PT mixtures is not ideal for the eventual use of these solutions for thin-film deposition because chlorine is an undesired impurity. It would have been desirable to form only copper thiolates and alkylammonium chloride species so that the chlorine impurity could be more easily removed by a postdeposition wash or by evaporation upon heating.

**Raman Spectroscopy of Thin Films.** To understand the relationship between the chemical composition of the precursor solutions and the films generated from these solutions, films generated from some of the solutions discussed above were characterized by Raman spectroscopy, XRD, and EDS. The films were prepared by drop-casting solutions of 0.2 M CuCl and CuCl<sub>2</sub> in BA/PT onto glass and heating at 80 °C and then at 350 °C. Annealing films to high temperatures has been shown to facilitate recovery of copper sulfide films in previous studies.<sup>14,44–46</sup> Films were also prepared from solutions into which elemental sulfur had been added at a concentration equal to that of copper as well as 3 times that of copper to determine the effects of added sulfur on the process used for the fabrication of copper sulfide films. While the addition of sulfur did not cause a color change or precipitation in the solutions, a dark-brown precipitate began to form when the solutions were aspirated into

a polypropylene pipet tip. This continued while the film dried on a piece of glass.

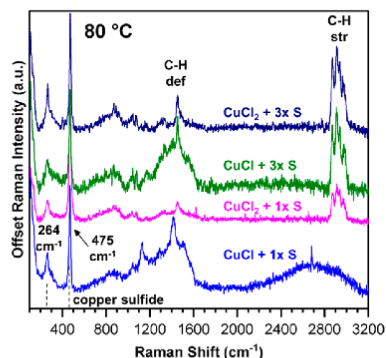
Films formed from solutions without added sulfur dried to form a light-yellow film at 80 °C, while those with added sulfur generated dark-brown/black films with a clearer flaky overlayer on top. This overlayer could be selectively scraped off to some extent to reveal the dark precipitate underneath (Figure S22). These films were characterized by Raman spectroscopy, XRD, and EDS.

Raman spectra of the films dried at 80 °C are shown in Figure 6 alongside the spectrum of a reference compound, BACl. The absence of peaks indicative of the S–H bond (2574 cm<sup>-1</sup>), S–S bond (510 and 524 cm<sup>-1</sup>), and NH<sub>2</sub> group (3300–3400 cm<sup>-1</sup>) in the spectra measured for the films indicates that these films do not contain free amines, disulfides, or thiols. However, a large peak corresponding to C–H stretching in the 2850–3000 cm<sup>-1</sup> region indicates the presence of organic compounds. The spectrum measured for the BACl reference (purple trace) shows many peaks and peak shapes similar to those of the spectra measured for the films, implying that this compound is present in these films. This effect is particularly noticeable for the solutions with added sulfur. However, the spectra measured for solutions of CuCl (black trace) and CuCl<sub>2</sub> (red trace) in BA/PT without added sulfur exhibit unique features not present in the other spectra. Specifically, the peaks at 721, 1028, and 1223 cm<sup>-1</sup> are not present or are significantly reduced in size in the spectra measured for films with added sulfur.

The large peak at ~721 cm<sup>-1</sup> corresponds to the C–S bond and has been observed in previous studies for other copper and metal thiolates.<sup>39,41</sup> This peak indicates that the conformation of the C<sub>α</sub>–C<sub>β</sub> bond near the S atom is mostly trans rather than gauche.<sup>39,41</sup> The shift for the C–S peak from 732 cm<sup>-1</sup> in solution to 721 cm<sup>-1</sup> in the films dried to 80 °C is characteristic of the shift in the trans rotamer in solution versus solid copper thiolates.<sup>39,43</sup> This implies the presence of copper thiolate compounds in the films prepared by drying solutions of CuCl and CuCl<sub>2</sub> in BA/PT at 80 °C. The gauche rotamer that was present in solution, as indicated by the peak at 651 cm<sup>-1</sup> (Figure 5), was not detected for the solid samples. The absence of the peak at 721 cm<sup>-1</sup> in the films with added sulfur (Figure 6, dried at

80 °C) indicates that the copper thiolate species are not present in the films with added sulfur.

The translucent overlayer for the films with added sulfur was removed to reveal the underlayer in order to allow its investigation using Raman spectroscopy. The resulting spectra are shown in Figure 7. The peak corresponding to C–S bonds

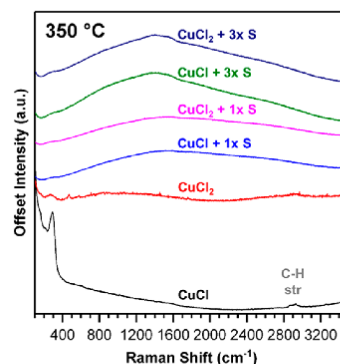


**Figure 7.** Raman spectra of films prepared from solutions with added sulfur by drop-casting and drying at 80 °C, with the translucent overlayer scraped away.

(721  $\text{cm}^{-1}$ ) was not observed in the underlayer, implying that metal thiolates are destabilized in the films with added sulfur. The spectra in Figure 7 contain the signature peaks for copper sulfide at 264 and 475  $\text{cm}^{-1}$ ,<sup>47,48</sup> implying its presence in the films. The absence of peaks corresponding to the C–S bond in the films with added sulfur is likely due to either cleavage of the C–S bonds or displacement of the entire thiolate by dissolved elemental sulfur, resulting in the observed copper sulfide phase (Figure 7). The data also suggest that BA/Cl is primarily present in the translucent overlayer because most of the peaks observed in Figure 6 are absent from the spectra in Figure 7. This is as expected because the copper sulfide precipitate should settle during drying. However, organic compounds are still present in the precipitate layer, as indicated by the peaks in the 2850–3000  $\text{cm}^{-1}$  region corresponding to C–H stretching.

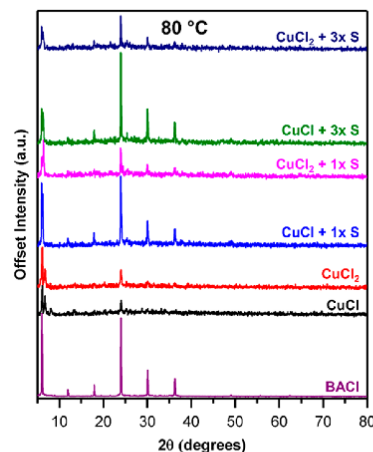
For films heated to 350 °C, a marked decrease in the size of the peaks related to organic compounds as well as most other peaks was observed (Figure 8). During the heating process, a significant fraction of the sample was observed to be volatilizing off as vapors from the films. This loss of sample as vapor persisted for 1 min when the films were kept at 350 °C. However, a small signal observed in the C–H region (2800–3000  $\text{cm}^{-1}$ ) for the films without added sulfur (Figure 8, black and red trace) suggests that organic compounds were not completely removed from these films. This is not the case when sulfur was added into the solutions used to generate the films. These findings imply that sulfur facilitates the removal of organic compounds from these films, which is in line with the above hypothesis that the addition of sulfur may cause displacement of thiolates.

A small amount of a copper sulfide may be present in the films generated from  $\text{CuCl}_2$  in BA/PT (Figure 8, red trace), indicated by the small peaks at 261 and 470  $\text{cm}^{-1}$ . However, these peaks are slightly shifted from the expected values. Surprisingly, the copper sulfide peaks evident in the Raman spectra of films with added sulfur and dried at 80 °C (Figure 7) were not observed when the films were heated to 350 °C (Figure 8).



**Figure 8.** Raman spectra of drop-cast films after heating to 350 °C and dwelling at this temperature for 4 min. Very little signal remains, although some C–H stretching is still observed for the films without added sulfur (red and black traces).

**XRD Analysis of Thin Films.** XRD patterns were measured to investigate the crystalline phases present in the films discussed above. The XRD patterns for the films annealed at 80 °C showed peaks that agree with the presence of BA/Cl, in addition to a few other minor peaks in some patterns that could not be identified (Figure 9). Interestingly, while a copper sulfide phase was



**Figure 9.** XRD patterns of drop-cast films annealed at 80 °C.

detected in the Raman spectra of the films heated at 80 °C, this phase was not detectable based on the XRD patterns. This result suggests that the copper sulfide phase is relatively amorphous because amorphous substances cannot be observed with this technique.

The films annealed at 350 °C were amorphous, with the exception of the films produced from solutions of  $\text{CuCl}$  annealed without added sulfur, which displayed a large peak at  $2\theta = 28.6^\circ$ , as well as minor peaks at  $2\theta = 47.5^\circ$  and  $56.4^\circ$ , belonging to an unidentified phase (Figure S23). Surprisingly, although the addition of sulfur eliminated the crystalline phase observed for the  $\text{CuCl}$  samples, it did not result in the formation of a copper sulfide phase upon annealing to 350 °C. While this is unexpected, it agrees with the Raman spectra measured for these films (Figure 8).

**EDS of Thin Films.** The films were further characterized using scanning electron microscopy–energy-dispersive spectroscopy (SEM–EDS). Representative results for the films without added sulfur and those with added sulfur (molar ratio of S/Cu = 3 in solution) are shown in Table 3, with additional data in Table

**Table 3. SEM–EDS Results for Films Prepared by Drop-Casting Copper Chloride Solutions in BA/PT Followed by Heating to 80 and 350 °C<sup>a</sup>**

	temp (°C)	C/Cu	S/Cu	N/Cu	Cl/Cu	N/Cl
CuCl	80	13.2	0.74	1.83	1.57	1.17
CuCl <sub>2</sub>	80	32.4	0.77	4.80	5.07	0.95
CuCl + 3xS (overlayer)	80	69.4	0.65	13.2	8.60	1.53
CuCl + 3xS (precipitate)	80	2.60	0.50	0.19	0.086	2.18
CuCl <sub>2</sub> + 3xS (overlayer)	80	841.6	1.03	165.7	98.3	1.69
CuCl <sub>2</sub> + 3xS (precipitate)	80	2.03	0.55	0.13	0.28	0.45
CuCl	350	1.42	0.24	0.063	0.41	0.15
CuCl <sub>2</sub>	350	2.26	0.36	0.076	0.28	0.27
CuCl + 3xS	350	0.84	0.52	0.0030	0.0083	0.36
CuCl <sub>2</sub> + 3xS	350	0.78	0.49	0.0081	0.0067	1.21

<sup>a</sup>Minor discrepancies observed between ratios are the result of rounding of final values.

**S3.** The films annealed at 80 °C show large amounts of carbon, nitrogen, and chlorine relative to copper because of the presence of BA/PT adducts and thiolates. Films prepared from CuCl<sub>2</sub> solutions show significantly larger amounts of chlorine, carbon, and nitrogen relative to copper compared to similarly prepared films from CuCl solutions. This is expected because the increased chlorine concentrations will result in more alkylammonium chloride products. The S/Cu ratios for the two films without added sulfur were both ~0.75. This value was expected to be less than 2, based on the fact that copper chloride salts were observed by using MS along with various copper thiolate compounds, the smallest of which (i.e., CuC<sub>6</sub>H<sub>14</sub>S<sub>2</sub>) would have the largest possible S/Cu ratio of 2. The observed value of ~0.75 is thus a reasonable average of the possible copper thiolates and copper thiolate chlorides observed by MS.

In the films with added sulfur (dried at 80 °C), significantly higher concentrations of carbon, nitrogen, and chlorine were observed in the overlayer relative to those of copper and sulfur compared to the films without added sulfur. This was found to be true for films with sulfur concentrations 3 times that of copper and for films with the same sulfur concentration as copper. The low concentration of copper and sulfur observed in the overlayer also supports the conclusion that the overlayer is mainly composed of BA/PT. The small amounts of sulfur and copper detected in the overlayer suggests that the S/Cu values reported here may contain significant error despite the averages lying between 0 and 2. EDS analysis of the particulates in the underlayer of these films revealed much higher copper and sulfur contents relative to carbon, nitrogen, and chlorine content. The observed S/Cu ratio for the precipitate was consistently near 0.5, which suggests the phase to be copper(I) sulfide, adding additional insight into the copper sulfide phase detected in the Raman spectroscopic analysis (Figure 7).

The films formed from the CuCl and CuCl<sub>2</sub> solutions and annealed at 350 °C had significantly reduced carbon, nitrogen,

and chlorine compared with their counterparts annealed at 80 °C. This was especially true of the films with added sulfur, which also had a S/Cu ratio of ~0.50. This ratio was higher than the average S/Cu ratio of the films without added sulfur, implying greater sulfur incorporation when sulfur is added. It is surprising that while the addition of sulfur facilitated the removal of impurities and resulted in a S/Cu ratio consistently near 0.5 [which is expected for copper(I) sulfide], a copper sulfide phase was not detected using Raman spectroscopy (Figure 8) or XRD for the films annealed at 350 °C (Figure S23).

The difficulty of removing impurities from solution-processed films is an ongoing discussion in the literature.<sup>10,15,16,49–52</sup> The EDS results for the films annealed at 350 °C suggest that much of the carbon-, nitrogen-, and chlorine-containing impurities can be volatilized, albeit not completely. Our data suggest that adding chalcogen to the solutions and annealing at high temperature can help to volatilize impurities, which is important for the fabrication of high-quality semiconducting films. These results agree with a previous study using chloride precursors to form Cu<sub>2</sub>ZnSn(S,Se)<sub>4</sub>, which found that the presence of chalcogen facilitated the removal of chlorine through the formation of volatile chalcogen chlorides.<sup>10</sup> However, chlorine may also form undesired volatile species in these solutions, which results in the removal of essential constituents. For example, in a study where Cu(In,Ga)Se<sub>2</sub> films were prepared in the presence of chloride, a significant loss of gallium from the films occurred because of the formation of volatile GaCl<sub>3</sub>.<sup>16</sup> On the basis of these studies and the results presented herein and in the absence of effective methods to remove residual chlorine, chloride precursors should be avoided when preparing films. Indeed, much recent work has focused on metal and metal chalcogenide precursor materials to avoid chlorine or other contaminants.<sup>11,13,14,18,53</sup>

## CONCLUSIONS

High-resolution ESI-MS/MS, XAS, Raman spectroscopy, XRD, and SEM–EDS were used to characterize solutions and films prepared from CuCl and CuCl<sub>2</sub> precursors dissolved in BA/PT mixtures. On the basis of MS analysis, the compositions of the two solutions are nearly identical. (–)ESI-MS revealed copper(I) chlorides, copper(I) thiolates, and copper(I) thiolate chlorides in the solutions. In positive-ion mode, predominantly alkylammonium ions were detected. They are the likely counterions of the negatively charged copper(I) compounds. Additionally, alkylammonium chloride adducts were observed using both ionization modes. XANES analysis verified that copper was exclusively in the 1+ oxidation state in the solutions. This is the desired oxidation state in many copper-based chalcogenide films (e.g., CuInSe<sub>2</sub>, Cu<sub>2</sub>ZnSnSe<sub>4</sub>). Raman spectroscopic analysis of the solutions indicated that DPDS was formed as an oxidation product in the dissolution and reduction of CuCl<sub>2</sub> in BA/PT from copper(II) to copper(I). On the basis of the above data, the dissolution mechanism is concluded to be initiated by proton transfer from the thiol to amine; this reaction does not occur spontaneously for monoamine–monothiol solutions but requires the presence of CuCl or CuCl<sub>2</sub>. The thiolate ion dissolves the copper salts by coordinating with the copper cations, while the propylammonium cation coordinates with the chloride anions. For copper(II) solutions, copper(II) is reduced to copper(I), while thiolates are converted to disulfides.

When the precursor solutions were drop-cast and dried at 80 °C (without any added sulfur), a light-yellow film was formed that showed signature peaks for copper thiolates in the Raman

spectra. Films dried at 80 °C with added sulfur generated films with two layers: a BaCl<sub>2</sub> flaky overlayer on top and copper sulfide particulates underneath. For films with added sulfur annealed at 350 °C, improved removal of carbon, nitrogen, and chlorine impurities as well as increased sulfur incorporation was observed. However, in neither case did annealing at 350 °C lead to the formation of copper sulfide, and it eliminated the amorphous copper sulfide that was present in the films with added sulfur at 80 °C. Annealing at 350 °C also failed to completely remove the impurities. The results presented herein provide significant insight into the chemistry of thiol-amine solutions and suggest that alternatives to chloride precursors should be pursued for the fabrication of high-quality copper chalcogenide functional materials via the thiol-amine solvent system.

## ■ ASSOCIATED CONTENT

### Supporting Information

The Supporting Information is available free of charge on the ACS Publications website at DOI: 10.1021/acs.inorgchem.7b01359.

Photographs of CuCl and CuCl<sub>2</sub> and drop-cast films, schematic of the gas-tight syringe setup, MS, NMR, and XANES spectra, optimized geometries, Cartesian coordinates, EXAFS fitting results, conductivity data, XRD patterns, and SEM-EDS results (PDF)

## ■ AUTHOR INFORMATION

### Corresponding Authors

\*E-mail: hilkka@purdue.edu. Tel.: +1 (765) 494-0882. Fax: +1 (765) 494-9421.

\*E-mail: agrawalr@purdue.edu. Tel.: +1 (765) 494-2257. Fax: +1 (765) 494-0805.

### ORCID

Priya Murria: 0000-0002-2513-6356

Ravikiran Yerabolu: 0000-0003-4628-4101

Hilkka I. Kenttämä: 0000-0001-8988-6984

Rakesh Agrawal: 0000-0002-6746-9829

### Author Contributions

\*These authors contributed equally to this work.

### Notes

The authors declare no competing financial interest.

## ■ ACKNOWLEDGMENTS

The authors thank Brian Graeser and Xin Zhao for helpful discussions and Jacob Milton for useful comments on the manuscript. We also thank Swapnil Deshmukh and John Harwood for their assistance in data collection. The authors gratefully acknowledge financial support by the U.S. Office of Naval Research (Contract N000141512833) and NSF DMREF (Grant 1534691-DMR). C.K.M. acknowledges financial support through the NSF GFRP (Grant DGE-0833366). This research used resources of the APS, a U.S. Department of Energy (DOE) Office of Science User Facility operated for the DOE Office of Science by Argonne National Laboratory under Contract DE-AC02-06CH11357. MRCAT operations are supported by the Department of Energy and the MRCAT member institutions.

## ■ REFERENCES

(1) Wang, W.; Han, S.-Y.; Sung, S.-J.; Kim, D.-H.; Chang, C.-H. 8.01% CuInGaSe<sub>2</sub> Solar Cells Fabricated by Air-Stable Low-Cost Inks. *Phys. Chem. Chem. Phys.* **2012**, *14* (31), 11154.

(2) Wang, W.; Su, Y. W.; Chang, C. H. Inkjet Printed Chalcopyrite CuIn<sub>x</sub>Ga<sub>1-x</sub>Se<sub>2</sub> Thin Film Solar Cells. *Sol. Energy Mater. Sol. Cells* **2011**, *95* (9), 2616–2620.

(3) McCarthy, C. L.; Brutchey, R. L. Solution Processing of Chalcogenide Materials Using Thiol-Amine “Alkalest” Solvent Systems. *Chem. Commun.* **2017**, 53 (36), 4888–4902.

(4) Tian, Q.; Huang, L.; Zhao, W.; Yang, Y.; Wang, G.; Pan, D. Metal Sulfide Precursor Aqueous Solutions for Fabrication of Cu<sub>2</sub>ZnSn(S,Se)<sub>4</sub> Thin Film Solar Cells. *Green Chem.* **2015**, *17* (2), 1269–1275.

(5) Liu, Y.; Yao, D.; Shen, L.; Zhang, H.; Zhang, X.; Yang, B. Alkylthiol-Enabled Se Powder Dissolution in Oleylamine at Room Temperature for the Phosphine-Free Synthesis of Copper-Based Quaternary Selenide Nanocrystals. *J. Am. Chem. Soc.* **2012**, *134* (17), 7207–7210.

(6) Walker, B. C.; Agrawal, R. Contamination-Free Solutions of Selenium in Amines for Nanoparticle Synthesis. *Chem. Commun.* **2014**, 50 (61), 8331–8334.

(7) Webber, D. H.; Brutchey, R. L. Alkalest for V<sub>2</sub>VI<sub>3</sub> Chalcogenides: Dissolution of Nine Bulk Semiconductors in a Diamine-Dithiol Solvent Mixture. *J. Am. Chem. Soc.* **2013**, *135* (42), 15722–15725.

(8) Webber, D. H.; Buckley, J. J.; Antunez, P. D.; Brutchey, R. L. Facile Dissolution of Selenium and Tellurium in a Thiol-amine Solvent Mixture under Ambient Conditions. *Chem. Sci.* **2014**, *5* (6), 2498–2502.

(9) Tian, Q.; Wang, G.; Zhao, W.; Chen, Y.; Yang, Y.; Huang, L.; Pan, D. Versatile and Low-Toxic Solution Approach to Binary, Ternary, and Quaternary Metal Sulfide Thin Films and Its Application in Cu<sub>2</sub>ZnSn(S,Se)<sub>4</sub> Solar Cells. *Chem. Mater.* **2014**, *26* (10), 3098–3103.

(10) Zhang, R.; Szczepaniak, S. M.; Carter, N. J.; Handwerker, C. A.; Agrawal, R. A Versatile Solution Route to Efficient Cu<sub>2</sub>ZnSn(S,Se)<sub>4</sub> Thin-Film Solar Cells. *Chem. Mater.* **2015**, *27* (6), 2114–2120.

(11) Guo, J.; Pei, Y.; Zhou, Z.; Zhou, W.; Kou, D.; Wu, S. Solution-Processed Cu<sub>2</sub>ZnSn(S,Se)<sub>4</sub> Thin-Film Solar Cells Using Elemental Cu, Zn, Sn, S, and Se Powders as Source. *Nanoscale Res. Lett.* **2015**, *10* (1), 335.

(12) Tian, Q.; Cui, Y.; Wang, G.; Pan, D. A Robust and Low-Cost Strategy to Prepare Cu<sub>2</sub>ZnSnS<sub>4</sub> Precursor Solution and Its Application in Cu<sub>2</sub>ZnSn(S,Se)<sub>4</sub> Solar Cells. *RSC Adv.* **2015**, *5* (6), 4184–4190.

(13) Yang, Y.; Wang, G.; Zhao, W.; Tian, Q.; Huang, L.; Pan, D. Solution-Processed Highly Efficient Cu<sub>2</sub>ZnSnSe<sub>4</sub> Thin Film Solar Cells by Dissolution of Elemental Cu, Zn, Sn, and Se Powders. *ACS Appl. Mater. Interfaces* **2015**, *7* (1), 460–464.

(14) Zhang, R.; Cho, S.; Lim, D. G.; Hu, X.; Stach, E. A.; Handwerker, C. A.; Agrawal, R. Metal-metal Chalcogenide Molecular Precursors to Binary, Ternary, and Quaternary Metal Chalcogenide Thin Films for Electronic Devices. *Chem. Commun.* **2016**, 52 (28), 5007–5010.

(15) Miskin, C. K.; Dubois-Camacho, A.; Reese, M. O.; Agrawal, R. A Direct Solution Deposition Approach to CdTe Thin Films. *J. Mater. Chem. C* **2016**, *4* (39), 9167–9171.

(16) Zhao, X.; Lu, M.; Koeper, M. J.; Agrawal, R. Solution-Processed Sulfur Depleted Cu(In,Ga)Se<sub>2</sub> Solar Cells Synthesized from a Monoamine-dithiol Solvent Mixture. *J. Mater. Chem. A* **2016**, *4* (19), 7390–7397.

(17) Zhao, D.; Fan, Q.; Tian, Q.; Zhou, Z.; Meng, Y.; Kou, D.; Zhou, W.; Wu, S. Eliminating Fine-Grained Layers in Cu(In,Ga)(S,Se)<sub>2</sub> Thin Films for Solution-Processed High Efficiency Solar Cells. *J. Mater. Chem. A* **2016**, *4* (35), 13476–13481.

(18) Arnou, P.; van Hest, M. F. A. M.; Cooper, C. S.; Malkov, A. V.; Walls, J. M.; Bowers, J. W. Hydrazine-Free Solution-Deposited CuIn(S,Se)<sub>2</sub> Solar Cells by Spray Deposition of Metal Chalcogenides. *ACS Appl. Mater. Interfaces* **2016**, *8* (19), 11893–11897.

(19) Deng, D.; Qu, L.; Achilefu, S.; Gu, Y. Broad Spectrum Photoluminescent Quaternary Quantum Dots for Cell and Animal Imaging. *Chem. Commun.* **2013**, 49 (82), 9494–9496.

(20) Deng, D.; Qu, L.; Gu, Y. Near-Infrared Broadly Emissive AgInSe<sub>2</sub>/ZnS Quantum Dots for Biomedical Optical Imaging. *J. Mater. Chem. C* **2014**, *2* (34), 7077–7085.

(21) Yang, W.-C.; Miskin, C. K.; Hages, C. J.; Hanley, E. C.; Handwerker, C.; Stach, E. A.; Agrawal, R. Kesterite Cu<sub>2</sub>ZnSn(S,Se)<sub>4</sub> Absorbers Converted from Metastable, Wurtzite-Derived Cu<sub>2</sub>ZnSnS<sub>4</sub> Nanoparticles. *Chem. Mater.* **2014**, *26* (11), 3530–3534.

- (22) Yao, D.; Liu, H.; Liu, Y.; Dong, C.; Zhang, K.; Sheng, Y.; Cui, J.; Zhang, H.; Yang, B. Phosphine-Free Synthesis of Ag–In–Se Alloy Nanocrystals with Visible Emissions. *Nanoscale* **2015**, *7* (44), 18570–18578.
- (23) Lu, X.; Zhuang, Z.; Peng, Q.; Li, Y. Wurtzite Cu<sub>2</sub>ZnSnS<sub>4</sub> Nanocrystals: A Novel Quaternary Semiconductor. *Chem. Commun.* **2011**, *47* (11), 3141.
- (24) Liu, Y.; Yao, D.; Yao, S.; Zhao, J.; Zhang, H.; Tian, W.; Yang, B. Phosphine-Free Synthesis of Heavy Co<sup>2+</sup>- and Fe<sup>2+</sup>-Doped Cu<sub>2</sub>ZnSnS<sub>4</sub> Nanocrystals by Virtue of Alkylthiol-Assisted Se Powder Dissolution. *J. Mater. Chem. A* **2013**, *1* (8), 2748.
- (25) Ma, Y.; Vartak, P. B.; Nagaraj, P.; Wang, R. Y. Thermoelectric Properties of Copper Chalcogenide Alloys Deposited via the Solution-Phase Using a Thiol–amine Solvent Mixture. *RSC Adv.* **2016**, *6* (102), 99905–99913.
- (26) Buckley, J. J.; McCarthy, C. L.; Del Pilar-Albaladejo, J.; Rasul, G.; Brutchey, R. L. Dissolution of Sn, SnO, and SnS in a Thiol–Amine Solvent Mixture: Insights into the Identity of the Molecular Solutes for Solution-Processed SnS. *Inorg. Chem.* **2016**, *55* (6), 3175–3180.
- (27) Ressler, T. WinXAS: A Program for X-Ray Absorption Spectroscopy Data Analysis under MS-Windows. *J. Synchrotron Radiat.* **1998**, *5* (2), 118–122.
- (28) Frisch, M. J.; Trucks, G. W.; Schlegel, H. B.; Scuseria, G. E.; Robb, M. A.; Cheeseman, J. R.; Scalmani, G.; Barone, V.; Mennucci, B.; Petersson, G. A.; et al. *Gaussian09*; Gaussian Inc.: Wallingford, CT, 2009.
- (29) Tong, G. S.-M.; Cheung, A. S.-C. Density Functional Theory Study of Alkali Metal–Noble Metal Diatomic Molecules. *J. Phys. Chem. A* **2002**, *106* (47), 11637–11643.
- (30) de Hoffmann, E.; Strooban, V. *Mass Spectrometry: Principles and Applications*, 3rd ed.; John Wiley & Sons, 2007.
- (31) Kebarle, P.; Verkerk, U. H. Electrospray: From Ions in Solution to Ions in the Gas Phase, What We Know Now. *Mass Spectrom. Rev.* **2009**, *28* (6), 898–917.
- (32) Hellinga, H. W. Construction of a Blue Copper Analogue through Iterative Rational Protein Design Cycles Demonstrates Principles of Molecular Recognition in Metal Center Formation. *J. Am. Chem. Soc.* **1998**, *120* (39), 10055–10066.
- (33) Smith, R. C.; Reed, V. D.; Hill, W. E. Oxidation Of Thiols By Copper(II). *Phosphorus, Sulfur Silicon Relat. Elem.* **1994**, *90* (1–4), 147–154.
- (34) Ording-Wenker, E. C. M.; Van Der Plas, M.; Siegler, M. A.; Bonnet, S.; Bickelhaupt, F. M.; Fonseca Guerra, C.; Bouwman, E. Thermodynamics of the CuII  $\mu$ -Thiolate and CuI Disulfide Equilibrium: A Combined Experimental and Theoretical Study. *Inorg. Chem.* **2014**, *53* (16), 8494–8504.
- (35) Ording-Wenker, E. C. M.; Siegler, M. A.; Bouwman, E. Coordination of New Disulfide Ligands to CuI and CuII: Does a CuII  $\mu$ -Thiolate Complex Form? *Inorg. Chim. Acta* **2015**, *428*, 193–202.
- (36) Ulery, A. L.; Drees, L. R. *Methods of Soil Analysis: Mineralogical Methods*; Soil Science Society of America, Inc.: Madison, WI, 2008; Vol. 5.
- (37) Nyquist, R. A. Thiols, Sulfides and Disulfides, Alkanethiols, and Alkanedithiols (S–H Stretching). *Interpreting Infrared, Raman, and Nuclear Magnetic Resonance Spectra*; Academic Press, 2001; Vol. 2, pp 65–83.
- (38) Nyquist, R. A. Aliphatic Amines. *Interpreting Infrared, Raman, and Nuclear Magnetic Resonance Spectra*; Academic Press, 2001; Vol. 1, pp 143–148.
- (39) Bensebaa, F.; Zhou, Y.; Brolo, A. G.; Irish, D. E.; Deslandes, Y.; Kruus, E.; Ellis, T. H. Raman Characterization of Metal-Alkanethiolates. *Spectrochim. Acta, Part A* **1999**, *55* (6), 1229–1236.
- (40) Bryant, M. A.; Pemberton, J. E. Surface Raman Scattering of Self-Assembled Monolayers Formed from 1-Alkanethiols: Behavior of Films at Au and Comparison to Films at Ag. *J. Am. Chem. Soc.* **1991**, *113* (22), 8284–8293.
- (41) Sandroff, C.; Garoff, S.; Leung, K. Surface-Enhanced Raman Study of the Solid/Liquid Interface: Conformational Changes in Adsorbed Molecules. *Chem. Phys. Lett.* **1983**, *96* (5), 547–551.
- (42) Joo, T. H.; Kim, K.; Kim, M. S. Surface-Enhanced Raman Scattering (SERS) of 1-Propanethiol in Silver Sol. *J. Phys. Chem.* **1986**, *90* (22), 5816–5819.
- (43) Ha Joo, T.; Kim, K.; Soo Kim, M. Surface-Enhanced Raman Scattering of 1-Butanethiol in Silver Sol. *J. Mol. Struct.* **1987**, *158* (C), 265–274.
- (44) McCarthy, C. L.; Webber, D. H.; Schueller, E. C.; Brutchey, R. L. Solution-Phase Conversion of Bulk Metal Oxides to Metal Chalcogenides Using a Simple Thiol–Amine Solvent Mixture. *Angew. Chem., Int. Ed.* **2015**, *54* (29), 8378–8381.
- (45) Lin, Z.; He, Q.; Yin, A.; Xu, Y.; Wang, C.; Ding, M.; Cheng, H.; Papandrea, B.; Huang, Y.; Duan, X. Cosolvent Approach for Solution-Processable Electronic Thin Films. *ACS Nano* **2015**, *9* (4), 4398–4405.
- (46) Liu, F.; Zhu, J.; Hu, L.; Zhang, B.; Yao, J.; Nazeeruddin, M. K.; Grätzel, M.; Dai, S. Low-Temperature, Solution-Deposited Metal Chalcogenide Films as Highly Efficient Counter Electrodes for Sensitized Solar Cells. *J. Mater. Chem. A* **2015**, *3* (12), 6315–6323.
- (47) Kumar, P.; Nagarajan, R. An Elegant Room Temperature Procedure for the Precise Control of Composition in the Cu-S System. *Inorg. Chem.* **2011**, *50* (19), 9204–9206.
- (48) Fernandes, P. A.; Salomé, P. M. P.; da Cunha, A. F. Study of Polycrystalline Cu<sub>2</sub>ZnSnS<sub>4</sub> Films by Raman Scattering. *J. Alloys Compd.* **2011**, *509* (28), 7600–7606.
- (49) Kemell, M.; Ritala, M.; Leskelä, M. Effects of Post-Deposition Treatments on the Photoactivity of CuInSe<sub>2</sub> Thin Films Deposited by the Induced Co-Deposition Mechanism. *J. Mater. Chem.* **2001**, *11* (2), 668–672.
- (50) Kaelin, M.; Rudmann, D.; Tiwari, A. N. Low Cost Processing of CIGS Thin Film Solar Cells. *Sol. Energy* **2004**, *77* (6), 749–756.
- (51) Dehghani, M.; Behjat, A.; Tajabadi, F.; Taghavinia, N. Totally Solution-Processed CuInS<sub>2</sub> Solar Cells Based on Chloride Inks: Reduced Metastable Phases and Improved Current Density. *J. Phys. D: Appl. Phys.* **2015**, *48* (11), 115304.
- (52) Stahl, M. S.; Azimi, H.; Brabec, C. J. A Facile One-Step Method to Reduce Surface Impurities in Solution-Processed CuInS<sub>2</sub> Nanocrystal Solar Cells. *J. Mater. Chem. A* **2015**, *3* (27), 14116–14120.
- (53) McCarthy, C. L.; Cottingham, P.; Abuyen, K.; Schueller, E. C.; Culver, S. P.; Brutchey, R. L. Earth Abundant CuSbS<sub>2</sub> Thin Films Solution Processed from Thiol–amine Mixtures. *J. Mater. Chem. C* **2016**, *4* (26), 6230–6233.